NASA Conference Publication 2408

Space Photovoltaic Research and Technology 1985

High Efficiency, Space Environment, and Array Technology

Proceedings of a conference
held at NASA Lewis Research Center
Cleveland, Ohio
April 30—May 2, 1985

NASA

National Aeronautics
and Space Administration

Scientific and Technical
Information Branch

1985

FOREWORD

Since the early days of the United States space program, the silicon solar cell has proven itself to be an efficient, reliable, and mission-enabling source of power for a wide variety of satellites and probes. Future projects, such as the space station, with requirements for multikilowatt power systems, will continue to offer challenges for the device researcher as well as the array designer. The need for high efficiency, long life, and inexpensive photovoltaic devices and systems is stronger than ever.

This meeting, the seventh of its kind over the past twelve years, serves as a forum to assess the progress made, the problems remaining, and the future strategy for space photovoltaic research. Each invited expert was expected to express his or her judgment to (1) help set suitable goals for space solar cell research and development, (2) define the obstacles preventing the attainment of these goals, and (3) surface the most viable approaches to overcoming these obstacles.

Three related overview papers were presented at this conference, continuing the practice started at the previous meeting. These covered the topics of future directions for photovoltaic research, power requirements for commercial spacecraft, and power management and storage for a space station. The intent was to present to the photovoltaic community the requirements dictated by the end users of the product of their research efforts.

The principle emphasis of the working meeting was placed on the exchange and discussion of ideas and opinions between individuals. This was fostered by an informal atmosphere and questions and discussion after each presentation. The discussions were focused on three areas. These areas and the individuals who generally accepted responsibility for managing them are as follows:

Cell research and technology, James Hutchby, Research Triangle Institute
Space environment, William Horne, Boeing
Array technology and applications, Paul Goldsmith, TRW

Oral reports from workshops in each of these three areas were presented and discussed in a plenary session. Written summaries of each workshop are included in this proceedings.

This seventh conference had the highest attendance (102) of any yet. The able leadership of David Brinker in organizing and coordinating it is sincerely and gratefully acknowledged.

Dennis J. Flood
NASA Lewis Research Center
Conference Chairman

PRECEDING PAGE BLANK NOT FILMED

CONTENTS

Page

OVERVIEW OF THE NASA PHOTOVOLTAIC TECHNOLOGY PROGRAM
Simon V. Manson, National Aeronautics and Space Administration . . . 1

FUTURE AIR FORCE SPACE POWER NEEDS
Joseph F. Wise, Air Force Wright Aeronautical Laboratories 17

OVERVIEW OF SERI'S HIGH EFFICIENCY SOLAR CELL RESEARCH
John P. Benner, Lee A. Cole and Cecile M. Leboeuf, Solar Energy Research Institute 23

FURTHER RESEARCH ON HIGH OPEN CIRCUIT VOLTAGE IN SILICON SOLAR CELLS
M.B. Spitzer and C.J. Keavney, Spire Corporation 27

GALLIUM ARSENIDE SOLAR CELL EFFICIENCY - PROBLEMS AND POTENTIAL
V.G. Weizer and M.P. Godlewski, NASA Lewis Research Center 41

N/P GaAs CONCENTRATOR SOLAR CELLS WITH AN IMPROVED GRID AND BUSBAR CONTACT DESIGN
Gregory D. DeSalvo, Ervin H. Mueller, and Allen M. Barnett, University of Delaware 51

HIGH-EFFICIENCY AlGaAs-GaAs CASSEGRAINIAN CONCENTRATOR CELLS
J.G. Werthen, H.C. Hamaker, G.F. Virshup, C.R. Lewis, and C.W. Ford, Varian Research Center 61

EVALUATION OF $Al_xGa_{1-x}As$ SOLAR CELLS
R.Y. Loo, G.S. Kamath, R.C. Knechtli, and A. Narayanan, Hughes Research Laboratories 69

GaAsP ON GaP TOP SOLAR CELLS
James B. McNeely, Gerald, H. Negley, and Allen M. Barnett, Astropower Division 77

VACUUM MOCVD FABRICATION OF HIGH EFFICIENCY CELLS FOR MULTIJUNCTION APPLICATIONS
L.D. Partain, L.M. Fraas, P.S. McLeod, and J.A. Cape, Chevron Research Company 87

CONTROL OF SUPERLATTICE MORPHOLOGY IN $GaAs_{1-x}P_x$ CASCADE CELLS
A.E. Blakeslee and A. Kibbler, Solar Energy Research Institute . . . 97

SUPERLATTICES AND MULTILAYER STRUCTURES FOR HIGH EFFICIENCY SOLAR CELLS
M. Wagner and J.P. Leburton, Department of Electrical Engineering and Coordinated Science Laboratory 103

A POSSIBLE RADIATION-RESISTANT SOLAR CELL GEOMETRY USING SUPERLATTICES
Chandra Goradia and Ralph Clark, Cleveland State University and David Brinker, NASA Lewis Research Center 111

PRECEDING PAGE BLANK NOT FILMED

EXPERIENCE WITH OMCVD PRODUCTION OF GaAS SOLAR CELLS
Y.C.M. Yeh, P.A. Iles, P. Ho, and K.S. Ling, Applied Solar Energy Corporation 119

BURST ANNEALING OF ELECTRON DAMAGE IN SILICON SOLAR CELLS
A.C. Day, W.E. Horne, M.A. Thompson, and C.A. Lancaster, Boeing Aerospace Company 127

I-V-T ANALYSIS OF RADIATION DAMAGE IN HIGH EFFICIENCY Si SOLAR CELLS
S. Banerjee, W.A. Anderson, and B.B. Rao, State University of New York at Buffalo 135

INFLUENCE OF DESIGN VARIABLES ON RADIATION HARDNESS OF SILICON MINP SOLAR CELLS
W.A. Anderson, S. Solaun, B.B. Rao, and S. Banerjee, State University of New York at Buffalo 147

RADIATION DAMAGE IN HIGH-RESISTIVITY SILICON SOLAR CELLS
I. Weinberg, C.K. Swartz, and C. Goradia, NASA Lewis Research Center 159

PROTON RADIATION EFFECTS ON $CdS/CuInSe_2$ THIN FILM SOLAR CELLS
H. Dursch, W. Chen, and D. Russell, Boeing Aerospace Company 165

DLTS ANALYSIS OF RADIATION-INDUCED DEFECTS IN ONE-MEV ELECTRON IRRADIATED GERMANIUM AND $Al_{0.17}Ga_{0.83}AS$ SOLAR CELLS
Sheng S. Li and C.G. Choi, University of Florida and R.Y. Loo, Hughes Research Laboratories 171

DEPLETION LAYER RECOMBINATION EFFECTS ON THE RADIATION DAMAGE HARDNESS OF GALLIUM ARSENIDE CELLS
G.F.J. Garlick, Spectrolab, Inc. 181

PERFORMANCE OF HUGHES GaAs CONCENTRATOR CELLS UNDER 1-MeV ELECTRON IRRADIATION
Henry B. Curtis and Clifford K. Swartz, NASA Lewis Research Center 189

INTERPLANETARY EXPLORATION - A CHALLENGE FOR PHOTOVOLTAICS
Paul M. Stella, Jet Propulsion Laboratory 195

TWO YEARS OF ON-ORBIT GALLIUM ARSENIDE PERFORMANCE FROM THE LIPS SOLAR CELL PANEL EXPERIMENT
R.W. Francis, The Aerospace Corporation and F.E. Betz, U.S. Naval Research Laboratory 203

PASP - A HIGH VOLTAGE ARRAY EXPERIMENT
John Scott-Monck, Jet Propulsion Laboratory and Robert Morris, Air Force Wright Aeronautical Laboratories 217

TESTING OF GALLIUM ARSENIDE SOLAR CELLS ON THE CRRES VEHICLE
Terry M. Trumble, Air Force Wright Aeronautical Laboratories 225

THERMAL STRESS CYCLING OF GaAs SOLAR CELLS
Bruce K. Janousek, Robert W. Francis, and Jerry P. Wendt,
The Aerospace Corporation 231

DEMONSTRATED RESULTS OF WELDED AND SOLDERED INTERCONNECTIONS
Russell E. Hart, Jr., NASA Lewis Research Center 239

THIN FILM COATINGS FOR IMPROVED α/ε RATIOS
M. Eric Krisl and I.M. Sachs, OLCI 243

POWER REQUIREMENTS FOR COMMERCIAL COMMUNICATIONS SPACECRAFT
W.J. Billerbeck, COMSAT Laboratories 257

SPACE STATION POWER MANAGEMENT AND DISTRIBUTION
Fred Teren, NASA Lewis Research Center 279

CELLS RESEARCH AND TECHNOLOGY WORKSHOP
James Hutchby, Research Triangle Institute 287

SPACE ENVIRONMENT WORKSHOP
W.E. Horne, Chairman, Boeing Aerospace Company 289

ARRAY TECHNOLOGY AND APPLICATIONS
Paul Goldsmith, TRW Space and Technology Group 293

OVERVIEW OF THE NASA PHOTOVOLTAIC TECHNOLOGY PROGRAM

Simon V. Manson
National Aeronautics and Space Administration
Washington, D.C.

The objective of the NASA-OAST photovoltaic technology program is to develop advanced photovoltaic energy conversion options for use in future space missions, illustrated generically in figure 1.

E-2706-1

PROGRAM STRUCTURE

The structure of the photovoltaic technology program is indicated in figure 2. The research and technology areas listed on the left side of this figure are aimed at producing technical options that can meet the objectives shown in the center of the figure (high efficiency, long life, low weight, reduced cost). From the alternative approaches that are developed, selections can be made to meet diverse mission performance requirements. The use of alternative solar cell and array options to achieve challenging mission-related performance goals is illustrated in figure 3.

PROGRAM CONTENT

The technology program's direction and content are substantially influenced by inputs from the national and international photovoltaic communities, and by recommendations from select industry-university-government advisory groups. In the current program, the following approaches are being pursued:

a) High efficiency options are being developed by working with promising single- and multiple-bandgap cells and promising geometries (fig. 4), solar concentrator cells and arrays (fig. 5), and advanced devices such as thermophotovoltaics and plasmons.

b) Long life array technology is being developed through efforts addressing array-environment interactions, which include radiation damage from protons and electrons (fig. 6), atomic oxygen attack thermal cycling due to alternate sunlight and darkness in Earth orbit (fig. 7), spacecraft charging at high altitudes (e.g., GEO) and spacecraft interactions with the surrounding plasma at lower altitudes (LEO) (fig. 8).

c) Lightweight array options are being studied using high-efficiency cells such as IR-transparent, back-gridded silicon cells with or without reflective coatings; III-V cells; thin blankets employing thin cells and thin substrates and superstrates; and lightweight structures.

d) Low cost options are being advanced (1) by using reduced amounts of photovoltaic material, currently achieved through use of very thin and/or high concentration-ratio cells, and (2) by reducing fabrication costs, currently

attempted through use of large cells and large superstrates and through automation, which is facilitated by wraparound cell contacts and automated welding.

FLIGHT EXPERIMENTS

The technology program includes flight experiments aimed at identifying space environment properties and their impacts, and at assessing whether available design procedures correctly determine beginning-of-life, operational, and end-of-life array performance.

RECENT PROGRAM AND PLANS

Program accomplishments in Fiscal Year 1984 are listed in figure 9. The program content in FY 1985 is shown in figure 10; this figure also identifies the generic areas addressed by the respective NASA Field Centers: cell development at the Lewis Research Center (LeRC), lightweight arrays at the Jet Propulsion Laboratory (JPL), and high power Low Earth Orbit arrays at the Marshall Space Flight Center (MSFC). Program directions for FY 1986 are outlined in figure 11. Five-year and twenty-five-year photovoltaic technology plans are indicated in figures 12 and 13, respectively.

SUMMARY

The NASA-OAST photovoltaic technology program continues to be broadly based and broad in scope. The goals shown in individual figures and summarized in figures 12 and 13 are highly challenging; the efforts of industry, universities, government laboratories, and technology managers will be required for achievement of these goals.

NATIONAL LANDMARK MISSIONS

CIVIL
- ★ UNMANNED OUTER PLANET
- ★ UNMANNED INNER PLANET
- ★ MANNED PLANETARY
- ★ LUNAR BASE
- ★ ADVANCED SPACE STATION
- ★ STARPROBE

COMMERCIAL
- ★ DIRECT BROADCAST SATELLITE
- ★ SPACE MANUFACTURING
- ★ GLOBAL RESOURCE MONITORING

MILITARY
- ★ SPACE BASED RADAR
- ★ SPACE DEFENSE
- ★ ADVANCED NAVIGATION SYSTEM
- ★ COMMUNICATION COMMAND & CONTROL
- ★ SURVEILLANCE & WARNING

TECHNOLOGY REQUIREMENTS
- ★ POWER
- ★ PROPULSION
- ★ ELECTRONICS
- ★ GUIDANCE & CONTROL
- ★ COMMUNICATION
- ★ MATERIALS & STRUCTURES
- ★ LAUNCH CAPABILITIES

Figure 1.

CD-84-14614

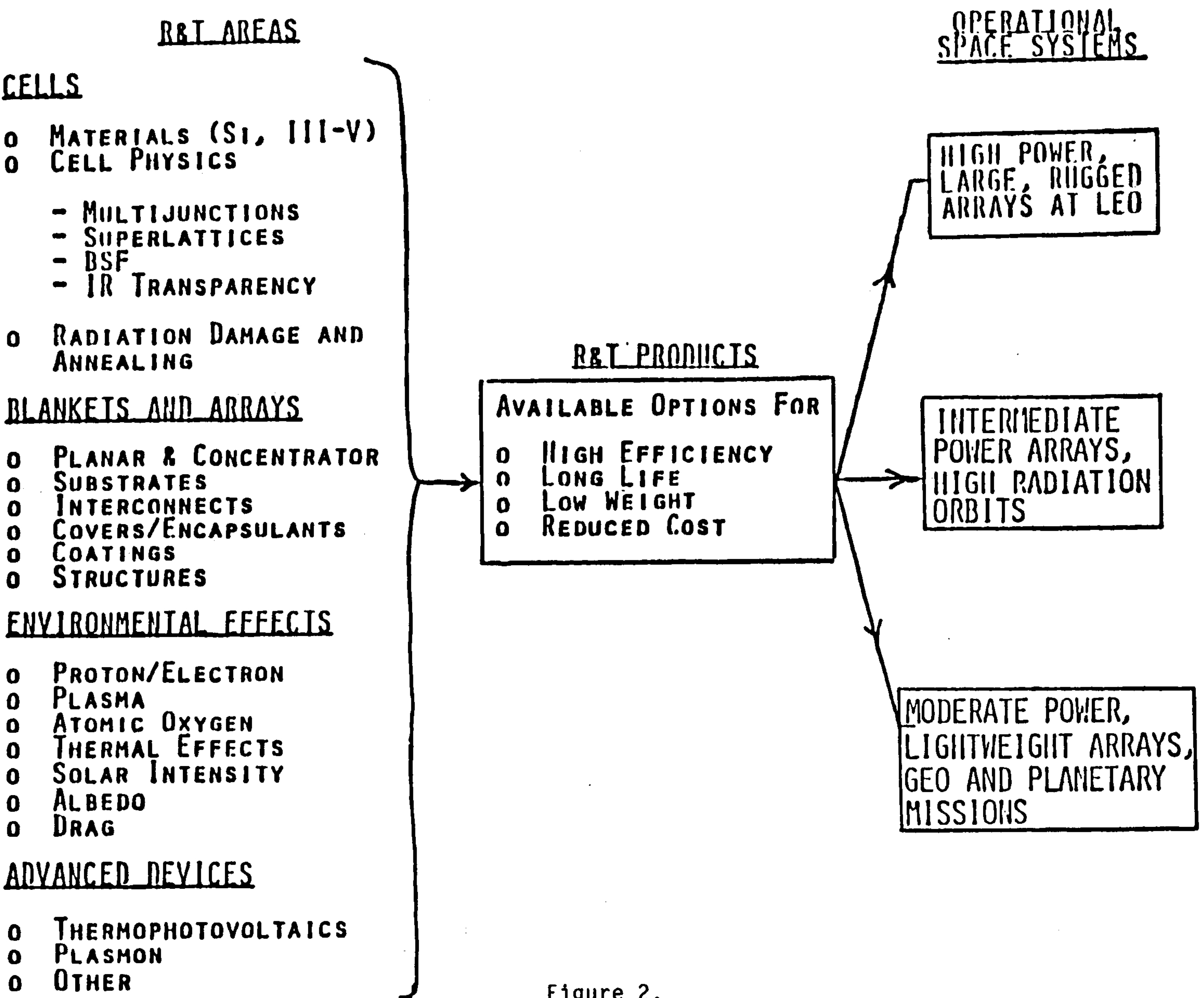

Figure 2.

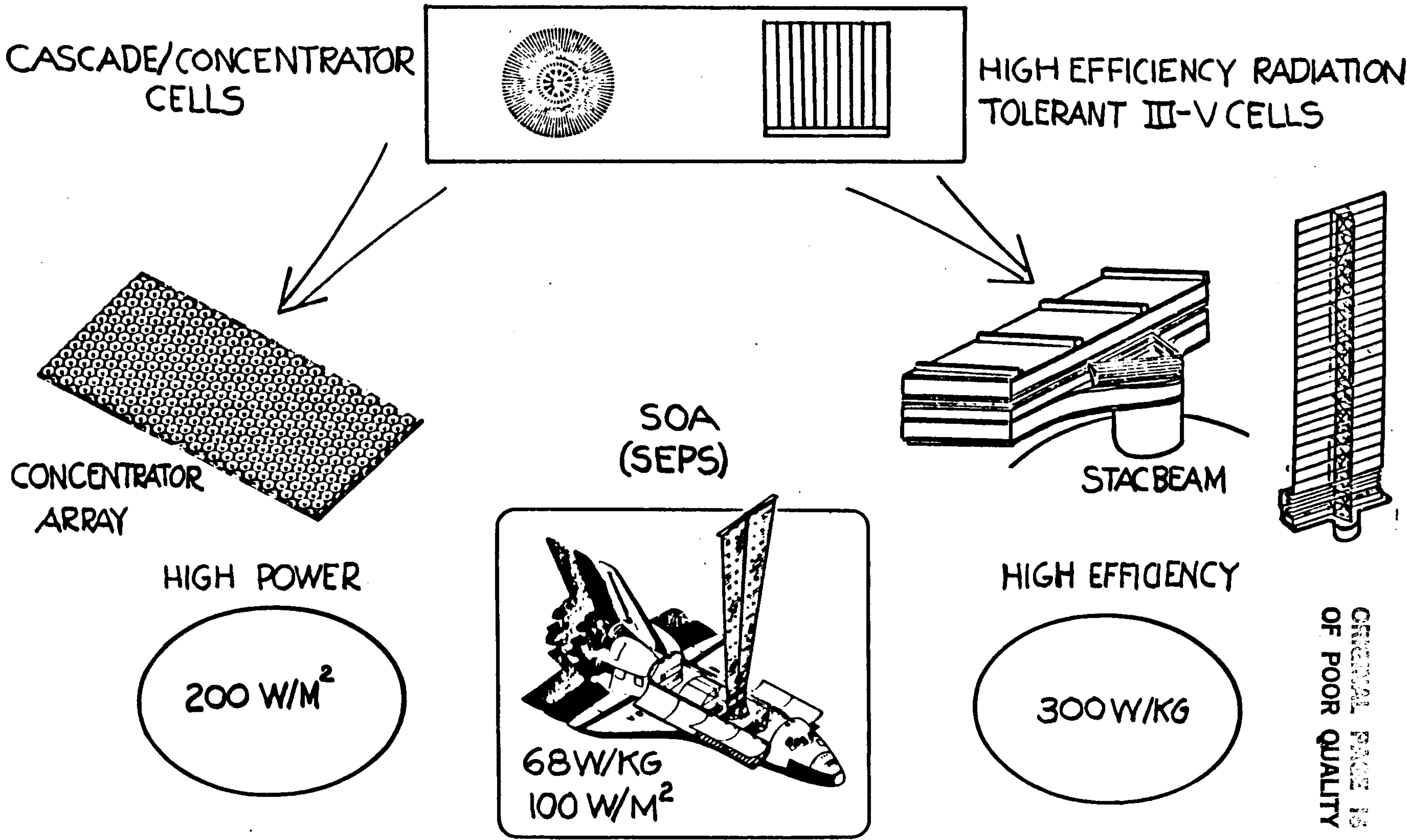

Figure 3.

ORIGINAL PAGE IS OF POOR QUALITY

ADVANCED CELLS

14% 50μ SILICON

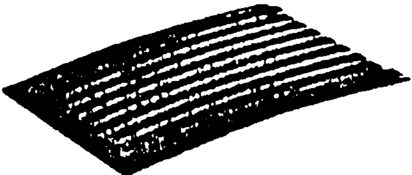

14% 16μ TRANSPARENT GALLIUM ARSENIDE

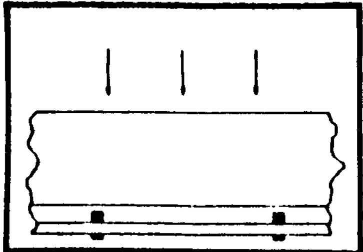

* ACHIEVED 14.1% AMO 6μm THICK CLEFT GaAs CELL
* DEMONSTRATED CLEFT AlGaAs LAYERS
* EXPLORING MECHANICALLY STACKED CASCADE

LARGE AREA MILSTAR CELL

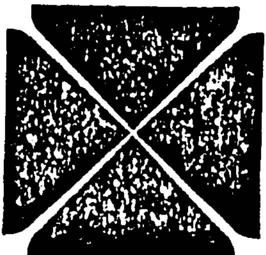

SHALLOW HOMOJUNCTION GaAs SOLAR CELL

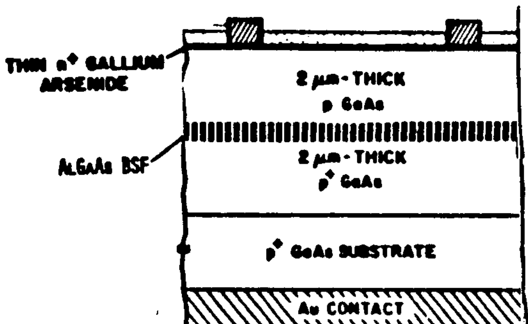

- o 18% EFFICIENCY ACHIEVED
- o INCORPORATION OF $Al_{.2}Ga_{.8}As$ P^{+} LAYER RESULTS IN AN IMPROVED BACK SURFACE FIELD, IMPROVED EFFICIENCY

GOAL: 30% EFFICIENCY

DOT GRATING CELL SURFACE PASSIVATED

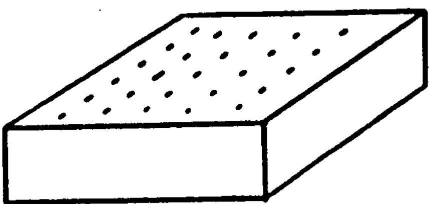

THREE JUNCTION CASCADE, VARIAN

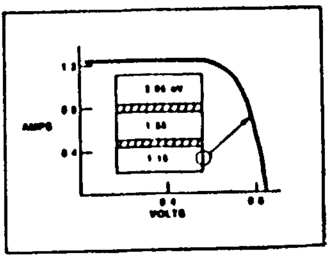

* 17.6% AMO, 1.15eV, GaInAs DEMONSTRATED, 100X, 25°C
* > 90% QUANTUM EFFICIENCY 1.55eV, GaAsP, GaAlAs
* STABLE Mg p-TYPE DOPANT DEVELOPED

Figure 4.

CONCENTRATOR ARRAY TECHNOLOGY

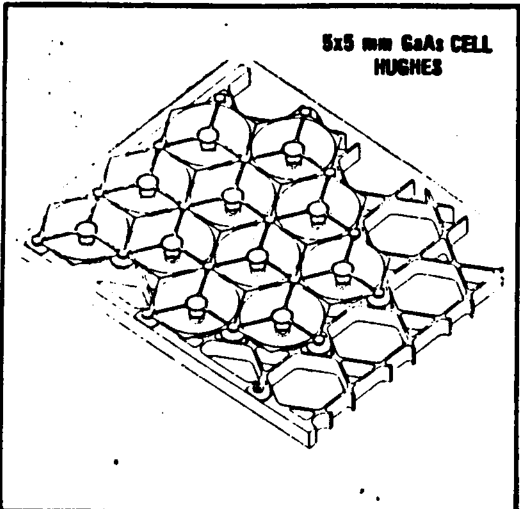

MINIATURE CASSEGRAINIAN TRI-HEX ISOGRID ARRAY PANEL CONCEPT TRW

- ★ 19% (100X, 80° C) CELL DEMONSTRATED
- ★ LIGHTWEIGHT, RIGID PANEL DESIGN

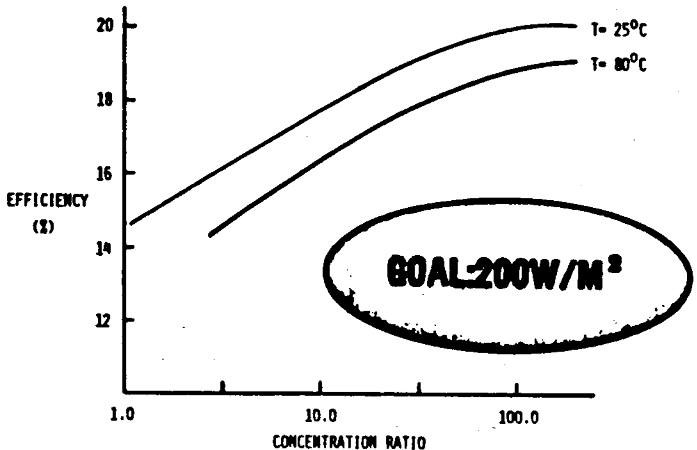

Concentrator Cell Performance

ORIGINAL PAGE IS OF POOR QUALITY

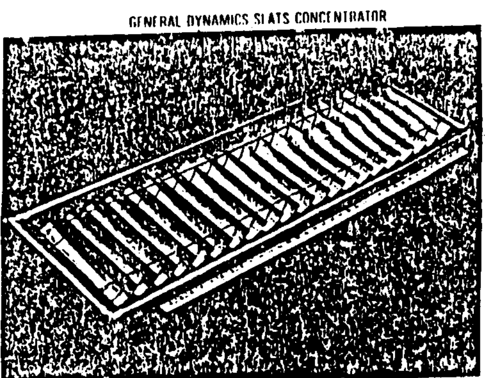

100-KW ARRAY SYSTEM ANALYSIS SUMMARY

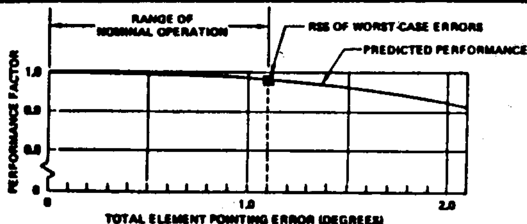

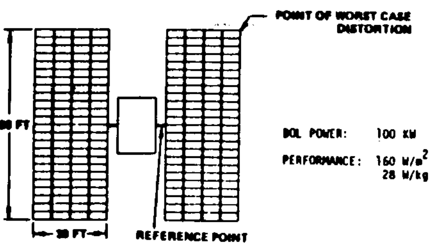

POINTING ERROR COMPONENT	POINTING ERROR (DEGREES)
THERMAL DISTORTION	± 0.2
MANUFACTURING*	± 0.0
CONTROL SENSING	± 0.1
DYNAMIC** DISTORTION	± 0.7
SUM	1.0
RSS	1.1

* WORST-CASE SUM

** WORST-CASE CREW MOTION (NOT TIME PHASED)

Figure 5.

RADIATION DAMAGE STUDIES

LITHIUM COUNTERDOPED n/p CELL

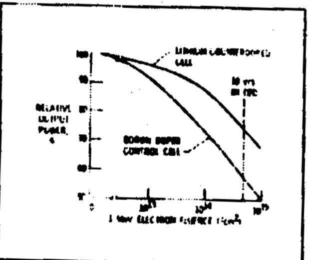

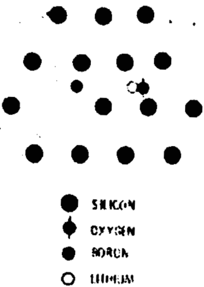

* DECREASED RADIATION DAMAGE
* ELIMINATION OF HARMFUL BORON-OXYGEN DEFECT
* SIGNIFICANT ANNEALING AT 100° C

Proton Radiation Damage in GaAs and Si Space Cells

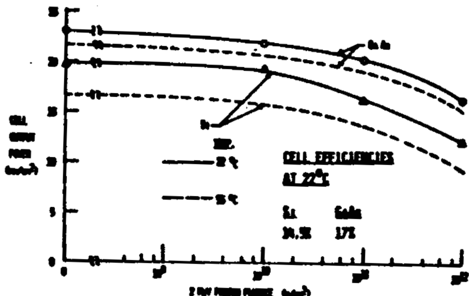

Arsenic Anti-Site Defect

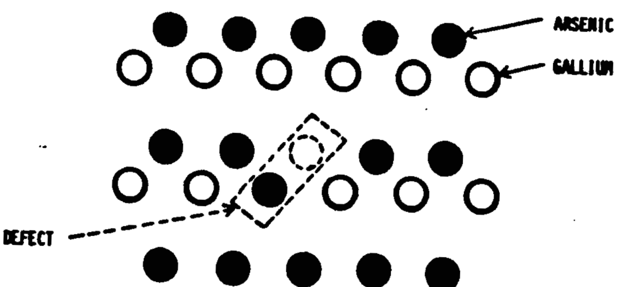

DEFECT CONCENTRATION DECREASED BY ADDING ATOMIC HYDROGEN

* CONCENTRATOR PROVIDES MORE POWER PER UNIT AREA
* CONCENTRATOR ARRAY SMALLER FOR ALL MISSIONS
* CONCENTRATOR ARRAY LIGHTER FOR VAN ALLEN BELT MISSIONS

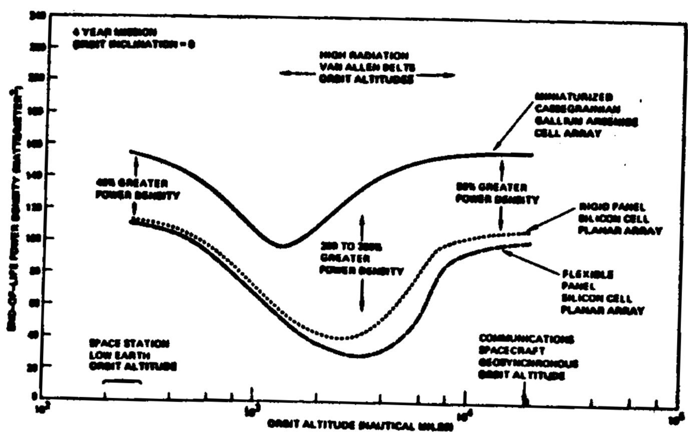

Figure 6.

ORIGINAL PAGE IS
OF POOR QUALITY

ENVIRONMENTAL EFFECTS: INTERCONNECT THERMAL CYCLING

WELDED CELLS TESTED; ≥ 6 YR LIFE DEMONSTRATED

Figure 7.

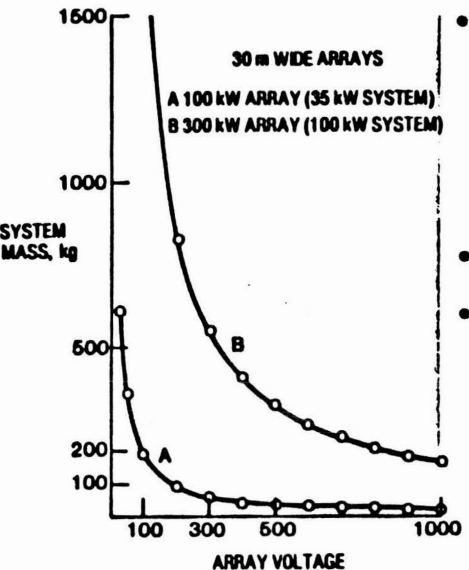

- FOR LARGE HIGH POWER SPACE SYSTEMS, HIGH VOLTAGE RESULTS IN SIGNIFICANT REDUCTION IN SYSTEM MASS
  e.g. FOR 35 kW POWER SYSTEM (CURVE A)
  ~600 kg AT 30 V
  ~60 kg AT 300 V
- KNOWN SAFE REGION IS BELOW ~100 VOLTS
- HIGHEST VOLTAGE SYSTEM IN LEO TO DATE WAS SKYLAB (100 V, 12 kW)

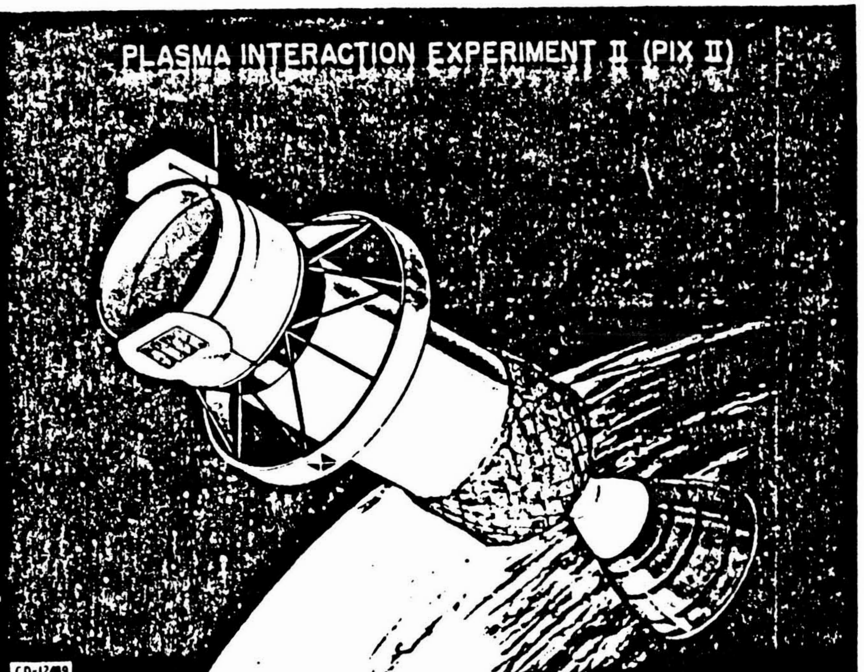

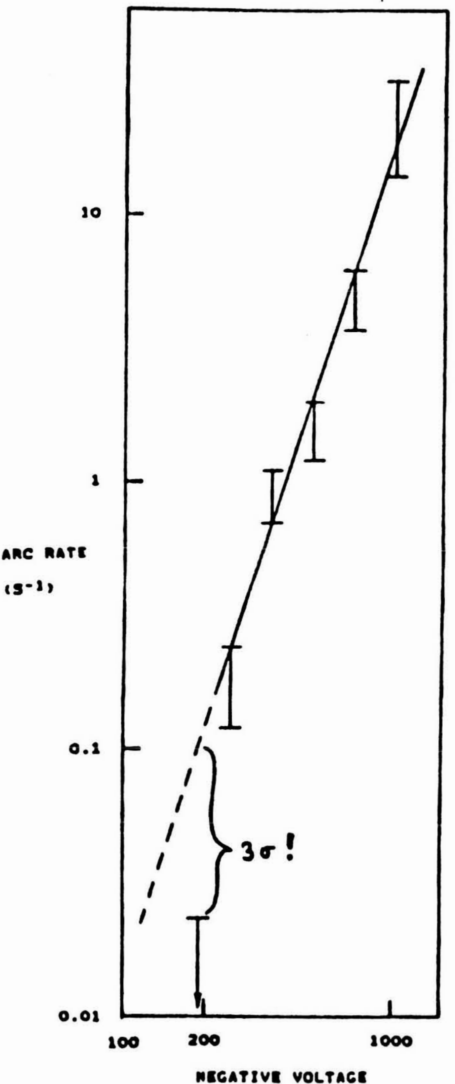

Figure 8.

ORIGINAL PAGE IS
OF POOR QUALITY

1984 ACCOMPLISHMENTS

CELLS

- INCREASED RADIATION RESISTANCE OF SILICON SOLAR CELLS BY LITHIUM COUNTERDOPING DEMONSTRATED
- INFRARED-TRANSPARENT SILICON SOLAR CELL TECHNOLOGY ADVANCED
- 18% EFFICIENT N/P GaAs HOMOJUNCTION CELL DEMONSTRATED
- LATTICE DEFECT IN GaAs PASSIVATED BY INTRODUCTION OF ATOMIC HYDROGEN
- GaAs COMPUTED TO BE SUPERIOR TO SILICON IN RESISTANCE TO PROTON RADIATION AT GEO
- InP TECHNOLOGY PROGRAM INITIATED

MODULES, PANELS

- GaAs PROTO-CELL AND MODULES DEVELOPED USING AUTOMATED WELDING
- MINIATURE CASSEGRAINIAN CONCENTRATOR (MC^2) SOLAR PANEL FABRICATION TECHNOLOGY ADVANCED

ARRAYS

- INTERCONNECT DURABILITY DEMONSTRATED
- LIGHTWEIGHT BLANKET DESIGNS SUCCESSFULLY THERMAL CYCLED
- STACBEAM II MODEL FABRICATED, DEMONSTRATED IN GROUND TESTS

FLIGHT EXPERIMENTS

- OAST-1
- APEX/LDEF
- MC^2 MIRROR MATERIALS/LDEF

Figure 9.

FY 1985 PHOTOVOLTAIC PROGRAM

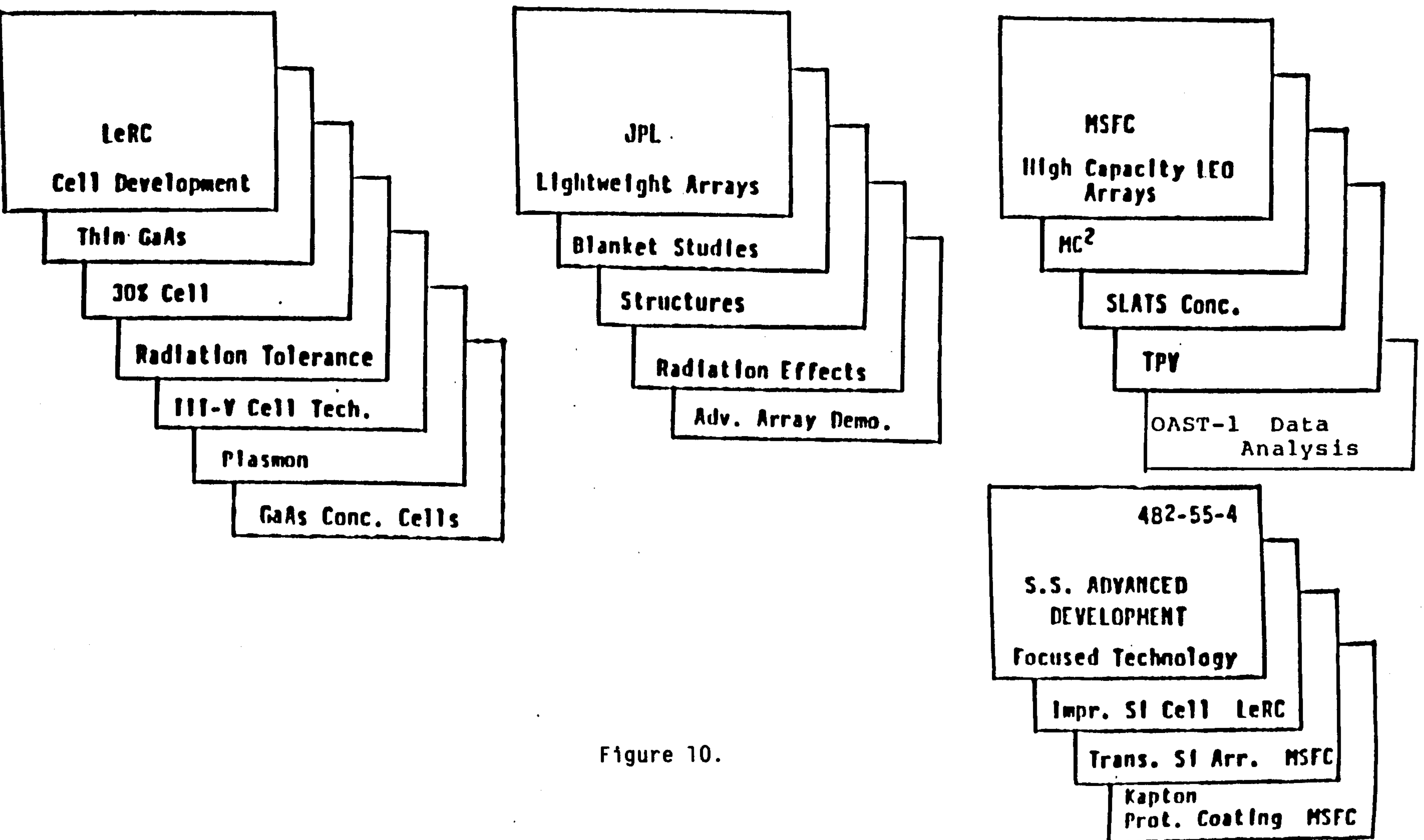

Figure 10.

FY 1986 DIRECTIONS

PHOTOVOLTAICS

CELLS AND DEVICES

- GaAs, InP, AND OTHER III-V COMPOUNDS
- CONCENTRATOR CELLS
- ULTRA-THIN CELLS
- PLASMON, MULTI-BANDGAP DEVICES, AND SUPERLATTICES
- RADIATION DAMAGE STUDIES, EXPERIMENTS

MODULES, PANELS

- MC^2, SLATS, TPV
- IR-TRANSPARENT SILICON

ARRAYS

- HIGH PERFORMANCE (300 W/KG) ARRAY DESIGN FINALIZATION
- FABRICATION START ON TRANSPARENT BLANKET, ARRAY HARDWARE

Figure 11.

PHOTOVOLTAIC ENERGY CONVERSION

Figure 12.

SPACE ENERGY SYSTEMS

25 YEAR OUTLOOK

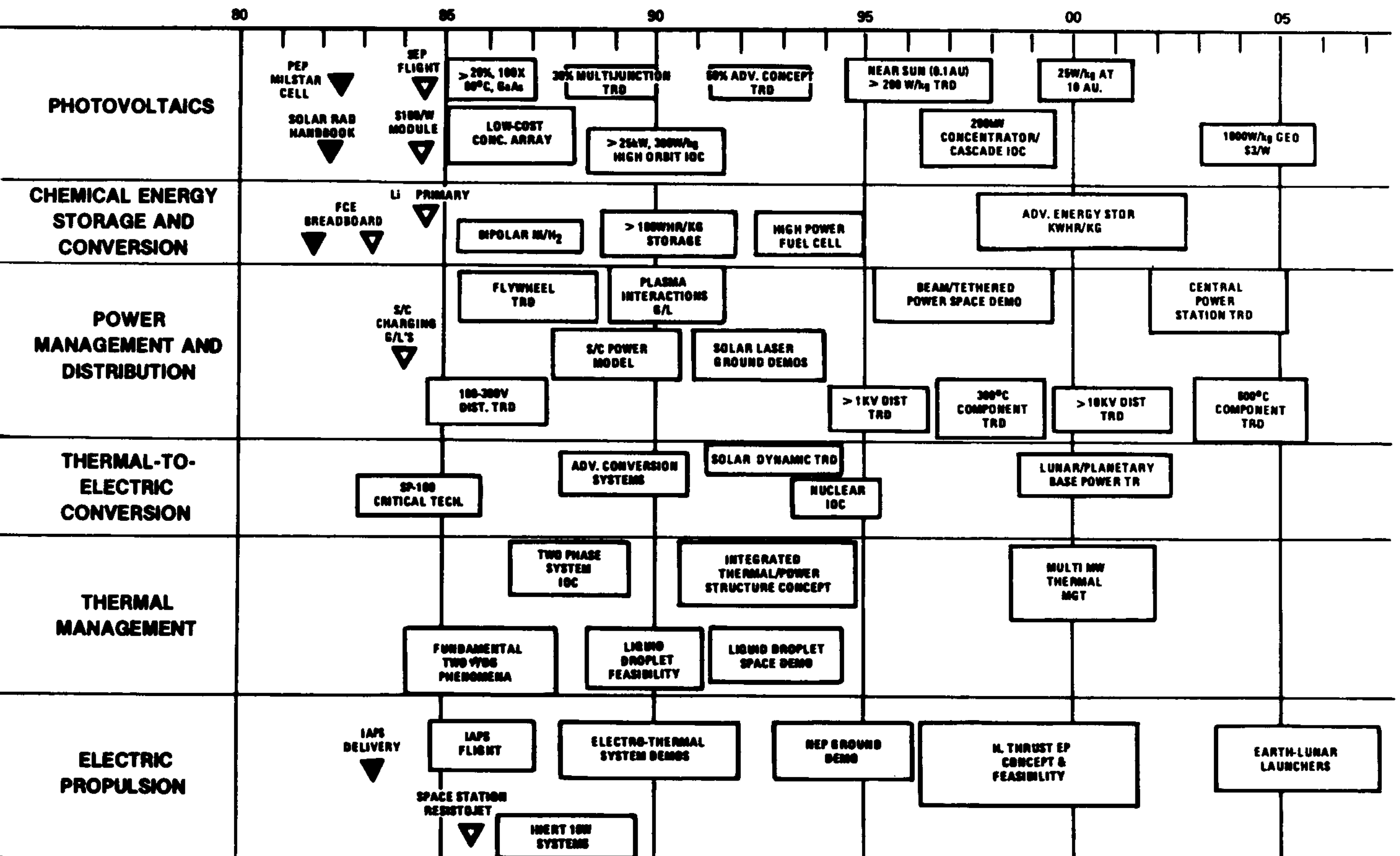

CD-84-14615

Figure 13.

N86-17840

FUTURE AIR FORCE SPACE POWER NEEDS

Joseph F. Wise
Air Force Wright Aeronautical Laboratories
Aero Propulsion Laboratory
Wright Patterson AFB, Ohio

This paper outlines those space power capabilities needed to meet future Department of Defense needs. The most immediate need is for survivable power systems up to 50 kilowatts. This implies capabilities need to be developed in the areas of increased size, higher reliability, hardening to weapon effects, and autonomy - to be independent of ground stations for satellite control.

Future power systems, as in the past, will need to be able to function in all earth orbits with different requirements for the various orbits. For low and medium altitude orbits the primary considerations are environmental effects and ground based threats. For the high orbits such as geosychronous, the primary considerations are system weight and lifetimes up to ten years. Also as the mission hardware becomes more critical, techniques for array control and pointing must be developed which minimize disturbances to the rest of the satellite vehicle.

Higher power requirements demand high voltage systems. This in turn introduces new considerations such as more interactions with the space environment, higher stress on electronic power control components, and more shielding due to enhanced conditions for arcing and corona. Some progress is underway in these areas. Now some communications satellites are generating voltages over 100 volts directly to provide power to traveling wave tubes. There are also several groups investigating the interactions of the space environments with satellite subsystems including plans for flight experiments (VOLT, IMPS/SPAS). Several high power system studies have been done for the Air Force and NASA which have also studied autonomy and AC vs DC systems. At what power level do the AC systems become attractive and at how high a frequency can we operate these systems? These issues and questions will need to be addressed in the next few years.

INTRODUCTION

The requirements for future power as outlined for various AF satellite mission vehicles in the Military Space System Technology Plan, Volume II, fall into two categories. The first category is in the 1 to 50 kW range for mission of a continuous nature such as communication, navigation, surveillance, data relay and meteorology. The second category is in the multi-megawatt range for either continuous or burst power durations and are for other than solar power sources. Requirements for longer life and survivability in varying degrees are

PRECEDING PAGE BLANK NOT FILMED

there for all-systems. While the power levels do not appear difficult to achieve in view of the large array developments pursued by NASA Space Station technology, the other military requirements are very challenging and continue to be system drivers. The development of solar cell arrays should be in conjunction with other power supply technologies such as regulation and control components and energy storage subsystems. The needs of future power systems are shown in Table 1.

SURVIVABILITY

The primary new requirement for future AF solar power systems is survivability. This requirement is different for each satellite vehicle and mission and can be approached from several different directions. Table 2 provides a brief history of these directions. In some cases the threat is directly on the satellites. For a direct threat hardening to withstand exposure to the weapons environment is contemplated through the use of concentrator technology . For higher altitude orbits wherein weight is important the hardening may be at a lower level in lightweight solar array concepts.

Active approaches to survivability imply at least two: (1) evasive maneuvering and (2) recovery after exposure. Both of these require autonomy of operation independent of ground stations. Autonomy is also needed if the ground stations themselves are vulnerable and mission survival depends on the satellite being capable of operation without their intervention. To achieve autonomy for the power system we need to develop the functions shown in Table 3.

To survive via redundancy or the use of decoys implies the flight of satellites that can look like active vehicles but can be low in cost and realistic in signature. Paramount considerations here would be low cost solar cell arrays.

SOLAR CELL TECHNOLOGY

The solar cells needed for the concentrator type solar cell arrays are those that can operate efficiently at temperatures of 100°C (or greater). The candidate cells to date for this are GaAs. Efficiency under concentration can be 20% or greater at operating temperatures. Future concentrating systems imply the use of small multi-bandgap solar cells with efficiency in the 25 to 30% range. Solar cells for lightweight minimum hardening high orbit application are thin GaAs solar cells to achieve solar cell blanket performance of 100 to 150 watts per pound. These cells need also be able to withstand temperature excursions and the effects of charge build up and arcing as they emerge from the dark to sunlit portions of the orbits. The multi-bandgap cells could also be of benefit here if they can be made efficient without high cost.

The potential use of decoys challenges us to search for low cost, high lifetime solar cells. Some of the cell types under development by the Department of Energy should be considered once reasonable efficiency is achieved.

Candidates in this case are amorphous silicon or polycrystaline cells wherein the satellite decoy is to have the same observable signature as the mission vehicle without the mission power requirements. Low cost fabrication and assembly are also needed.

HIGH POWER CONSIDERATIONS

Satellite power requirements increase for several reasons such as more functions in the same vehicle, more sensitivity in such missions as surveillance, or higher power signal to avoid jamming or power to communicate with mobile systems in the air or on the earth's surface. Table 4 identifies considerations for High Power

The mission hardware on these satellites may therefore require larger solid angles of observation or greater accuracy to lock on and dwell on target. The solar cell arrays must minimize the blockage or disturbance of this mission hardware. The demand therefore is to minimize solar array size thus dictating high solar cell efficiency. Also, pointing of the array at the sun should be decoupled from the mission vehicle or other means must be used to minimize disturbances.

As these power requirements increase we need to develop building blocks for array standardization. Such modular subarrays should be in the 5 kW power range and be for easy build up into complete solar arrays. This approach should provide economy of fabrication using automated production equipment and could be the first step toward in-orbit assembly and replacements. As the Space Station and Shuttle utility matures, more Extra Vehicular Activity (EVA) is likely to assemble and service or refurbish satellite vehicles. Modular, easily replaced solar cell array packages should be a part of these activities.

The issues involved in interactions with the space environment become more critical as the size and voltage of the solar cell array increase. These effects were briefly discussed in last year's space power systems conference[1]. and are presented in Table 5. These issues are being addressed in the Interactions Measurements Platform for Shuttle (IMPS) programs through analysis and ground tests as well as flight tests as will be discussed later in this conference.

CONCLUSIONS

Military requirements for solar power will continue to increase at a moderate rate up to 50 to 100 kW. Future emphasis for all Department of Defense hardware will be on survivability. We must continue to search for and develop technology to react to the various threat and survival scenarios in reliable, light weight and cost effective ways. The bottom line for new technology is reliability and end of life efficiency.

---

1. Space Power, NASA Conference Publication 2352, April 10 - 12, P286, L. C. Childester & J. F. Wise.

ORIGINAL PAGE IS
OF POOR QUALITY

TABLE 1. - FUTURE AIR FORCE POWER REQUIREMENTS

0	Survivability	Laser nuclear weapons effects
0	Power level	1 - 100 kW (1990 - 2000)
0	Power level peak	1:10 ratio
0	Orbits	All earth orbits Low, mid, high, elliptical
0	Lifetime	5 - 10 years
0	Reduce	Area, weight and cost

TABLE 2. - SURVIVABILITY OPTIONS/METHODOLOGY

Passive	Harden to exposure levels of weapon species
Active	0 Evasive maneuvering 0 Autonomy, sense/reconfigure
Detection/disguise	0 Silent spares 0 Decoys 0 Dummy vehicles

TABLE 3. - ACTIVE SURVIVABILITY TECHNOLOGY

0 Autonomy of power system

0 Sense damage and malfunction

0 Adjust and reconfigure to minimize degradation

0 Become independent of vulnerable ground stations

0 Load management to meet needs and prolong life

0 Monitor and assess system health

0 Maintain system i.e. solar cell annealing, battery reconditioning

TABLE 4. HIGH POWER CONSIDERATIONS MISSION CONTSTRAINTS

- Look Angles, Disturbance
- Modularity - Size
Activity
- Environmental interactions
- Orientation and power transfer
- Autonomous functions - Switching

TABLE 5. - ENVIRONMENTAL EFFECTS

- Radiation Damage
- Arcing/Discharge at High Voltage
- Atomic Oxygen Erosion
- Thermal Cycling
- Atmospheric Drag
- Corona in Enclosed Volumes
- Combined Effects of the Above

N86-17841

OVERVIEW OF SERI'S HIGH EFFICIENCY SOLAR CELL RESEARCH

John P. Benner, Lee A. Cole and Cecile M. Leboeuf
Solar Energy Research Institute
Golden, Colorado

The general level-of-interest in high efficiency terrestrial solar cells is increasing. Projected efficiencies of more than 20% are now considered attainable, not only in GaAs based cells, but also in multijunction amorphous and polycrystalline devices. As III-V solar cells approach this high performance level, increasing concern is directed toward questions regarding large area production potential. SERI's program will increase research emphasis on the study of mechanisms involved in growth of III-V semiconductors in order to develop answers to these questions.

INTRODUCTION

In 1983, the U.S. Department of Energy established the Five Year Research Plan for the National Photovoltaics Program.(1) The objective of this plan is to perform the high risk research needed to establish a technology base from which industry can develop photovoltaic systems for central station applications. The targeted performance of such installations is to provide power to the grid at a cost of less than fifteen cents per kilowatt hour. (thirty-year levelized cost). One approach to achieve this goal is to greatly increase the efficiency of flat plate and concentrator solar cells. The plan contains milestones to achieve efficiencies of 20% in thin-film gallium arsenide (GaAs) solar cells in 1986 and to reach 35% efficiencies in multijunction concentrator cells in 1988. In order to achieve these goals, research is needed to improve the quality of the III-V semiconductor crystal layers and to improve the solar cell structures to compensate for less-than-ideal semiconductor properties. The High Efficiency Concepts Task at the Solar Energy Research Institute (SERI) supports research to achieve these milestones.

Currently, the task supported research can be grouped into three different techniques for preparation of semiconductor layers. These are growth on low cost substrates which typically results in polycrystalline layers; growth of single crystal thin films and separation from the substrate; and heteroepitaxial growth of GaAs or ternary alloys on GaAs or silicon. Each of these approaches presents some difficult problems for the crystal grower and device designer.

Polycrystalline Gallium Arsenide

The first approach has so far proved to be most difficult. The films are generally polycrystalline with an average grain size less than a few millimeters. Achievement of this grain size requires various recrystallization processes. This can result in segregation of impurities and possibly precipitates at the grain boundaries.(2) The grain boundaries may then provide shunt paths reducing the performance of the cells. Several studies of films prepared with impurity-free grain boundaries have shown the validity of the double depletion layer model for polycrystalline GaAs.(3,4) This model suggests that even clean boundaries will be detrimental to solar cell performance. One study has shown that the intragrain properties of a few defective grains may be the dominant cause of poor performance in some solar cells.(4) Thus, the approach using low-cost substrates presents several challenging problems. Some

PRECEDING PAGE BLANK NOT FILMED

topics of interest include grain size enhancement or formation of single crystal films on low-cost substrates; passivation or neutralizaton of grain boundaries; doping of polycrystalline films; and development of device structures which minimize the detrimental effects of the non-ideal films.

Single Crystal Thin Films

The second approach, relying on reuse of a more expensive substrate which promotes single crystal growth, has shown more success. Using lateral overgrowth of a masked GaAs substrate, with film separation by controlled cleavage, thin film cells have achieved reported efficiencies of nearly 19%.(5) Continued research on this approach (termed Cleavage of Lateral Epitaxial Films for Transfer or CLEFT) is expected to achieve the 1986 DOE Five Year Plan milestone for thin-film gallium arsenide. Other techniques for separation of single crystal films heteroepitaxially grown on low melting point or selectively etchable layers provide promise of useful alternative technologies.(6,7) Another opportunity for this general approach is the separation of high efficiency cells having a bandgap of approximately 1.75 eV which can be mechanically stacked or silicon solar cells to form a very high efficiency optically cascaded stacked concentrator cell or flat plate module. Given that the films are single crystal, the device design and development are somewhat more straight forward. However, control of the solar cell's thickness may yield higher performance than is obtainable in a bulk device.(8) This area will benefit from research on alternatives to the CLEFT process for growth, separation and handling of thin single crystal films.

Heteroepitaxy

The final area, heteroepitaxial growth of single crystal layers, covers both growth of ternary and quaternary alloys on GaAs substrates for concentrator cells as well as growth of III-V semiconductors on silicon or germanium-silicon substrates. The preparation of monolithic multijunction cells of very high efficiency is attractive for both concentrator and flat plate modules due to the simplicity of interconnection in the overall system. They also offer potential for lower optical losses and fewer problems with removal of heat. With the exception of the AlGaAs/GaAs system, heteroepitaxial III-V systems introduce problems of control of lattice misfit dislocations and, in some systems, mismatch of thermal expansion coefficients. Various techniques for composition grading and superlattices are under study to provide control of propagation of dislocations.(9,10) The use of controlled strain between layers is seen to minimize propagation of dislocations. However, in the case of growth of GaAs solar cells on silicon substrates, it is suggested that the strain induced by dopants forming the p-n junction actually causes dislocations to bend over at the junction.(11) This would place the highest density of recombination centers in the space charge region. This reasoning would explain the lower measured open circuit voltage and fill factor than would be expected from the observed defect density at the surface of the sample. In systems with mismatched thermal expansion coefficients, some samples will develop micro-cracks upon cooling from growth temperatures. These problems can be best addressed by joint efforts in crystal growth and device design.

Basic Studies

In addition to the specific problem areas listed above, the High Efficiency Concepts Task at SERI is interested in several other general research problems. Most of the current efforts use metalorganic chemical vapor deposition (MO-CVD). Several studies have identified impurities

in current source materials which create electrically active defects (12,13) in the resulting semiconductors. MO-CVD is still a relatively new crystal growth technology with new generations of potential source materials still being introduced. There is considerable room for improvement in the understanding of the chemistry of the reactions which result in growth of the crystals and production of effluents. Analysis of gas flows and of source depletion is important for the development of an analytic approach to design of CVD reactors.

Reducing the temperature required to grow high quality III - V semiconductors may also provide an important tool for achieving high efficiency solar cells. A wider range of allowable growth temperatures may provide greater control over the strain in heteroepitaxial crystals. This may be important for minimizing dislocation density and microcracks in III-V layers. The predicted existence of superalloys has also generated increased interest in low temperature crystal growth. Alloys of III - V binary compounds are generally thought to exist only as random metastable systems. Research at SERI has shown that minimization of the total quantum mechanical energy of ordered phases of alloys predicts that, if grown at low enough temperatures (but with sufficient surface mobility), stable ordered intermediate phases "superalloys" would form, e.g. ordered phases of $GaInP_2$, Ga_3AsP_4, etc. Relative to random alloys of the same composition these superalloys would have the same lattice constant, somewhat larger bandgaps, and significantly higher carrier mobilities, and would be thermodynamically stable. These new materials may be very valuable for reaching new levels of photovoltaic efficiency.

As the high efficiency cell technology begins to approach the limits imposed by the best materials, increased attention will be placed on further developing "tools" for device designers to optimize cell performance. Measurements of critical electronic parameters of III-V semiconductors present new areas for research. Studies of potential techniques for passivating surfaces (and grain boundaries) could improve efficiencies. Studies of techniques for interconnecting top and bottom cells of a monolithic tandem device will also be needed. Research to improve light collection and improve open circuit voltage and fill factor to bulk recombination limits will be essential for achieving and exceeding the efficiency goals of the Five Year Plan.

Conclusions

The bulk of the research efforts supported by SERI's High Efficiency Concepts area have been directed towards establishing the feasibility of achieving very high efficiencies, 30% for concentrator and more than 20% for thin film flat plate, in solar cell designs which could possibly be produced competitively. The research has accomplished a great deal during the part two years. Even though the desired performance levels have not yet been demonstrated, based on the recent progress, a greater portion of the terrestrial photovoltaics community believes that these efficiencies are attainable.

The program can now allocate a larger portion of resources to low cost, large area deposition technology. The program is currently shifting greater emphasis on to the study of crystal growth in order to provide the understanding and tools needed to design a large area process.

REFERENCES

1. National Photovoltaics Program: Five Year Research Plan, DOE/CE-0072, available from NTIS.*

2. S. S. Chu et al, "Large Grain Gallium Arsenide Thin Films", Conf. Record 17th IEEE PV Specialist, Conference, p. 896, Kissimmee (1984).

3. J. P. Salerno et al, "Electronic Properties of Grain Boundaries in GaAs:A Study of Oriented Bicrystal, Prepared by Epitaxial Lateral Overgrowth", Lincoln Laboratory Technical Report 669, May 1984, available from NTIS.*

4. M. G. Salerno, W. G. Schaft and D. K. Wagner, in Grain Boundaries in Semiconductors, eds. H. V. Leamy, G. E. Pike and C. H. Seager (North-Holland, New York, 1982), p. 125.

5. J. C. C. Fan, R. W. McClelland and B. D. King, "GaHs Cleft Solar Cells for Space Applications", Conf. Record 17th IEEE PV Spec. Conf., p. 31, Kissimmee (1984).

6. M. S. Cook, "Method of Peeling Epilayers" U. S. Patent 4, 396, 456, August 2, 1983.

7. A. J. Shukus and M. E. Cowher, "Fabrication of Monocrystalline GaAs Solar Cells Utilizing NaCl Sacrificial Substrates", Annual Report SERI Subcontract XE-2-02142-01, available from NTIS*

8. R. P. Gale, J. C. C. Fan, G. W. Turney, and R. L. Chapman, "A New High-Efficiency GaAs Solar Cell Structure Using a Heterostructure Back-Surface Field", Conf. Record 17th PV Spec. conf. p. 1422 Kissimmee (1984).

9. L. R. Lewis, "Advanced High-Efficiency Concentrator Cells", Conf. Record 16th PV Spec. Conf., p. 584, San Diego (1983).

10. M. W. Wanlass, and A. E. Blakeslee, "Superlattice Cascade Solar Cell" Conf. Record 16th PV spec. Conf. p. 584, San Diego (1982).

11. R-Y. Tsaur et al, "GaAs/Ge/Si Solar Cells", Conf. Record 17th IEEE PV Spec. Conf., p. 440, Kissimmee (1984).

12. L. M. Fraas, J. A. Cape, P.S. McLeod, and L. D. Partain, "Measurement and Reduction of Water Vapor Contnet in AsH_3 and PH_3 Source Gases Used in Epitaxy" to be published in Vac. Sci. Tech.

13. C. Lewis, W. Dietze, and M. V. Ludowise, J. Elect. Mat. v. 12, p. 507 (1983).

14. G. P. Srivastava, J. L. Martins and A. Zunger, to be published in Phys. Rev. B, Rapid Commun.

* National Technical Information Service, U.S. Department of Commerce, Springfield, Virginia 22161.

N86-17842

FURTHER RESEARCH ON HIGH OPEN CIRCUIT VOLTAGE IN SILICON SOLAR CELLS*

M. B. Spitzer and C. J. Keavney
Spire Corporation
Bedford, Massachusetts

This paper presents the results of new research on the use of controlled dopant profiles and oxide passivation to achieve high open circuit voltage (V_{oc}) in silicon solar cells. In this work, ion implantation has been used to obtain nearly optimal values of surface dopant concentration. The concentrations are selected so as to minimize heavy doping effects and thereby provide both high blue response and high V_{oc}. Our ion implantation technique has been successfully applied to fabrication of both n-type and p-type emitters. V_{oc} of up to 660 mV is reported and AMO efficiency measured by NASA-LeRC of 16.1% has been obtained.

INTRODUCTION

The attainment of silicon solar cell conversion efficiency approaching the theoretical limit requires reduction of recombination in all volumes and at all surfaces of the cell (ref. 1). One method of reducing base recombination comprises the use of thin substrates and minority carrier reflecting surfaces of the type formed by p-p^+ junctions (ref. 1, 2). However, achievement of the very highest performance requires minimal recombination not only in the base region, but also in the p^+ region and at the p^+/contact interface. Moreover, as the base is perfected, recombination in the n^+ emitter and at its surface emerges as a limiting mechanism and must also be minimized. Thus, one general prerequisite to the attainment of high efficiency is the perfection of n^+ and p^+ regions that, while remaining useful for junction formation, introduce only minimal recombination. Following Shibib at al. (ref. 3), we call these low recombination doped regions "transparent."

To effectively utilize transparent regions in solar cells, passivation must be applied to the cell surface (ref. 4). Although in theory the construction of a transparent passivated structure appears straightforward, in practice such structures are not so easily fabricated. Some of the difficulties arise as a consequence of the need to limit heavy-doping effects to obtain transparency. Also, as has been noted by others, recombination at the interface between the silicon and the metal contact must be minimized (ref. 5-8). These factors conspire to make the attainment of low recombination (and resultant high V_{oc}) using conventional cell fabrication techniques rather difficult.

* This work has been supported by the U.S. Department of Energy through contracts with the Solar Energy Research Institute and Sandia National Laboratories.

In this paper, we present the results of research on fabrication techniques that minimize heavy-doping effects and surface recombination. In the work to be reported, we have used ion implantation to vary over a wide range dopant concentration in both phosphorus-doped n^+ regions and boron-doped p^+ regions. Unlike conventional diffusion, in which the surface dopant concentration is usually quite high ($\sim 10^{20} cm^{-3}$), in our technique, the number of ions implanted can be easily varied to achieve concentrations from about $10^{18} cm^{-3}$ to over $10^{20} cm^{-3}$. A further advantage of ion implantation is that a high quality surface oxide of controllable thickness may be easily grown during the junction anneal. As we will show, this technique has yielded AMO V_{oc} of 660 mV, without the use of an antireflection (AR) coating (which would increase V_{oc} by at least 7mV).

In the next section of this paper, we will describe our method and cell fabrication techniques. This will be followed by separate discussions of experiments with n^+ and p^+ doping, and results on high efficiency cells will be reported. In the conclusion we review the implications of this work in future space solar cell design.

CELL FABRICATION

All work to be reported here is based on the use of float-zone silicon obtained from Wacker. The wafers were 380 micrometers (μm) in thickness, polished on the front and etched on the back, and were of <100> orientation. Except as noted in the discussion to follow, the resistivity was 0.3 ohm-cm. Both boron-doped and phosphorus-doped wafers were used. We observed that the boron-doped wafers typically had a minority carrier diffusion length (L_D) of about 150 μm; the phosphorus-doped wafers were characterized by L_D of about 170 μm. While for space solar cell applications we are primarily interested in a p-type base, the use of n-type wafers provides us with a convenient method of investigating p^+ doping (i.e., by formation of p^+n cells) and the advantages of this approach will become apparent in the discussion to follow.

The n^+ and p^+ regions were formed by ion implantation and furnace annealing. The implantation of boron and phosphorus was carried out at 5 keV to obtain shallow junctions ($x_j \sim 0.2\ \mu m$). The dose was varied over the range $10^{14} cm^{-2}$ to $5 \times 10^{15} cm^{-2}$ to produce doping profiles having a peak concentration of between $10^{18} cm^{-3}$ and $10^{20} cm^{-3}$. Annealing of phosphorus was carried out using a three-step process (550°C-2 hr.; 850°C-15 min.; 550°C-2 hr.) in dry flowing nitrogen. Dry oxygen was admitted to the gas stream during the second step to grow a passivating silicon dioxide surface layer having a thickness of about 10 nanometers (nm). Annealing of boron implants was similar, with the exception that the second step of the anneal was carried out at 950°C.

Metallization on all cells comprised lift-off patterned Ti-Pd-Ag on the fronts and full-area Ti-Pd-Ag on the backs. The metal was deposited by electron beam evaporation, and after lift-off was plated with Ag. Except as noted, AR coatings were not employed. Final cell area was 4 cm^2.

An important feature that we shall refer to later in our discussion is the use of silicon dioxide surface passivation, both at the exposed (non-metallized) surface and beneath the metallization. While some

investigators have employed tunneling-based passivation beneath the contacts, we have used an older approach previously employed by Minnucci and Matthei (ref. 8) and Arndt et al. (ref. 6). The technique comprises placing the grid on top of the passivating oxide, with ohmic contact made via patterned openings in the oxide. These openings limit contact area to values much less than the total grid area. Figure 1 illustrates two configurations that have been used to achieve this end. These techniques allow us to limit the ohmic contact area to 0.1 percent of the total area.

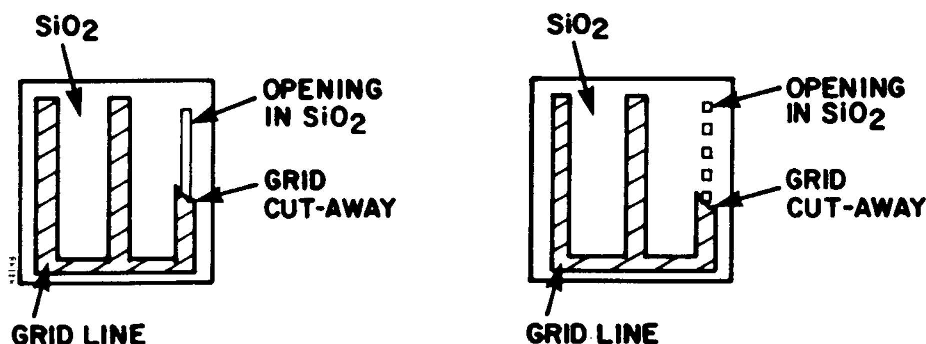

Figure 1. Two Configurations for Limiting Ohmic Contact Area Beneath the Front Contact Grid.

PHOSPHORUS EMITTER DOPING

We have used the ion implantation technique described above to identify the optimum n^+ concentration in the emitter of n^+-p-p^+ cells. Figure 2 replicates spreading resistance data obtained from samples that were ion-implanted with various doses. It can be seen that by using the ion implantation technique, the peak dopant concentration may be varied over a wide range.

Solar cells were fabricated with each of the profiles shown in Figure 2 and early results of this type of research were reported in reference 9. We recently repeated the experiment with a narrower range of doses and show the V_{OC} as a function of phosphorus implant dose in figure 3 for both 0.2 ohm-cm (curve b) and 0.3 ohm-cm (curve c) substrates. It is important to note that ohmic contact interaction area was about 4% in this experiment. Complete data is tabulated in tables I and II. It can be seen that best results are obtained with an ion implantation dose of 10^{15} ions/cm^2, corresponding to a peak dopant concentration of approximately 2 x 10^{19}cm^{-3}.

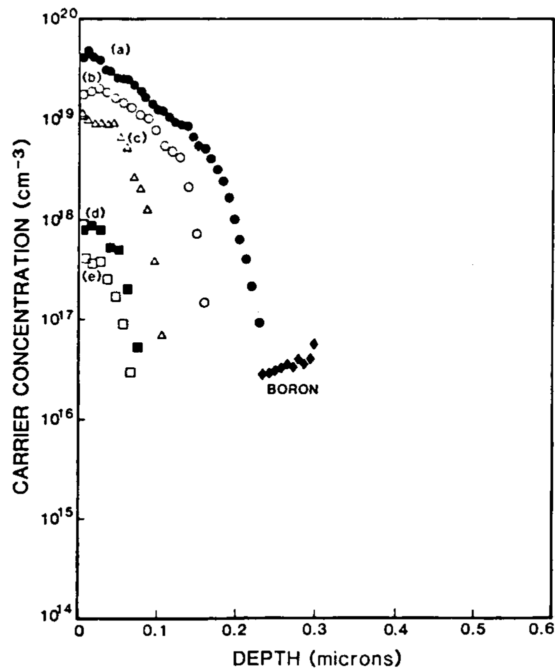

Figure 2. Spreading Resistance Analysis of n^+ Emitters. The doses used were: (a) $2.5x10^{15}cm^{-2}$, (b) $10^{15}cm^{-2}$, (c) $4x10^{14}cm^{-2}$, (d) $2x10^{14}cm^{-2}$, and (e) $10^{14}cm^{-2}$.

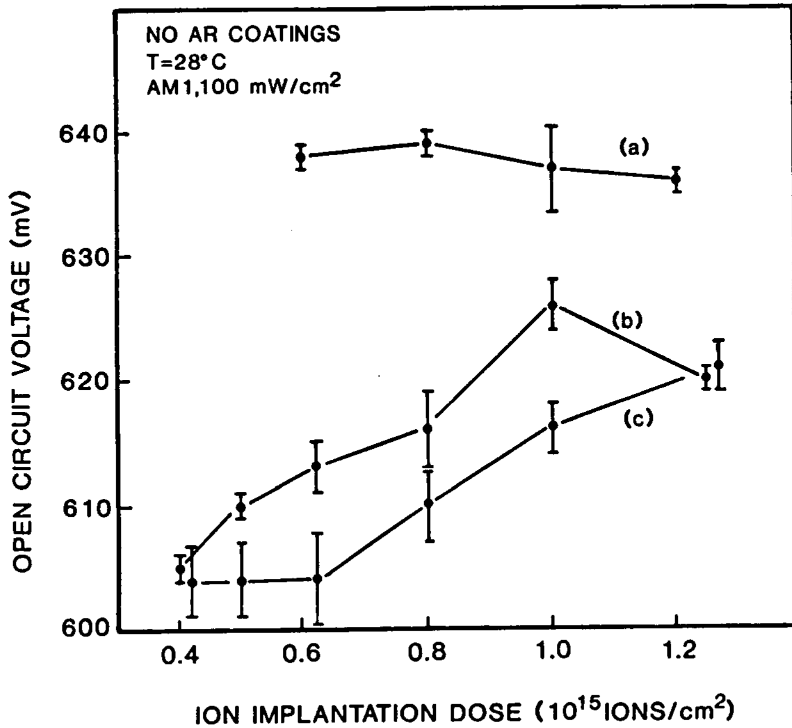

Figure 3. V_{oc} as a function of ion implantation dose. The data points indicate average V_{oc} at each dose. The error bars indicate the standard deviation. (Measurements at AM1, 100 mW/cm^2, T=28°C).

We digress at this point to note our observation that the minority carrier diffusion length in the base is strongly affected by the phosphorus concentration in the emitter. An example of this effect can be seen in tables I and II in which we have also indicated the base L_D for each ion implantation dose. We find a reproducible decrease in L_D as dose is decreased. This effect cannot be attributed to implantation of a lifetime degrading impurity, since in such a case increasing the phosphorus dose would increase the lifetime degrading impurity and decrease L_D. Perhaps it is an indication of phosphorus gettering; however, the source of the lifetime degrading impurities is uncertain. Indeed, laser-annealed cells in which no thermal processing is used and in which no gettering is possible have yet higher L_D. Experiments that combine Si implantation with P implantation to maintain constant implant damage as the P dose is reduced indicate that the observed effect is not a consequence of differences in the crystal damage. The same effect is observed with arsenic implantation, but not with boron. The cause of the observed effect is unresolved.

To identify the optimal ion implantation dose more accurately, we repeated the above dose experiment with implantation dose in a range from $6x10^{14}cm^{-2}$ to $1.2x10^{15}cm^{-2}$. We utilized silicon with a base resistivity of 0.2 ohm-cm to maintain a low base contribution to the saturation current. We also reduced the ohmic contact area (as shown in figure 1) to 0.1 percent. The V_{oc} data are shown in figure 2 (curve a). The resultant complete cell performance data are shown in table III. The average V_{oc} is maximized at a dose of $8x10^{14}cm^{-2}$; however V_{oc} greater or equal to 640 mV on at least one cell at each dose except $1.2x10^{15}cm^{-2}$ was obtained. Comparison of this data to data in table I indicates the advantage that is obtained when ohmic contact interaction area is limited.

We have also applied these implants to textured wafers and have recently reported on an estimation of the dopant distribution in textured material (ref. 10). Our principal finding is that dopant distributions that are equivalent to distributions in polished silicon may be obtained in textured silicon by simply doubling the implantation dose. In this way, we have made textured cells with V_{oc} of 640 mV, equivalent to V_{oc} obtained from polished wafers. This indicates to us that the base saturation current dominates our best cells, since the emitter saturation current, which is higher for textured cells, does not adversely affect V_{oc} when texture is used.

The emitters described above have been applied in the fabrication of high efficiency cells. One cell that was tested under AM0 insolation (137.2 mW/cm^2) at NASA-LeRC exhibited the following performance: FF=0.796, J_{sc}=43.5 mA/cm^2, V_{oc}=640 mV, and Eff.=16.1%. This cell had a thickness of 380 μm, and a diffusion length of about 150 μm. We believe that its performance can be further improved by thinning the substrate to 200 μm. For this approach to be successful, a high quality back surface field (BSF) must be employed. We will describe in a later section how such a BSF may be formed.

TABLE I
AVERAGE AM1 PERFORMANCE OF P-TYPE SOLAR CELLS AS A FUNCTION OF ION IMPLANTATION DOSE (0.2 OHM-CM SUBSTRATES)

Dose (ions/cm^2)	L_D (μm)	V_{oc} (mV)	J_{sc} (mA/cm^2)	FF (%)	EFF (%)
4×10^{14}	63	605 (1)	21.7 (0.2)	78.8 (0.2)	10.3 (0.2)
5×10^{14}	77	610 (1)	21.9 (0.2)	79.2 (2.0)	10.6 (0.3)
6.25×10^{14}	85	613 (3)	22.1 (0.2)	79.0 (1.7)	10.7 (0.3)
8×10^{14}	90	616 (3)	22.4 (0.2)	79.9 (0.9)	11.0 (0.2)
1×10^{15}	138	626 (2)	23.8 (0.2)	79.2 (1.9)	11.8 (0.3)
1.25×10^{15}	137	620 (1)	23.7 (0.2)	78.5 (1.4)	11.6 (0.3)

Notes: Cell area is 4 cm^2. Insolation is simulated AM1, 100 mW/cm^2. T = 28°C. Standard deviation in parenthesis. No AR coatings employed.

TABLE II
AVERAGE AM1 PERFORMANCE OF P-TYPE SOLAR CELLS AS A FUNCTION OF ION IMPLANTATION DOSE (0.3 OHM-CM SUBSTRATES)

Dose (ions/cm^2)	L_D (μm)	V_{oc} (mV)	J_{sc} (mA/cm^2)	FF (%)	EFF (%)
4×10^{14}	60	604 (3)	21.8 (0.2)	80.3 (0.4)	10.6 (0.1)
5×10^{14}	77	604 (3)	22.0 (0.1)	78.9 (1.1)	10.5 (0.2)
6.25×10^{14}	74	604 (4)	22.0 (0.3)	79.5 (1.4)	10.5 (0.3)
8×10^{14}	95	610 (3)	22.5 (0.3)	80.4 (1.0)	11.0 (0.3)
1×10^{15}	133	616 (2)	23.5 (0.2)	79.7 (0.8)	11.5 (0.2)
1.25×10^{15}	150	621 (2)	24.2 (0.1)	80.9 (0.6)	12.2 (0.1)

Notes: Cell area is 4 cm^2. Insolation is simulated AM1, 100 mW/cm^2. T = 28°C. Standard deviation in parenthesis. No AR coatings employed.

TABLE III
AVERAGE AM1 PERFORMANCE OF P-TYPE SOLAR CELLS WITH IMPROVED CONTACTS AS A FUNCTION OF ION IMPLANTATION DOSE (0.2 OHM-CM SUBSTRATES)

Dose (ions/cm^2)	L_D (μm)	V_{oc} (mV)	J_{sc} (mA/cm^2)	FF (%)	EFF (%)
$6x10^{14}$	67	638 (1)	22.0 (0.3)	79.0 (1.3)	11.1 (0.3)
$8x10^{14}$	101	639 (1)	23.1 (0.1)	78.4 (1.5)	11.6 (0.3)
$1x10^{15}$	119	637 (4)	23.6 (0.2)	79.8 (0.8)	12.0 (0.2)
$1.2x10^{15}$	118	636 (1)	23.6 (0.1)	80.0 (1.4)	12.0 (0.2)

Notes: Cell area is 4 cm^2. Contact interaction area is 0.1%. Insolation is simulated AM1, 100 mW/cm^2. T = 28°C. Standard deviation in parenthesis. No AR coatings employed.

BORON EMITTER DOPING

A similar investigation has been carried out using boron implantation into n-type wafers. A beam energy of 5 keV was used to obtain shallow junctions. Implantation doses in the range of $3x10^{14}cm^{-2}$ to $1x10^{15}cm^{-2}$ were used to obtain peak dopant concentrations of between $5x10^{18}cm^{-3}$ and $10^{19}cm^{-3}$. It can be seen from the spreading resistance analysis in figure 4 that dopant profiles similar to those that have been used for phosphorus emitters have been attained.

Solar cells have been fabricated from n-type wafers using the profiles shown in figure 4. We have investigated both standard ohmic contacts and contacts with ohmic contact interaction area reduced to 0.1%, and complete cell performance data are shown in table IV. It can be seen that best V_{oc} is obtained when the peak doping concentration is limited to about $5x10^{18}$ cm^{-3}. As in the case of n^+ emitters, reduction of ohmic contact area improves V_{oc}. Note also that the FF is reduced when the ohmic contact area is reduced. This low FF is attributable to the use of Ti-Pd-Ag contacts on the p^+ silicon and arises from contact series resistance. Use of Al would probably eliminate this problem.

High V_{oc} n-type cells have also been tested at AM0 by NASA-LeRC. Performance of the best non-AR-coated cell is: J_{sc}=28.8 mA/cm^2, FF=.77, V_{oc}=662 mV, and Eff.=10.7%. An AR coating would improve efficiency to about 15%, and V_{oc} to nearly 670 mV.

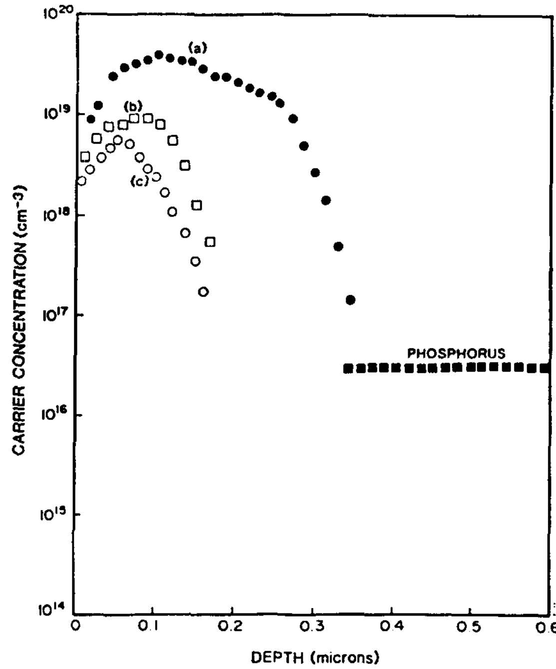

Figure 4. Spreading Resistance Analysis of p^+ Emitters. The doses used were: (a) $1\times10^{15}cm^{-2}$, (b) $5\times10^{14}cm^{-2}$, and (c) $3\times10^{14}cm^{-2}$.

TABLE IV
AVERAGE AM1 PERFORMANCE OF N-TYPE SOLAR CELLS
AS A FUNCTION OF ION IMPLANTATION DOSE (0.3 OHM-CM SUBSTRATES)

Dose ($ions/cm^2$)	Contact Interaction Area	V_{oc} (mV)	J_{sc} (mA/cm^2)	FF (%)	EFF (%)
3×10^{14}	0.1%	653 (1)	24.7 (0.1)	73.8 (2.8)	11.9 (0.5)
3×10^{14}	4%	634 (3)	24.6 (0.1)	77.7 (3.4)	12.1 (0.6)
5×10^{14}	0.1%	644 (2)	24.6 (0.1)	78.3 (1.0)	12.4 (0.2)
5×10^{14}	4%	634 (2)	24.6 (0.1)	78.6 (1.5)	12.3 (0.3)
1×10^{15}	4%	591 (2)	22.2 (0.1)	79.7 (1.8)	10.5 (0.3)

Notes: Cell area = 4 cm^2. Insolation was AM1, 100 mW/cm^2. T = 28°C. Standard deviation shown in parenthesis. No AR coatings employed.

It is interesting that better V_{OC} is obtained with n-type wafers. This may be a consequence of the lower minority carrier (hole) mobility in n-type silicon which would serve to reduce the base saturation current.

TRANSPARENT REGIONS

To show conclusively that we have attained transparent emitter regions, we have examined solar cell performance with and without silicon dioxide passivation. Figure 5 replicates log(I)-V data obtained from one n^+-p-p^+ solar cell before and after removal of the oxide. It can be seen that the saturation (or dark) current increases in accordance with theory when the oxide is removed. The change in V_{OC} upon removal of the oxide was 47 mV. In figure 6 we show the quantum efficiency data, before and after oxide removal. It is clear from this data that the blue response is much improved by the presence of the oxide.

Figure 7 replicates log(I)-V data for a typical p^+-n-n^+ solar cell. Removal of the oxide increases the saturation current as it did in the n^+-p-p^+ example. In this case the change in V_{OC} was 75 mV. Quantum efficiency data (fig. 8) show that the blue response is also sensitive to surface recombination. These measurements indicate that we have indeed formed transparent n^+ and p^+ regions.

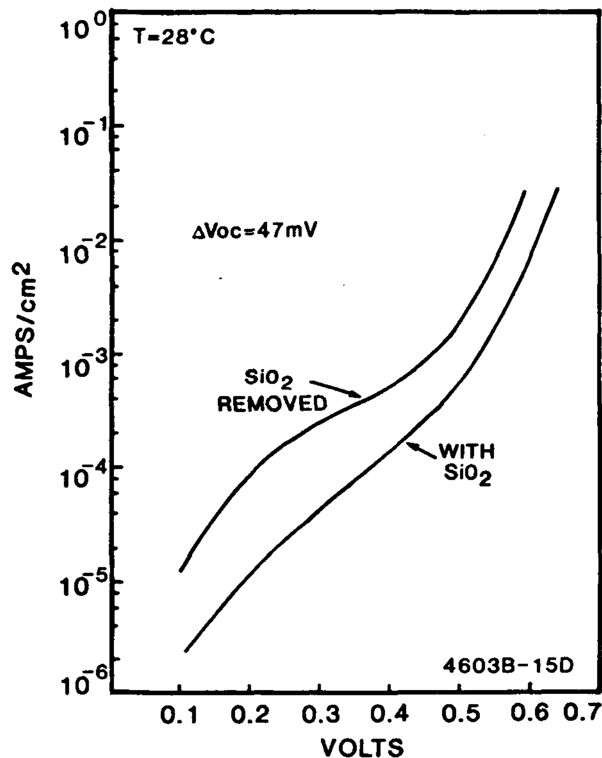

Figure 5. Log(I)-V Data for the n^+-p-p^+ Cell With and Without Oxide Passivation.

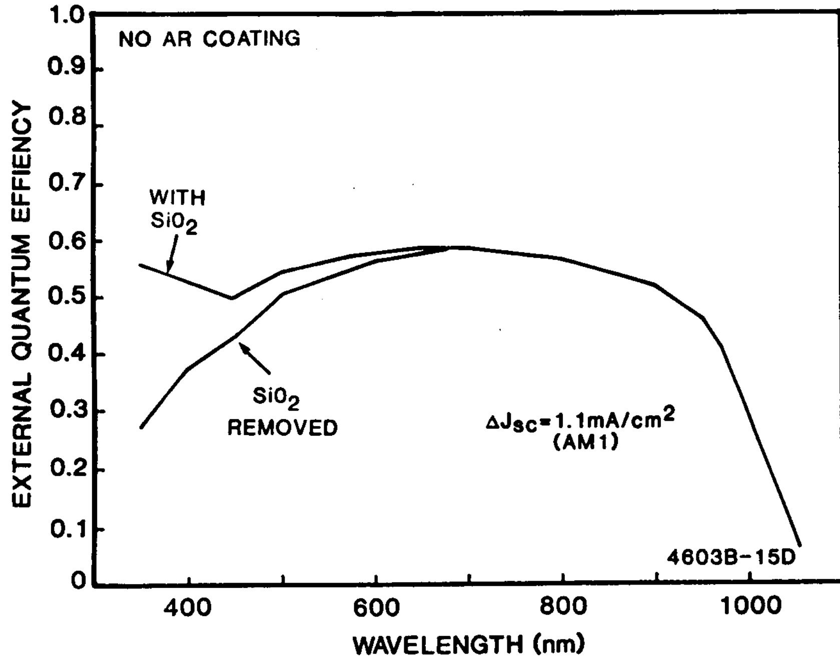

Figure 6. External Quantum Efficiency of the n^+-p-p^+ Cell With and Without Oxide Passivation.

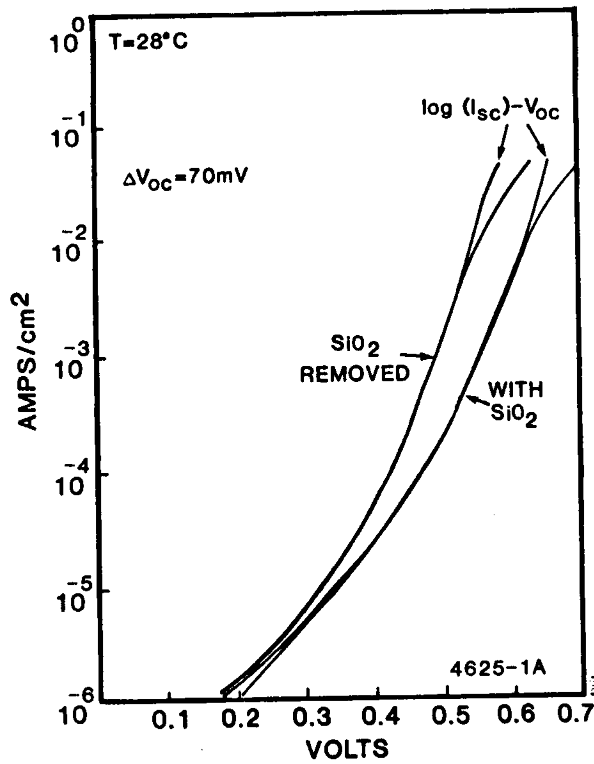

Figure 7. Log(I)-V Data for the p^+-n-n^+ Cell With and Without Oxide Passivation. Also shown are Log (I_{sc})-V_{oc} Data.

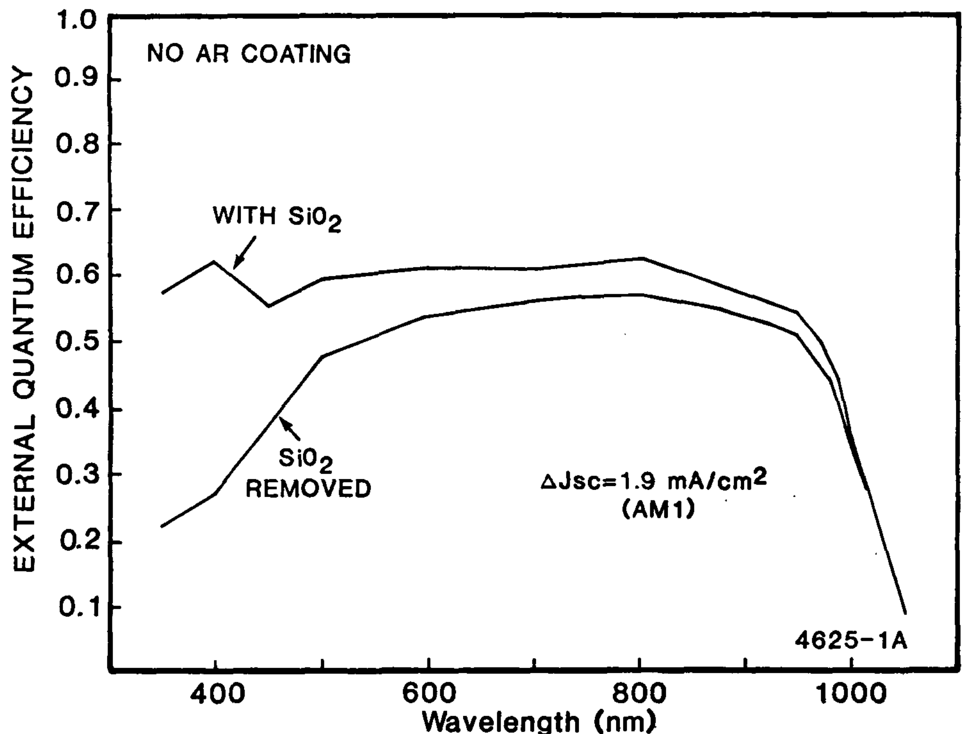

Figure 8. External Quantum Efficiency of the p^+-n-n^+ Cell With and Without Oxide Passivation.

HIGH EFFICIENCY CELL DESIGN

As was noted at the beginning of this paper, the attainment of high conversion efficiency requires limiting all forms of recombination. The best cell design should therefore include low-recombination transparent doped regions and surface passivation. This idea is of course not new, but we now have in hand a fabrication process that, by using ion implantation, will let us realize such doped regions.

Figure 9 illustrates the cell design we believe at this time will yield best performance. The device comprises an n^+-p-p^+ structure with the n^+ and p^+ regions formed by the transparent doped layers discussed above. Total thickness should be less than 250 μm, but the optimal value will depend upon the diffusion length in the substrate. A back surface reflector should be used to double the optical path and to reject unabsorbed radiation. Since the back surface has low recombination velocity, the cell may be made as thin as is desired for weight reasons, without loss of V_{OC}. At present, we are in the process of developing this type of cell. If light-trapping can be obtained (ref. 2), very high efficiency will be possible using substrates as thin as 50μm.

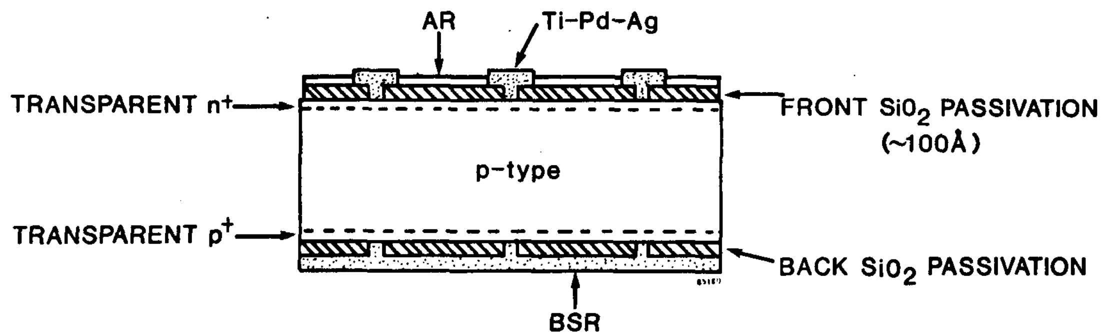

Figure 9. High Efficiency Space Solar Cell Design.

SUMMARY

This paper has reported on techniques that may be used to avoid heavy doping effects in silicon solar cells. In this way, transparent n^+ and p^+ layers have been formed. By combining these layers with silicon dioxide passivation, solar cells that are mainly limited by base recombination can be fabricated. Once this is accomplished, the problem of improving solar cell efficiency is reduced to gaining improvements in L_D, or alternately, to thinning of the substrate. Proper integration of these results in a BSF-BSR cell design should lead to AM0 efficiency in the 17 to 18% range in the near future.

REFERENCES

1. Wolf, M.: Updating the Limit Efficiency of Silicon Solar Cells. IEEE Trans. Electron Devices ED-27, 751 (1980).

2. Spitzer, M., Shewchun, J., Loferski, J.J., and Vera, E.S.: Ultra High Efficiency Thin Silicon p-n Junction Solar Cells Using Reflecting Surfaces. Rec. of the 14th IEEE Photovoltaic Specialists Conference (1980) p. 375.

3. Shibib, M.A., Lindholm, F.A., and Therez, F.: Heavily Doped Transparent-Emitter Regions in Junction Solar Cells, Diodes, and Transistors. IEEE Trans. Electron Devices ED-26, 959 (1979).

4. Fossum, J.G., Lindholm, F.A., and Shibib, M.A.: The Importance of Surface Recombination and Energy-bandgap Narrowing in p-n-junction Silicon Solar Cells. Trans. Electron Devices ED-26, 1294 (1979).

5. Lindholm, F.A., Mazer, J.A., Davis, J.R., and Perreota, J.T.: Degradation of Solar Cell Performance by Areal Inhomogeneity. Solid-State Electronics 23, 967 (1980).

6. Arndt, R.A., Meulenberg, A., Allison, J.F.: Advances in High Output Voltage Silicon Solar Cells. Rec. of the 15th IEEE Photovoltaic Specialists Conference, 1981, p. 92.

7. Green, M.A., Blakers, A.W., Shi, J., Keller, E.M. and Wenham, S.R.: 19.1% Efficient Silicon Solar Cell. Appl. Phys. Lett. 44, 1163 (1984).

8. Minnucci, J.A., and Matthei, K.W.: Study Program to Improve the Open-Circuit Voltage of Low Resistivity Single Crystal Silicon Solar Cells. NASA CR-159833 (1980).

9. Spitzer, M.B., Keavney, C.J., Tobin, S.P., Lindholm, F.A. and Neugroschel, A.: Mechanisms Limiting Open Circuit Voltage in Silicon Solar Cells. Rec. of the 17th IEEE Photovoltaic Specialists Conference, 1984, p. 1218.

10. Keavney, C.J., and Spitzer, M.B.: Solar Cell Junction Profiles in Ion-Implanted Texture-etched Surfaces. J. Appl. Phys. 56, 592 (1984).

N86-17843

GALLIUM ARSENIDE SOLAR CELL EFFICIENCY - PROBLEMS AND POTENTIAL

V.G. Weizer and M.P. Godlewski
NASA Lewis Research Center
Cleveland, Ohio

Under ideal conditions the GaAs solar cell should be able to operate at an AMO efficiency exceeding 27 percent (ref. 1), whereas to date the best measured efficiencies barely exceed 19 percent. Of more concern is the fact that there has been no improvement in the past half decade, despite the expenditure of considerable effort. The present paper analyzes state-of-the-art GaAs efficiency in an attempt to determine the feasibility of improving on the status quo. We will first consider the possible gains to be had in the planar cell, and then attempt to predict the efficiency levels that could be achieved with a grating geometry.

THE PLANAR CELL

The best efforts of the eight laboratories most involved in the development of the GaAs solar cell are listed in table I. The N-base cells are all basically similar in construction in that they have a passivating P-type AlGaAs window layer deposited on the emitter surface. The P-base MIT cell, on the other hand, uses an AlGaAs layer to form a heteroface BSF structure. The N-base cells appear to have a slight efficiency edge over the P-base devices.

E-2706-5

Figure 1 is a plot of the N-base cell short circuit current as a function of AlGaAs window thickness. These cells are quite different in their externals (AR coatings, window thicknesses, etc.). In order to get an idea of their relative internal perfection we calculated the short circuit densities expected from each of them assuming 100 percent internal collection efficiency, and compared this value with that actually achieved. When we did this, Hughes cell 2598 stood out from the rest in that its measured J_{sc} coincided with that calculated assuming a 100 percent internal collection efficiency. This indicates, among other things, that the Hughes group has succeeded in reducing the AlGaAs-GaAs interface recombination velocity IRV at least an order of magnitude lower than the emitter diffusion velocity ($\leq$0.1 D/L).

However, even though this cell is internally perfect, it has several external problems. It has a thick (0.5 μm) window and a 10 percent shadowing loss due to the front grid coverage. The solid curve in figure 1 indicates the J_{sc} increases that would accompany a reduction in window thickness. The dashed curve indicates the gains possible if the grid coverage were reduced to 5 percent. As can be seen, if the window thickness and grid coverage were reduced to 0.05 μm and 5 percent, respectively, it would not be unreasonable to expect J_{sc} values exceeding 35 mA/cm^2.

Using 0.1 D/L for the AlGaAs-GaAs IRV and the values of the parameters in table II, we attempted to estimate the voltage and efficiency potential of this cell. The results are shown in table III. The low fill factor (FF) measured for this cell indicates a diode quality factor n greater than 1. The calculations, which assume a unity n value, indicate that the low FF has a depressing effect on

PRECEDING PAGE BLANK NOT FILMED

V_{OC}. If we give this cell a unity n value and a good fill factor, a V_{OC} of 1.040 V and an AMO efficiency of almost 21 percent result. Thus, merely by fabricating this cell with a decent fill factor, we could realize an efficiency two percentage points higher than has been achieved thus far. If we then reduce the AlGaAs window thickness to 0.05 μm and reduce the grid coverage to 5 percent, efficiency levels exceeding 23 percent should result.

We then performed essentially the same calculations for the P-base MIT cell number 8477 with its unpassivated emitter surface. As mentioned previously, this cell has an AlGaAs-GaAs interface at the "rear surface" that acts as a BSF layer. In the calculations, the same AlGaAs-GaAs IRV that we found for the Hughes cell (0.1 D/L) was used along with the values of the various parameters listed in table IV. As seen in table III, when the FF is raised to 0.86 the efficiency rises by about a point to 18.4 percent. If the emitter surface is then passivated (SRV = 0) and the anodic oxide AR coating is replaced by a dual layer coating, efficiencies comparable to those in the N-base cell are possible. It is evident that the critical need in this cell is the reduction of the emitter SRV.

To summarize, both the N-base and the P-base GaAs cells (in their planar configurations) have the potential to operate at AMO efficiencies between 23 and 24 percent. For the former the enabling technology is essentially in hand, while for the latter the problem of passivating the emitter surface remains to be solved.

THE GRATING CELL

A grating cell can be defined as a cell in which the junction (emitter) area has been reduced to a fraction of the total front (or rear) surface area. The purpose of going to a grating geometry is to secure an increase in voltage while maintaining (hopefully) a current level characteristic of a planar cell. The two simplest grating geometries are the stripe junction and the dot junction configurations. In the former the emitter is composed of an array of parallel stripes, and in the latter it is composed of an array of equally spaced dots.

Although previous theoretical analyses have indicated that the stripe grating geometry does not hold much promise for increased voltage (ref. 10), more recent calculations show that significant voltage gains are possible with the dot geometry (ref. 12). It has been shown that the effective base saturation current component of the dot grating cell decreases with the square root of the junction area. At the same time, because the emitter volume varies with the emitter area, the saturation current component from that region decreases linearly with junction area. A cell with a junction composed of an array of dots whose aggregate area is only 1 percent of the total cell area, for instance, would have its emitter component reduced by a factor of 100 and its base component reduced by a factor of 10 as compared to a planar cell with the same total area. The dot grating geometry thus has the potential for producing significant increases in cell voltage.

This concept is especially intriguing in the case of the P-base cell with its unpassivated emitter surface. In this case, the reduction of the N-type emitter surface area by several orders of magnitude would result in a cell almost completely bounded by passivatable P-type surfaces. The need to passivate the remaining N-type areas would be obviated by virtue of the relatively small contribution these areas would make to cell performance. Thus in the P-base cell the dot grating geometry is not only capable of producing a large decrease in J_0 but it also would eliminate essentially all of the hard-to-passivate N-type surfaces. The latter improvement

is a necessary, but, as we shall see, not a sufficient requirement for maintaining grating cell current levels comparable to those achieved in the planar cell.

We therefore calculated the efficiency of a 1 percent junction coverage, P-base dot grating cell using the MIT cell 8477 parameters (table IV) assuming planar cell current levels and a good FF. The results, according to table V, indicate that efficiencies in the 24.5 percent range are achievable.

Maintaining a high current level in a grating cell, however, requires more than just passivating the cell surfaces. It has been shown that to maintain full current capability in a grating cell, the base diffusion length must be much larger than the distance between junction areas in the grating structure[1] (ref. 10). If we assume that photolithographic limitations put a lower limit of 1 μm on the diameter of the emitter dots, then the smallest grating spacing possible for a cell with a 1 percent junction coverage would be 10 μm. This, unfortunately, is about the same magnitude as the diffusion lengths measured in most GaAs solar cells. In order to make use of the potential of the grating geometry a means would have to be found to raise L by at least an order of magnitude.

One way to obtain long diffusion lengths would be to go to a higher resistivity base material in which L values approaching 500 μm have been measured (refs. 13 to 15). Figure 2 summarizes measured hole and electron diffusion length data as a function of doping concentration. The problem with going to lower doping levels to achieve increased current is that one would expect (a priori) the base saturation current to rise precipitously, resulting in a serious decline in V_{oc}.

When one actually calculates the variation of efficiency with base doping level for the planar MIT cell 8477, however, it is found (fig. 3) that cell efficiency is surprisingly independent of base resistivity. In this plot J_{sc} and FF were assumed to be 29 mA/cm^2 and 0.86, respectively, while diffusion length data were taken from figure 2. Based on our previous analysis of the J_{sc} levels in the N-base cells, we have concluded that it is possible to reduce the AlGaAs-GaAs IRV to a level an order of magnitude below the diffusion velocity or lower. Measurements made by Nelson (ref. 16), although not made on solar cells, indicate that the IRV can in fact be two or three orders of magnitude less than D/L. We have therefore plotted the efficiency-doping relationship in figure 3 for several values of the IRV that bracket Nelson's measured 300 cm/sec (0.004 D/L) value (ref. 16).

The significance of figure 3 is that it shows that it should be possible to fabricate high efficiency GaAs solar cells with long (>200 μm) diffusion lengths. The fact that such a cell is possible indicates that we should be able to fabricate a high current, and thus a high efficiency, dot grating GaAs cell.

A few words should be said at this point concerning electrical contacts to the dot grating cell. Because of the large number of emitter dots that would be required, and because of the close spacing between them, the metallization making contact to the emitter areas on the front surface of the cell would probably shadow

---

[1]Unpublished data obtained from V.G. Weizer. An analysis of the dot-grating cell fabricated Swanson, et al. (ref. 11) indicates that this cell (with a diffusion length/grating-separation ratio of about 18) has an internal quantum efficiency close to 100 percent).

a significant portion of the cell front face. It thus appears that we would be forced to resort to an interdigitated back contact scheme such as that used by Swanson, et al. (ref. 11). This type of contacting, while being technically more difficult to achieve, does have the advantage of completely eliminating all shadowing effects. Thus, when we calculate the value of J_{sc} expected from a back contacted dot grating cell, we find that current levels over 36 mA/cm^2 are possible since the only losses are due to reflectivity and window absorption.

Figure 4 shows the calculated efficiency of a 1 percent junction coverage, back contacted dot grating cell as a function of base doping from $N = 1 \times 10^{15}$ cm^{-3} ($L = 200$ μm) to $N = 1 \times 10^{14}$ cm^{-3} ($L = 500$ μm). When the AlGaAs-GaAs IRV = 0, an efficiency of 25.3 percent is seen for a doping concentration of 1×10^{15} cm^{-3}. A penalty of about 1 percentage point is paid if the IRV is as high as 800 cm/sec (0.01 D/L).

The previous calculations were performed for a cell with a base width w of 2 μm. Since a change in w is expected to affect cell current and voltage in opposite directions, we should, by varying w, be able to observe an efficiency maximum at some optimum value of the base width. Figure 5 shows the variation of efficiency with w for the case where $N = 1 \times 10^{15}$ cm^{-3}. The efficiency is seen to be rather independent of base width for values above about 2 μm. When the IRV = 0, the efficiency peaks at about 25.7 percent at a base width of about 10 μm. For the higher value of the IRV a maximum of just over 25 percent occurs at a width of about 25 μm. Not only is the efficiency independent of the base width, it also becomes insensitive to the AlGaAs-GaAs IRV as the width is increased. As can be seen, high efficiency is maintained to thicknesses of 100 μm. This fact should facilitate the construction of this device since it would permit the use of thick cell fabrication techniques such as those employed by Swanson, et al. (ref. 11).

To summarize, both the N-base and the P-base GaAs cells in their planar configurations have the potential to operate at AMO efficiencies between 23 and 24 percent. For the former the enabling technology is essentially in hand, while for the latter the problem of passivating the emitter surface remains to be solved. In the dot grating configuration, P-base efficiencies approaching 26 percent are possible with minor improvements in existing technology. N-base grating cell efficiencies comparable to those predicted for the P-base cell are achievable if the N surface can be sufficiently passivated.

REFERENCES

1. Hovel, H.J.: Thickness. Semiconductors and Semimetals, Vol. 11, Solar Cells, Academic Press, 1975, Chapter 5, pp. 93-111.

2. Kamath, S.; Knechtli, R.C.; and Loo, R.: Fabrication of High Efficiency and Radiation Resistant GaAs Solar Cells. Solar Cell High Efficiency and Radiation Damage 1979, NASA CP-2097, 1979, pp. 209-216.

3. Knechtli, R.C.; Loo, R.Y.; and Kamath, G.S.: High-Efficiency GaAs Solar Cells. IEEE Trans. Electron Devices, vol. 31, no. 5, May 1984, pp. 577-588.

4. Werthen, J.G.: 18.7% Efficient (1-sun, AMO) Large-Area GaAs Solar Cells. Appl. Phys. Lett., vol. 46, no. 8, Apr. 15, 1985, pp. 776-778.

5. Sahai, R.: High Efficiency Thin Window $Ga_{1-x}Al_xAs$ - GaAs Solar Cells. 12th Photovoltaic Specialists Conference, IEEE, 1976, pp. 989-992.

6. Woodall, J.M.; and Hovel, H.J.: An Isothermal-Etchback Regrowth method for High Efficiency $Ga_{1-x}Al_xAs$ - GaAs Solar Cells. Appl. Phys. Lett., vol. 30, no. 9, May 1, 1977, pp. 492-493.

7. Yeh, Y.C.M.; Chang, K.I.; and Tandon, J.L.: Large Scale OM-CVD Growth of GaAs Solar Cells. 17th Photovoltaic Specialists Conference, IEEE, 1984, pp. 36-41.

8. Vernon, S.M.: Heteroepitaxial (Al)GaAs Structures on Ge and Si for Advanced High Efficiency Solar Cells. 17th Photovoltaic Specialists Conference, IEEE, 1984, pp. 434-439.

9. Yoshida, S.: Liquid Phase Epitaxy Technology of Large Area AlGaAs - GaAs Wafers of GaAs Solar Cells for Space Applications. 17th Photovoltaic Specialists Conference, IEEE, 1984, pp. 42-45.

10. Kong, Anthony K.; and Green, Martin A.: The Efficiency of Grating Solar Cells. J. Appl. Phys., vol. 49, no. 1, Jan. 1978, pp. 437-442.

11. Swanson, R.M.: Prime-Contact Silicon Solar Cells. IEEE Trans. Electron Devices, vol. 31, no. 5, May 1984, pp. 661-664.

12. Weizer, V.G.; and Godlewski, J.: Effect of Solar-Cell Junction Geometry on Open-Circuit Voltage, vol. 57, no. 6, Mar. 15, 1985, pp. 2292-2294.

13. Nelson, R.J.: Measurement of 100 μm Minority Carrier Diffusion Lengths in p-Gallium Arsenide by a New Photoluminescence Method. Gallium Arsenide and Related Compounds, C.M. Wolfe, ed., Inst. Physics Conf. Series No. 45, Bristol: Institute of Physics, 1979, pp. 256-262.

14. Ryan, R.D.; and Eberhardt, J.E.: Hole Diffusion Length in High Purity in n-GaAs. Solid State Electron., vol. 15, no. 8, Aug. 1972, pp. 865-868.

15. Sekela, A.M.; Feucht, D.L.; and Milnes, A.G.: Diffusion Length Studies in n-Gallium Arsenide. Gallium Arsenide and Related Compounds, C.M. Wolfe, ed., Inst. Physics Conf. Series No. 45, Bristol: Institute of Physics, 1979, pp. 245-253.

16. Nelson, R.J.: Interfacial Recombination in GaAlAs Heterostructures. J. Vac. Sci. Technol., vol. 15, no. 4, July/Aug. 1978, pp. 1475-1477.

TABLE I. - AMO PERFORMANCE DATA

Cell	Reference	V_{oc}, V	J_{sc}, mA/cm^2	FF, percent	Efficiency, percent
N-base cells					
Hughes 2598	2	1.015	32.0	75.2	18.1
Hughes ED-31	3	1.024	30.0	84.0	19.0
Hughes 13610	(a)	1.031	28.4	78.2	16.7
Varian	4	1.012	30.5	81.8	18.7
Rockwell	5	.960	30.3	80.3	17.2
IBM	6	1.025	33.1	74.5	18.5
ASEC	7	1.004	28.0	80.0	16.6
Spire	8	[b]1.020	[b]28.3	85.3	[b]17.9
Mitsubishi	9	.990	31.4	80.1	18.4
P-base cells					
MIT 8477	(a)	1.036	28.7	79.0	17.3
Varian	4	.995	31.3	80.0	18.4

[a]Unpublished data obtained at NASA Lewis Research Center.
[b]Estimated AMO values.

TABLE II. - N-BASE CELL PARAMETERS: HUGHES CELL 2598

Parameter	Base	Emitter
L, μm	5	10
D, cm^2/sec	6	77
d, μm	10	0.5
N, cm^{-3}	10^{17}	10^{18}
S, cm/sec	10^4	8×10^3
n_i, cm^{-3}	2×10^6	2×10^6

TABLE III. - CALCULATED AMO PERFORMANCE PARAMETERS

	J_{sc}, mA/cm^2	V_{oc}, V	FF, percent	Efficiency, percent
Hughes cell 2958				
Experimental data	32.0	1.015	75.2	18.1
Optimized fill factor	31.96	1.040	86.0	20.9
Window, grid optimized	35.77	1.043	86.0	23.4
MIT cell 8477				
Experimental data	28.7	1.036	79.0	17.3
Optimized fill factor	28.30	1.034	86.0	18.4
SRV optimized, DLAR	34.94	1.061	86.0	23.3

TABLE IV. - P-BASE CELL PARAMETERS: MIT CELL 8477

Parameter	Base	Emitter
L, µm	20	0.5
D, cm^2/sec	121	3
d, µm	2	0.07
N, cm^{-3}	10^{17}	$5x10^{18}$
S, cm/sec	0	10^7
n_i, cm^{-3}	$2x10^6$	$2x10^6$

TABLE V. - P-BASE CELL PERFORMANCE: MIT CELL 8477

	J_{sc}, mA/cm^2	V_{oc}, V	FF, percent	Efficiency, percent
Optimized fill factor	28.30	1.034	86	18.4
1-Percent dot grating	(35.00)	1.118	86	24.5

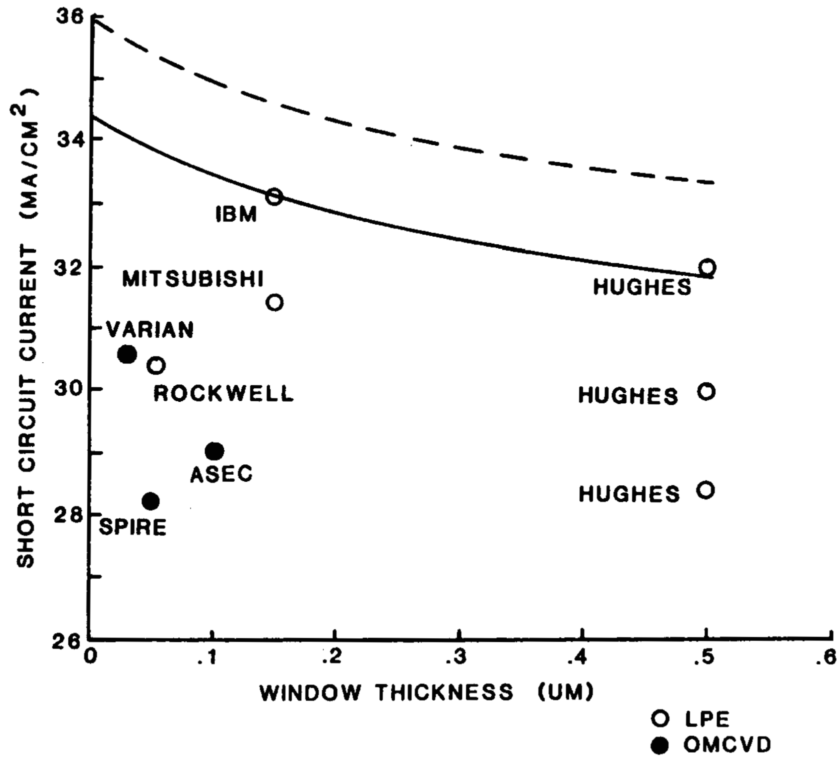

Figure 1. - A Plot of measured AMO short circuit current density vs AlGaAs window thickness.

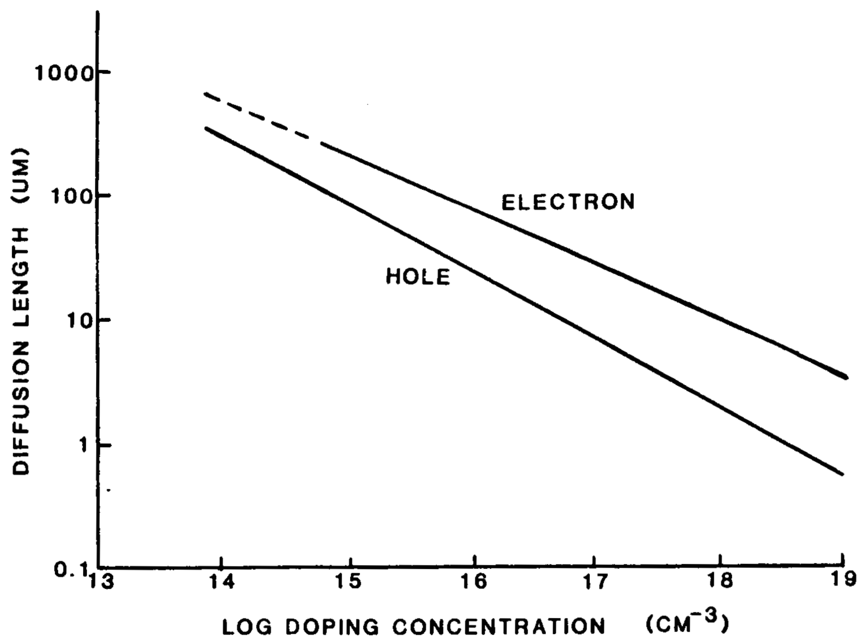

Figure 2. - Electron and hole diffusion lengths as function of doping concentration.

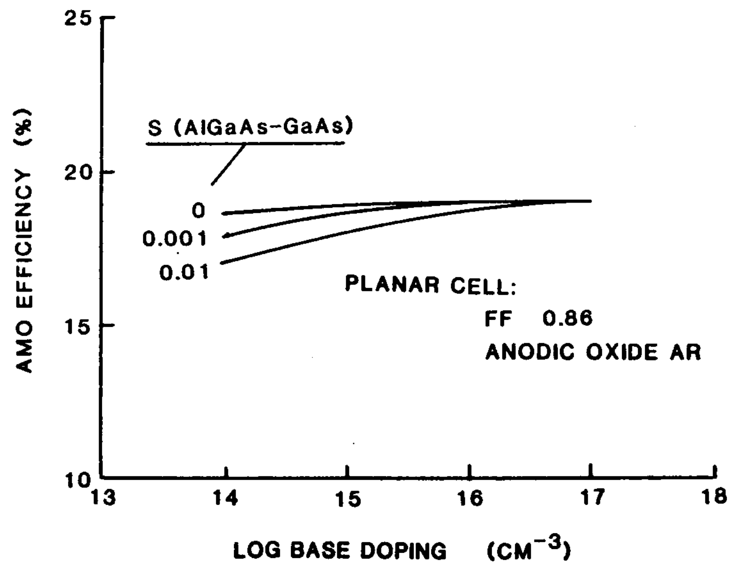

Figure 3. - Variation of P-base GaAs cell AMO efficiency with base doping level.

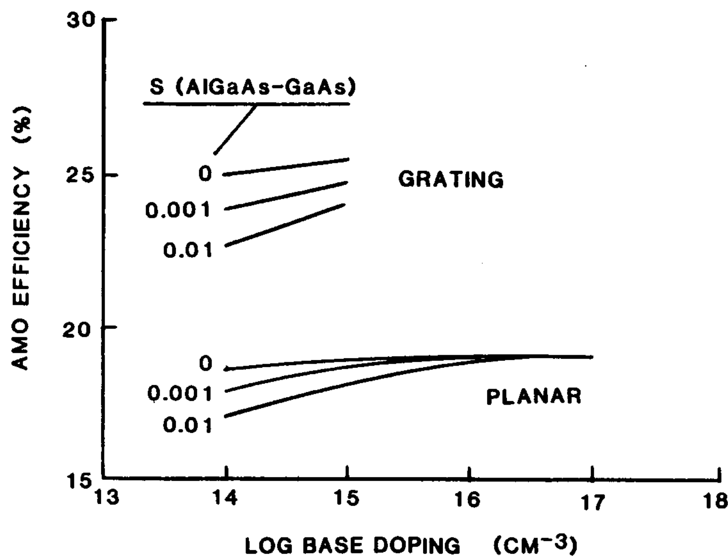

Figure 4. - Variation of P-base GaAs cell AMO efficiency with base doping level, planar vs 1 percent dot geometry.

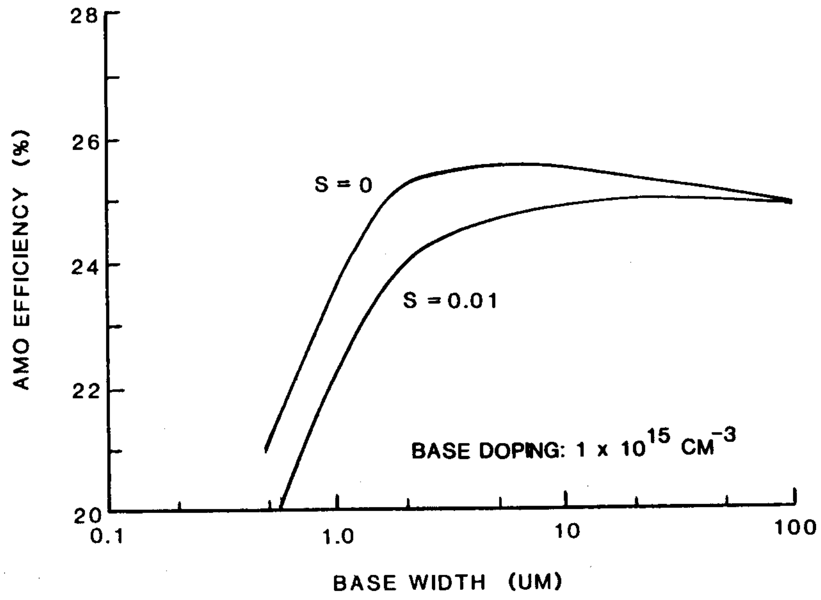

Figure 5. - Variation of P-base GaAs cell AMO efficiency with base width.

ORIGINAL PAGE IS
OF POOR QUALITY

N86-17844

N/P GaAs CONCENTRATOR SOLAR CELLS WITH AN IMPROVED GRID AND BUSBAR CONTACT DESIGN

Gregory C. DeSalvo, Ervin H. Mueller, and Allen M. Barnett*
University of Delaware
Newark, Delaware

1. GaAs Solar Cell

The major requirements for a solar cell used in space applications are high efficiency at AMO irradiance and resistance to high energy radiation. Gallium arsenide, with a band gap of 1.43 eV, is one of the most efficient sunlight to electricity converters (25%) when the simple diode model is used to calculate efficiencies at AMO irradiance. GaAs solar cells are more radiation resistant than silicon solar cells and the N/P GaAs device has been reported to be more radiation resistant than similar P/N solar cells [1]. This higher resistance is probably due to the fact that only 37% of the current is generated in the top N layer of the N/P cell compared to 69% in the top layer of a P/N solar cell. This top layer of the cell is most affected by radiation. It has also been theoretically calculated that the optimized N/P device will prove to have a higher efficiency than a similar P/N device [2].

This N/P GaAs solar cell will have a thin GaP window layer to reduce the minority carrier surface recombination velocity from 10^6 cm^2/sec to 10^4 cm^2/sec. GaP has been chosen as the window layer material instead of $Ga_xAl_{1-x}As$ to insure the formation of ohmic contacts that do not suffer degradation upon exposure to air. The problem of the 3.6% lattice mismatch between GaAs and GaP will be minimized by keeping the thickness of the epitaxially grown window layer thin enough so that its lattice constant may be strained elastically to equal that of the underlying GaAs.

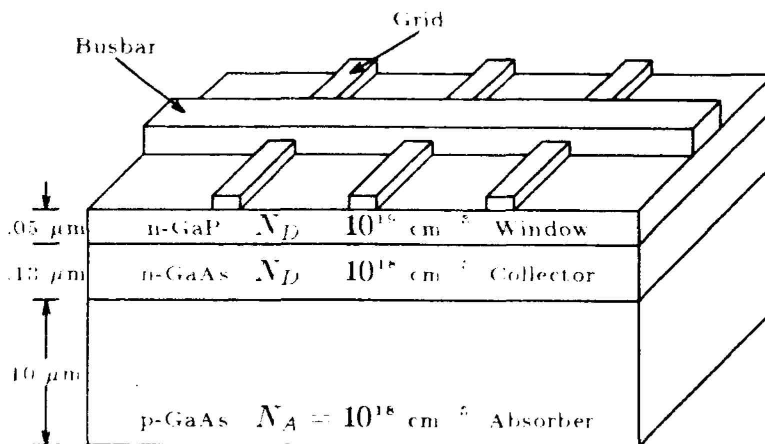

Figure 1 Optimized N/P GaAs solar cell

*This work supported by the NASA Lewis Research Center under contract #NAG3-422.

The optimized N/P GaAs solar cell with a thin GaP window layer is shown below in Figure 1 along with theoretical efficiencies and a loss analysis [2].

Table 1

Calculated Theoretical Efficiencies and Loss Analysis for N/P GaAs

Loss Mechanism	% Loss	J_{sc} mA/cm^2	V_{oc} volts	Fill Factor	AM0 η 1× Sun
Theoretical Maximum	—	38.6	1.09	.892	27.7
Recombination	4.7	36.8	1.07	.891	25.9
a. Top Layer	1.6	13.6*	–	–	—
b. Bottom Layer	3.1	18.8*	—	-	—
Absorption	1.0	36.4	1.07	.890	25.6
Reflection	2.6	35.4	1.07	.890	24.9
Grid Transparency	4.0	34.0	1.07	—	—
Resistive	4.6	—	—	.890	23.9

* The balance of J_{sc} is generated in the depletion region

$\therefore\ J_{sc} = J_{top} + J_{bottom} + J_{depl}$

2. Top Contacts

The generic solar cell structure, including grid lines and busbars, is shown in Figure 2. The top contacts are designed to remove the generated current from the solar cell. Ideally, grid lines act as the primary current collectors and receive all of the current from the semiconductor region. Busbars are the secondary collectors which pick up current from the grids and carry it out of the active region of the solar cell. This separation of functions allows for a multi-layer metallization design, so that busbars can be made larger (in cross section) than the grids since they carry more current. This multi-layer design is usually not used, even when grid optimization is performed [3-5], however, this design can be shown to provide a higher efficiency solar cell [6].

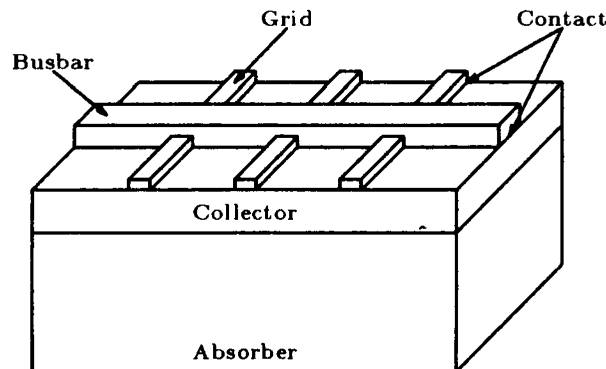

Figure 2 Generic solar cell.

ORIGINAL PAGE IS
OF POOR QUALITY

ORIGINAL PAGE IS
OF POOR QUALITY

2.1 Grid Losses

The grid pattern contains several loss mechanisms which reduce the available output power. Unlike many losses which are dependent on basic physical principles or intrinsic material properties, the grid losses are mainly dependent on engineering design. Thus, by using loss minimization [7], an optimum grid geometry can be found which provides for the best output power for a given solar cell.

Top contact losses consist mainly of electrical (I^2R) losses and optical losses (transparency/shading). A mathematical description of these grid losses is necessary in order to perform loss minimization.

Electrical Losses — These losses are basically due to ohmic losses (heating) incurred during removal of power from the solar cell. The geometry of the grid affects the current flow throughout the cell, so each region will have a loss component [Figure 2]. The total electric power loss can be modelled as the sum of these individual loss components [7].

$$P_{loss} = I^2 R_{loss} = I^2(R_{absorber} + R_{collector} + R_{grid} + R_{busbar}) \tag{1.1}$$

Optical Losses The top contacts block some of the light that would normally enter the solar cell. This optical loss can be defined in terms of the percentage of light that penetrates to the active region of the solar cell (i.e., the transparency T).

$$T \stackrel{\text{def}}{=} \frac{SA_{cell} - SA_{grids/busbars}}{SA_{cell}} \qquad (0 \leq T \leq 1) \tag{1.2}$$

where SA is the surface area.

The minimizing process requires a low electrical loss (R_{loss} small) as well as a low optical loss ($T \to 1$). Since both processes compete with each other, a compromise must be reached to obtain the minimum total grid loss. By describing the photogenerated current in terms of a percentage (T) of the maximum possible current I_{max}, both losses can be combined into a single "power loss equation."

$$I_{light} = qA\eta\phi = qA\eta(\phi_{max}T) = I_{max}T \tag{1.3}$$

$$P_{loss} = (I_{max}T)^2(R_{abs} + R_{coll} + R_{grid} + R_{bus}) \tag{1.4}$$

Finally, using Poynting's vector, a description of the current flow in point form can be derived for P_{loss}, such that:

$$P = \int_V J^2 \rho \, dV \equiv (I_{max}T)^2 R_{loss} \tag{1.5}$$

In this form, the current density $\vec{J}(x, y, z)$ can be described thoroughly in any region of the solar cell. Solution of the integral for each solar cell region can then be compared to $(I_{max}T)^2 R_{region}$ to determine the "lumped resistance" belonging to that region. Once each R_{region} has been found, the total top contact resistance R_{loss} can be minimized.

2.2 Current Flow in a Solar Cell

A schematic of how current might flow in an actual cell is given by Figure 3a.

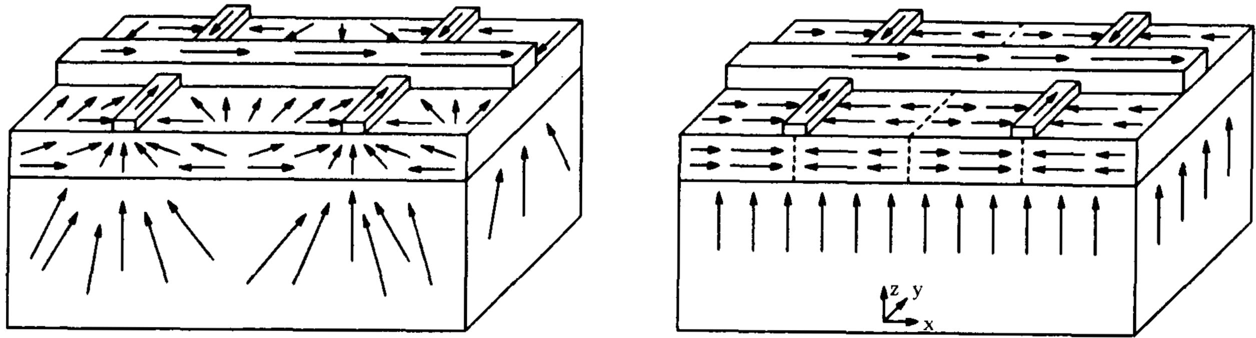

Figure 3 (a) Actual current flow model in a solar cell and (b) theoretical current flow.

This description can be simplified without significant error by using several useful assumptions:

1. Solar cell operates at the short circuit current point.
2. Uniform photon flux ϕ is incident over the entire x y planar surface of the cell.
3. Uniform current generation rate throughout the cell.
4. Constant current density enters the collector region from the absorber region in the z direction.
5. Thickness of collector region (t) is much smaller than lateral x y dimensions.
6. Grid/Busbar contacts are equipotentials
   $\rho_{grid}, \rho_{busbar} \ll \rho_{absorber}, \rho_{collector}$
7. Resisitivities are uniform within a given region.
   $\rho_{region}(x, y, z) \equiv \rho_0$

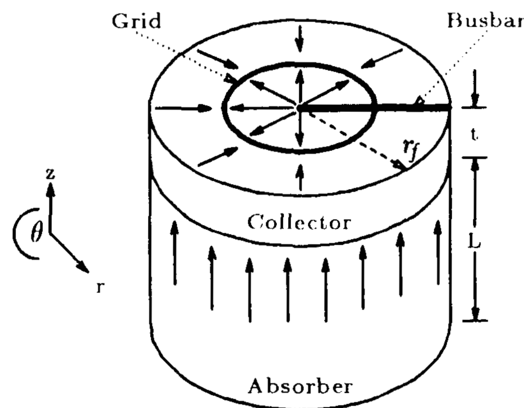

Figure 4 Cylindrical solar cell model.

The resulting theoretical current flow is shown in Figure 3b. However, an optimum grid pattern for a solar cell concentrator is desired. Since the spot of illumination will be circular in nature, a circular grid design is suggested. Figure 4 shows a cylindrical solar cell model with a theoretical current flow using these same assumptions.

2.3 Solution of R_{loss}

The easiest means of solving R_{loss} is to individually solve for each R_{region}. The general placement of the grids and busbars is shown in Figure 4. The grids are circular rings and the busbars project radially from the center of the solar cell. For a circular solar cell, current traveling to a grid will be parabolic ($J(r) \propto r^2$) since the area increase as r^2. If grids are placed to inscribe equal areas, then each grid will receive an equal amount of the total current.

$$\text{Grid placement} \qquad R_l = \sqrt{\frac{2l-1}{2N}}\, r_f \qquad l = 1, 2, 3, \ldots, N \text{ Grids} \tag{1.6}$$

Radial busbars provide the shortest path out of the solar cell while intersecting each grid once. Tapered busbars are used for ease of calculation in cylindrical coordinates. Once the current densities in each region have been determined, the power loss equation (2.4) can be solved, yielding the individual resistances.

$$R_{abs} = \frac{\rho_{abs} L}{\pi r_f^2} \tag{1.7}$$

$$R_{coll} = \frac{\rho_{coll} \pi r_f^2}{32 \pi t N^2} \sum_{l=1}^{N} \left[8l^2 \ln \frac{2l}{2l-1} + 2(2l-2)^2 \ln \frac{2l-1}{2l-2} - 8l + 4 \right] \tag{1.8}$$

$$R_{grid} = \frac{\rho_{grid} \pi r_f}{6 N M^2 w_g t_g} \sum_{l=1}^{N} \sqrt{\frac{2l-1}{2N}} \tag{1.9}$$

$$R_{bus} = \frac{\rho_{bus} r_f}{4 M w_b t_b} \tag{1.10}$$

$$T = \frac{\pi r_f^2 - \left[2\pi r_f w_g \sum_{l=1}^{N} \sqrt{\frac{2l-1}{2N}} + \frac{1}{2} M w_b r_f \right]}{\pi r_f^2} \tag{1.11}$$

Grids are made at the narrowest practical limit (with $\frac{t_g}{w_g} = 2$), and this ratio is maintained as dimensions are increased ($\frac{t_b}{w_b} = 2$). So, a scale factor (m) can be introduced to represent the larger busbar dimensions (w_b, t_b) relative to the grid line dimensions (w_g, t_g). That is:

$$\left. \begin{array}{l} t_b = m t_g \\ w_b = m w_g \end{array} \right\} \quad \frac{t_b}{w_b} = \frac{m t_g}{m w_g} = 2 \tag{1.12}$$

2.4 Grid Optimization

The optimum grid pattern can be found by solving the output power equation (2.4). The criterion for the best grid pattern occurs when the output power (P_{out}) is at a maximum (i.e., when P_{loss} is minimized).

$$P_{out} = P_{max} - P_{loss} \tag{1.13}$$

$$P_{max} = I_{max} V_{max} T \tag{1.14}$$

$$P_{loss} = (I_{max} T)^2 R_{loss} \tag{1.15}$$

A computer program was written to calculate and find the maximum output obtainable by varying the three unknowns (N, M, and m), and using the given design parameters [Table 2] for the GaAs solar cell concentrator. An example of one optimized grid pattern for 1000 × AM0 sunlight is shown in Figure 5, with numerical results given in Table 3.

ORIGINAL PAGE IS OF POOR QUALITY

Table 2

N/P GaAs Input Parameters for Grid Optimization					
$J_{sc}^{1\times}$	35.4 $\frac{mA}{cm^2}$	L	10 μm	ρ_{abs}	$1.56 \times 10^{-2}\ \Omega\,cm$
$V_{oc}^{1\times}$	1.07 V	t	.13 μm	ρ_{coll}	$7.10 \times 10^{-5}\ \Omega\,cm$
	1000	w_g	10 μm	ρ_{grid}	$1.68 \times 10^{-6}\ \Omega\,cm$
r_f	2 mm	l_g	5 μm	ρ_{bus}	$1.68 \times 10^{-6}\ \Omega\,cm$

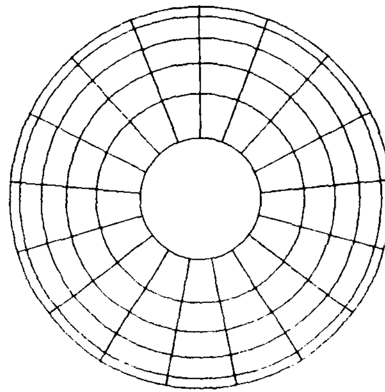

Figure 5 Optimized grid pattern for 1000× AM0.

Table 3

Numerical Results from the Best Grid Pattern		
$J_{sc}^{1000\times}$ 35400 $\frac{mA}{cm^2}$	$\eta = .9172$	$R_{abs} = .1243$ mΩ
$V_{oc}^{1000\times}$ 1.249 V	$T = .9479$	$R_{coll} = 5.656$ mΩ
$I_{max} = 4.351$ mA	$N = 5$	$R_{grid} = .8167$ mΩ
$V_{max} = 1.150$ V	$M = 17$	$R_{bus} = 2.444$ mΩ
$P_{max} = 5.003$ W	$m = 2$	$R_{loss} = 9.041$ mΩ

2.5 Multi-Layer Metallization

A comparison between single layer and multi-layer grids is given in Table 4. The multi-layer design has its maximum impact at higher concentrations and larger cell areas (i.e., high currents). A pictorial comparison of the transparency savings with a multi-layer grid pattern is shown in Figure 6.

ORIGINAL PAGE IS
OF POOR QUALITY

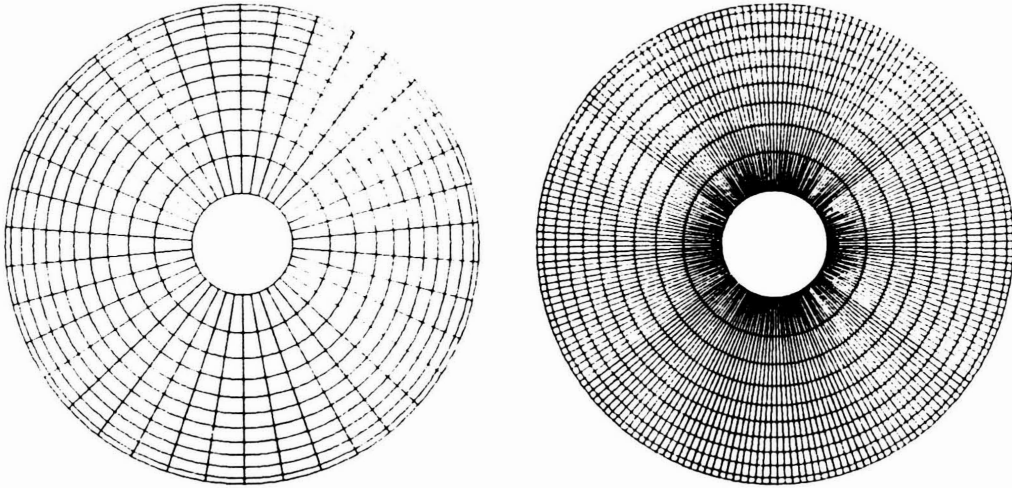

Figure 6 Comparison of thick busbar vs. thin busbar pattern: (a) 11 grids, 38 busbars, 4 scale (m) (b) 10 grids, 200 busbars, 1 scale (m).

Table 4

Diameter (cm)	Concentration (×)	Thick Busbar (η)	Thin Busbar (η)	Improvement (%)
1.0	100	.9447	.9293	1.66
	300	.9129	.8832	3.36
	1000	.8605	.8016	7.35
2.0	100	.9160	.8728	4.95
	300	.8703	.7931	9.73
	1000	.7944	.6606	20.25

2.6 Experimental Results

The computer program provides specific power losses for each of the semiconductor and metal layers as part of the optimization. These theoretical values were compared to another grid program from Sandia National Laboratories 8 5 and found to give similar results for the same grid design.

Several experimental test solar cells were made using the grid pattern described in Figure 5. The solar cell is N/P GaAs and closely matches the optimum design given in Figure 1 (but

ORIGINAL PAGE IS
OF POOR QUALITY

with a GaAlAs window). A picture of a test cell is shown in Figure 7 along with an I-V curve measured on a curve tracer.

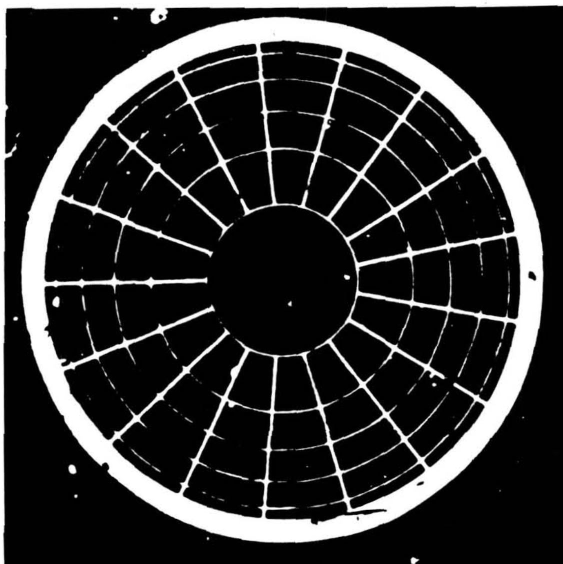

Figure 7 Experimental solar cell with optimized grid pattern.

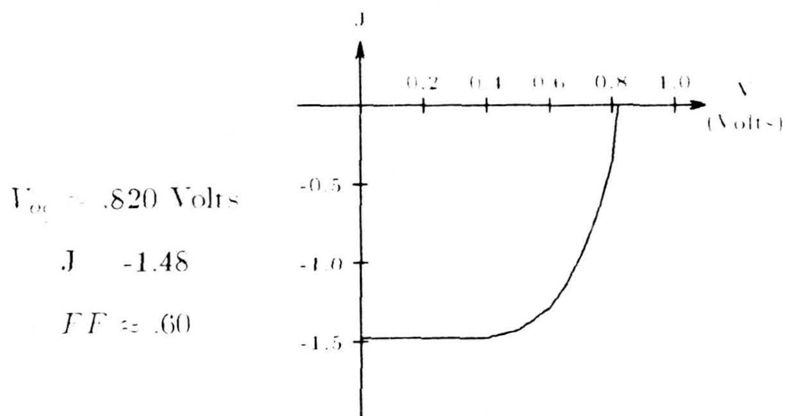

Figure 8 I-V curve of experimental solar cell.

3. Conclusions

The use of a GaP window layer on a GaAs solar cell will avoid many of the inherent problems normally associated with a GaAlAs window, while still proving good passivation of the GaAs surface. An optimized circular grid design for solar cell concentrators has been shown which incorporates a multi-layer metallization scheme. This multi-layer design allows for a greater current carrying capacity for a unit area of shading, which results in a better output efficiency.

ORIGINAL PAGE IS
OF POOR QUALITY

References

[1] C. Amano, M. Yamaguchi, and A. Shibukawa, "Optimization of Radiation-Resistant GaAs Solar Cell Structures," Tech. Digest International PVSEC-1, Kobe, Japan (1984), p. 11.

[2] R.H. Parekh and A.M. Barnett, "Improved Performance Design of GaAs Solar Cells for Space," IEEE Trans. Electron Devices, **ED-31**, 689 (1984).

[3] M. Wolf, "Limitations and Possibilities for Improvement of Photovoltaic Solar Energy Converters," Proceedings of the IRE, **48**, 1246 (1960).

[4] R.S. Sharlack, "The Optimal Design of Solar Cell Grid Lines," Solar Energy, **23**, 199 (1979).

[5] P.A. Basore, "Optimum Grid-Line Patterns for Concentrator Solar Cells under Nonuniform Illumination," IEEE 17th Photovoltaics Specialists Conference, Kissimmee, FL (1984), p. 637.

[6] A. Flat and A.G. Milnes, "Optimization of Multi-Layer Front-Contact Grid Patterns for Solar Cells," Solar Energy, **23**, 289 (1979).

[7] A.M. Barnett, "Analysis of Photovoltaic Solar Cell Options," 16th IEEE Photovoltaics Specialists Conference, San Diego, CA (1982), p. 1165.

[8] Program courtesy of J.M. Gee, Sandia National Laboratory. Program written by P.A. Basore.

N86-17845

HIGH-EFFICIENCY AlGaAs-GaAs CASSEGRAINIAN CONCENTRATOR CELLS*

J. G. Werthen, H. C. Hamaker, G. F. Virshup, C. R. Lewis, and C. W. Ford
Varian Research Center
Palo Alto, California

AlGaAs-GaAs heteroface space concentrator solar cells have been fabricated by metalorganic chemical vapor deposition. AMO efficiencies as high as 21.1% have been observed both for p-n and np structures under concentration (90-100X) at 25°C. Both cell structures are characterized by high quantum efficiencies and their performances are close to those predicted by a realistic computer model. In agreement with the computer model, the n-p cell exhibits a higher short-circuit current density.

INTRODUCTION

GaAs solar cells are becoming increasingly important for space applications. An attractive approach is offered by the concentrator space cell (Ref. 1), which has the potential for reaching efficiencies higher than those predicted for one-sun space solar cells (Ref. 2).

A concentrator cell will operate at a temperature of approximately 80°C; however, the predicted efficiency is still higher than for one-sun cells operating at 25°C. In this work, we are studying heteroface AlGaAs-GaAs p-n and n-p small-area concentrator solar cells grown by metalorganic chemical vapor deposition (MOCVD). The cells are intended for use in a miniaturized Cassegrainian concentrator assembly operating at approximately 100 suns, AMO. The cell has a circular configuration with 4-mm diameter active area, and the total dimensions are 5 mm x 5 mm. Cell efficiencies as high as 21.1% have been obtained under simulated 92 suns, AMO.

CELL DEVELOPMENT

The concentrator cells are designed by a realistic computer model which solves the transport equations and determines the current-voltage (I-V) characteristics. The model uses measured values of relevant parameters such as mobility, minority-carrier diffusion lengths, absorption coefficients, etc. Cells are optimized for operating conditions such as temperature and concentration. Under concentrated light, it is crucial that the emitter and grid pattern on top of the solar cell each have very low series resistance. At the same time, the internal spectral response must remain high and the obscuration must be minimized. A one-dimensional distributed resistance model incorporating dark current mechanisms such as injection and recombination is used to determine the I-V curve. Obscurations caused by the grid pattern and the AlGaAs window layer are also included in the model.

The cell structure used in the model is shown in Fig. 1. Starting from the substrate, a highly-doped buffer layer (0.5 μm) is grown to provide a smooth surface for overlying growths and also reduce recombination at the back of the cell. Next

* Work supported by NASA-Lewis Research Center under Contract NAS3-23876.

PRECEDING PAGE BLANK NOT FILMED

lie the two active layers, the base and the emitter, followed by a thin, highly-doped AlGaAs (90% Al) window layer. This layer reduces the surface recombination velocity in the emitter, and its thickness is optimized to couple with the antireflection (AR) coating to minimize the reflectance. Finally, the cell structure is terminated with a highly-doped GaAs cap layer serving as a contact layer for good ohmic contacts. This layer, which also protects the cell during processing, is selectively etched away immediately before deposition of a single-layer AR coating.

Calculations of the quantum efficiency are limited to the emitter, base, and depletion regions. Two optimized responses are shown in Fig. 2 for p-n and n-p structures, respectively, with the individual contributions from the various regions being indicated. In the p-n structure, most photons are absorbed in the p-type emitter, whereas in the n-p structure, all regions make significant contribution to the photogenerated current. Inherently lower resistivity of n-type versus p-type GaAs allows the use of a much thinner emitter in the n-p configuration. Consequently, a better radiation tolerance for n-p cells may be expected.

In addition to the quantum efficiency, the computer model finds the optimum performance. Figure 3 shows the I-V characteristics of an optimized p-n structure under 100X, AMO at 80°C. Efficiencies of 20.7% are predicted for both p-n and n-p cell structures. With the addition of gradients both in doping and in composition, even higher efficiencies are predicted, as indicated in Table I. These gradients can be added both in the base and emitter regions where they give rise to built-in fields that aid in the collection of photogenerated carriers. Over a 2% increase in efficiency is observed with the additional gradients.

For each optimized cell structure, the computer model provides doping levels and layer thicknesses. Thus far, fabrication and testing efforts have been concentrated primarily on cells without intentional gradients. The structures are grown in a horizontal rf-heated MOCVD reactor at 730°C, as described in Ref. 3. Selenium and zinc or magnesium (Ref. 4) are used as n-type and p-type dopants, respectively. An optimized grid pattern (shown in Fig. 4) is defined using conventional photolithographic techniques. Metallizations are typically deposited by evaporation to a thickness of 0.2 μm, and normally consist of Au/Ge/Ni/Au for n-type GaAs and Pd/Au for p-type GaAs. The front contact grid pattern is plated to 3-μm thickness.

Cell performances were measured both at Varian and at Sandia National Laboratories. All measurements are based on the total circular area with a 4-mm diameter. Figure 5 shows the I-V characteristics for a p-n cell under simulated concentrated light. The measurement was obtained at 28°C. The cell efficiency versus solar concentration is shown in Fig. 6, together with the theoretically-predicted behavior. The poor performance of the experimental cell at one sun may be attributed to shunt currents which become less significant at higher concentrations. However, the measured values are still below the theoretical values, which indicates that further improvements are necessary.

Cells having the n-p configuration have also been fabricated. Compared to p-n cells, these cells show larger values of short-circuit current, in agreement with the theoretical prediction. Similar behavior has been observed for large-area, 1-sun GaAs cells (Ref. 5). However, lower values of open-circuit voltage and fill factor are predicted and also experimentally observed. Therefore, the efficiencies of p-n and n-p cells are comparable. The n-p structure has a very thin emitter, which may be of importance for increased radiation hardness. Experiments will have to be conducted to assess whether the n-p cell exhibits better radiation tolerance. The

addition of doping and compositional gradients, which provide built-in fields, may also improve radiation hardness by retaining good carrier collection even in damaged material.

High-efficiency cells intended for much higher concentrations have also recently been fabricated for terrestrial use. In this case, the doping levels were raised further to accommodate much higher current levels. These cells have the p-n configuration and are doped with Mg in the emitter. Efficiencies in excess of 26% have been observed at 753X (AM1.5, 100 mW/cm^2), as shown in Fig. 7.

CONCLUSIONS

Heteroface AlGaAs-GaAs cells for space concentrator applications have been demonstrated with efficiencies as high as 21.1% at 92X, AMO. Both p-n and n-p cell structures have been fabricated using MOCVD. The cells still need to be tested at temperatures up to 80°C. Similarly, the effects of intentional gradients in doping and composition must be evaluated. Radiation hardness may be increased by including gradients and using the n-p configuration.

REFERENCES

1. Patterson, R. E.; and Rauschenback, H. S.: Miniaturized Cassegrainian Concentrator Concept Demonstration. TRW Space & Technology Group, Space Photovoltaic Research and Technology, 1982, NASA Conf. Pub. 2256, April 1982.

2. Knechtli, R. C.; Loo, R. Y.; and Kamath, G. S.: High-Efficiency GaAs Solar Cells. IEEE Trans. Electron Devices, Vol. ED-31, 1984, p. 577.

3. Lewis, C. R.; Dietze, W. T.; and Ludowise, M. J.: The Growth of Magnesium-Doped GaAs by the OM-VPE Process. J. Electron. Mater., Vol. 12, 1983, p. 507.

4. Lewis, C. R.; Ford, C. W.; and Werthen, J. G.: Magnesium Doping of Efficient GaAs and $Ga_{0.75}In_{0.25}As$ Solar Cells Grown by Metalorganic Chemical Vapor Deposition. Appl. Phys. Lett., Vol. 45, 1984, p. 895.

5. Werthen, J. G.; Hamaker, H. C.; Virshup, G. F.; and Ford, C. W.: 18.7% Efficient (1-Sun, AMO) Large-Area GaAs Solar Cells. Appl. Phys. Lett., Vol. 46, 1985, p. 776.

TABLE I. RESULTS OF CELLOPT OPTIMIZATION RUNS FOR CELLS OPERATING UNDER 100X, AMO AT 80°C.

E = exponential profile
L = linear profile
U = constant level of dopant or aluminum fraction

Type	Doping Profile	Aluminum Profile	Efficiency (%)
p-n	U	U	20.71
p-n	E	U	22.50
p-n	E	L	22.70
p-n	E	E	23.15
p-n	L	U	22.23
p-n	L	L	22.54
p-n	L	E	23.15
n-p	U	U	20.79
n-p	E	U	22.73
n-p	E	L	22.85
n-p	E	E	23.08
n-p	L	U	22.46
n-p	L	L	22.50
n-p	L	E	23.13

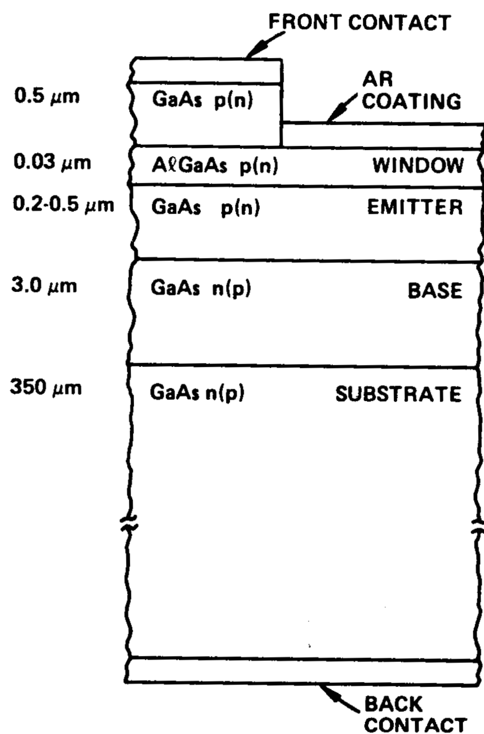

Fig. 1 Schematic solar cell structures in the computer model development.

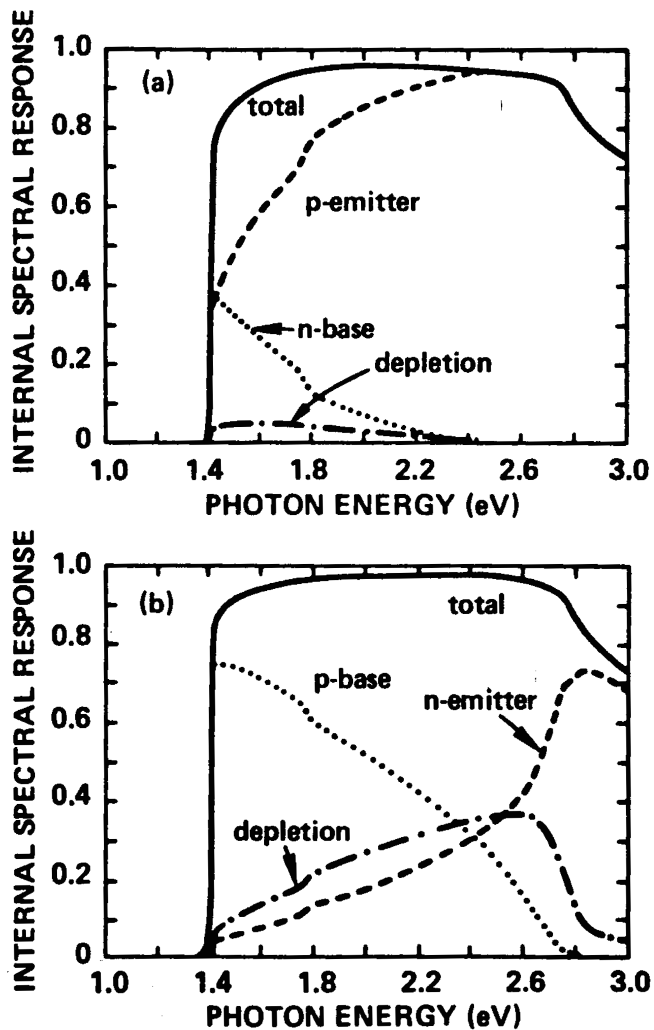

Fig. 2 Internal spectral response versus photon energy determined by the computer modeling program for optimized (a) p-n and (b) n-p structures.

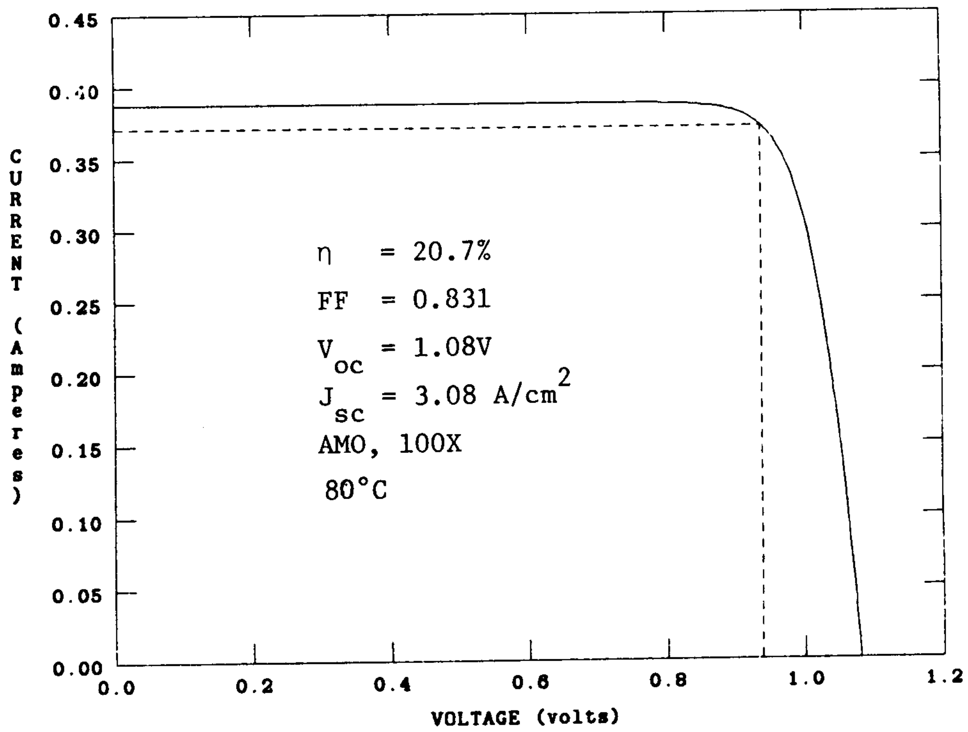

Fig. 3 Current-voltage characteristics for an optimized p-n cell as predicted by computer model. The cell operating conditions are indicated.

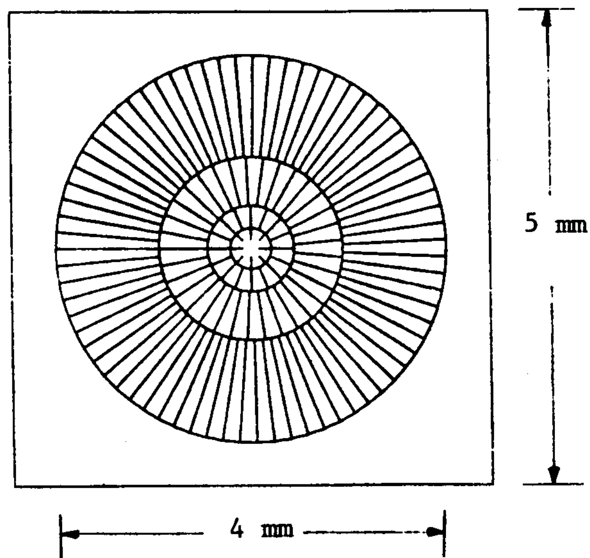

Fig. 4 Grid pattern for space concentrator cell.

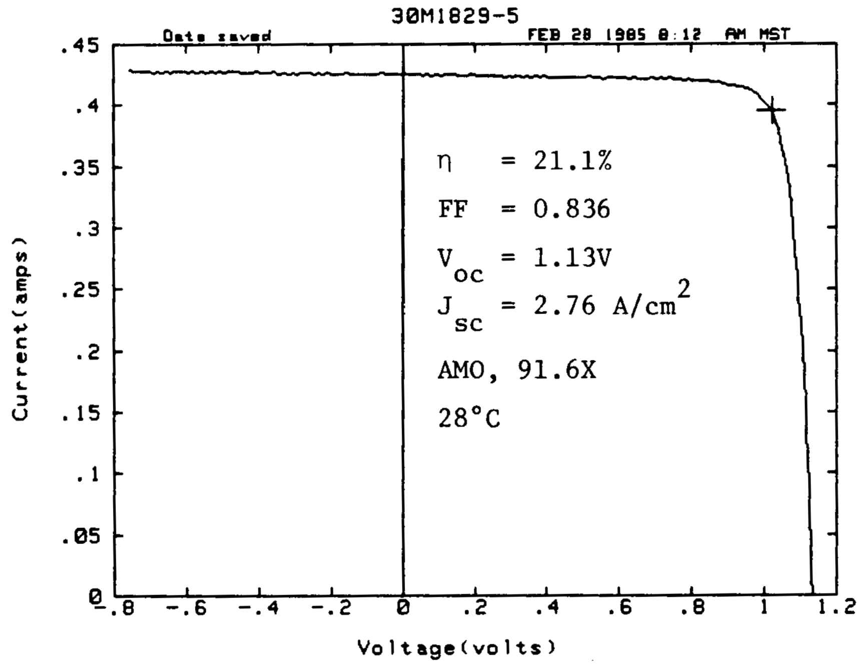

Fig. 5 Current-voltage characteristics for a p-n cell under simulated concentrated light.

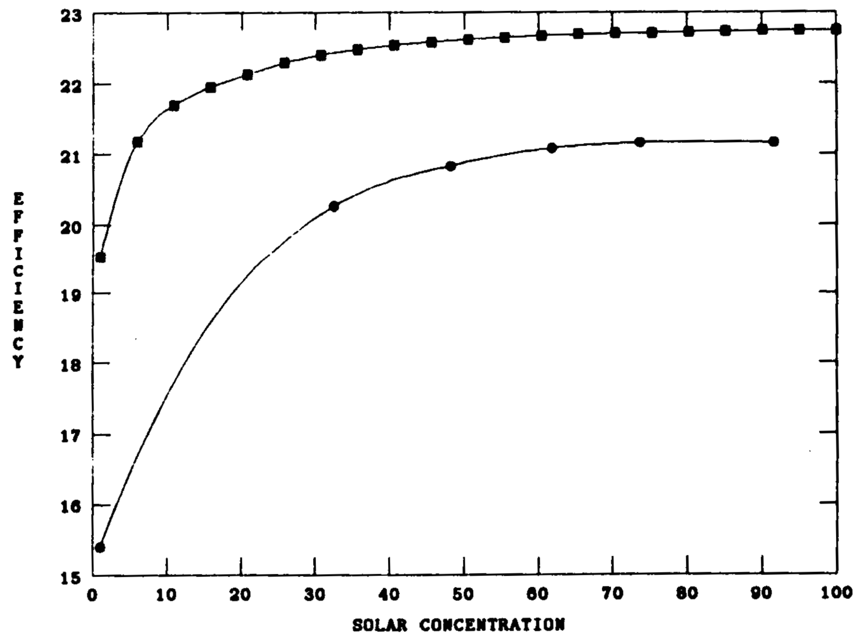

Fig. 6 Cell efficiency versus solar concentration at 28°C, AMO: computer model (■), experimental (●).

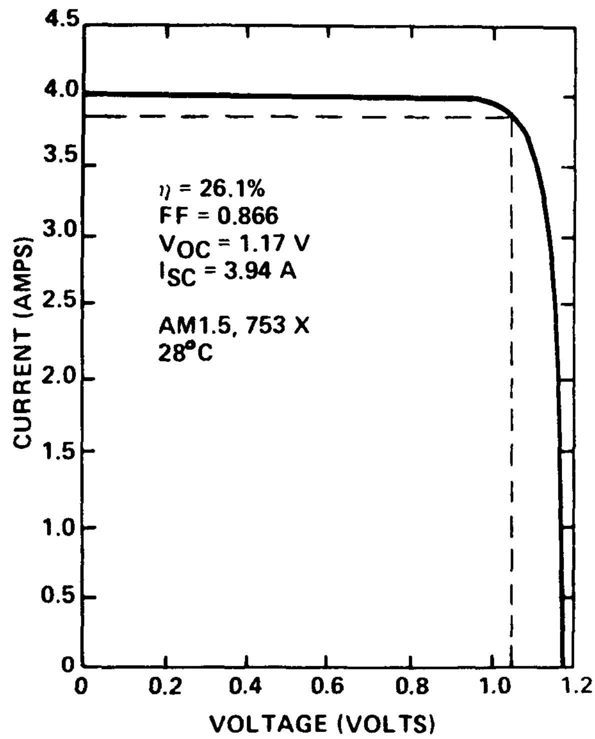

Fig. 7 Current-voltage characteristics for an experimental p-n solar cell under simulated terrestrial concentrated light.

N86-17846

EVALUATION OF $Al_xGa_{1-x}As$ SOLAR CELLS

R.Y. Loo, G.S. Kamath, R.C. Knechtli, and A. Narayanan
Hughes Research Laboratories
Malibu, California

S.S. Li
University of Florida
Gainesville, Florida

Single junction GaAs solar cells have already attained an efficiency of 19% AMO which could potentially be increased to ~20 %, with some optimization. To achieve the higher efficiency we must employ the concept of multibandgap solar cells which utilizes a wider region of the solar spectrum. One of the materials for fabricating the top cell in a multibandgap solar cell is AlGaAs because it is compatible with GaAs in bandgap and lattice match. This is a very important consideration from the materials technology point of view; this paper evaluates the viability of this approach. It is interesting to note that in this context the technology for AlGaAs has been well developed for applications to lasers and to high speed transitors.

AlGaAs LPE GROWTH

During the past few years we have developed and perfected the infinite solution LPE growth technique for the fabrication of single junction GaAs solar cells. We are now extending the technology to the fabrication of AlGaAs solar cells. Since Al is a very reactive element and is easily oxidized when exposed to air, we need to grow two AlGaAs layers in succession on a GaAs substrate. To achieve this goal we modified the crucible in our LPE furnace to a multiwell crucible using different AlGaAs solutions, including the p-type AlGaAs solution with Be as the dopant. The other solutions are n-type, Sn-doped $Al_xGa_{1-x}As$ solutions. Figure 1 shows a sketch of our multiwell crucible and Table I indicates the composition of each solution. Figure 2 shows the baseline design of an AlGaAs solar cell; it is identical to our AlGaAs-GaAs homojunction solar cell. Figure 3 shows the entire temperature cycle for growing the AlGaAs solar cell from a multiwell system. The first layer is an n-type AlGaAs base layer grown directly on a GaAs substrate and the second layer is the p-type AlGaAs window layer. The AlGaAs window layer is necessary to reduce the surface recombination velocity at the front surface of the cell. During the growth of the window layer, the dopant (Be) diffuses into the base n-AlGaAs layer to form an active photovoltaic junction.

RESULTS AND DISCUSSIONS

We have fabricated a number of AlGaAs solar cells with three different Al concentrations in the base region of the cell. Figures 4, 5, and 6 show the photo IV and spectral response of these cells. Table II summarizes the results from these measurements. The short circuit currents measured from these cells are lower than expected for the Al concentration in the base layer. The reduction in the cell's short circuit current is not caused solely by the increase of the bandgap in the material as the Al concentration is increased. In our experimental cells made to date, this loss of short circuit current was caused to a large extent by decreased electrons and hole diffusion lengths, combined with an excessive junction depth.

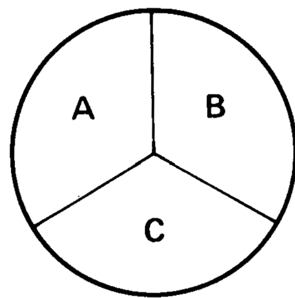

Figure 1. Multiwell crucible (top view) for growing $Al_xGa_{1-x}As$.

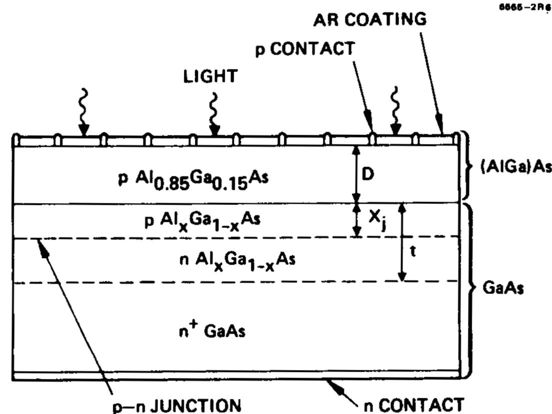

NUMBER OF FINGERS = 24

p CONTACT: Au–Zn–Ag

n CONTACT: Au–Ge–Ni–Ag

AR COATING: Ta_2O_x

CELL SIZE = 2 cm x 2 cm

Figure 2. $Al_xGa_{1-x}As$ solar cell structure.

Table I. Melt Composition in the Multiwell Crucible

Melt	Melt Size	Solution	Type
A	1500 g	$Al_{0.85}Ga_{0.15}As$	p^+ (Be)
B	1500 g	$Al_xGa_{1-x}As$	n (Sn)
C	1500 g	Al_xGa_{1-x}	n (Sn)

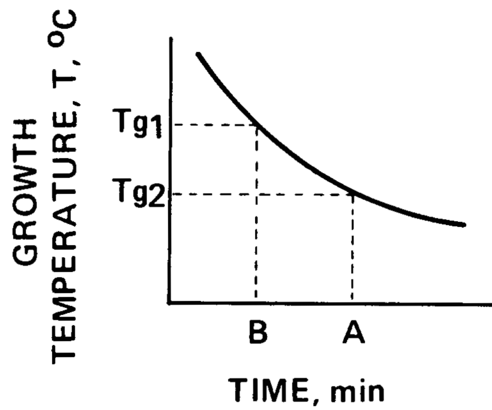

Figure 3. Temperature cycle for growing $Al_xGa_{1-x}As$ (growth sequence: 1 B → 2 A).

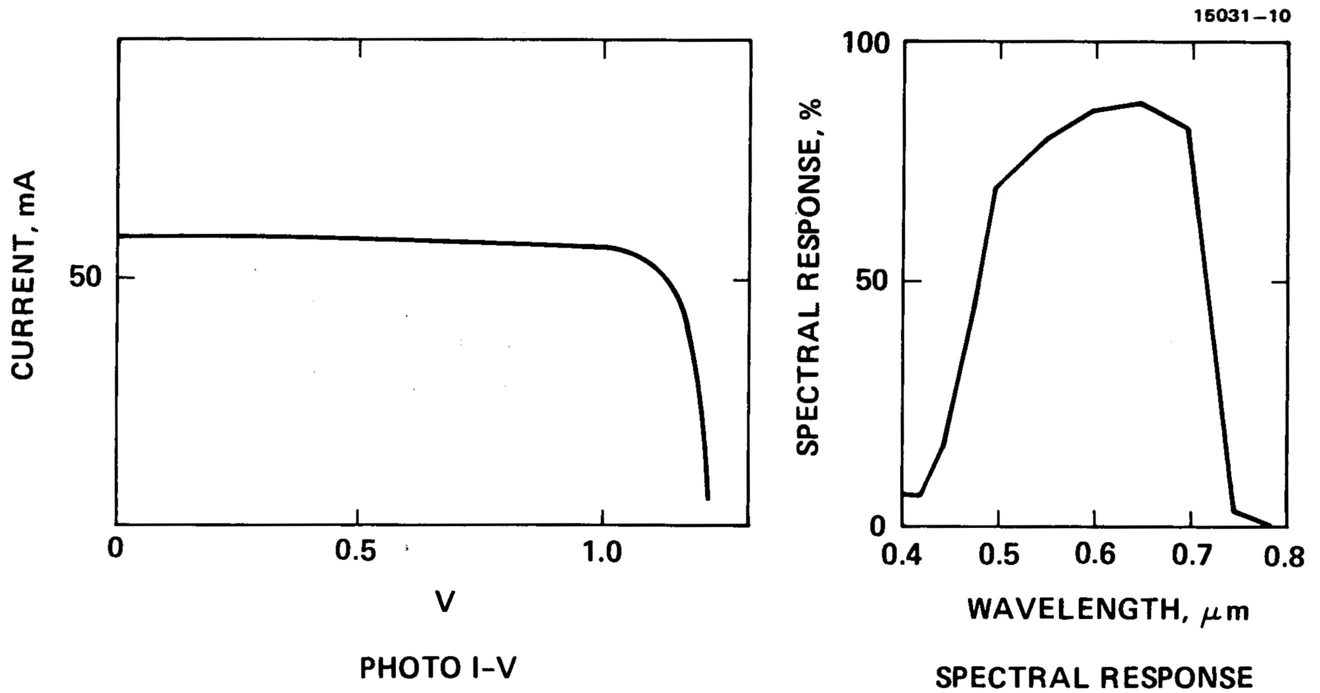

Figure 4. AlGaAs solar cell characteristics (Al concentration = 20%; cell area, 2 cm x 2 cm).

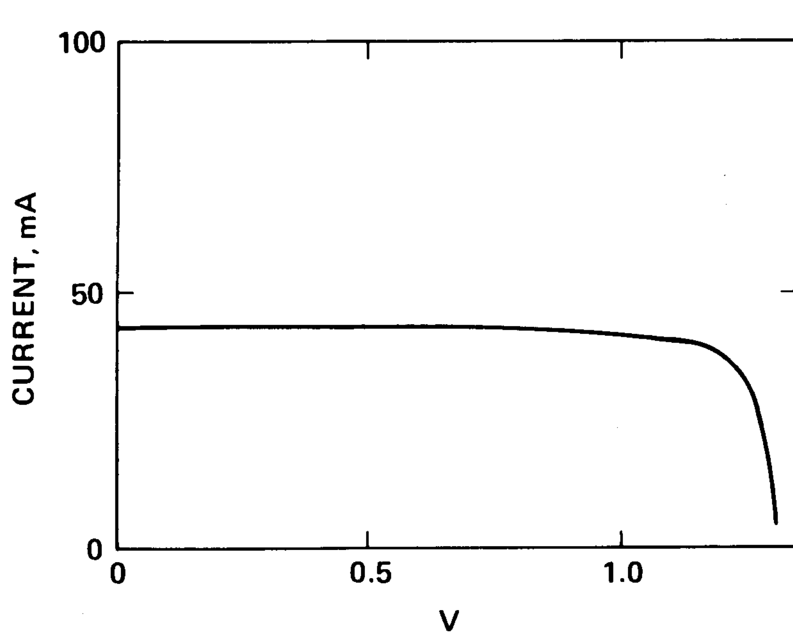

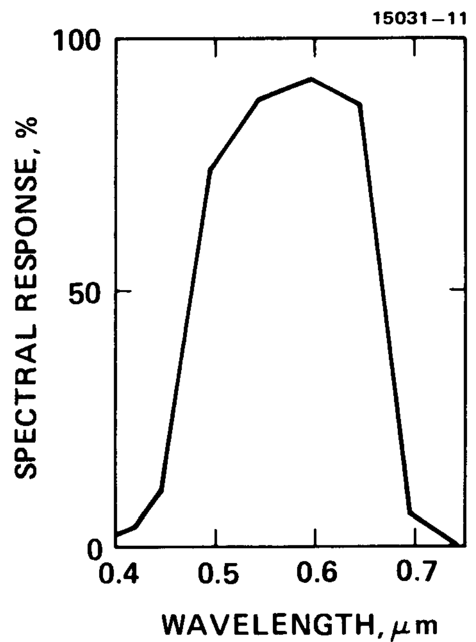

Figure 5. AlGaAs solar cell characteristics (Al concentration = 30%; cell area, 2 cm x 2 cm).

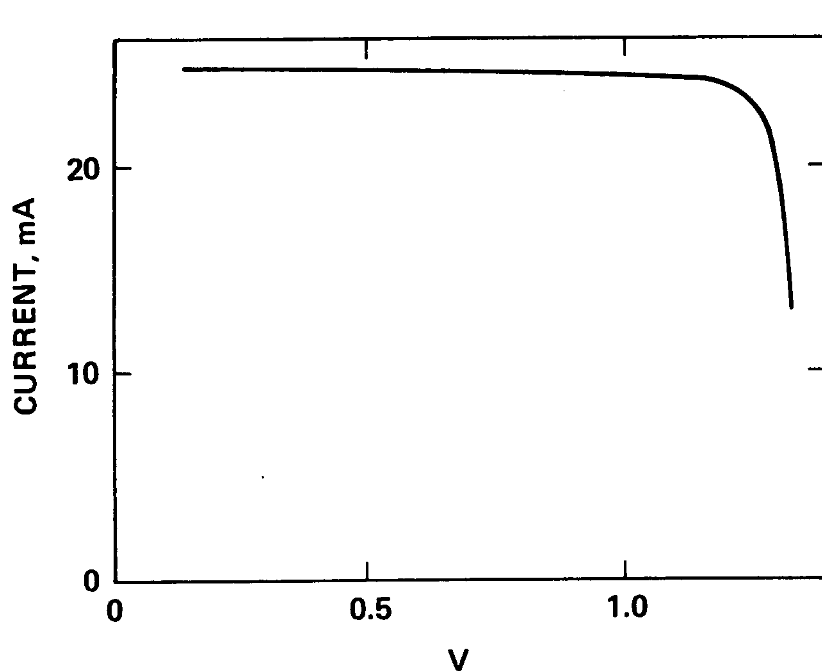

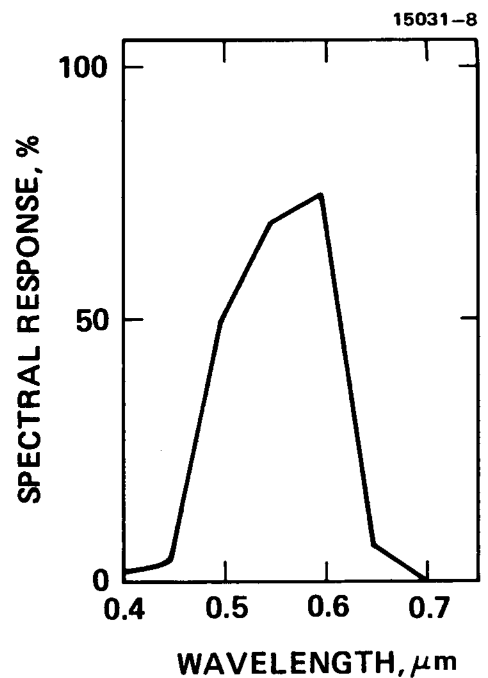

Figure 6. AlGaAs solar cell characteristics (Al concentration = 40%; cell area, 2 cm x 2 cm).

Table II. $Al_xGa_{1-x}As$ Solar Cell Performance (cell area, 2 cm x 2 cm)

Al CONCENTRATION %	I_{SC} mA	V_{OC} V	FF	P_{MAX} mW	η %
20	59.0	1.22	0.810	58.32	10.77
30	43.0	1.31	0.800	44.84	8.3
40	25.5	1.34	0.864	29.52	5.45

Figure 7 shows the measured Hall electron mobility as a function of Al concentration. The mobility is reduced from close to 2000 to 550 $cm^2 V^{-1} s^{-1}$ when the Al concentration is increased from 20 to 40 %. The decrease in mobility is due to the Al alloy composition in the materials. The lower value of mobility reflects lower diffusion lengths since diffusion length is related to the mobility by $L = ((kT/q) * *\tau)^{1/2}$. In addition, AlGaAs may be heavily compensated in our layers. The reason for such a high compensation level is due to the increase of the impurity activation energy when the Al concentration is increased. Since solar cells require high doping density, we had to add more Sn to the AlGaAs solution, which may also adversely affect the electrical properties of the material. In addition to the Hall mobility, the lifetime of the minority carriers can also be shortened, resulting in the observed lower diffusion length. Thus, we believe that the mobility and lifetime limitations are the main reasons for the lower performance of the cells. Use of dopants such as Te or Se may reduce the problem, but their behavior in AlGaAs needs to be carefully evaluated.

Many small area (1.6E-4 cm^{-2}) AlGaAs mesa diodes identical to the structure of the large area AlGaAs solar cells described above were fabricated for Deep Level Transient Spectrascopy (DLTS) measurements to detect the defect levels as a function of Al concentration in the AlGaAs material. Figures 8 and 9 show DLTS scans of electron traps in AlGaAs material for two different Al concentrations, x = 0.2 and x = 0.3, respectively. However, we did not observe any defects in our LPE GaAs epilayers. Table III summarizes the DLTS results of the measured defect parameters in AlGaAs. The measured activation energies of electron traps for both materials are different. For the $Al_{0.2}Ga_{0.8}As$ sample, the activation energies are 0.2 and 0.44 eV below the conduction band, while the activation energies of electron traps for the $Al_{0.3}Ga_{0.7}As$ sample are 0.18 and 0.28 eV below the conduction band. The difference in the activation energy of the deeper electron trap observed in these two samples may be attributed to the different DX center formed in these two samples. For example, Lang and Logan (1) have observed the E_c-0.43 eV level in the Te-doped AlGaAs specimen, while Zhou et al. (2) and Kumagai et al. (3) have observed an E_c-0.44 eV electron trap in the Si-doped AlGaAs material. Thus, the E_c-0.44 eV electron trap observed in AlGaAs material could be attributed to either the Si-impurity or the Te-impurity related defect center formed in these layers. According to Lang and Logan, this impurity center is in fact a donor and a vacancy defect complex known as a DX center. Further, Kumagai et al. have shown that the activation energies of the DX centers with group IV impurities become shallower as the mass number of impurities is increased, while those with group VI impurities remain constant. Our result is consistent with those reported by Kumagai et al. and Lang and Logan.

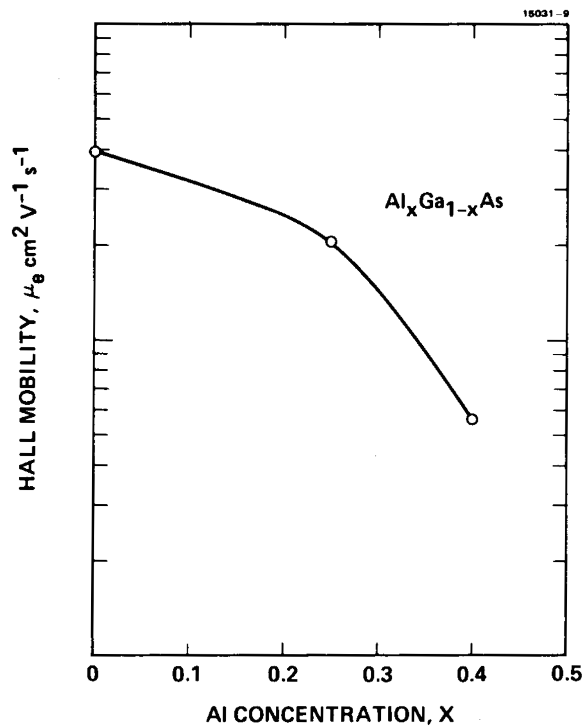

Figure 7. Electron Hall mobility, μe, as a function of alloy composition, x, for $Al_xGa_{1-x}As$ alloys.

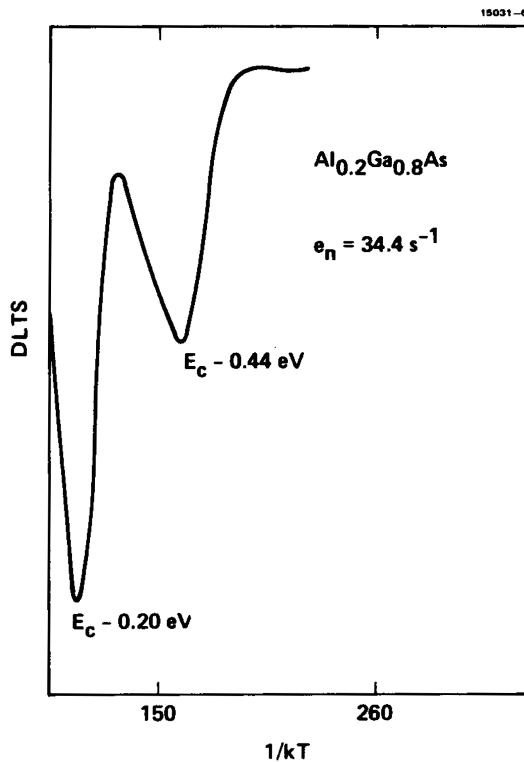

Figure 8. DLTS scan of electron traps in $Al_{0.2}Ga_{08}As$.

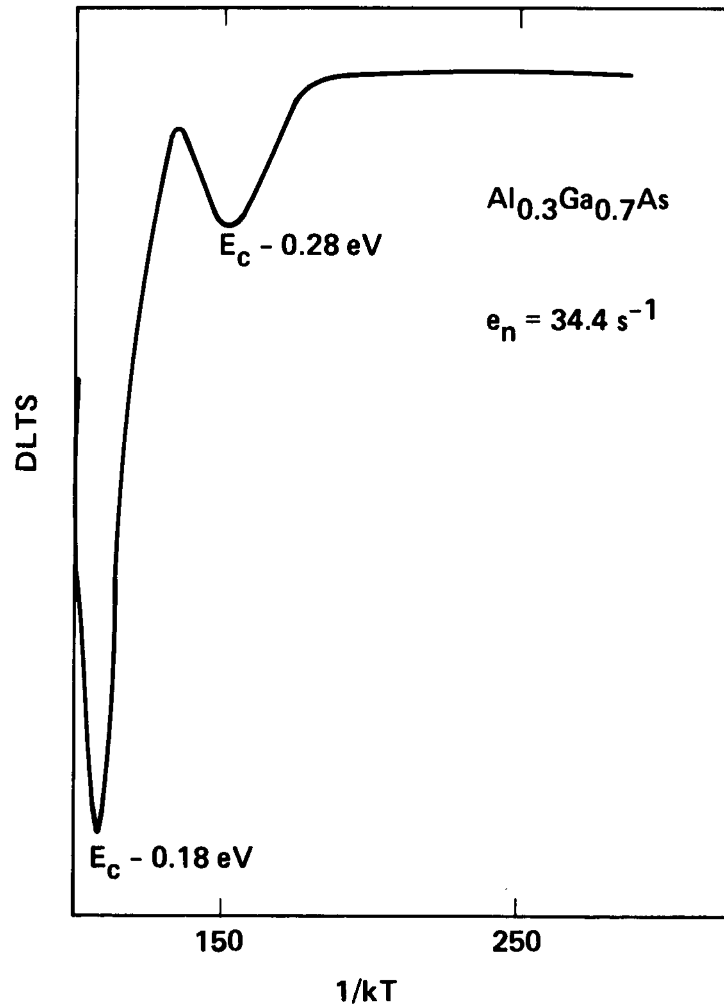

Figure 9. DLTS scan of electron traps in $Al_{0.3}Ga_{0.7}As$

Table III. Defect Parameters of $Al_xGa_{1-x}As$ as Determined by DLTS Measurements for x = 0.2 and 0.3

15031-5

(AREA = 4.153 x 10^{-4} cm^2)	N_D (cm^{-3})	E_T (eV)	N_T (cm^{-3})	6_n (cm^2)
$Al_{0.3}Ga_{0.7}As$	7.01 x 10^{16}	E_c - 0.18	5.70 x 10^{16}	6.89 x 10^{-15}
		E_c - 0.28	7.92 x 10^{15}	8.00 x 10^{-15}
$Al_{0.2}Ga_{0.8}As$	2.92 x 10^{17}	E_c - 0.20	3.10 x 10^{16}	
		E_c - 0.44	9.83 x 10^{15}	

SUMMARY

In summary, we have fabricated a number of AlGaAs solar cells using our LPE growth technique, and also two sets of AlGaAs mesa diodes with different Al concentrations. The AlGaAs solar cell efficiency decreases as the Al concentration is increased. We attribute the observation to the shortened diffusion length, which in turn is caused by the low electron and hole mobilities and also the lower minority carrier lifetime. This is verified by both the Hall measurements and DLTS studies on the AlGaAs materials. Our study is consistent with earlier studies by other workers; the defect centers are related to the defect complex formed by an impurity and a vacancy. We are studying methods to limit the number of these defect centers in order to improve the AlGaAs solar cell performance by optimizing the Al concentration and different dopants and dopant concentrations to reduce the problem caused by the amphorteric nature of tin.

REFERENCES

1. Land and Logan, Phys, Rev. Lett. 39, 635 (1977).

2. Zhou et al., Appl. Phys. A 28, 223 (1982).

3. Kumagai et al., Appl. Phys. Lett. 45, 1322 (1984).

N86-17347

GaAsP ON GaP TOP SOLAR CELLS*

James B. McNeely, Gerald H. Negley, and Allen M. Barnett
Astropower Division
Astrosystems, Inc.
Newark, Delaware

GaAsP on GaP top solar cells as an attachment to silicon bottom solar cells are being developed. The GaAsP on GaP system offers several advantages for this top solar cell. The most important is that the gallium phosphide substrate provides a rugged, transparent mechanical substrate which does not have to be removed or thinned during processing. Additional advantages are that 1) gallium phosphide is more oxidation resistant than the III-V aluminum compounds, 2) a range of energy band gaps higher than 1.75 eV is readily available for system efficiency optimization, 3) reliable ohmic contact technology is available from the light-emitting diode industry, and 4) the system readily lends itself to graded band gap structures for additional increases in efficiency.

INTRODUCTION

The optimum band gap for a top solar cell on a silicon bottom cell (1.1 eV) lies between 1.75 and 2.07 eV [1]. Top solar cell layer compositions corresponding to band gaps of 1.75 eV or higher are being investigated to determine the optimum band gap as a function of real device and system performance. For example, the potential gain in minority carrier diffusion lengths at 2.1 eV, due to a reduced lattice mismatch, may net a higher system efficiency.

GaAsP TOP SOLAR CELL DESIGN

The GaAsP on GaP top solar cell design is based on a model used to calculate theoretical maximum efficiencies of tandem solar cell systems. The model that is being used follows that described by Fan [1].

Assuming unity quantum efficiency and no losses, the model predicts a maximum tandem solar cell efficiency of 34.8% for the AMO spectrum at a one sun insolation. This optimum performance is based on a four-terminal configuration. The top solar cell has an energy gap of 1.97 eV and the calculated performance for both ideal solar cells is shown in Table I.

*Partial support has been provided by the Air Force AeroPropulsion Laboratory under Contract No. F33615-84-C-2486.

Table I.

Ideal Tandem Solar Cell Model - AMO
(Bottom Cell - Silicon)

Gap (eV)	Jsc (mA/cm^2)	Voc (volts)	FF	Efficiency (%)
1.97	20.75	1.50	0.91	21.1
1.12	32.68	0.67	0.84	13.7
				34.8

The actual anticipated efficiencies can be modeled by considering losses [2]. The one sun losses are tabulated below in Table II.

Table II.

Tandem Solar Cell Model with Losses:

- Optical and recombination losses which reduce Jsc as follows:

Top surface reflection -	2.6%
Grid Shading - top cell	4.0%
Absorption losses - top cell	2.0%
bottom cell	9.0%
Recombination losses - top & bottom cell	6.2%
Bottom grid shading loss - bottom cell only	4.0%
Reflection loss - bottom cell only	1.0%

- Electrical losses, which reduce fill factor:

Series resistance losses - both solar cells	2.0%

Gap (eV)	Jsc (mA/cm^2)	Voc (volts)	FF	Efficiency (%)
1.97	17.8	1.50	0.89	17.6
1.12	24.8	0.67	0.82	10.1
				27.7

Another useful case is based on an energy gap larger than the optimum of 1.97 eV. For example, at 2.07 eV, the arsenic concentration can be reduced from x = 0.54 to x = .40, leading to a reduced lattice mismatch of 1.5% from 2.0%. The energy conversion efficiency reduction from the optimum may be offset by longer actual diffusion lengths based on reduced lattice mismatch. This design clearly merits further examination. The analysis of this design (2.07 eV) leads to a predicted tandem solar cell efficiency of 34.5% which is similar to that predicted by the optimized design at 1.97 eV.

Finally, the GaAsP on GaP system lends itself to graded energy gaps on both sides of the junction. It has been shown that this can lead to as much as an 11% increase in energy conversion efficiency

[3]. This graded energy gap design will be studied to maximize system conversion efficiency.

A range of energy gaps between 1.75 eV and 2.07 eV for the top solar cell junctions is being explored during this program.

DEVICE PREPARATION

The solar cell structure is being grown using liquid phase epitaxial growth. The advantages of liquid phase epitaxy are excellent transport properties, minimum contamination, uniform thickness control, and reductions in point defects and dislocations. Liquid phase epitaxial growth has, in general, demonstrated devices that are superior in performance to those grown by the other methods [4,5]. These superior performance devices include light emitting diodes, semiconductor lasers, magnetic garnet bubble memories and GaAs solar cells. The improved performance of liquid phase epitaxial, LPE, devices when compared to vapor phase or diffused devices can be attributed to the exact stoichiometry control, longer diffusion lengths, fewer deep levels and the tendency of impurities to segregate to the liquid rather than the solid.

Ideally, one would like to grow epitaxial layers on lattice-matched substrates. While this is not possible with the GaAsP on GaP devices, we have demonstrated lattice-mismatched liquid phase epitaxial growth of GaAsP on gallium phosphide substrates. Recently multiple graded layers of GaAsP on GaP with a composition of $GaAs_{.68}P_{.32}$ corresponding to a band gap of 1.81 eV have been grown with smooth morphologies in our laboratories. The overall degree of lattice mismatch between $GaAs_{.68}P_{.32}$ (a_o = 5.5886) and GaP (a_o = 5.45117) is 2.52%. This growth was accomplished by three individual grading layers each accommodating 1.86%, 0.33%, and 0.33% of the lattice mismatch, respectively. Grading was readily accomplished by melt depletion. Moon and co-workers [6] have independently shown feasibility of liquid phase epitaxial grading to obtain smooth layers that are mismatched relative to the substrate for the GaAsP and other ternary and quaternary systems. The $GaAs_{1-}P_x$ graded layer from Moon's work shows uniform compositional grading for GaAsP system and smooth growth morphology for a $GaAs_{0.6}P_{0.4}$ layer on which corresponds to a 2.22% lattice mismatch in a single layer.

These results are indeed encouraging. The optical transmission of the three GaAsP layers grown by us are shown in Figure 1.

Mismatch dislocations result from compositional discontinuities and from composition variations that are too large for the layers to accommodate the mismatch within the graded layer. A method of reducing misfit dislocations to zero has been described [7]. This method uses a two-stage top layer growth from similar melts to achieve zero misfit dislocation growth. Misfit dislocations are pinned at the termination of the first layer growth, making extension of the misfit dislocation in the second homo-epitaxy layer difficult.

Characterization of these layers is by optical transmission, optical microscopy, spectral response, scanning electron microscopy,

EDAX and misfit dislocation decoration and analysis. Minority carrier diffusion length will be optimized based on variations in growth parameters and compositions.

Solution growth of multi-layer structures of GaAs-GaP will be performed using the slider method developed for liquid phase epitaxial growth [8]. The slider apparatus serves as a substrate holder and melt container for the growth solutions. Advantages of the slider apparatus over other techniques, such as dipping, are 1) the substrate wafer can be brought in and out of contact with the melts, 2) several melts can be used in sequence, 3) growth is restricted to a single side of the wafer, 4) substrate-solution contact is from the bottom of the melt where there are no floating oxides or other contaminants, 5) excess solution can be wiped off the wafer by the slider action of the boat, and 6) thermal equilibrating and temperature profiling are greatly facilitated. The graphite slide apparatus fits into a cooling or temperature gradient furnace, as appropriate. The furnace zones can be controlled to better than 1^oC. We use a furnace atmosphere based on a high purity mixture of hydrogen or 15% hydrogen and 85% nitrogen, which is continuously sweeping the furnace and slider apparatus during the furnace operation.

A feature of the slider boat apparatus particular to this program is the grading of the width of the growth wells shown in Figure 2. This graded well width design permits individual access to each of the grown layers after the substrate is removed from the boat.

Based on thermodynamic considerations, the preferred solvent for the p-layer is gallium, and for the n-layer, gallium or tin. Both of these materials are available commercially with purities in excess of 99.9999%. Both p-type and n-type single crystal gallium phosphide are available commercially with various dopants and doping levels, consistent with device design considerations. Melts are composed of about 10 grams of solvent and appropriate amounts of GaP and GaAs. Growth is accomplished by placing the GaP substrates under the first melt to grow a transition layer of $GaAs_xP_{1-x}$ by controlling the temperature level, cooling rate, and time of exposure, and continuing, in turn, to each melt shown in the growth apparatus in Figure 2 until all requisite layers are grown.

Phase equilibria data have been determined for both the gallium and tin solvent systems.

The specific multi-layer structure being grown is based on our demonstrated growth to date tailored to have a uniformly graded structure. The structure is shown in figure 3 and is composed of four basic layers. The first three layers are graded in composition in a controlled manner either as finite composition steps, or as continuous compositional variations shown in Figure 4. The continuous compositional variations are achieved by melt depletion. The fourth layer is a thin cap layer. These layers, the method for preparation, and methodology for optimization are described in the next four paragraphs.

This structure can be produced readily in the LPE apparatus with equal facility for either n on p or p on n structures. Either zinc or

magnesium will be used in the top $GaAs_xP_{1-x}$ layer to form the p/n junction, and tellurium will be used to form the n/p junction. The salient feature of this design is that the band gap of top of each layer is 2.07 eV, 1.95 eV, and 1.75 eV band gaps. Growth may be truncated at individual layers of interest, and comparison of otherwise equivalent material may be made with only the stated variations in band gap. This permits experimental optimization of band gap during preparation of the structure. The added benefit of this structure is that each successive layer has only about 0.6% lattice mismatch, and at no point in the top two graded layers does the structure grade more than 2 mole % GaAs per micron of growth. This allows the top layers to be reasonably thin and insures their equivalency for the optimization experiments.

This graded layer structure does not represent an excessive number of layers even with intermediate layers. Our current boat design operates with up to nine melts.

The compositional variation with layer thickness is shown in Figure 4. For the top two layers, the curvature is very slight and the compositional variation is nearly a linear function. Indeed, the differential or slope of composition with respect to thickness increases only slightly as the final compositions with each layer are approached. Other variables, growth time, temperature level, growth rate and melt size, can be varied based on detailed comparison of the experimental results. Initial and final temperature and melt compositions establish the grown layer composition. Melt size and wafer area determine layer thickness. Cooling rate and growth time are dependent on each other since initial and final temperatures are fixed for a given growth situation. For example, slowing the actual growth rate can be done to improve crystal morphology, leading to increased growth time. Intermediate dislocation blocking layers are also planned after the first layer and the second layer are grown if necessary.

The cap layer is a thin grown layer. The cap serves to reduce surface recombination and can also serve as a source of dopant for a diffused junction [9]. This layer will be either GaP or $Ga_yAl_{1-y}As_xP_{1-x}$ material with initial experiments using gallium phosphide. $Ga_yAl_{1-y}As_xP_{1-x}$ will be used if interface dislocations due to GaP lattice mismatch prove to be a problem. Gallium phosphide has a high oxidation resistance, and it has been studied extensively in terms of metallic ohmic contacts. The cap layer will be thin enough so that it minimizes the effect on the crystal structure in the underlying active region. The cap layer is basically a conducting layer and serves to reduce the surface recombination velocity of the adjacent layer; it is probably not necessary that this layer possess the crystalline perfection of the preceding layers. Therefore, a interfacial compositional discontinuity may be tolerated between the cap layer and the top active layer. However, aluminum additions to the structure will be used, if needed, to optimize lattice matching for the cap layer. The cap layer may be grown from a tin solution for n-type layers, or from gallium for p-type layers.

CONTACTS

With the grown multi-layer wide band gap structure described above, the next task is to form ohmic contacts on the top and bottom surfaces of the wafer. No thinning prior to contact formation is required with this solar cell design because the gallium phosphide substrate is transparent to photons less energetic than the band gap of the active junction of the top cell. The structure is, in fact, quite sound mechanically and, therefore, is expected to have low breakage and high fabrication yields during subsequent processing.

The n-type contact consists of thermally evaporated Au/Ni or Au/Ge/Ni on a clean wafer surface. Surfaces are etched prior to evaporation using 1:1 $HCl-H_2O$ and are rinsed thoroughly in 18-meg ohm deionized water, dried, and placed immediately in the evaporator. Evaporation is done using tungsten wire baskets to contain the individual sources, and layer thickness is controlled by evaporation to completion (Au: 1200-1600A^o; Ni: 50-150A^o). alloying is accomplished at an optimum established to be 525°C for two minutes. Contacts are processed using standard photolithography techniques. Pulse-plating of 1-3 microns of gold or silver to the base metallization pattern will be employed to assure sharp vertical plating features and to reduce unnecessary shadowing or overlap of metallization patterns.

P-contacts will be fabricated similarly to the n-contacts except gold-zinc alloy is used instead of Au/Ge/Ni or Au/Ni during the evaporation step. Stable contacts to semiconductor laser and LED GaP and GaAsP structures have become a well-controlled manufacturing science and we do not expect this area to be a problem.

EXPERIMENTAL RESULTS

The growth of smooth, uniform layers of $GaAs_xP_{1-x}$ on GaP substrates with x of the top layers ranging from 0.4 to 0.68 and energy gaps of 2.07 eV to 1.81 eV has been successfully demonstrated. These layers were grown using a combination of step grading and depletion grading.

A GaAsP structure has been designed which will allow the exploration of a range of energy band gaps between 1.75 eV and 2.07 eV for the top solar cell. The higher energy gaps may lead to improved "real" system performance in a four terminal configuration.

The solar cell structure is being grown using liquid phase epitaxial growth techniques. Three-layer structures grading from $GaAs_{.4}P_{.6}$ (2.07 eV) to $GaAs_{.68}P_{.32}$ (1.81 eV) have been produced in our laboratories using LPE.

The solar cell development to date has been most encouraging. The overall goal is to produce GaAsP top cell having Voc 1.50 volts, Jsc 17.8 mA/cm^2, a fill factor of 0.89, and an overall efficiency of 17.6%, based on the details shown in Table II. To date we have achieved a maximum Jsc of 10.6 mA/cm^2 (corrected for reflection losses), a maximum Voc of 1.394 volts and fill factors greater than 0.75. The present plan is to optimize each parameter separately using simplified col-

lector structures to optimize Voc, and Schottky and MIS structures to optimize, measure, and improve diffusion lengths and Jsc. Ohmic contacts for these structures, which are reproducible and reliable and have shown good mechanical adhesion in tests to date, have been developed.

CONCLUSIONS

Preliminary results are encouraging for the development of a wide band gap GaAsP top solar cell for attachment to conventional silicon solar cells. Solar conversion efficiency increases of over 50% may be expected with the successful development of this technology.

References:

[1] J. C. C. Fan, B.- Y. Tsaur, B. J. Palm, "Optical Design of High Efficiency Tandem Cells", Conf. Rec. 16th IEEE Photovoltaic Specialists Conference, p. 692, (1982).

[2] A. M. Barnett, M. G. Mauk, J. C. Zolper, I. W. Hall, W. A. Tiller, J. B. McNeely and R. B. Hall, "Thin Film Silicon and GaAs Solar Cells", Conf. Rec. 17th IEEE Photovoltaic Specialists Conf., 747, Orlando (1984).

[3] G. Sassi, "Theoretical Analysis of Solar Cells based on Graded Band-Gap Structures", J. Appl. Phys., 54, (9), 5421, (1983).

[4] L. R. Dawson, "Liquid Phase Epitaxy", Progress in Solid State Chemistry, Chapter 4, 7, 117, Pergamon Press (1972).

[5] R. L. Moon, "Liquid Phase Epitaxy" Chapter 11, Crystal Growth, ed. B. Pamplin, 2nd ed., p. 421, Pergamon Press, (1980).

[6] R. L. Moon, G. A. Antypas, Y. G. Chai, "Continuous Compositional Grading by LPE in Al-Ga-V Quaternary Alloys", Proceedings of the 7th International Symposium on GaAs and Related Compounds, p. 78, ed. C. M. Wolfe, Institute of Physics, London, (1978).

[7] S. Yamazaki, K. Nakajima, S. Komiya, Y. Kishi and K. Akita, "Liquid Phase Epitaxial Growth of InP/InGaAsP/InP Double-Heterostructure Wafers Free of Misfit dislocations", Appl. Phys. Lett. 43, (1), 82 (1983).

[8] H. Nelson, "Depositing Successive Layers from the Liquid Phase", U. S. Patent 3,565,702, February 23, 1971.

[9] H. J. Hovel and J. M. Woodall, "An Isothermal Etchback-Regrowth Method for High Efficiency $Ga_{1-x}Al_xAs$-GaAs Solar Cells", Appl. Phys. Lett., 30, 492 (1977).

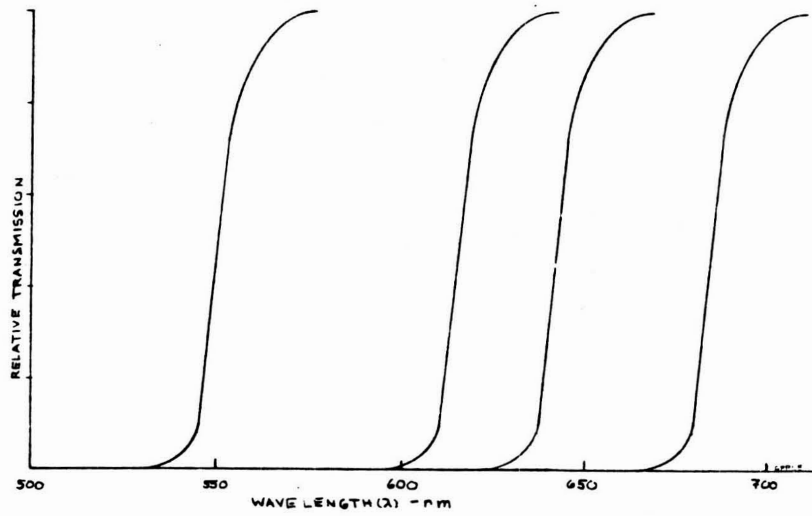

Figure 1. GaAsP on GaP Transmission Data

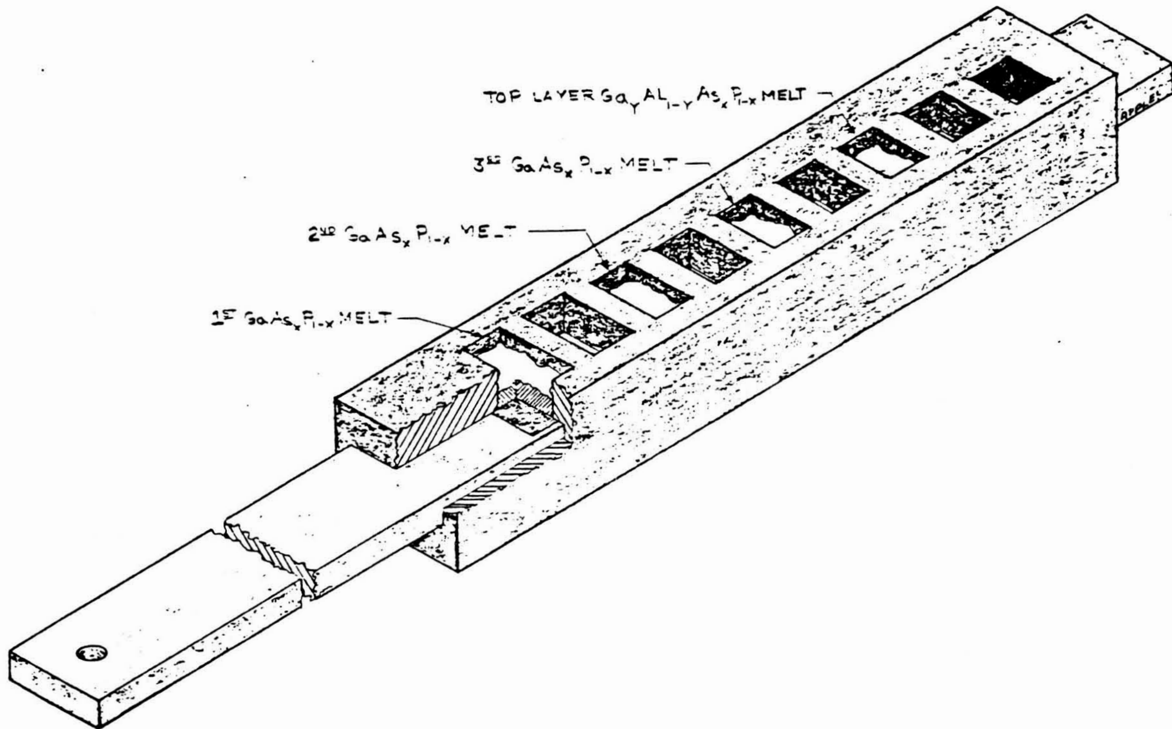

Figure 2. Slider boat growth apparatus showing the graded well width.

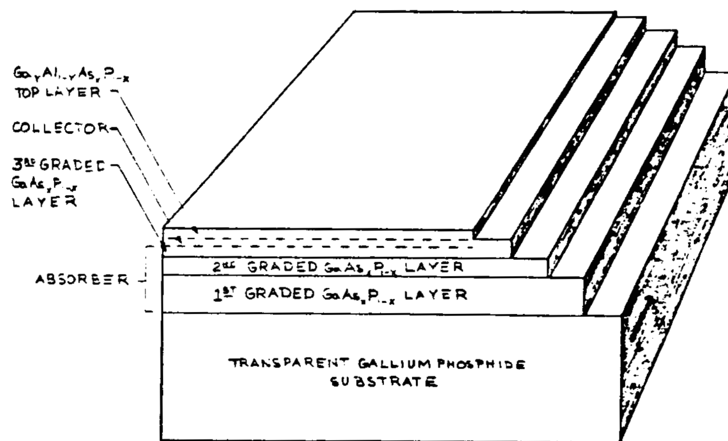

Figure 3. Multi-layer GaAsP on GaP solar cell structure (not to scale). Each successive layer is narrower than its predecessor, which allows easy access to areas of the individual growth surfaces for diagnostic purposes.

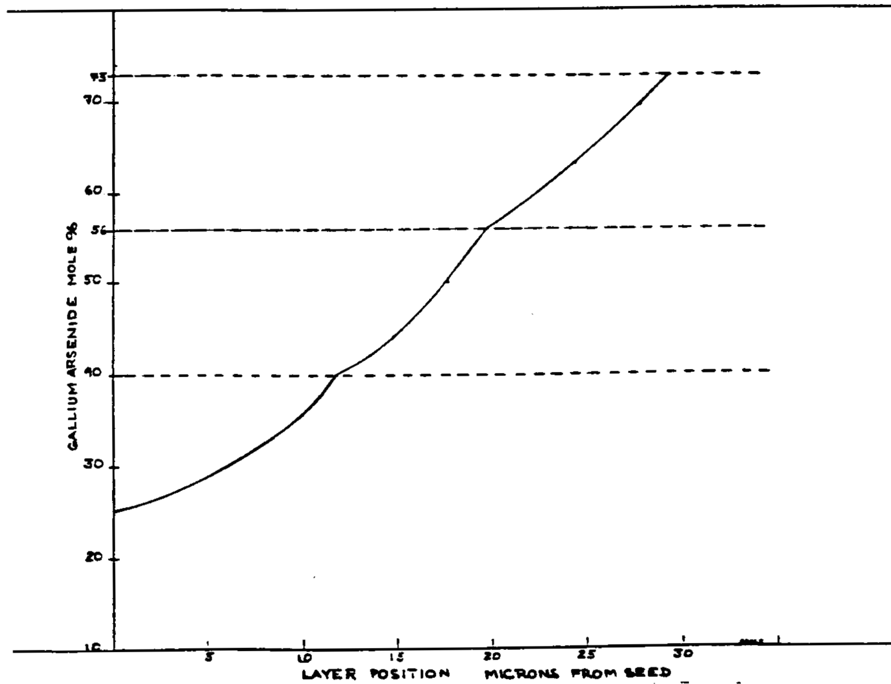

Figure 4. Compositional graded three-layer GaAsP on GaP Structure

N86-17848

VACUUM MOCVD FABRICATION OF HIGH EFFICIENCY CELLS FOR MULTIJUNCTION APPLICATIONS*

L. D. Partain, L. M. Fraas, P. S. McLeod, and J. A. Cape
Chevron Research Company
Richmond, California

Vacuum metal-organic-chemical-vapor-deposition (MOCVD) is a new fabrication process with improved safety and easier scalability due to its metal rather than glass construction and its uniform multiport gas injection system. It uses source materials more efficiently than other methods because the vacuum molecular flow conditions allow the high sticking coefficient reactants to reach the substrates as undeflected molecular beams and the hot chamber walls cause the low sticking coefficient reactants to bounce off the walls and interact with the substrates many times. This high source utilization reduces the materials costs per device and substantially decreases the amounts of toxic materials that must be handled as process effluents. The molecular beams allow precise growth control. With improved source purifications, vacuum MOCVD has provided p GaAs layers with 10-μ minority carrier diffusion lengths and GaAs and GaAsSb solar cells with 20% AM0 efficiencies at 59X and 99X sunlight concentration ratios. Mechanical stacking has been identified as the quickest, most direct and logical path to stacked multiple-junction solar cells that perform better than the best single-junction devices. The mechanical stack is configured for immediate use in solar arrays and allows interconnections that improve the system end-of-life performance in space. A GaAsP cell of 13% AM0 efficiency has been fabricated onto a transparent GaP substrate (GaAsP/GaP). Mechanically stacking this GaAsP/GaP on current technology silicon cells would give a combined 20% AM0 performance. Practical efficiency levels of fully developed systems should be 27% AM0 for GaAsP/GaP on silicon and approaching 30% AM0 for GaAsP/GaP on a direct band gap bottom cell. Incorporating these devices in light concentrator systems offers the highest efficiencies, the best tolerance of nonideal device behavior, and the most protection against damaging radiation.

INTRODUCTION

Vacuum MOCVD is a new fabrication process that has been under development at Chevron Research for the past several years (ref. 1) to produce high efficiency solar cells. A novel and beneficial feature of the vacuum configuration is that gas transport is by molecular flow, while in higher pressure, conventional MOCVD it is by laminar flow. The vacuum configuration incorporates some of the best features of molecular beam epitaxy (MBE). It produces high quality layers and solar cell junctions equivalent to the best obtained by other methods. It is well suited to the formation of solar cells on a transparent substrate which can readily be stacked mechanically onto another cell to form multiple-junction devices. Multiple junctions offer the potential for significantly improved device performance (ref. 2). Mechanical stacking circumvents many of the problems encountered in other multiple-junction configurations and it provides cell interconnections that improve the end-of-life efficiencies limited by different junction degradation rates in space.

*This work was supported in part by contracts with the Solar Energy Research Institute and with the Air Force Wright Aeronautical Laboratory.

PRECEDING PAGE BLANK NOT FILMED

When the series resistance and device temperature can be kept sufficiently low, concentrated light systems offer the best overall performance characteristics.

VACUUM MOCVD

A simplified schematic of the vacuum MOCVD system is shown in figure 1. The operating pressure of the reactor is in the 1 millitorr range where convective heat loss is negligible. In conventional higher pressure systems, such convective losses are large enough that multikilowatt, radiant, or RF induction heaters are required to maintain the 600-700°C reaction temperatures. For heating energy transmission, these systems use glass- or quartz-walled chambers. In contrast, the required temperatures in the present vacuum system are produced by a 600-watt resistance heater. The whole figure 1 system, including the heater, is enclosed by a stainless steel outer chamber (not shown) which remains at room temperature. This improves the safety in handling the toxic and pyrophoric gas sources because there are no strong temperature stresses on the outer walls and because the metal does not shatter like glass. In addition, any small gas leaks are into, rather than out of, the vacuum enclosure. Since the main structural element is steel, the system can be scaled up in size more easily than glass-based systems. The multiple gas injection ports shown in figure 1 maintain the growth uniformity during such scaling.

Figure 1 illustrates the epitaxial growth of GaAs onto a GaAs substrate. The source gases of arsine (AsH_3) and triethylgallium (TEG) are fed in from the side and bottom, respectively, of the inner graphite reactor chamber, which has hot walls. This configuration combines some of the best features of MBE and traditional CVD while avoiding some of their serious problems. The expensive and comparatively rare TEG is used efficiently. In the molecular flow vacuum, the TEG molecular beam delivers Ga directly to the substrate without deflection and with a high sticking coefficient (ref. 3) that is dependent on the AsH_3 overpressure (ref. 4). The sticking coefficient is less than one since some GaAs forms on the bottom wall of the graphite chamber. Essentially all the TEG reacts in the chamber with none detected at the exit port with a residual gas analyzer (RGA). This indicates a Ga utilization efficiency of the order of 50% or greater for large-scale systems with planar geometry where multiple TEG injection nozzles provide growth uniformity. The AsH_3 distributes uniformly throughout the reaction chamber due to its low sticking coefficient (estimated 0.01 value) and its multiple bounces off the hot chamber walls. This provides many opportunities for the AsH_3 to react on the substrate surface. An AsH_3 overpressure is required for good epitaxy (ref. 3), and the AsH_3/TEG flow ratio of 6:1 used in this system indicates an AsH_3 utilization of the order of 15%. Upstream decomposition of the AsH_3 in a thermal cracker (shown in fig. 1) gives more efficient growth with a reduced AsH_3/TEG flow ratio of 3:1 and a 30% estimated AsH_3 utilization. A strong AsH_3 signal is detected by the exit port RGA under all these conditions.

The gas utilization is much lower in the conventional, higher pressure, laminar flow MOCVD systems. Only those molecules in the boundary layer next to the substrate contribute to the epitaxial growth. Most of the gas is swept past the substrates without touching them. This gives Ga utilization of the order of a tenth or less. These systems are cold walled and require much higher AsH_3 over pressures with arsenic-to-gallium flow ratios typically in the 20-100 range (ref. 5). Such wastes increase the materials cost per device by at least a factor of two. The problems of safe effluent management are multiplied by the orders of magnitude higher volumes of toxic AsH_3 released through the exit port of higher pressure systems. In MBE machines using AsH_3 (ref. 4), most of this gas is lost since it has essentially a single chance to strike the substrate. MBE growth uniformity is

difficult to achieve with a single Ga injector nozzle (ref. 3). The multiple molecular Ga beams in the present vacuum MOCVD system provide for uniformity along with the precise growth control characteristics of MBE.

MATERIALS AND DEVICES

A continuing problem of MOCVD is that source material quality is only beginning to be improved to the level of older techniques like liquid phase epitaxy (LPE). However, recent advances in moisture removal from AsH_3 (ref. 6) and purification of the p dopant source (ref. 7) have provided layer growths of high quality. Figure 2 shows the quantum yield spectra measured on a special n^+ on p GaAs sample fabricated by vacuum MOCVD. The n^+ layer was degenerately doped so that its contribution to the quantum yield was negligible due to Auger recombination (ref. 8 and 9). The resulting curve fits show that the electron diffusion length (L_n) in the p layer is 10 μ. This is equivalent to the best values achieved by other growth techniques including LPE.

Figure 3 shows the I-V properties of two p on n solar cells grown by vacuum MOCVD with 20% AM0 efficiencies at sunlight concentration ratios of 59X and 99X. The ternary GaAsSb cell was formed with molecular beams (see fig. 1) of both TEG and triethylantimony using a GaAs substrate and a graded Sb composition transition layer. The external quantum yields of these devices are shown in figure 4. Their peak values are 90% and 95% and flat, indicative of long diffusion lengths and low surface recombination velocities. The GaAsSb band gap is 1.35 eV. Both cells had surface passivation by a several hundred-angstrom thick layer of AlGaAs or AlGaAsSb formed by switching on a triisobutylaluminum molecular beam at the end of their growths. Both cells also had two-layer antireflection coating applied. This performance is equivalent to the state-of-the-art results reported for other fabrication techniques. All the solar cells reported in this paper have 0.0386 cm^2 active areas, and all the efficiencies are active area values.

We have previously reported the I-V properties and quantum yield (ref. 10) for a vacuum MOCVD p on n GaAsP cell with 15% AM0 efficiency at a 112X concentration ratio. (The corresponding AM1.5 efficiency was 17% at 133X concentration.) This cell had a band gap of 1.6 eV and was grown on top of a GaAsSb device on a GaAs wafer. It was grown with PH_3 gas injected into the reaction chamber through a port similar to that used for AsH_3 injection. This illustrates the variable band gap fabrication capability of vacuum MOCVD for ternary III-V solar cells.

MECHANICAL STACK

The 20% AM0 performance is beginning to approach the practical limits of efficiencies that can be readily achieved with single-junction solar cells (ref. 11). However, stacking two different band gap cells one on top of the other offers the potential for substantially higher performance levels (ref. 2). In particular, stacking a GaAsP cell onto a current technology Si cell is promising. Figure 5 shows the 13% AM0 efficiency with 64X concentration achieved in a preliminary experiment with a GaAsP cell grown onto a transparent GaP substrate. The calculations show (ref. 12) that mechanically laying this device on top of a silicon cell would give a combined AM0 conversion efficiency of slightly over 20% with a 250-μ thick GaP wafer and appropriate antireflection coatings. A fully developed GaAsP/GaP top cell should alone approach an efficiency of about 20%. Mechanically stacking such a cell on a silicon device should then provide practical performance levels in the 27% AM0 range (ref. 12). Much of the ground work for GaAsP on GaP has already been laid by the development of light-emitting diodes which use the same

materials layers and p-n junction structure. Replacing the bottom silicon cell with a fully developed, direct band gap material with higher quantum yield (for example, GaAsSb--see figure 4) should provide mechanical stack performance approaching the 30% AMO level.

The mechanical stack circumvents many of the problems that are currently impeding the progress of other stacked, multijunction designs. It is a four-terminal device that eliminates the need for the shorting junction that has proved difficult to achieve in monolithic layered devices. It simplifies the problems of transition layers. With a GaAsP cell monolithically stacked onto a GaAsSb cell as described in reference 10, a several-micron thick transition layer is required between the two junctions to attain high performance in the top GaAsP; but this thick layer absorbs photons and limits the efficiency of the bottom cell (to 4% in reference 10). Addition of Al to the transition layer reduces the absorption, but the performance of the top GaAsP junction is substantially reduced because of problems related to the Al layer. These basic materials problems are all solvable given enough time and effort. However, the quickest, most direct and logical path to high performance multijunctions ready to use in arrays is the mechanical stack.

The monolithic, two-junction stack of reference 10 is a three-terminal device that circumvents shorting junction problems by using a p-n-p configuration. Before it could be used in an array, the complimentary n-p-n two-junction device would have to be developed. All the involved junctions would need to be current matched for series connections.

The four-terminal versatility of mechanical stacks allows the devices to be connected so that end-of-life system performance is improved. With different junctions exposed to the space radiation environment, each junction would be expected to degrade at a different rate. If stacked cells were designed for series connection with currents matched at the beginning of life, their currents would be mismatched at end of life with performance loss greater than the efficiency loss of each individual junction. Voltage matching provides a more robust space design since device voltages only vary logarithmically with current changes. Figure 6 shows a 4 by 2 module wiring diagram for voltage matching of top and bottom cells whose output voltages differ by a factor of two. This can be achieved in GaAsP and silicon by selecting the correct GaAsP band gap. For the eight-element configuration, four of the bottom cells and two of the top cells are connected in series to provide the voltage match. For the other operating voltage ratios, other series-parallel connections schemes (e.g., 4 by 3, 7 by 5, etc.) can be used to achieve voltage matching.

CONCENTRATORS

Since the short circuit current of solar cells increases linearly with light intensity, their efficiency would remain constant under concentrated light if their open circuit voltage and fill factor remained constant. However, the voltage increases logarithmically with this current rise and the fill factor also increases (ref. 13). The net result is an increase in device performance with concentration as long as series resistance and device temperature can be kept sufficiently low. For 100X concentration and 5% grid contact coverage, grid contact resistances below about 10^{-4} ohm-cm^2 are required to prevent loss of fill factor. Values in this range were achieved in the figure 3 p on n devices using a silver alloy p layer contact, 500-μ grid line spacing, and 15-μ wide grids. The silver, containing 4.5% manganese by weight (Cominco), was electron beam deposited 1500 angstoms thick onto the p layer. This was annealed in forming gas for one minute at 450°C and then

electroplated with 2-3 μ of silver. Ohmic contact was assured as long as the p layer doping level was above 1 (10^{18}) cm^{-3}. The diffusion length was not seriously decreased by Auger recombination (ref. 8 and 9), as long as the p doping was less than 2 (10^{18}) cm^{-3}. Curtice (ref. 11) has calculated the trade-offs among device temperature, efficiency, and concentration ratio for GaAs cells used in space. He found the 50-100X range as near optimal. This range spans the figure 3 conditions where the 20% devices were measured.

An additional advantage of concentrators is that shunt leakage paths can become saturated at the higher current levels encountered. This means that devices can exhibit near ideal performance with high efficiency at concentration even though their characteristics would be dominated by efficiency lowering leakage at unconcentrated light levels. Thus, the concentrator applications are more tolerant of nonideal device behavior. A final advantage of concentrators is the extra protection they afford the devices. Most concentrator designs for space have the devices completely surrounded by metal structures (ref. 14). This provides shielding from damaging radiation like cosmic rays or from high intensity optical radiation not directly aligned with the optical axis of the concentrator.

CONCLUSIONS

Vacuum MOCVD is a novel fabrication method being developed at Chevron to produce high quality materials for high efficiency solar cells. It combines the precise control of MBE with the high throughput of CVD. It uses the source materials more efficiently than alternate methods and reduces the materials costs per device by at least a factor of two. It decreases the volume of toxic effluents that must be handled by an order of magnitude and reduces the dangers of toxic gas escape by replacing fragile glass outer walls of higher pressure MOCVD with steel. It is more easily scalable to higher volume production because the steel structural parts can be increased in size in a more straightforward manner than glass, while the multiple injection ports maintain uniformity. Recent improvement in source quality have given materials with properties equivalent to the best produced by other fabrication techniques including LPE. These properties include p material with a 10-μ minority carrier diffusion length. Solar cell devices have been produced with 20% AM0 efficiencies at concentration ratios of 59X and 99X using GaAs and GaAsSb p on n junctions.

A mechanical stack has been identified as the most rapid, direct, and logical path to stacked, multijunction devices that can be immediately incorporated into actual arrays and that have performance levels exceeding the best single-junction performance. A preliminary experiment has given a GaAsP device of 13% AM0 efficiency on a transparent GaP substrate. Mechanically stacking this device on present technology silicon cells would provide 20% AM0 efficiency. Full development of this configuration should give practical performance levels around 27% AM0 with silicon and approaching 30% AM0 with a direct band gap device for the bottom junction. Module wiring schemes to produce voltage matching are easily achieved with mechanical stacks and these schemes give multijunction systems with superior end-of-life performance in space. Concentrator systems give the highest device performance, are the most tolerant of nonideal device behavior, and provide extra protection against radiation damage as long as series resistance is sufficiently low. Silver-manganese metalizations have given low enough contact resistance for 20% efficient (AM0), concentrated light performance at up to 100X.

REFERENCES

1. Fraas, L. M.; McLeod, P. S.; Cape, J. A.; and Partain, L. D.: Expitaxial Films Grown by Vacuum MOCVD. J. Crystal Growth, vol. 68, 1984, pp. 490-496.

2. Fraas, L. M.; Cape, J. A.; Partain, L. D.; and McLeod, P. S.: High Efficiency Concentrator Solar Cells. Solar Cells, vol. 12, 1984, pp. 67-80.

3. Veuhoff, E.; Pletschen, W.; Balki, P.; and Luth, H.: Metalorganic CVD of GaAs in a Molecular Beam System. J. Crystal Growth, vol. 55, 1981, pp. 30-34.

4. Putz, N.; Veuhoff, E.; Heinecke, H.; Heyen, M.; Luth, H.; and Balk, P.: GaAs Growth in Metal-Organic MBE. J. Vac. Sci. Technol. B, vol. 3, 1985, pp. 671-673.

5. Dapkus, P. D.; Manasevit, H. M.; Hess, K. L.; Low, T. S.; and Stillman, G. E.: High Purity GaAs Prepared From Trimethylgallium and Arsine. J. Crystal Growth, vol. 55, 1981, pp. 10-23.

6. Fraas, L. M.; Cape, J. A.; McLeod, P. S.; and Partain, L. D.: Measurement and Reduction of Moisture Content in AsH_3 and PH_3 Source Gases Used in Epitaxy. J. Vacuum Science and Technology, May 1985.

7. Lewis, C. R.; Dietze, W. T.; and Ludowise, M. J.: The Growth of Magnesium-Doped GaAs by the OM-VPE Process. J. Electronic Materials, vol. 12, 1983, pp. 507-524.

8. Casey, H. C., Jr.; Miller, B. I.; and Pinkas, E.: Variation of Minority-Carrier Diffusion Length With Carrier Concentration in GaAs Liquid-Phase Epitaxial Layers. J. Appl. Phys., vol. 44, 1973, pp. 1281-1287.

9. Pankove, J. I.: Optical Processes in Semiconductors (Prentice-Hall, Englewood Cliffs, N.J., 1971), pp. 161-164.

10. Fraas, L. M.; McLeod, P. S.; Cape, J. A.; and Partain, L. D.: Monolithic Two-Color, Three-Dimensional GaAsP/GaAsSb Solar Cells. 17th IEEE Photovoltaic Specialists Conf., Kissimmee, FL, May 1984, pp. 734-738.

11. Curtice, H. B.: Determination of Optimum Sunlight Concentration Level in Space for Gallium Arsenide Solar Cells. 15th IEEE Photovoltaic Specialists Conf., Kissimee, FL, May 1981, pp. 52-55.

12. Fraas, L. M.; Cape, J. A.; McLeod, P. S.; and Partain, L. D.: High-Efficiency $GaAs_{0.7}P_{0.3}$ Solar Cell on a Transparent GaP Wafer. J. Appl. Phys., vol. 57, 1985, pp. 2302-2304.

13. Hovel, H. J.: Solar Cells, Semiconductors, and Semimetals, vol. 11, Willardson, R. K.; and Beer, A. C., Eds. (Academic Press, N.Y., 1975), pp. 59-61.

14. Mullin, J. P.; Loria, J. C.; and Brandhorst, H. W.: The NASA Photovoltaic Technology Program. 17th IEEE Photovoltaic Specialists Conf., Kissimmee, FL, May 1984, pp. 12-16.

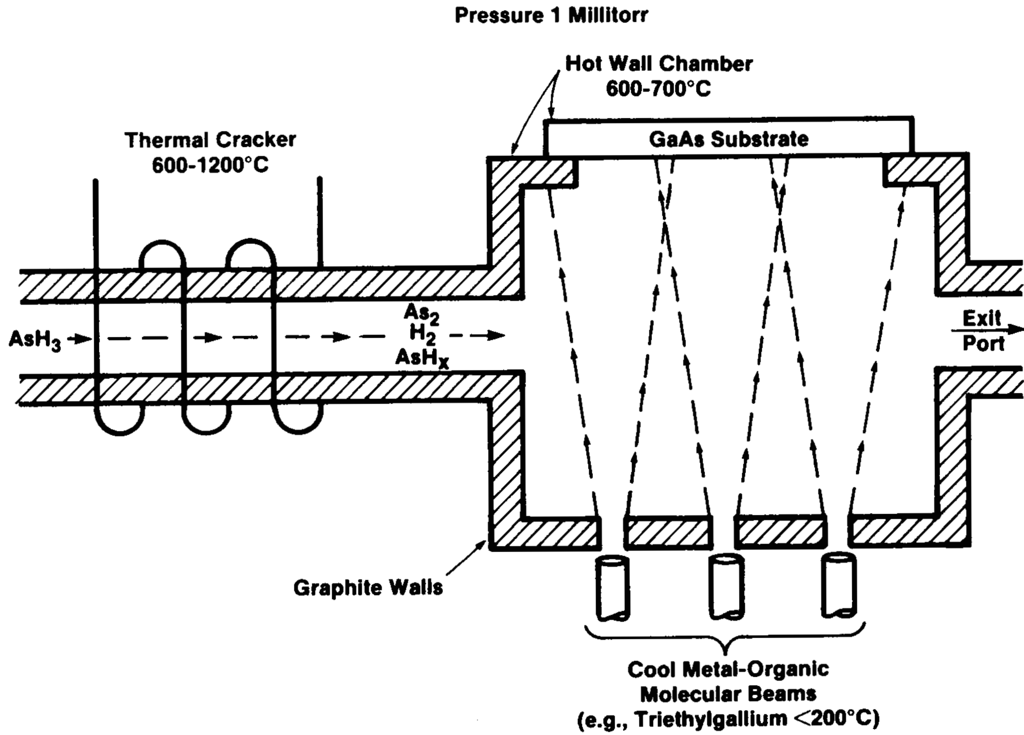

Figure 1. Schematic diagram of the vacuum MOCVD system showing the growth of GaAs epitaxial layers on a GaAs substrate.

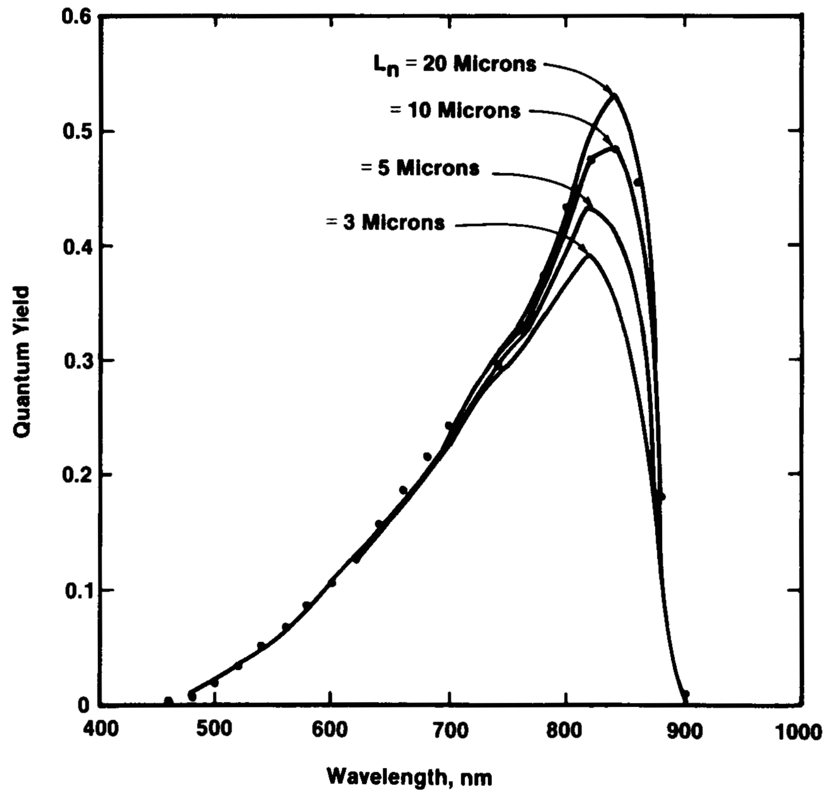

Figure 2. Theoretical curve fit of measured quantum yield data points indicating a 10-μ diffusion length in the p layer of a n^+-p junction.

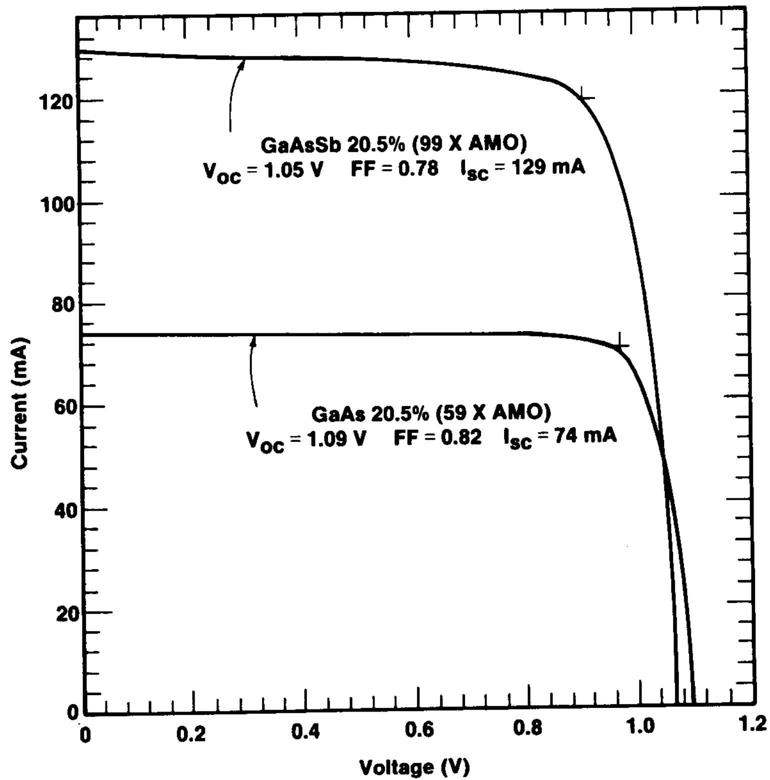

Figure 3. The flash simulator measurements of the I-V properties of GaAs and GaAsSb solar cells with 20% AMO efficiencies.

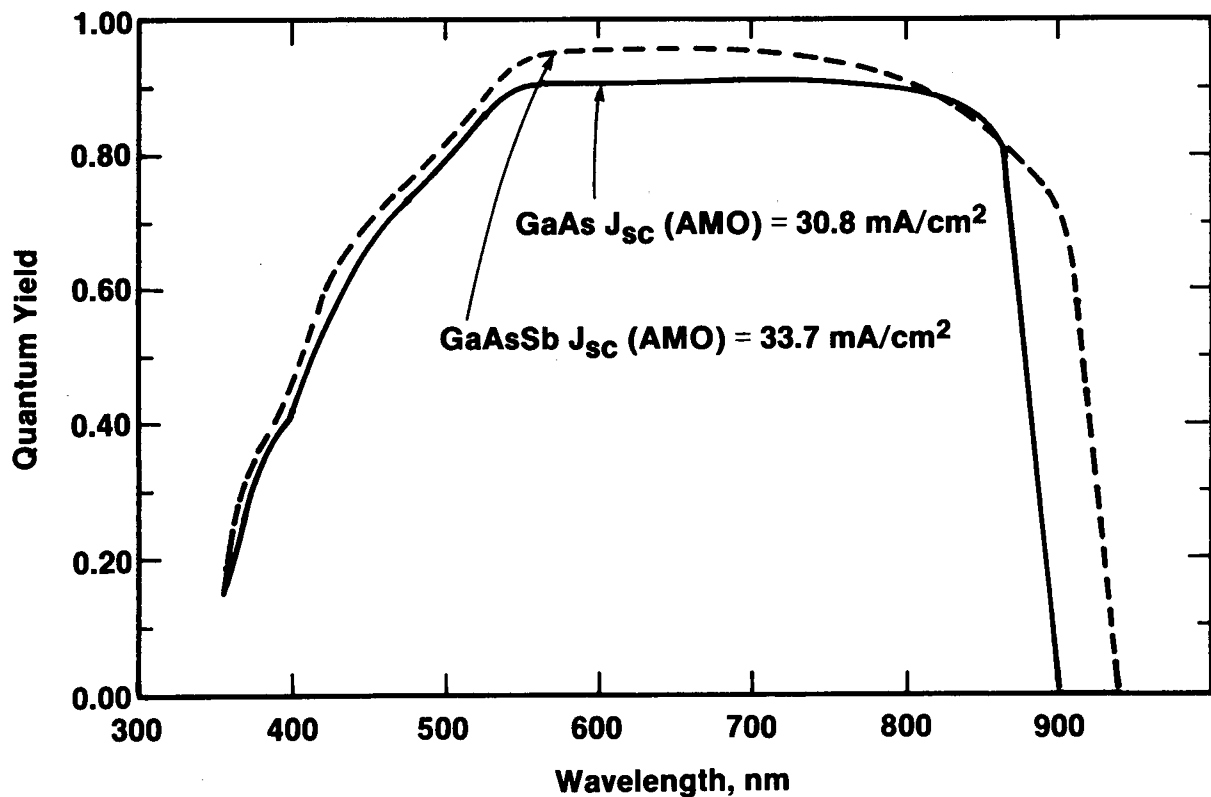

Figure 4. The external quantum yields measured on the two cells whose I-V properties are shown in figure 3.

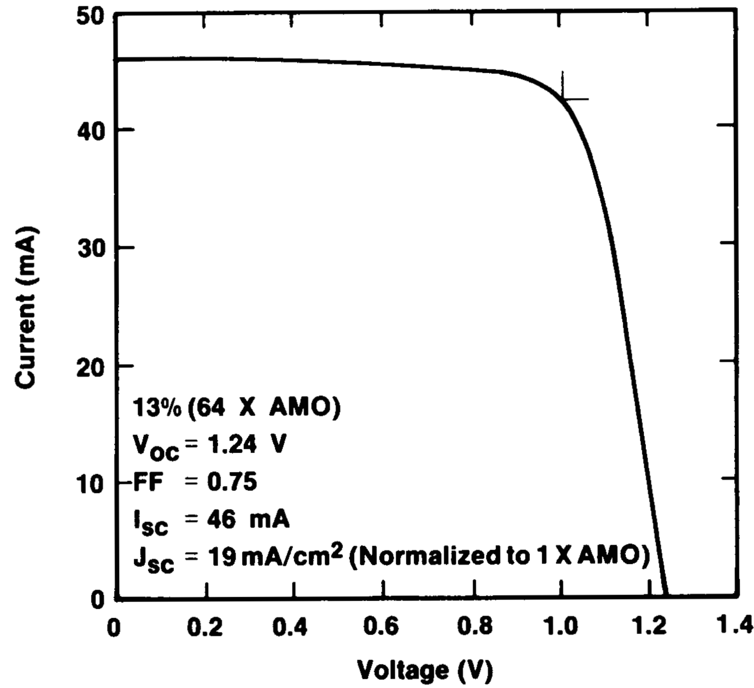

Figure 5. The flash simulator measurement of the I-V properties of the GaAsP solar cell formed on a transparent GaP wafer.

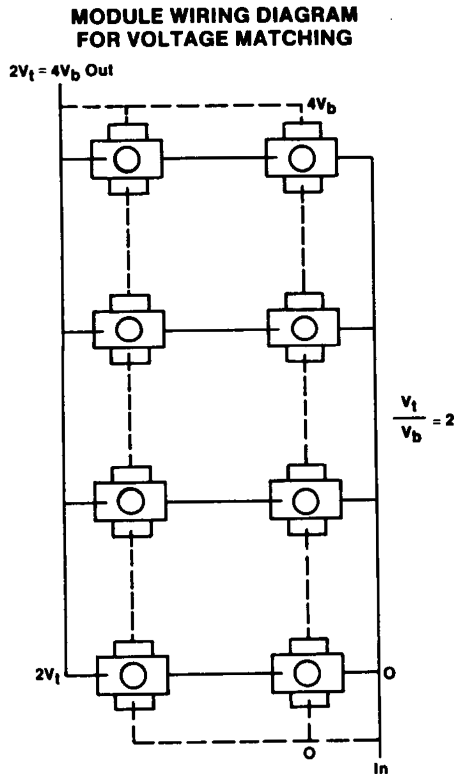

Figure 6. The 4 by 2 module wiring diagram for voltage matching stacked solar cells with a 2:1 voltage output ratio and four terminals available for interconnections.

N86-17849

CONTROL OF SUPERLATTICE MORPHOLOGY IN $GaAs_{1-x}P_x$ CASCADE CELLS

A. E. Blakeslee and A. Kibbler
Solar Energy Research Institute
Golden, Colorado

INTRODUCTION

$GaAs_{1-x}P_x$ superlattices are being incorporated into cascade solar cell structures in order to reduce the dislocation density in the top cells and thus reduce recombination loss and increase output voltage.[1] For a superlattice to effectively block the propagation of dislocations, its average composition must be equal to that of the layer beneath it[2] (from efficiency considerations for a cascade cell, the average composition should be about $GaAs_{.7}P_{.3}$).

When superlattices of this approximate composition were grown on GaAs by MOCVD, severe distortion of the crystal layers was observed. The essential features of this distortion are nonplanar morphology and accelerated etching in regions containing excess phosphorus and clusters of dislocations. Similar observations have been made with superlattices grown with two other MOCVD systems[3], indicating that the problem is of fundamental technological significance, not just an artifact of one particular growth system. This paper describes the nature of the distortion effect and presents several strategies for preventing its occurrence.

EXPERIMENTAL

The multilayer specimens were grown by standard MOCVD techniques, using $Ga(CH_3)_3$, AsH_3 and PH_3 as the primary sources. The substrates were GaAs wafers misoriented 2° from the (100) plane. Computer control was used to set the gas flows through mass flow controllers and rapidly switch them for growth of a superlattice. The composition of the superlatttice was governed by the duration of and PH_3/AsH_3 ratio in the alternating gas pulses. The multilayers were examined by Nomarski optical, scanning electron microscope, electron microprobe, and transmission microscope techniques.

RESULTS

The morphology of the cleaved and etched specimens exhibited a wide range of appearance, varying from flat, parallel, nearly perfect superlattice bands to samples containing extremely distorted layers. Figure 1 shows examples of a flat and a distorted superlattice. The distortion is seen to consist of two components. One is a warping of the sublayers, yielding traces of progressively nonplanar vapor-solid interfaces. The other is a roughly sinusoidal deviation in and out of the cleavage plane, caused by nonuniform action of the etchant over the originally planar cleaved surface. The sites of maximum etching are also the centers of dense dislocation clusters, as revealed by transmission electron microscopy (figure 2), which also provided the information that these regions contain an excess of phosphorus.

PRECEDING PAGE BLANK NOT FILMED

If no other layers are grown above the superlattice, its top surface can be observed microscopically, and if distortion is present a cellular texture is seen on this surface. The average period of the cells corresponds to the spacing of the etch streaks traversing the superlattice.

Numerous variations in the growth procedure were investigated in order to learn how to eliminate the distortions. The largest effect was achieved by minimizing the interlayer misfit, Δf, i.e. the interlayer compositional difference, Δx, while keeping the average value of x constant. For example, the $GaAs_{.75}P_{.25}/GaAs_{.65}P_{.35}$ ($\Delta x = .10$) superlattice shown in figure 1a is planar, whereas the $GaAs_{.8}P_{.2}/GaAs_{.6}P_{.4}$ ($\Delta x = .20$) superlattice of figure 1b shows considerable distortion.

Another key factor determining the amount of distortion was the rate of growth of the superlattice. It is usually true that slow growth favors the development of better crystallinity, but in the present situation that is not the case. In an experiment where the run conditions were such as to cause a wide variation in growth rate across a 2-cm wafer, it was noticed that the superlattice quality was very much better in the faster-growing central part of the wafer. In subsequent experiments where the growth rate was uniform, increasing the growth rate by factors of two or more produced distortion-free superlattices.

It has also been found that lowering the growth temperature reduces the tendency toward layer distortion, and increasing the total pressure of Group V hydrides in the source gas increases this tendency. Although not as dramatic as the affects of the factors described above, a significant difference in distortion could be seen between layers grown at 715 °C and at 800 °C and between layers where the total hydride pressure (ratio kept constant) differed by a factor of three.

An important requirement in the prescription of Matthews and Blakeslee[2] for a superlattice to block dislocation propagation is that a compositionally graded layer be grown between the substrate and the superlattice. It has been found that such a layer is also beneficial in reducing the tendency toward distortion. The shallower the concentration gradient, the less severe the distortion. However, this is perhaps the least effective remedy of all those discovered. Flat undistorted layers can probably be grown without any graded layer if the other beneficial factors are sufficiently optimized, although they might not act as dislocation filters.

POSSIBLE MECHANISMS

The distortion of $GaAs_{1-x}P_x$ superlattices has been extensively characterized, and several crystal growth procedures have been developed for reducing or eliminating it, but the basic cause of the inhomogeneity leading to the distortion has not been established. Several possible mechanisms for the distortion have been considered, but so far no single one is in keeping with all the experimental evidence. The main points of several of these hypotheses are addressed in the following.

Diffusion-Induced Disorder

Interdiffusion of $Al_xGa_{1-x}As$ and $GaAs_{1-x}P_x$ superlattice layers has been thoroughly investigated in recent years.[4] In this effect, which is promoted

by high anneal temperatures and high concentrations of Zn or other dopants, the interlayer barriers wash out and the material becomes a uniform ternary alloy. In the present case the barriers are not eliminated; rather the whole superlattice is disturbed or destroyed at isolated locations, and the distortion is independent of whether the layers are Zn-doped or undoped. Therefore a mechanism of diffusional disorder does not appear to be operative here.

Elastic Stress

The large improvement in morphology brought about by reducing the interlayer misfit (or its attendant compositional difference) must somehow be taken into account in any tenable explanation of the phenomenon. Yet it is difficult to envision how unrelieved elastic stress *per se* could produce the observed phenomena. It seems more likely that the misfit stress acts in some as yet unknown manner to magnify the effects due to the operation of some other mechanism.

Constitutional Supercooling

The cellular texture and streaked etch patterns are strongly reminiscent of nonuniform segregation effects associated with constitutional supercooling. By pre-pyrolyzing the PH_3, it was possibly to strongly decrease the phosphorus concentration gradient in the growth system, which should decrease the likelihood of constitutional supercooling. However, this experiment did not improve the morphology at all, and anyhow the fact that increasing the growth rate decreases the distortion is inconsistent with the hypothesis of constitutional supercooling.

Impurity Segregation

Bauser and Rozgonyi[5] have studied heterogeneous impurity incorporation in Czochralski-grown Si and Ge crystals and liquid phase epitaxial GaAs. They observed etching striae in crystals which are similar to the etch figures of the present work. They have developed a generally applicable model of terrace growth which can explain the occurrence and properties of their striations. Their model is being studied because of the possibility that it can be extended to explain the distortion of $GaAs_{1-x}P_x$ superlattices and the etch striations which occur in them. Such a model would predict the observed dependence on growth rate, since rapid growth would cause fewer impurities to accumulate at the growth steps.

Other

Several papers have been published recently attributing observations of inhomogeneous deposition of ternary III-V semiconductor layers to the phenomenon of spinodal decomposition.[6], and nonuniform growth of Si/Ge superlattices has been associated with three-dimensional nucleation.[7]. Both of these mechanisms are currently under investigation as possible causes of the morphological instabilities observed in the present work.

REFERENCES

1. M.W. Wanlass and A.E. Blakeslee, Proc. 16th Photovoltaic Specialists Conf., San Diego, CA, Sept. 1982, (IEEE, New York), p. 584.
2. J.W. Matthews and A.E. Blakeslee, J. Crystal Growth 32 265 (1976).
3. A second MOCVD system operated at SERI and a system used by R.M. Biefeld at Sandia Laboratories.
4. W.D. Laidig, N. Holonyak, Jr., J.J. Coleman and P.D. Dapkus, J. Electron. Mater., 11 1 (1982).
5. E. Bauser and G.A. Rozgonyi, Appl. Phys. Lett., 37 1001 (1981).
6. H. Launois, M. Quillec, F. Glas and M.J. Tracy, GaAs and Related Compounds (Albuquerque) 1982, (Inst. of Phys., London, 1983) p.537.
7. R. Hull, A.T. Fiory, J.C. Bean, J.M. Gibson, L. Scott, J.L. Benton and S. Nakahara, Proc. 13th Int. Conf. on Defects in Semiconductors, Coronado, CA, August 12-17, (AIME, New York) p.505.

ORIGINAL PAGE IS
OF POOR QUALITY

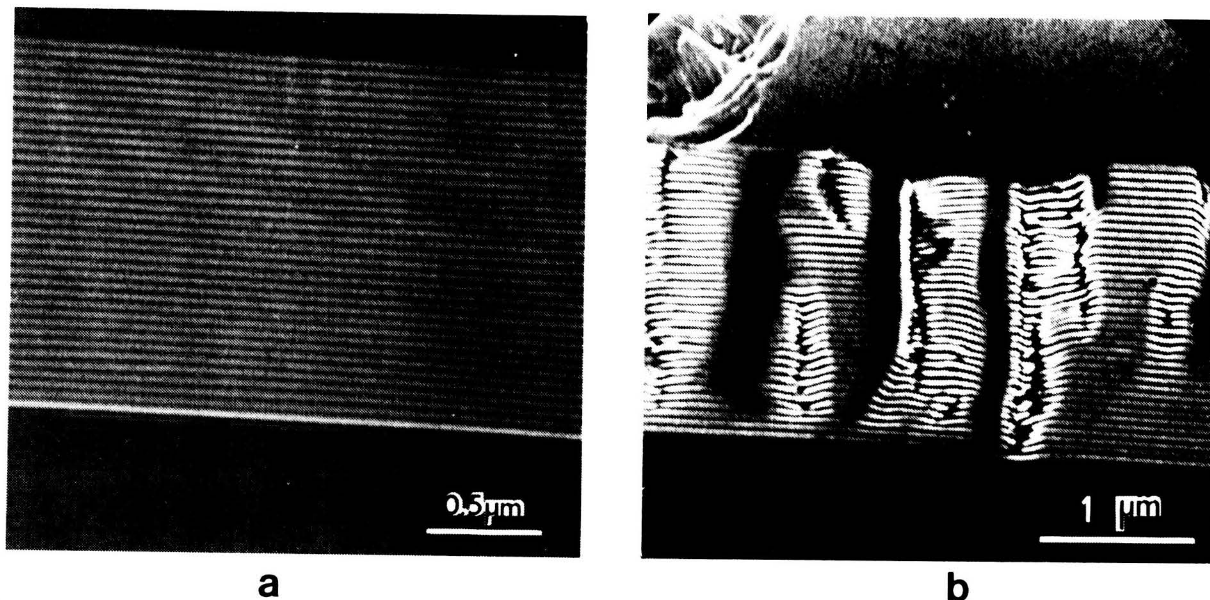

Figure 1. SEM photographs of cleaved and etched superlattice structures illustrating the effect of Δf (misfit) on superlattice morphology: (a) $GaAs_{.75}P_{.25}/GaAs_{.65}P_{.35}$; (b) $GaAs_{.80}P_{.20}/GaAs_{.60}P_{.40}$.

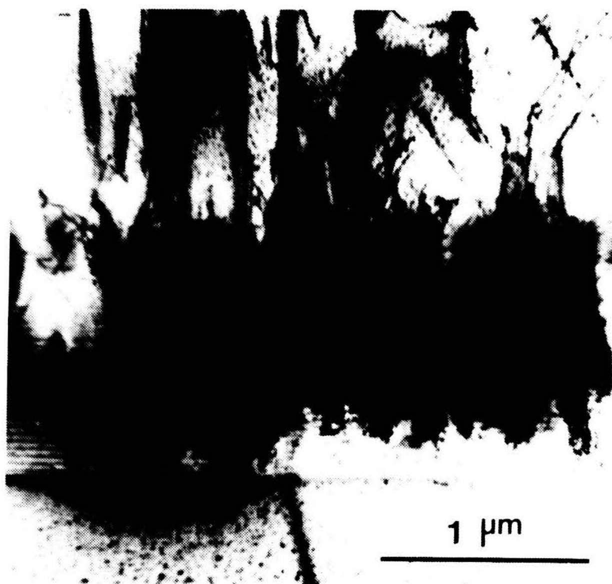

Figure 2. Cross-sectional TEM view of distorted superlattice. The black patches are phosphorus-rich regions and the lines emanating from them are dislocations.

N86-17850

SUPERLATTICES AND MULTILAYER STRUCTURES FOR HIGH EFFICIENCY SOLAR CELLS*

M. Wagner and J. P. Leburton
Department of Electrical Engineering and
Coordinated Science Laboratory
Urbana, Illinois

Possible applications of superlattices to photovoltaic structures are discussed. A new concept based on doping superstructures (NIPI) can be exploited to significantly reduce recombination losses in III-V compound solar cells. A novel multijunction structure with lateral current transport is proposed. A computer simulation has been performed which shows that by optimizing the multilayer structure, short circuit current is substantially increased with minimum drop in open circuit voltage. An additional advantage of the structure is enhanced radiation tolerance. It is anticipated that this multilayer structure can be incorporated in multibandgap cells to achieve high efficiencies.

INTRODUCTION

Advances in epitaxial growth technologies, such as MBE and MOCVD, have made possible a large variety of new artificial materials ranging from compositional superlattices, e.g. lattice matched III-V compounds like AlGaAs/GaAs (ref. 1), to NIPI (N-doped Intrinsic P-doped Intrinsic) crystals where band structure periodicity is induced by different doping of alternate layers (ref. 2). An important advantage of these recent techniques is the ability to grow very thin layers with precise thickness and doping.

Compositional superlattices have been proposed as an alternative to homogeneous alloys for high efficiency solar cells because of lower defect densities (ref. 3). A potential difficulty though is the presence of quantized states caused by carrier confinement in the small gap layers (fig. 1.a). These states promote the capture of energetic minority carriers, enhancing recombination (ref. 4). The suitability of compositional superlattices for photovoltaic cells is therefore not apparent.

The NIPI structures, however, have a novel property of obvious interest (fig. 1.b). An indirect real space gap exists between electron states in the conduction band and hole states in the valence band (ref. 5). Photogenerated electrons and holes are spatially separated within picoseconds, allowing them almost no chance to recombine. In more familiar terms, semiconductor layer thicknesses much shorter than electron and hole minority carrier diffusion lengths yield a very high collection probability. Bulk recombination losses could seemingly be almost eliminated.

* Work supported by the National Aeronautics and Space Administration.

PRECEDING PAGE BLANK NOT FILMED

N86-17850

Device Structure

A schematic representation of a NIPI photovoltaic cell is shown in figure 2. The structure is essentially a succession of back to back pn junctions. Heavily doped contact regions, which selectively connect to either p or n layers, allow lateral transport of collected carriers. Since the junctions are connected in parallel, the open circuit voltage is determined by the layers of smallest bandgap. For this reason, only single gap NIPI cells are considered. We focus on the AlGaAs alloy system because it is currently the most promising material for high efficiency photovoltaic conversion.

Modelling

In order to evaluate the performance potential of such structures, it was decided to begin with layers sufficiently thick that the depletion region approximation would be valid. Although very thin layers reduce bulk recombination losses by allowing rapid carrier collection, a large number of layers increases the dark current. Series resistance could also become significant if the layers are so thin that adjacent space-charge regions begin to overlap.

A simulation program was developed that produces cell designs by optimizing layer thicknesses for a given set of material parameters and operating conditions. Any number of layers (greater than one) may be specified by the user. Important features of the model will be briefly described.

The p^+ and n^+ contact regions shown in figure 2 are assumed to cover a negligible fraction of the cell surface. Effects of these regions on the minority carrier distribution may then be disregarded and a one-dimensional analysis performed. To further simplify the calculation, all n-layers are assigned the same doping concentration, as are all p-layers. Future extensions of the modelling program will include individual optimization of doping for each layer.

The contributions of every layer to short circuit current, reverse saturation current, and depletion region recombination are calculated and summed. The equivalent circuit therefore consists of multiple current sources shunted by multiple diodes. We may write the resulting I-V characteristic as

$$J(V) = \sum_{m=1}^{N} J_{sc_m} - \left(\exp\frac{qV}{kT} - 1\right) \sum_{m=1}^{N} J_{o_m} - (N-1)\, J_{gr} \frac{\sinh \frac{qV}{2kT}}{\frac{q}{kT}(V_b - V)} \quad (1)$$

where N is the number of layers. Depletion region recombination terms are identical for all junctions because of the stipulation that N_A and N_D are fixed. Expressions for the contributions to J_{sc} and J_o of the top and bottom layers are well known and have been presented elsewhere (ref. 6). The middle layer contributions are easily derived from the minority carrier continuity and current density equations with the boundary condition of zero excess carrier density at the depletion region edges:

$$J_{o_m} = \frac{2qD_n n_i^2}{L_n N_A} \left\{ \frac{\cosh \frac{t'_m}{L_n} - 1}{\sinh \frac{t'_m}{L_n}} \right\} \tag{2}$$

$$J_{sc_m} = \frac{qF_m \alpha L_n}{\alpha^2 L_n^2 - 1} \left\{ \alpha L_n (1 - e^{-\alpha t'_m}) - (1 + e^{-\alpha t'_m}) \left(\frac{\cosh \frac{t'_m}{L_n} - 1}{\sinh \frac{t'_m}{L_n}} \right) \right\} \tag{3}$$

where t'_m is the quasi-neutral region thickness of the mth layer and F_m is the incident photon flux. Corresponding expressions for an n-doped layer are obtained simply by changing each n-subscript to a p-subscript and substituting N_D for N_A. The absorption coefficient is modelled as in reference 7.

Operation under one sun AMO conditions is assumed so J_{sc} is small enough that resistive effects may be neglected. Simulation of a NIPI cell under high concentration is substantially more complex because resistive losses cause interaction among adjacent layers. The simple parallel interconnection model no longer suffices.

A p-doped top layer was chosen to take advantage of the longer electron diffusion length. Reflection and grid coverage are assumed to cause a combined loss of 5%. The model also includes a 500 Å $Al_{0.9}Ga_{0.1}As$ window layer.

Discussion

The proposed structure is seen to enhance short circuit current at the cost of a drop in open circuit voltage (fig. 3). The fill factor also drops, but its fractional decrease is smaller than that of Voc for $x > 0.2$. As the number of layers is increased, bulk recombination losses become negligible and Jsc approaches a limiting value determined primarily by reflection, grid coverage, and window losses. The open circuit voltage continues to decrease, however, due to the dark current contributions of additional layers.

The trade-off between J_{sc} and V_{oc} produces a peak in efficiency at three layers (fig. 4). Note that the largest increase in efficiency over a two-layer cell occurs for $x = 0.4$. This is because the shorter minority carrier diffusion lengths associated with higher mole fractions of Al allow a greater margin for improved collection. The dashed curves in figure 4 indicate the performance that could be attained if the dark current contributions of the additional layers are suppressed.

The structure also exhibits higher radiation tolerance than a conventional cell. Our simulation results predict that a two-layer GaAs cell drops to 75% of its beginning-of-life efficiency after its minority carrier diffusion lengths are degraded by a factor of 3.4. However, a six-layer GaAs cell must undergo a factor of 6.5 decrease in diffusion lengths to suffer the same efficiency loss. For two-layer and six-layer $Al_{0.4}Ga_{0.6}As$ cells the degradation factors are 2.6 and 6.1 respectively. Figure 5 shows the improved performance that results from just a few additional layers when a cell has received radiation damage. Diffusion lengths were decreased by a factor of three and optimum cell designs determined for each case. The structure appears most advantageous for high mole fractions of AlAs.

CONCLUSIONS

Single bandgap multijunction structures have been studied as a means to boost the efficiency of photovoltaic cells. A computer simulation has demonstrated the potential for significant enhancement of short circuit current, especially for high gap materials with short diffusion lengths. Three or four layers appears to be optimal for highest beginning-of-life efficiency because of the dark current trade-off. An important advantage of the structure is excellent radiation tolerance. These preliminary results are encouraging, and may lead to development of more sophisticated devices where NIPI-like structures are incorporated in multibandgap solar cells.

REFERENCES

1. Dingle, R. B.: Confined Carrier Quantum States in Ultrathin Semiconductor Heterostructures. Festkorper Probleme (Advances in Solid State Physics). Edited by J. J. Queisser, Vieweg, Braunschweig 15, 21, 1975.

2. Döhler, G. H.: Doping Superlattices. J. Vac. Sci. Technol., vol. 16, 1979, 851.

3. Chaffin, R. J.; Osbourn, G. C.; Dawson, L. R.; and Biefeld, R. M.: Strained Superlattice, Quantum Well, Multijunction Photovoltaic Cell. Proc. 17th IEEE Photovoltaic Spec. Conf., Orlando, FL, 1984, Proc. p. 743.

4. Hess, K. and Holonyak, N.: Hot-electron and Phonon Effects in Layered Semiconductor Structures and Heterostructures. Comments, Solid State Phys., vol. 10, 1981, p. 67.

5. Döhler, G. H.: NIPI Doping Superlattices - Metastable Semiconductors with Tunable Properties. J. Vac. Sci. Technol. B, vol 1 (2) Apr.-June 1983, p. 278.

6. Hovel, H. J.: Solar Cells. Semiconductors and Semimetals, vol. 11, 1975.

7. Hutchby, J. A. and Fudurich, R. L.: Theoretical Analysis of $Al_xGa_{1-x}As$-GaAs Graded Band-gap Solar Cell. J. Appl. Phys., vol. 47, 1976, p. 3140

ORIGINAL PAGE IS
OF POOR QUALITY

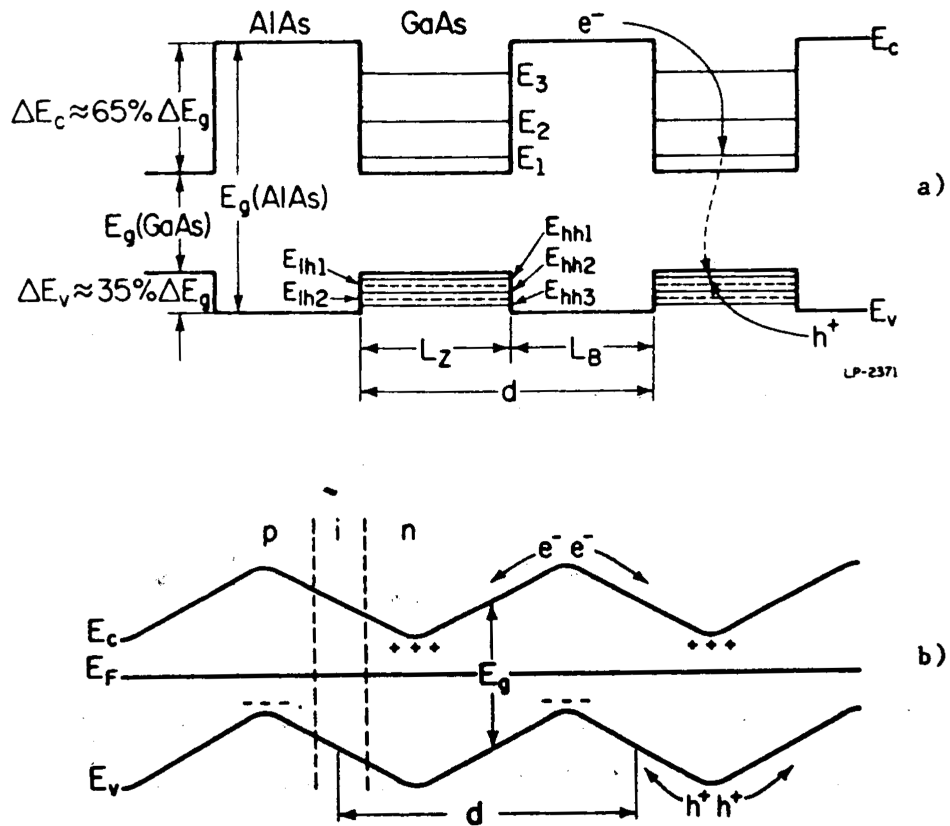

Figure 1. - Band structures of a) compositional superlattice with recombination process shown in the right-hand well and b) NIPI crystal.

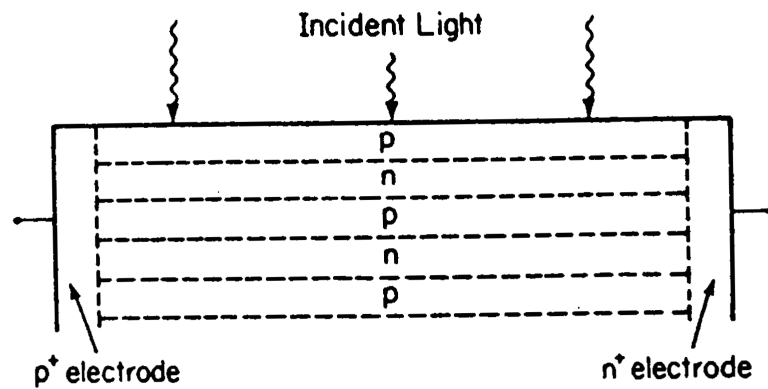

Figure 2. - Schematic cross section of proposed NIPI solar cell.

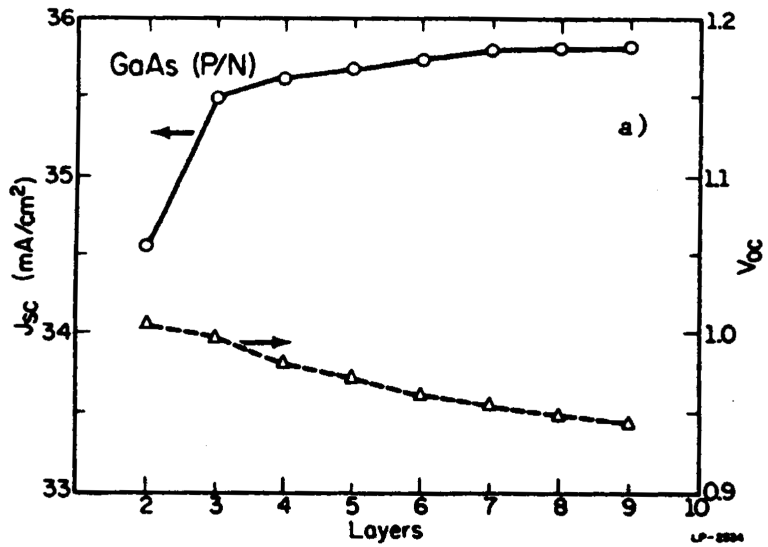

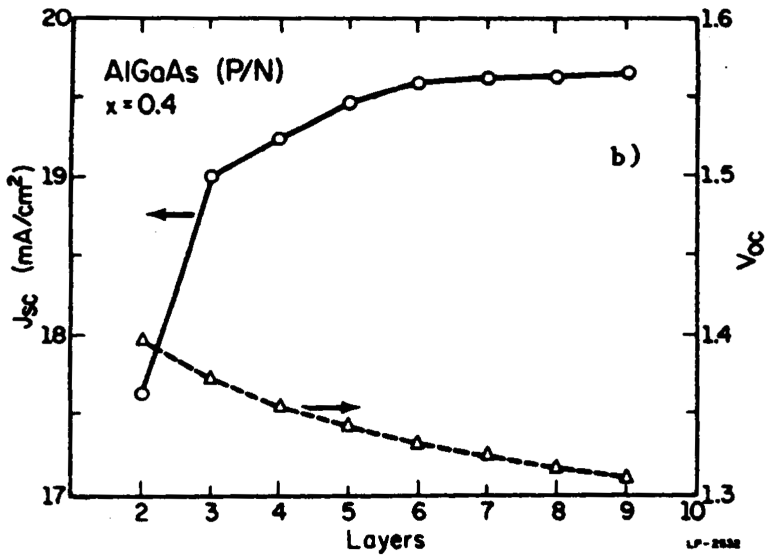

Figure 3. - Trade-off between open circuit voltage and short circuit current for a) GaAs and b) $Al_{0.4}Ga_{0.6}As$ cells.

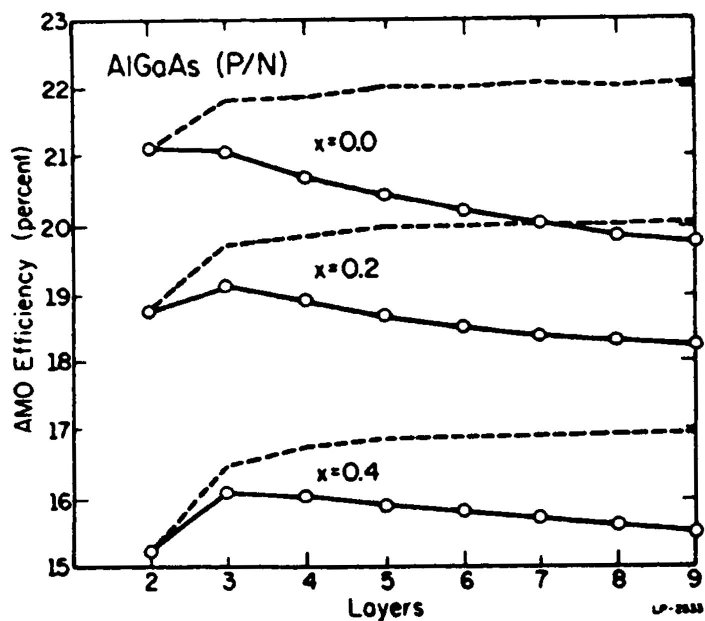

Figure 4. - Performance of cell designs optimized for one sun AMO operation at 300 K.

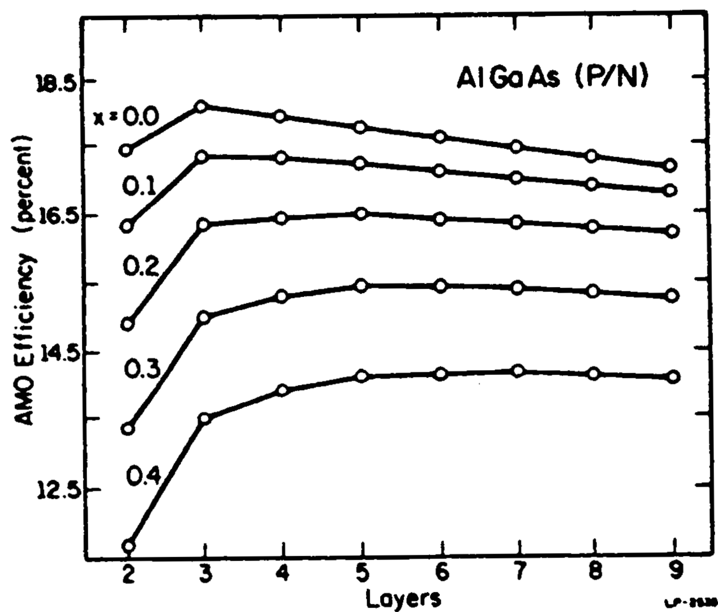

Figure 5. - Performance of radiation damaged cells optimized for end-of-life efficiency.

N86-17851

A POSSIBLE RADIATION-RESISTANT SOLAR CELL GEOMETRY USING SUPERLATTICES

Chandra Goradia and Ralph Clark
Cleveland State University
Cleveland, Ohio

David Brinker
NASA Lewis Research Center
Cleveland, Ohio

A solar cell structure is proposed which uses a GaAs nipi doping superlattice. An important feature of this structure is that photogenerated minority carriers are very quickly collected in a time shorter than bulk lifetime in the fairly heavily doped n and p layers and these carriers are then transported parallel to the superlattice layers to selective ohmic contacts. Assuming that these already-separated carriers have very long recombination lifetimes, due to their being across an indirect bandgap in real space, it is argued that our proposed structure may exhibit superior radiation tolerance along with reasonably high beginning-of-life efficiency.

INTRODUCTION

In recent years, semiconductor superlattice (SL) structures have exhibited several attractive features. These include: 1) the ability to tailor-make a semiconductor with a desired bandgap and lattice constant over ranges of these two parameters which do not occur in normal materials (ref. 1), 2) the ability of a superlattice to act as a dislocation barrier which significantly reduces the propogation of dislocations from one semiconductor layer to another when an appropriate superlattice is interposed between them (ref. 2), 3) the exhibition of high electron mobility in undoped layers, in directions parallel to the layers, when such layers are alternated with heavily doped n-type layers of larger bandgap (ref. 3), and 4) the exhibition of very long carrier recombination lifetimes for excess carriers created in certain compositional and doping superlattice structures due to electrons and holes being confined in separate layers, thereby creating an effective "indirect bandgap in real space" (ref. 4).

A question naturally arises as to how one or more of these attractive features could be put to good use in solar cells. Blakeslee and Mitchell (refs. 2, 5), and Chaffin et al. (ref. 1) have proposed solar cell structures which utilize the first two features listed above in the monolithic multibandgap cascade solar cell geometry using binary and ternary III-V compounds. The principal advantage here is to be able to grow top and bottom cells of optimum bandgaps, ~1.7eV and ~1.1eV respectively, while minimizing lattice mismatch and/or the propagation of dislocations. Additionally, their structures make it possible to use the relatively inexpensive material silicon for the substrate and the bottom cell. It is not clear yet whether the requirement of carrier flow perpendicular to the superlattice layers in these

PRECEDING PAGE BLANK NOT FILMED

structures, a direction generally regarded as having poor carrier transport properties, will pose a problem.

In this paper, we propose a superlattice solar cell structure in which carrier transport is parallel to the superlattice layers. It is a single-bandgap single-junction structure and therefore does not have the potential for the nearly 27 percent efficiency expected of the two-bandgap two-junction cascade device. However, by exploiting the very short carrier separation time and the very long carrier lifetime in a superlattice, our proposed GaAs-based structure is expected to yield a high radiation tolerance coupled with the 20% or so efficiency expected of a conventional GaAs solar cell designed for and operated under moderate sunlight concentration.

PROPOSED SUPERLATTICE SOLAR CELL STRUCTURE

Figure 1 shows our proposed GaAs-based superlattice solar cell structure. While quite different from them, it uses elements from two existing concentrator solar cell geometries, namely, the V-Grooved Multi-Junction (VGMJ) (ref. 6) and the Interdigitated Back Contact (IBC) (ref. 7) solar cells. Both of these structures have demonstrated high efficiencies in silicon.

The active region consists of a GaAs nipi doping superlattice of about 10 periods or 41 individual layers with a total thickness of 2.5 to 4 μm, grown on an appropriate semi-insulating substrate (all GaAs or GaAs on Ge-coated Si). The n^+ and p^+ regions in figure 1 are ion-implanted selective contacts to the n and p superlattice layers, respectively, and may be photolithographically fabricated using the same techniques as employed in the VGMJ solar cell (ref. 6). The n^+ and p^+ contacts are interdigitated as in the IBC cell (albeit in front instead of in the back), with all n^+ metallization stripes connected to one bus bar and all p^+ metallization stripes connected to another bus bar on the opposite edge.

OPERATION

Figures 2a and 2b show, under thermal equilibrium and under a forward bias respectively, the energy band diagram in a direction normal to the superlattice layers, say along the line aa in figure 1. If the dopings in the n and p layers and the thickness of the n, p and i layers are properly designed, then, in thermal equilibrium, the n and p layers will be completely covered by space charge, primarily due to ionized donors and acceptors respectively, so that E_c and E_v will be approximately parabolic functions of the space coordinate z. In the intervening i layers, E_c and E_v will be approximately linear functions of z. The total built-in band bending or diffusion potential depends on the dopings in the n and p layers and on the thicknesses of the n, p, and i layers.

The superlattice periodicity in the z direction, superimposed on the crystalline periodicity, causes the formation of electron and hole sub-bands within the conduction and valence bands respectively. The sub-band energies, widths, and densities-of-states depend on the exact manner in which E_c, E_v vary with z, and these, in turn, depend on the previous quantities, so that it turns out that all pertinent quantities, including $E_c(z)$, $E_v(z)$, the electron and hole concentrations n and p and their distribution in the sub-bands, must be solved self-consistently in thermal equilibrium and at any desired forward bias. Such calculations are

rather laborious and, to our knowledge, have been performed only for the case of the npnp superlattice without the i layers. Figures 3a, 3b and 3c show the results of such calculations as published by Brand and Abram (ref. 8). Such calculations are a first step toward the theoretical modelling and optimum design of the superlattice solar cell we are proposing. We have begun the project of doing such calculations for the nipi structure so that they will allow us to predict cell performance as a function of the widths of the n, p and i layers and the dopings in the n and p layers, and to optimize these parameters.

The i layers are needed to give the largest possible built-in band bending while still providing reasonably wide high-electric-field regions without requiring relatively thick heavily doped n and p regions. The large build-in band bending is needed in order to get a high open circuit voltage V_{oc}, and a wide high-electric field region is needed for a high carrier collection efficiency and high radiation tolerance.

Next, let us consider figure 2b, where the superlattice of figure 2a is shown under a forward bias, say that corresponding to the maximum power voltage under illumination. In this case, it is seen that part of the space charge in the n and p regions is compensated by mobile carriers, so that flat spots, corresponding to quasi-neutral regions, appear in E_c and E_v. In our solar cell structure, these quasi-neutral regions are not expected to be more than about 600 angstroms wide, so that a photogenerated electron in the middle of a p layer would diffuse to the nearest high electric field region in less than $3x10^{-11}$ seconds (using a diffusion velocity of $\geq 10^5$ cm/s for electrons in GaAs) and then drift at nearly the thermal velocity to the lowest available sub-band in the conduction band in another 10^{-12} second or less. Thus it is seen that an electron which is photogenerated anywhere in the structure is very quickly transported into the nearest n layer, where it is a majority carrier. By the same token, a hole which is photogenerated anywhere would also be transported into the nearest p layer in less than $3x10^{-10}$ second (using a diffusion velocity of $\geq 10^4$ cm/s for holes). Once they become majority carriers, these separated photogenerated carriers must still be transported, without recombination, to the nearest selective contacts before they can be regarded as being collected (that is, having contributed to external current).

In an ordinary solar cell, a photogenerated minority carrier would be regarded as having been collected once it had been separated, that is, once it crossed the junction space charge region and became a majority carrier. However, in a superlattice solar cell, in which relatively large numbers of electrons and holes are spatially confined in close proximity such that their wavefunctions overlap, band-to-band recombination of already-separated photogenerated electrons and holes can occur between a sub-band in the conduction band and a corresponding sub-band in the valence band. Such recombination is said to occur across an "indirect bandgap in real space". The larger the overlap between the electron and hole wavefunctions, the larger the rate of recombination. It is seen from figure 2b that electrons and holes in the lowest energy sub-bands do not have any significant overlap of their wavefunctions. Only the higher-energy sub-bands will have any significant overlap of wavefunctions. However, because of a rather large energy gap between these, the recombination probability is rather low. Thus, the overall recombination probability across an indirect bandgap in real space can be rather low, yielding an effective recombination lifetime that can be very long. In this regard, we have also taken a look at the use of Type I and Type II compositional superlattices in our proposed structure and have found that the nipi doping superlattice appears to offer the longest recombination lifetime of already-separated carriers across the indirect bandgap in real space.

We have performed some rather crude calculations for a GaAs nipi doping superlattice cell of dimensions shown in figure 4. This geometry is very similar to that of the GaAs concentrator cell designed for use with the venetian blind or slats type concentrator at moderate concentrations up to 20 AMO (ref. 9). The total illuminated cell area is 0.25 cm x 1 cm with 50 grid lines, 25 each for the n and p selective contacts and each approximately 10 μm wide and 0.25cm long. The n, p, and i layers are each 1000A thick, and there are 10 complete pini periods (11 p layers, 20 i layers and 10 n layers). With about 200 μm separation between adjacent selective n and p contacts, dopings of about 5×10^{18} cm^{-3} in the n and p layers, an illumination level of ∿ 5xAMO, and a short circuit current density of about 180 mA/cm^2, the time required by the already-separated electrons and holes to drift the farthest distance (equal to the grid separation of 200 μm) to the nearest selective contact is about 0.6 millisecond. Thus, the required recombination lifetime across the indirect bandgap in real space is about 1 millisecond or larger at the cell operating temperature (300-350K). Preliminary theory predicts such lifetimes to be possible. More detailed calculations and experimental verification have yet to be done.

DISCUSSION

The superlattice solar cell device structure we propose is expected to have a high short circuit current density J_{sc}, at least as high as with a well-designed conventional GaAs solar cell. This is because of the nearly complete collection of photogenerated carriers expected if the recombination lifetime for already-separated carriers is longer than 1ms. The slightly lower (than for bulk GaAs) effective bandgap (indirect in real space) is not expected to increase the number of photogenerated carriers and J_{sc} to any significant degree.

One may expect the open circuit voltage V_{oc} in this device to be lower than in the conventional GaAs solar cell for two reasons: 1) for a given illuminated area, the junction area is N times larger, where N is the number of nipi periods, 10 in our example, and 2) the forward or loss current pre-exponential factor J_o may be dominated by space charge recombination. It is not so much the larger junction area per se which is a problem. It is the larger overall volume of the space charge region compared to that in a conventional GaAs solar cell which may make the J_o of our superlattice cell relatively larger and give rise to a smaller V_{oc}. Even so, it is felt that a reasonably large V_{oc} may be obtainable at moderate sunlight concentrations.

It thus appears that the beginning-of-life (BOL) efficiency of our proposed cell might be somewhat smaller than that of a well-designed conventional GaAs solar cell, say, 20% instead of 22 to 23%. However, our proposed superlattice cell structure is expected to exhibit a high degree of radiation tolerance. This is because, at radiation exposures equivalent to a fluence of 10^{15} 1MeV electrons/cm^2 or less, the carrier collection efficiency is expected to stay very high, close to 100%, since for both electrons and holes, the minority carrier diffusion length after irradiation is expected to be longer than the 300-500A they have to diffuse in the quasi-neutral portions of the n and p layers before being separated. Additionally, since the recombination lifetime of already-separated carriers depends on the overlap in their wavefunctions, that lifetime is not expected to be affected by irradiation. Thus, the short circuit current density should suffer negligible degradation under irradiation. The open circuit voltage V_{oc} and fill factor FF are expected to degrade in our proposed cell because of increased J_o due to increased

recombination in the space charge region. It is not clear at this time whether the degradations in V_{oc} and FF can be kept low enough to yield an overall high radiation tolerance, but the present expectation is that with proper design they can. That is what we aim to find out through a detailed modelling and parameter optimization study of our proposed structure.

REFERENCES

1. Chaffin, R.J., et. al., "Strained Superlattice, Quantum Well, Multijunction Photovoltaic Cell", Conf. Rec. 17th IEEE PVSC, Orlando, Fla., May 1984, IEEE Publ. No. 84CH2019-8, pp. 743-746.

2. Blakeslee, A.E. and K.W. Mitchell, "Incorporation of Superlattice Crystal Layers in Multijunction Solar Cells", Conf. Rec. of Space Photovoltaic Research and Technology Conf., NASA Lewis, Cleveland, Oct. 1980, NASA Conf. Publ. No. 2169, pp. 131-134.

3. Dingle, R., H.L. Stormer, A.C. Gossard, and W. Wiegman, "Electron Mobilities in Modulation-doped Semiconductor Heterojunction Superlattices", Appl. Phys. Lett. Vol. 33, No. 7, 1 Oct. 1978, pp. 665-667.

4. Dohler, G.H., "Electrical and Optical Properties of Crystals with 'nipi-Superstructure'", Phys. Stat. Sol., Vol. 52, 1972, pp. 533-545.

5. Blakeslee, A.E., "Control of Superlattice Morphology in $GaAs_{1-x}P_x$ Cascade Cells", this proceedings.

6. Chappell, T.I., "The V-Groove Multijunction Solar Cell", Conf. Rec. 13th IEEE PVSC, Washington, D.C., June 1978, IEEE Publ. No. CH1319-3/78/0000-0791, pp. 791-796, also IEEE Trans. Electron Devices, ED-26, No. 7, 1979, pp. 1091-1097.

7. Schwartz, R.J. and M.D. Lammert, "Silicon Solar Cells for High Concentration Applications", Technical Digest, International Electron Devices Meeting (IEDM), Washington, D.C., Dec. 1975, p. 350, also IEEE Trans. Electron Devices, ED-24, No. 1977, p. 337.

8. Brand, S. and R.A. Abram, "Self-consistent Calculations of Electron and Hole Sub-band Energies for an n-p Superlattice in GaAs", J. Phys. C., Vol. 16, 1983, pp. 6111-6120.

9. Goradia, C.P., M. Ghalla-Goradia, and H. Curtis, "Near-optimum Design of GaAs-based Concentrator Space Solar Cells for 80°C Operation", Conf. Rec. 17th IEEE PVSC, Orlando, Fla., May 1984, IEEE Publ. No. 84CH2019-8, pp. 56-62.

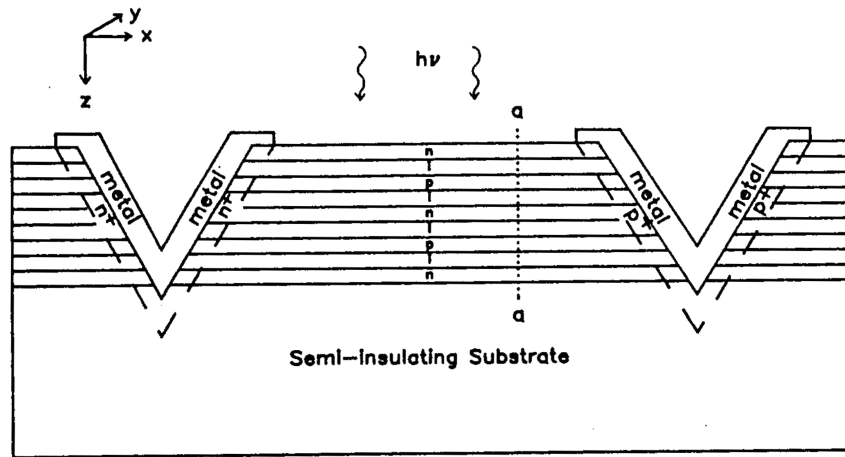

Figure 1: Schematic diagram of proposed solar cell structure using nipi doping superlattice.

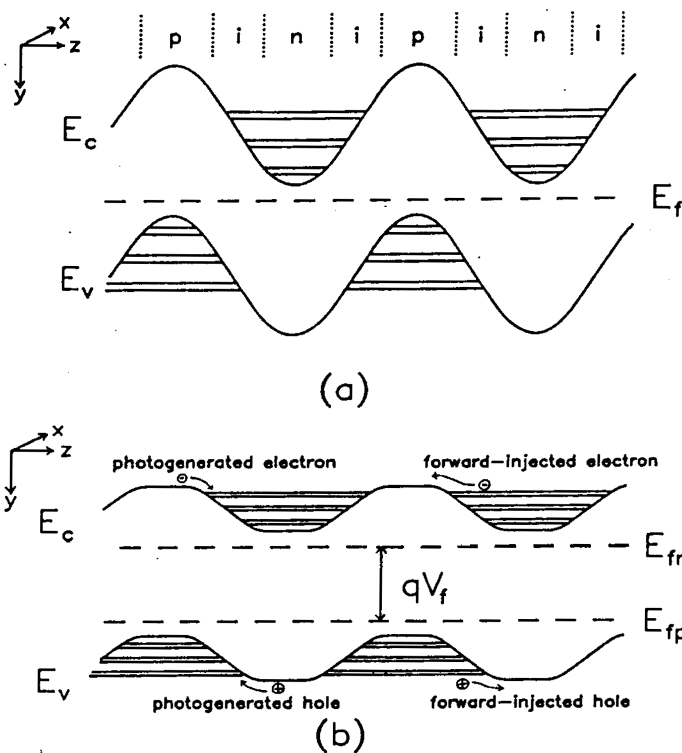

Figure 2: Band diagram of nipi superlattice, (a) in thermal equilibrium, and (b) under forward bias.

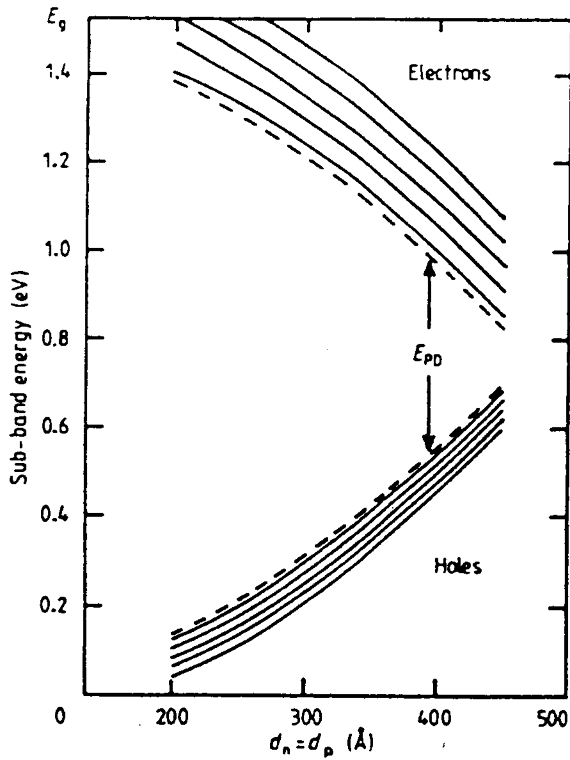

(a)

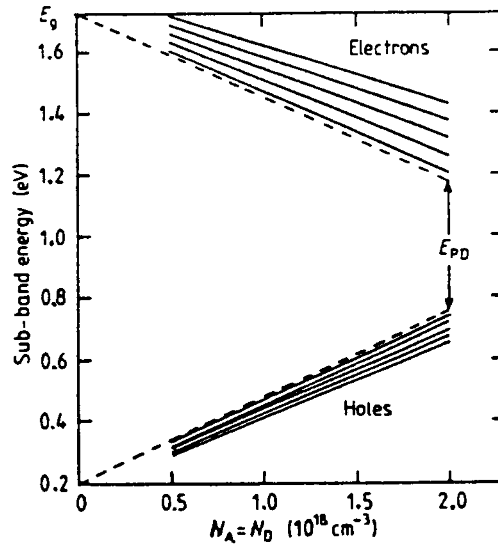

(b)

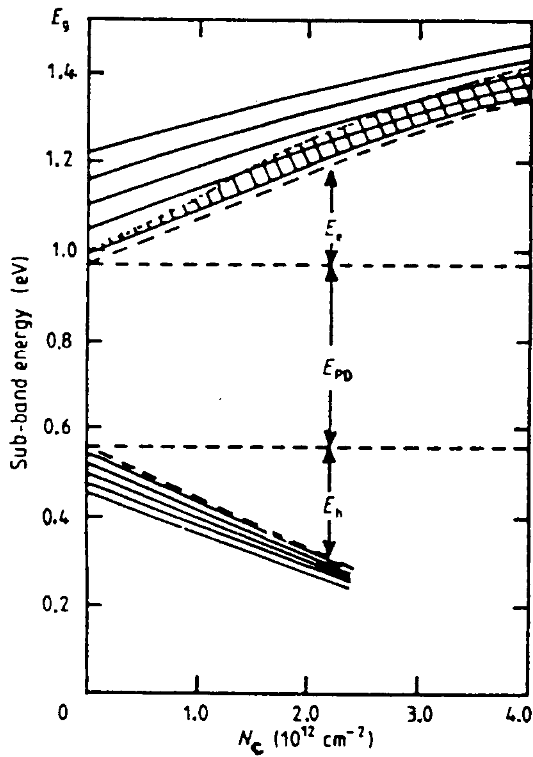

(c)

Figure 3: Electron and hole sub–band levels as a function of (a) layer thickness $d_n = d_p$, for $N_d = N_a = 2 \times 10^{18}$ cm^{-3}; (b) doping level $N_d = N_a$, for $d_n = d_p = 400$ Å; (c) 2–dimensional injected carrier concentration N_c, for $N_d = N_a = 2 \times 10^{18}$ cm^{-3} and $d_n = d_p = 400$ Å (the shaded area represents filled states). From reference 8.

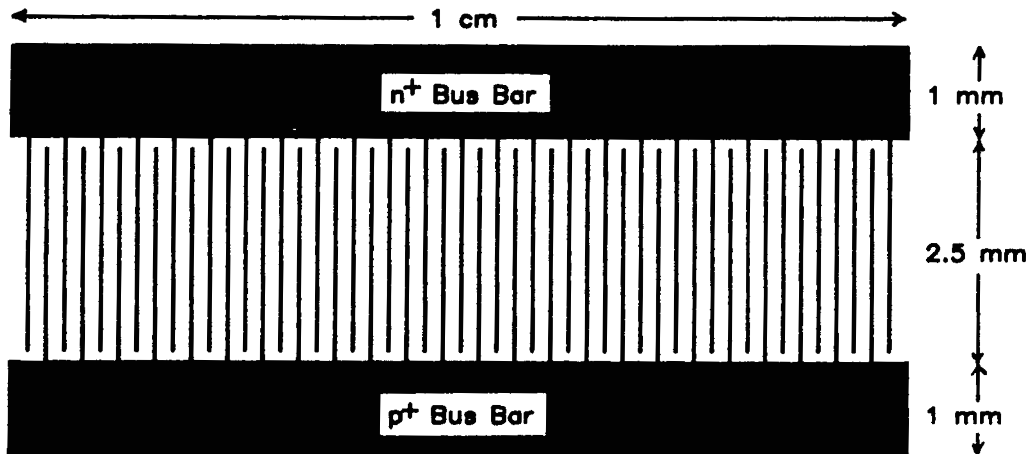

Figure 4: Top view of proposed superlattice cell, showing collection grid geometry and typical dimensions.

N86-17852

EXPERIENCE WITH OMCVD PRODUCTION OF GaAS SOLAR CELLS

Y.C.M. Yeh, P.A. Iles, P. Ho, and K.S. Ling
Applied Solar Energy Corporation
City of Industry, California

Update 1983 SPRAT paper with experience accumulated running at 1200 2x2cm GaAs cells per week. Show results on best cell performance achieved under production conditions, and uniformity achievable for successive cell runs. Also some production topics will be addressed.

Results of typical space-environmental tests and discussion of critical areas, including substrate supply and specification will be presented.

INTRODUCTION

This paper updates the report given at the 1983 SPRAT Conference. It describes the experience gained in operating a production-level OMCVD reactor and in processing cells made from layers grown in the reactor.

We have improved the uniformity in thickness and doping of deposited layers, by improved susceptor design and by modification of gas injection and flow conditions.

The throughput to date was slightly below that originally planned (is now at about 1200 2x2cm cells/week per machine) but this level was sufficient to show the potential of the approach and has indicated areas for further increase in throughput.

RUNNING EXPERIENCE

A wide range of substrates have been processed through to finished cells, and the space-worthiness of the cells produced has been confirmed. The experience is summarized in the following areas:

Substrates

The suppliers have cooperated well, to provide large (about $11.3cm^2$), near-rectangular substrates of good quality. The control of wafer processing and cell fabrication is sufficient to show that over a wide sample range, there have been variations in bulk crystal defects and in surface quality, although the average quality has been sufficient to provide good cell efficiency (greater than 16%).

The suppliers continue to improve their product, and with stronger conviction that the potential solar cell market is significantly large, have continued a trend of reduced costs per square inch.

OMCVD Deposition

Continuous operation at realistic production levels has shown apparently mundane but essential needs, in housekeeping and maintenance, especially preventive maintenance to cope with typical performance specifications, critical spare parts, safety concerns and waste disposal.

This experience has been applied to include improved features, in later models of the reactor.

Sources

The suppliers have increased the delivery capacity of key elements, especially TMG and AsH_3, without apparent adverse effects from impurities. The larger bottles and cooling means were made readily by the suppliers. We have added monitoring to ensure that the carrier gas (H_2) has low water content.

Cell Processing

The post layer processing has been simplified and consolidated to give reproducible cell properties and acceptable performance in space. The test data manipulation has been expanded to display yields and detailed PV parameters.

Diagnostics

The cell line is supported by a systematic diagnostic effort, to determine the allowable range of properties which still give good cells and to trace the effects of variations (intentional or unplanned) in the substrate or layer properties.

Sample Results

To illustrate the present level of performance, we present data for six consecutive runs made in the past month. These runs include several different substrates and different geometry cells (2x2, 2x4cm^2). The "best" cells resulting from production runs have been steadily improving.

CONCLUSIONS

ORIGINAL PAGE IS
OF POOR QUALITY

The projected promise of the OMCVD approach, to make high efficiency GaAs space cells has been demonstrated. The properties and control of the deposited GaAs and AlGaAs layers and the uniformity of the post layer processing have been most satisfactory. In particular the control of the critical thin layers (p-GaAs, p-AlGaAs) has been impressive.

Experience has also been gained in routine areas, connected with continuous operation at high capacity.

There are still a few areas for improvement, to further increase capacity, and to anticipate and prevent mechanical equipment problems.

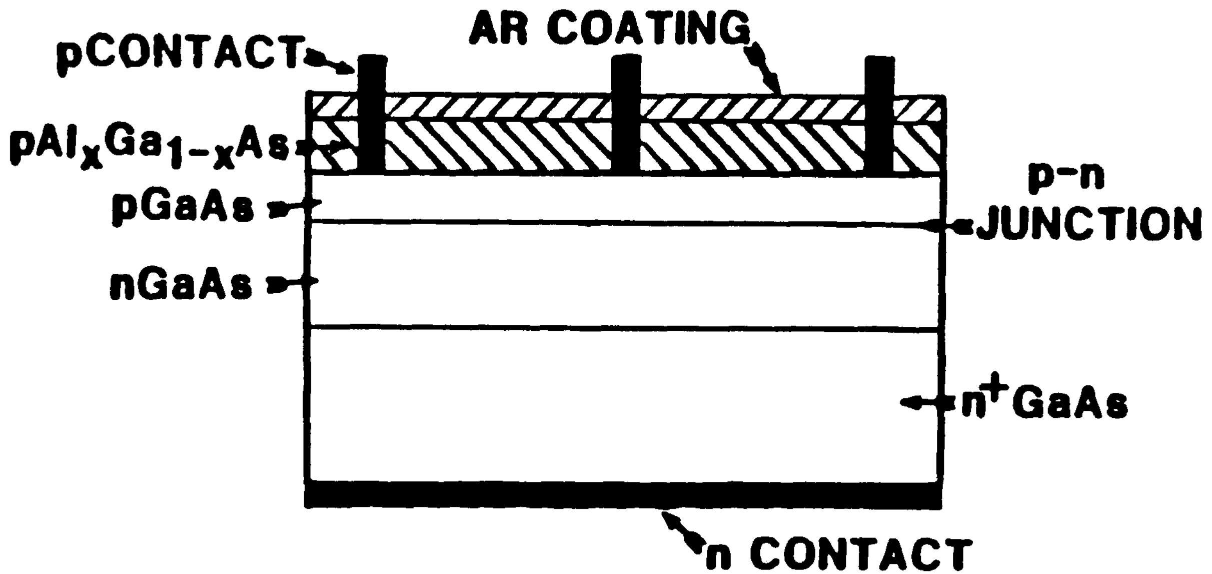

FIGURE 1: AlGaAs/GaAs HETEROFACE SOLAR CELL STRUCTURE

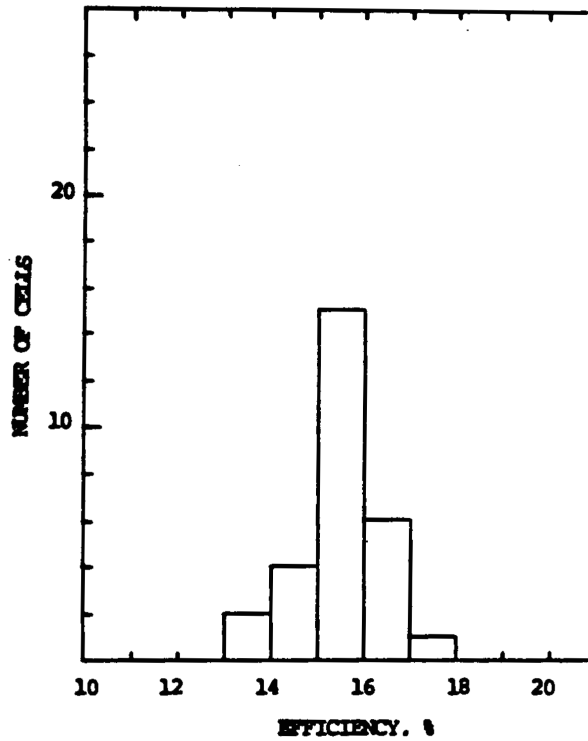

FIGURE 2: HISTOGRAM OF AMO EFFICIENCY FOR LOT 233

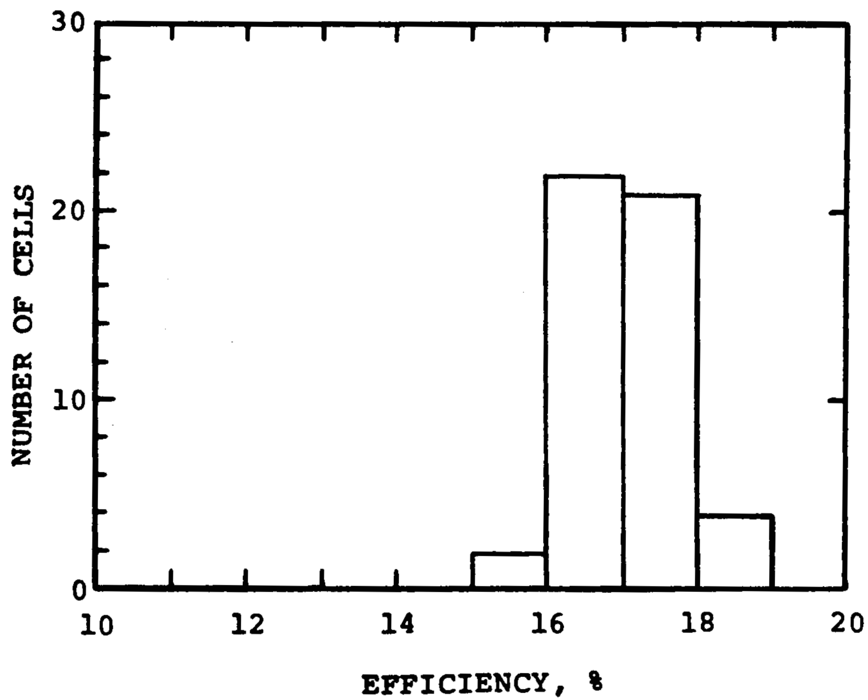

FIGURE 3: HISTOGRAM OF AMO EFFICIENCY FOR LOT 692

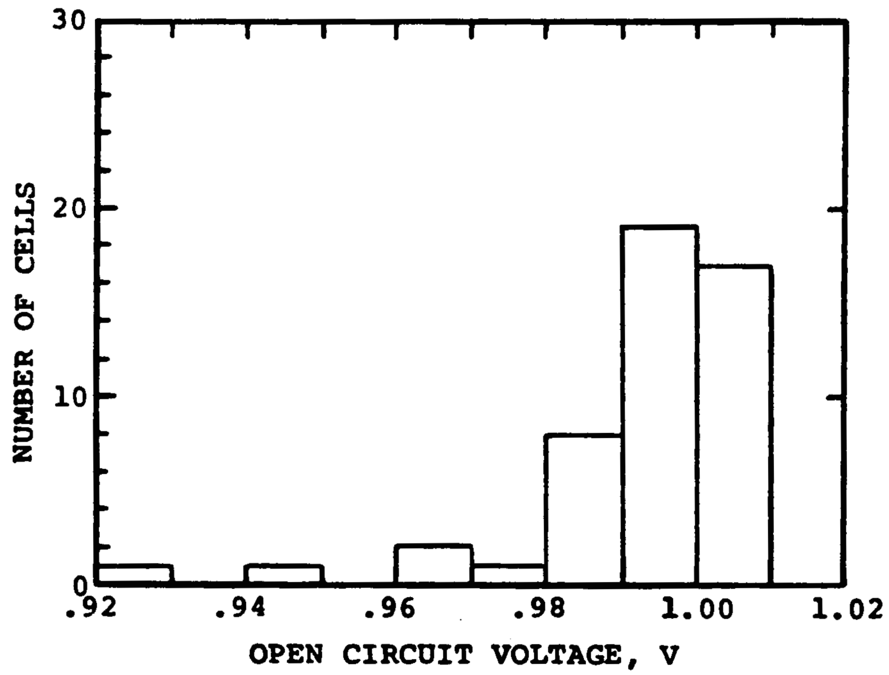

FIGURE 4: HISTOGRAM OF OPEN CIRCUIT VOLTAGE FOR LOT 692

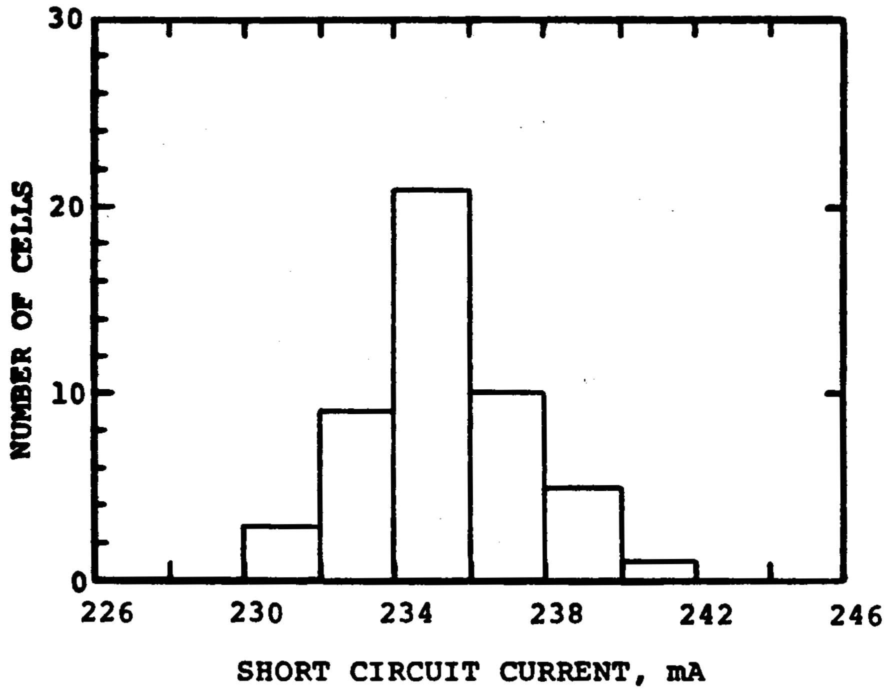

FIGURE 5: HISTOGRAM OF SHORT CIRCUIT CURRENT FOR LOT 692

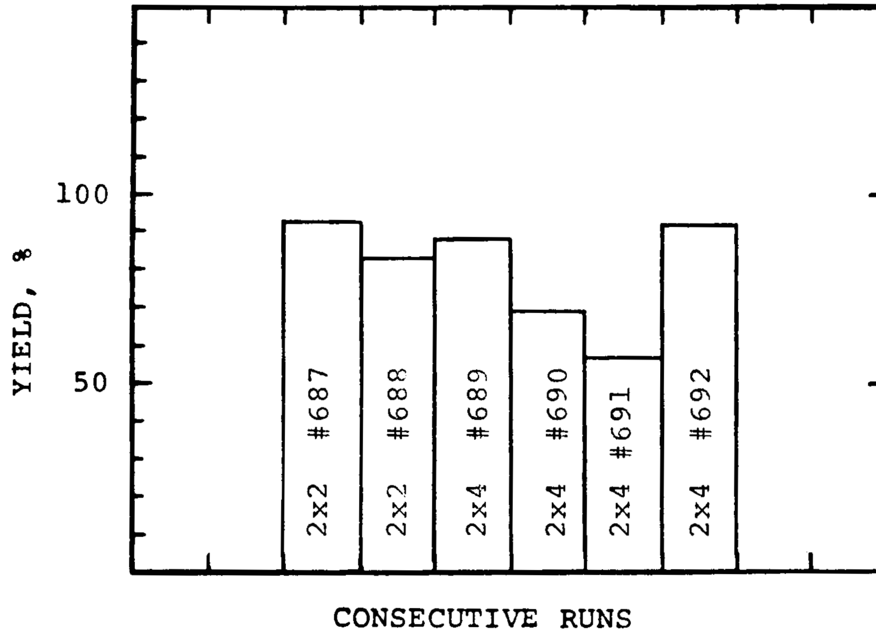

FIGURE 6: HISTOGRAM OF YIELD IN SIX CONSECUTIVE RUNS FOR AMO EFFICIENCY GREATER OR EQUAL TO 16%

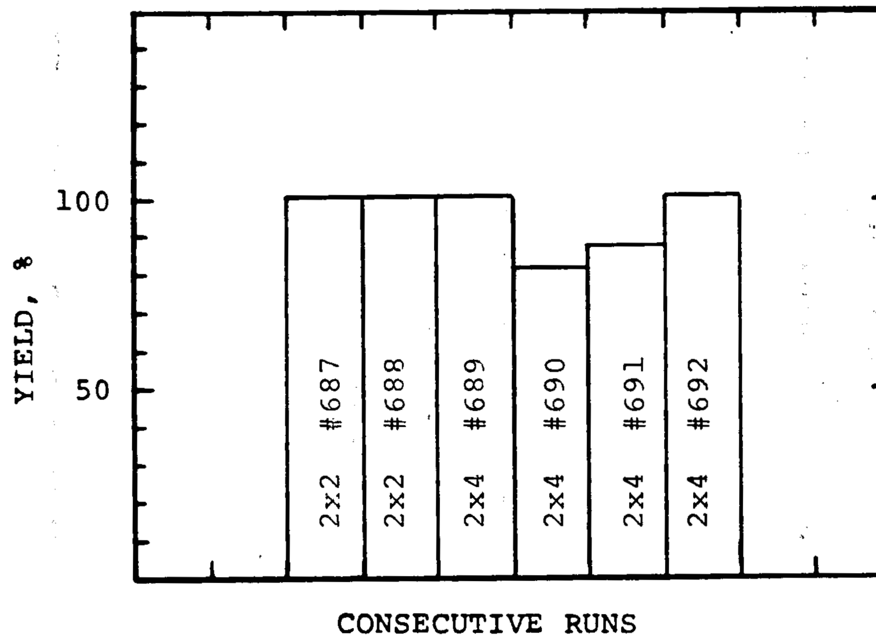

FIGURE 7: HISTOGRAM OF YIELD IN SIX CONSECUTIVE RUNS FOR AMO EFFICIENCY 16% AVERAGE OR GREATER AND 15% MINIMUM

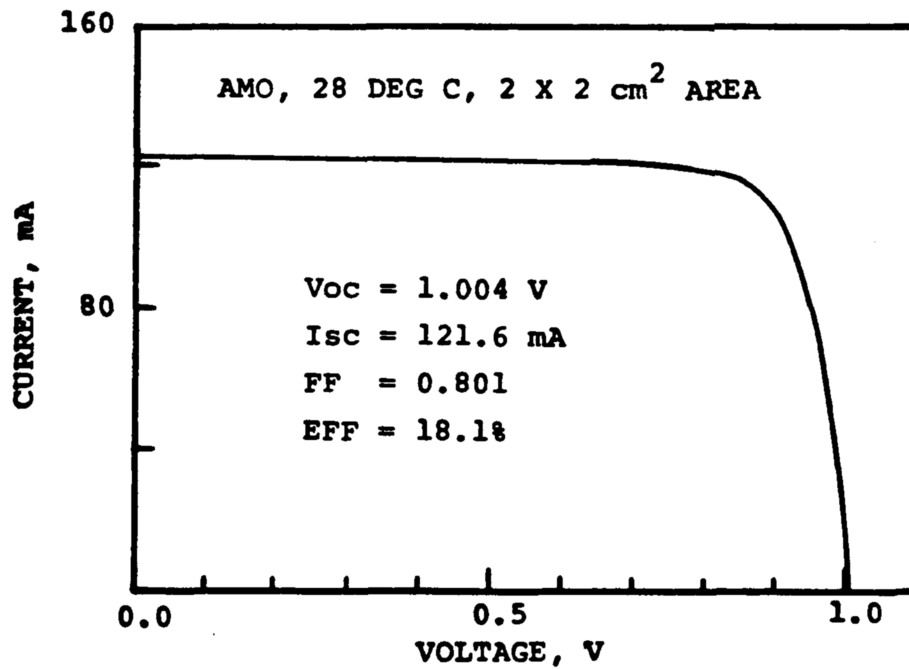

FIGURE 8: LIGHT I-V CHARACTERISTICS OF AN AlGaAs/GaAs SOLAR CELL

N86-17853

BURST ANNEALING OF ELECTRON DAMAGE IN SILICON SOLAR CELLS

A. C. Day, W. E. Horne, M. A. Thompson, and C. A. Lancaster
Boeing Aerospace Company
Seattle, Washington

A study has been performed of burst annealing of electron damage in silicon solar cells. Three groups of cells consisting of 3 and 0.3 ohm-cm silicon were exposed to fluences of 2 x 10^{14}, 4 x 10^{14}, and 8 x 10^{14} 1-MeV electrons/cm^2 respectively. They were subsequently subjected to 1-minute bursts of annealing at 500°C. The 3 ohm-cm cells showed complete recovery from each fluence level. The 0.3 ohm-cm cells showed complete recovery from the 2 x 10^{14} e/cm^2 fluence; however, some of the 0.3 ohm-cm cells did not recover completely from the higher fluences. From an analysis of the results it is concluded that burst annealing of moderate to high resistivity silicon cell arrays in space is feasible and that with more complete understanding, even the potentially higher efficiency low resistivity cells may be usable in annealable arrays in space.

INTRODUCTION

Electron and proton damage presents a problem to space power system designers. Generally, in order to meet the requirements of a given mission, heavy shielding in the form of cover glasses and over sizing of the array have been the approaches taken to ensure adequate end-of-life performance. Depending on the mission, the radiation damage penalty can be 25 to 50 percent. Since the early 1960's researchers have investigated various techniques for reducing the extent of radiation damage in photovoltaic cells in order to minimize the need for shielding and over design. Early attempts included a study of thermal annealing of arrays in space by periodically covering the array with a special cover so that it heated up by a "greenhouse" effect to anneal the radiation damage. However, certain components of the damage in silicon cells would not anneal completely at temperatures compatible with the cell structures and array materials available at that time. Considerable effort was also expended on the development of lithium doped silicon cells which tended to spontaneously anneal at relatively low temperatures. However, there were problems with inherent instabilities in the lithium cells and certain components of the radiation damage would not readily anneal. These problems limited the application of the lithium cells.

Due to the factors mentioned above, the use of annealing of radiation damage has been limited to that of a research tool for better understanding the nature of radiation damage. In the course of these research studies, two methods of annealing have been employed, isochronal and isothermal. In the isochronal studies, irradiated samples are soaked for specific intervals of time, usually 15 or 20 minutes at a series of increasing temperatures. The number and types of defects remaining are measured between each interval. For both electron and proton damage certain "parent-daughter" relationships have been observed in which some defects break up or anneal at a relatively low temperature; one or more of the constituents of that defect then combine with another site or impurity to form a new, more stable defect which can be annealed only at much higher temperatures. In isothermal studies the irradiated

PRECEDING PAGE BLANK NOT FILMED

samples are soaked at a single temperature and their annealing progress monitored. The results of both types of experiments have indicated certain anomalies. For example, cells annealed isothermally at high temperatures tend to anneal more rapidly and completely than would be expected based on the results of lower temperature anneals and on isochronal annealing studies (ref. 1).

The inference from these observations is that the soak at relatively low temperatures may create an environment that induces the formation of stable, annealing-resistant defects. This observation is substantiated by the data in figure 1 which shows a comparison between isochronally annealed cells at different soak times. The shorter soak times result in more rapid and complete recovery. Based on this hypothesis and the recent development of high-temperature silicon cells at Boeing (ref. 2), the concept of "burst annealing" was developed. In burst annealing, the irradiated cells are ramped very rapidly to high temperatures (500°C or more in < 10 seconds) and allowed to soak for times on the order of one minute.

An earlier study of burst annealing on proton irradiated silicon cells (ref. 1) showed that a 25 percent degradation in short circuit current could be recovered completely by a burst anneal at 500°C for one minute or less. Therefore this paper reports the results of a recent burst annealing study on 1-MeV electron damaged cells. Data in the literature indicates that electron damage can require higher annealing temperatures than proton damage silicon cells (ref. 3).

EXPERIMENTAL

The samples were crucible-grown boron doped, 3 Ω-cm or .3 Ω-cm silicon cells with special high-temperature metallizations developed at Boeing. A detailed description of the fabrication techniques and performance characteristics of the cells has been presented in an earlier publication. In this earlier work the cells were found to be stable in their electrical output after thermal soaks of up to 20 minutes at 700°C in vacuum. Therefore, the short burst anneals of one minute at 500°C present no stability problems for the cells.

Three groups of four cells each were selected for the study. Each group contained cells from three different process batches. Two of the process batches used 0.3 ohm-cm silicon and one used 3.0 ohm-cm silicon. Three groups of cells were exposed to fluences of approximately 2×10^{14}, 4×10^{14}, and 8×10^{14} 1-MeV electrons/cm^2 respectively. The irradiations were performed in vacuum at room temperature using the Boeing Dynamitron. Dosimetry was performed using a shielded Faraday cup. I-V characteristics were taken at 25°C under simulated AMO sunlight (Spectrolab X25L) at one-sun intensity.

The burst annealing was performed in vacuum using a thermally isolated mount for the cells and a shuttered concentrated incandescent light beam directed through a quartz window onto the front of the cell in the vacuum chamber for heating. This arrangement allowed the cells to be raised to temperatures as high as 700°C in time intervals on the order of a few seconds. Figure 2 shows a typical thermal cycle characteristic as a function of time. This fast ramp to high temperature gives rise to the term burst annealing. The cells were removed from the vacuum chamber following each burst anneal and their I-V curves measured as described earlier.

DISCUSSION OF DAMAGE AND ANNEALING

Protons and electrons are the major components of the space radiation environment. Cover glasses can partially shield the cells from proton damage; however, electrons of 1-MeV energy and higher penetrate throughout the cell/array stack. The result is a nearly homogeneous production of isolated point defects throughout the cell base. The point defects, vacancies and interstitial atoms in the crystalline lattice, are highly mobile and tend to pair with other vacancies or with other impurity atoms within the crystal. The resulting defects are very stable and isochronal annealing studies have shown that temperatures in excess of 500°C are sometimes required in order to anneal them as illustrated in figure 3. Thus, the burst annealing approach is being studied in order to determine if it can successfully inhibit the formation of such high-temperature stable defects.

The number of initial defects formed in the silicon is generally treated as being directly proportional to the electron fluence.

Immediately following electron bombardment with energetic particles, the newly formed defects discussed above will consist almost entirely of single interstitials and single or multiple vacancies with single vacancies predominating. The vacancies and interstitials are highly mobile at room temperature in silicon, resulting in interaction of the vacancies and interstitials with each other or with impurities within the silicon. These interactions with impurities usually result in more stable defects that persist at higher temperatures.

As discussed earlier, it appears that the formation of more stable defect-impurity complexes can be minimized by rapidly ramping the cells to high temperature. However, even in the burst annealing situation if either the defect density or the impurity density is high enough, then there is increased probability of some of the defects encountering and pairing with impurities. In order to study this effect the three groups of cells were exposed to three fluences or defect densities and within each group there were cells made from 0.3 ohm-cm (high dopant impurity content) and 3.0 ohm-cm silicon material.

Figures 4, 5, and 6 shows the degradation and recovery curves typical of the 3-ohm-cm silicon cells after burst annealing from the three different damage levels. Within the accuracy of the measurements the recovery in these cells is complete at all three fluence levels. At the impurity density level of 3 ohm-cm silicon the burst annealing is successful at inhibiting the formation of secondary, more stable defects. This observation is supported by the results in the 0.3 ohm-cm cells. Figure 7 shows the worst case for one of these cells. As can be seen the cell shows considerably more electrical degradation for the same initial fluence than the 3 ohm-cm cells indicating that significant pairing of defects with dopant impurities has already occurred. As can be seen from the recovery curve the high temperature stable defects are already formed and no significant recovery is achieved until after the third anneal attempt of five minutes at 500°C. However, there was considerable scatter in the recovery characteristics of the low resistivity cells as indicated by figures 8 and 9. The almost complete recovery of the low-resistivity cell #207 shown in figure 9 suggests that if the annealing phenomena were better understood then the recovery of burst annealing could possibly be achieved for low resistivity cells also. The extent of recovery in the low resistivity cells was also a function of defect density as illustrated by the curves in figures 10 and 11. At the lower fluences or defect densities the low resistivity cells could be burst annealed effectively.

Thus, from these data it is concluded that burst annealing can be an effective tool for annealing cells in space. The degree of recovery is a function of initial defect density with respect to the existing impurity density, however, for cells of 3 ohm-cm or higher material (typical of most current space cells) the recovery from even heavy degradation is complete for practical purposes. Thus, it is concluded that burst annealing of electron damage in silicon cells is feasible for moderate resistivity cells and that a better understanding of the phenomena might make it feasible to use very low resistivity cells in space which would yield higher beginning of life efficiencies.

ANNEALING OF ARRAYS IN SPACE

From the above data, certain observations can be made about the optimum conditions for annealing radiation damage in space. First, a temperature range for annealing of about 500°C ± 50°C has been found to be adequate. Second, the best way to accomplish the anneal is a single burst to high temperature, stepping the cell to the annealing temperature (500°C) in as short a time as is practical. The present data indicate that a burst of 60 seconds at 500°C with a ramp time of 0 to 10 seconds is sufficient to anneal greater than 99 percent of the electrical degradation out of the cells. After the damage is annealed the slower return to normal temperature necessitated by thermal radiation to space does not matter.

A suggested approach for accomplishing the burst anneal cycles is the use of thin film resistors deposited on the substrate of each cell string in the array. The cells strings could then be periodically switched onto the array bus line by an autonomous power management system. The subsequent joule heating would accomplish the anneal consuming negligible power from the array during the one minute anneal. When the cell string has cooled and returned to power production another string would be annealed.

Such an annealable array could reduce the size of array required for a particular mission by as much as 50 percent.

CONCLUSIONS

Based on the results discussed in this paper and in references 1 and 2, it is concluded that:

1. Silicon cells can be produced which are stable under multiple cycles to 500°C temperatures required for burst annealing.

2. Burst annealing can yield essentially complete recovery of 3 ohm-cm n/p silicon solar cells in very short times; hence, with less energy than previously thought possible.

3. High efficiency low resistivity cells also show promise of being fully annealable.

The questions remaining regarding the feasibility of burst annealing is the repeatability of the recovery cycle after multiple anneals and the effectiveness of the annealing in cells exposed to simultaneously combined environments of protons and electrons.

REFERENCES

1. Lowe, V., and Day, A. C., "High Temperature Metallization Technology for Solar Cells," IEEE Trans. on Electron Devices, Nov. 1983.

2. Horne, W. E., Day, A. C., Thompson, M. A., "Burst Annealing of Proton Damage in Silicon Solar Cells," Proc. 17th IEEE Photovoltaics Specialists Conf., Orlando, Florida, 1984.

3. Carter, J. R., Jr., "Defect-Impurity Relationships in Electron-Damaged Silicon," IEEE Trans. on Nucl. Sci., Vol. NS-13, No. 6, December, 1966.

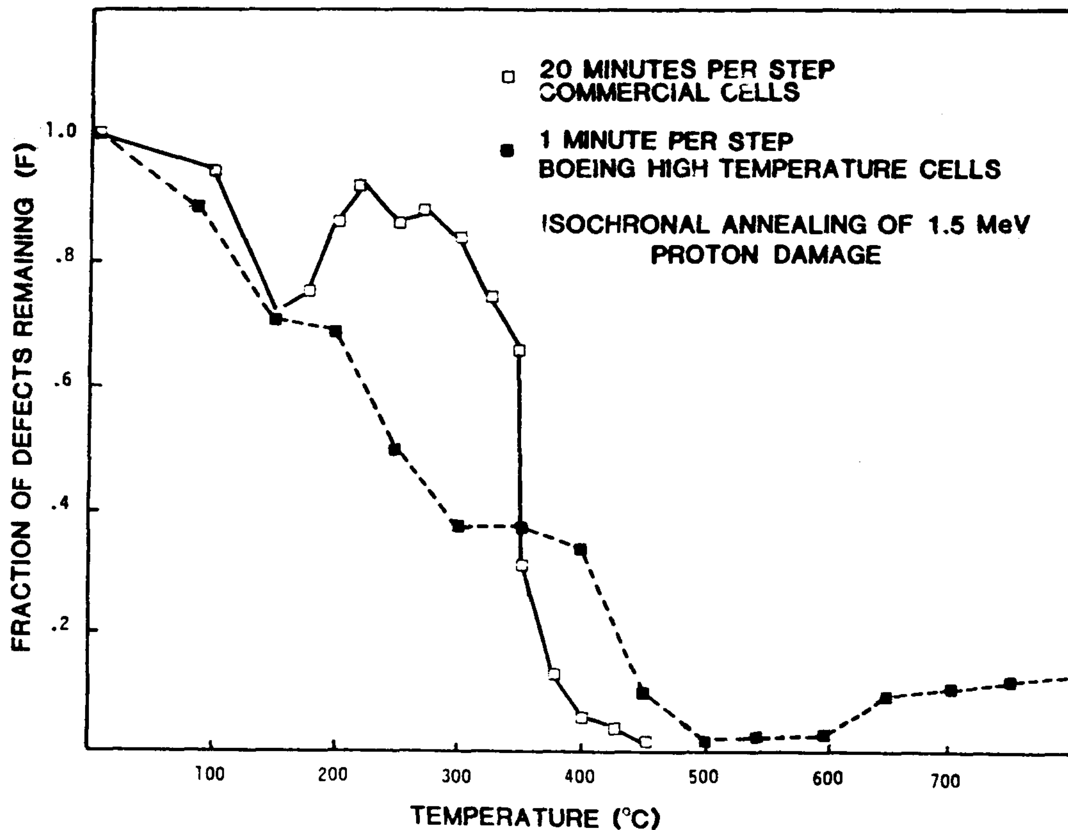

Figure 1. Comparison of Isochronal Annealing With Long and Short Annealing Times in Silicon Cells

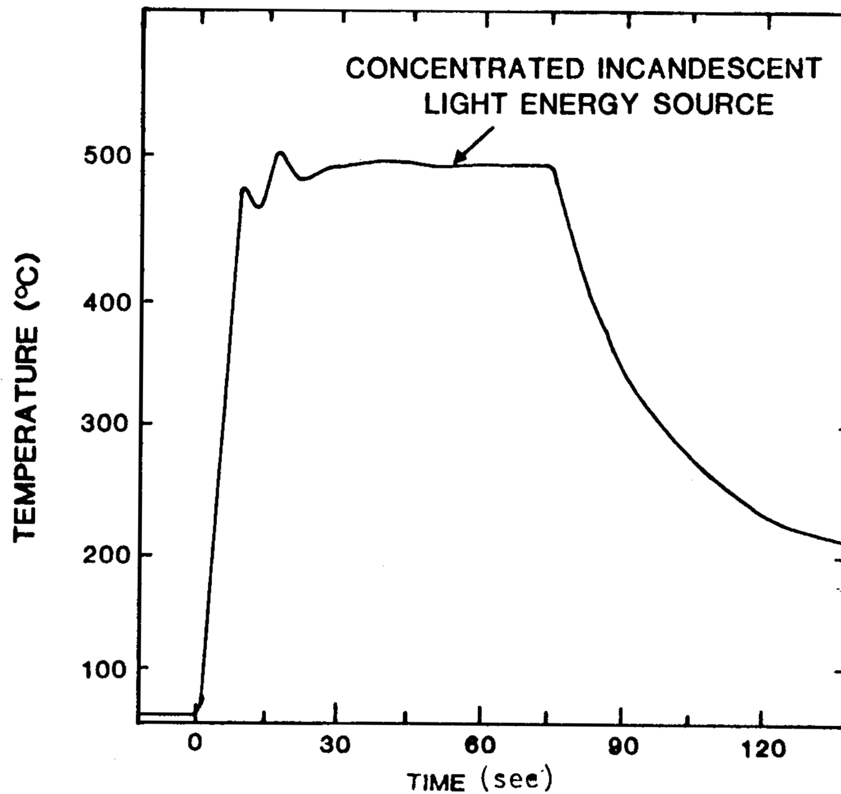

Figure 2. Typical Thermal Cycle for Burst Annealing

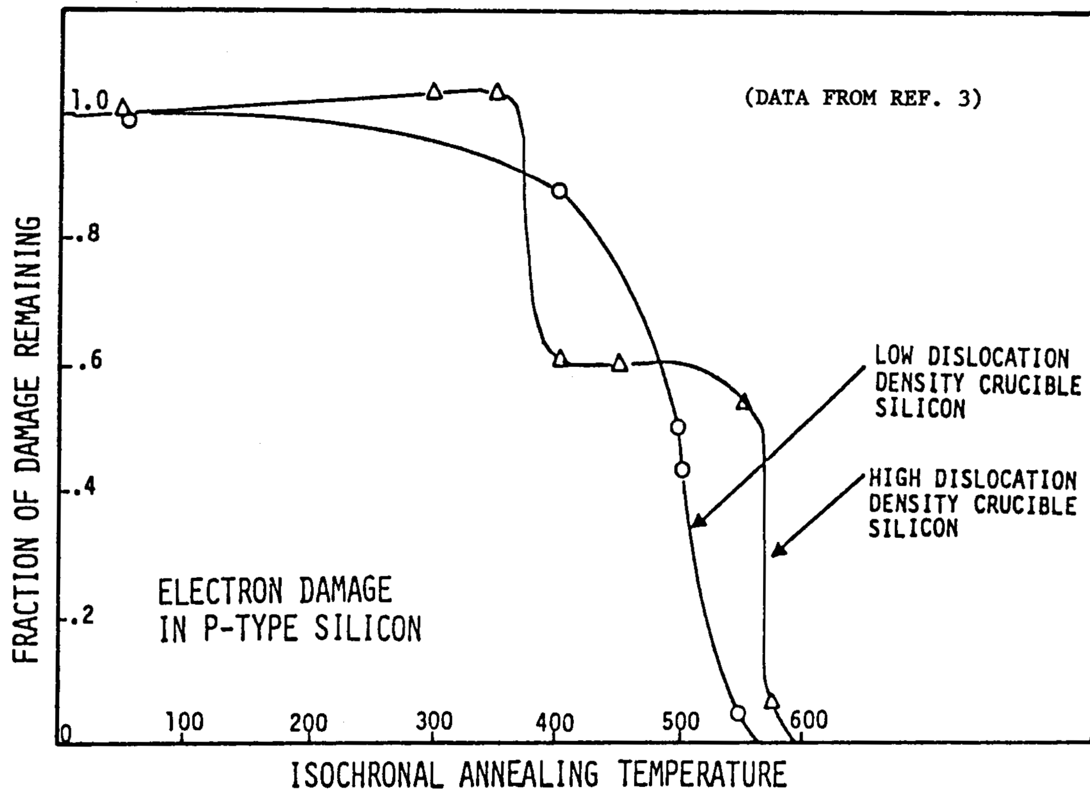

Figure 3. Electron Damage Recovery in Two Types of P-Type Silicon Material

ORIGINAL PAGE IS
OF POOR QUALITY

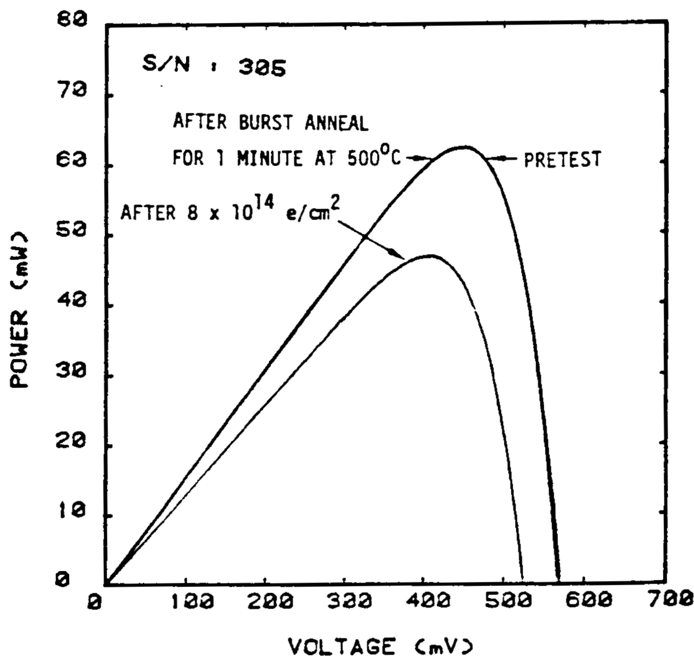

Figure 4. Burst Annealing of 3 ohm-cm Silicon Cell #305 From High Fluence Level

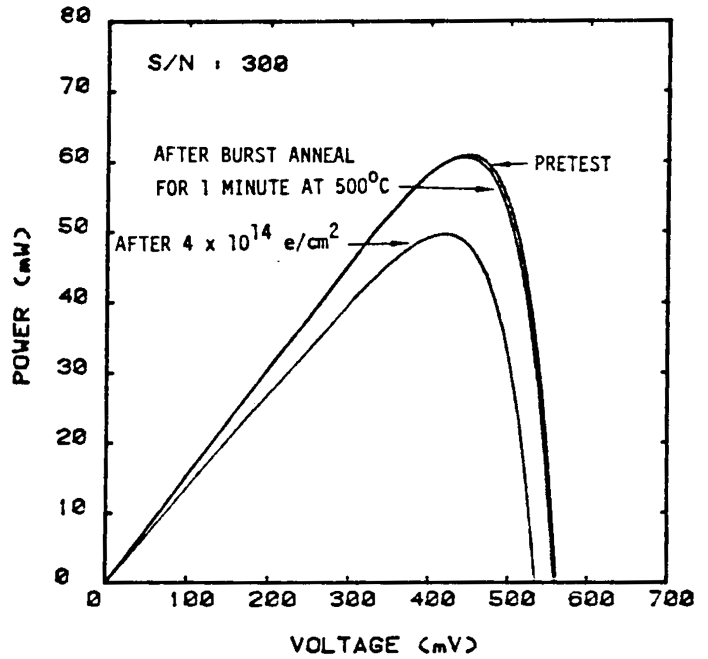

Figure 5. Burst Annealing of 3 ohm-cm Cell #300 From Intermediate Fluence Level

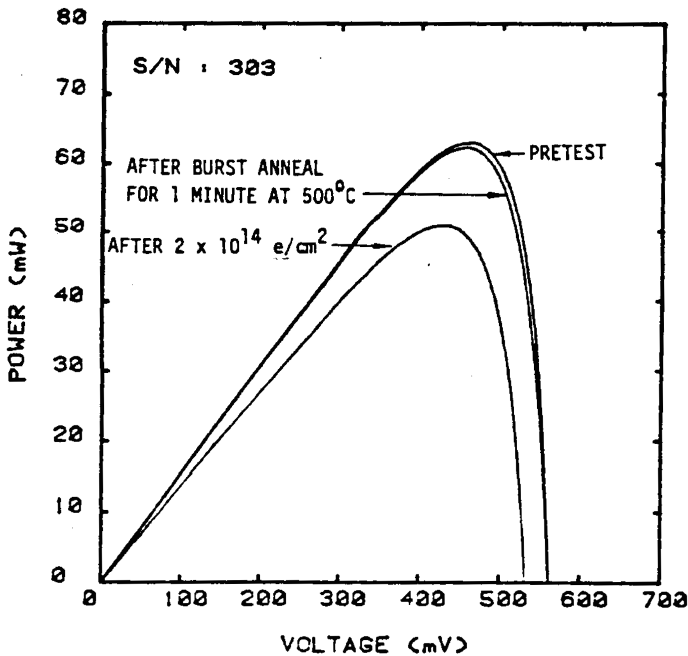

Figure 6. Burst Annealing of 3 ohm-cm Cell #303 From Low Fluence Level

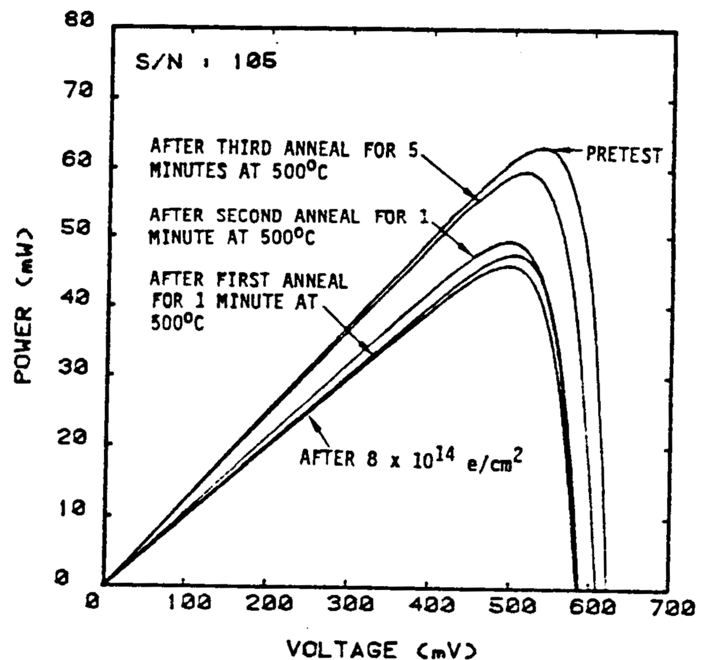

Figure 7. Burst Annealing 0.3 ohm-cm Cell #105 From High Fluence Level

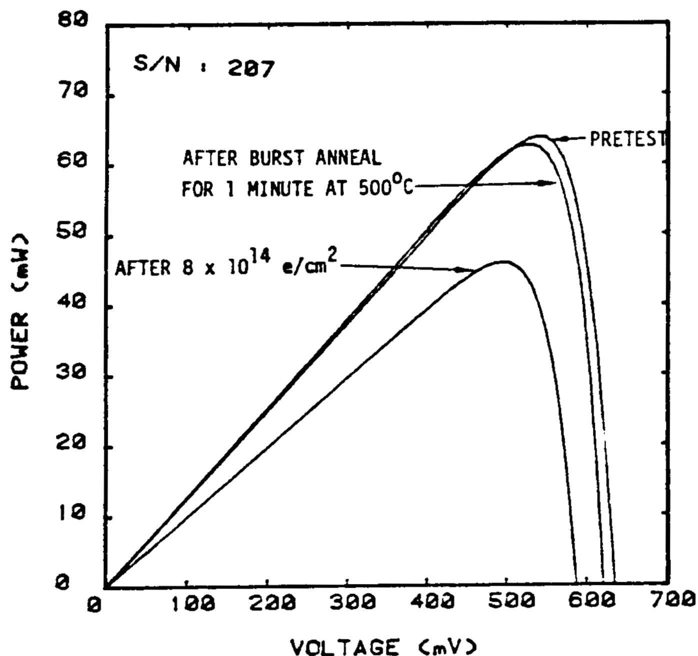

Figure 8. Burst Annealing of 0.3 ohm-cm Cell #207 From High Fluence Level

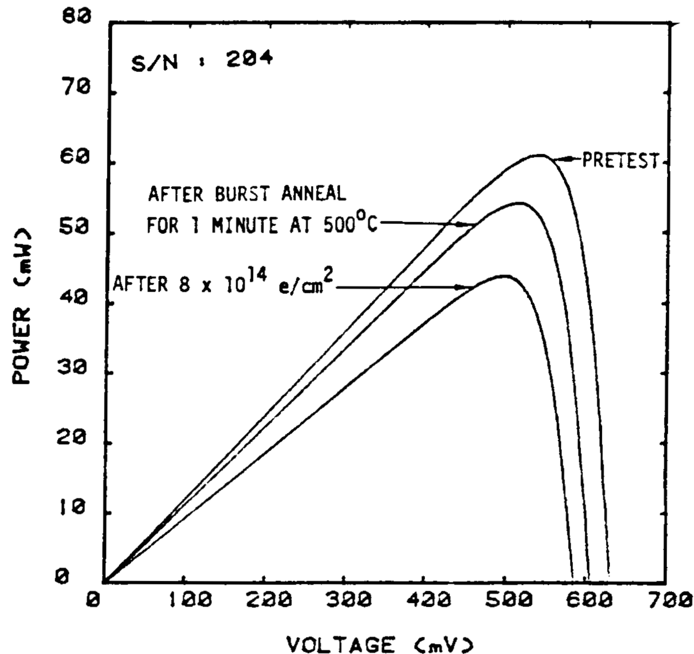

Figure 9. Burst Annealing of 0.3 ohm-cm Cell #204 From High Fluence Level

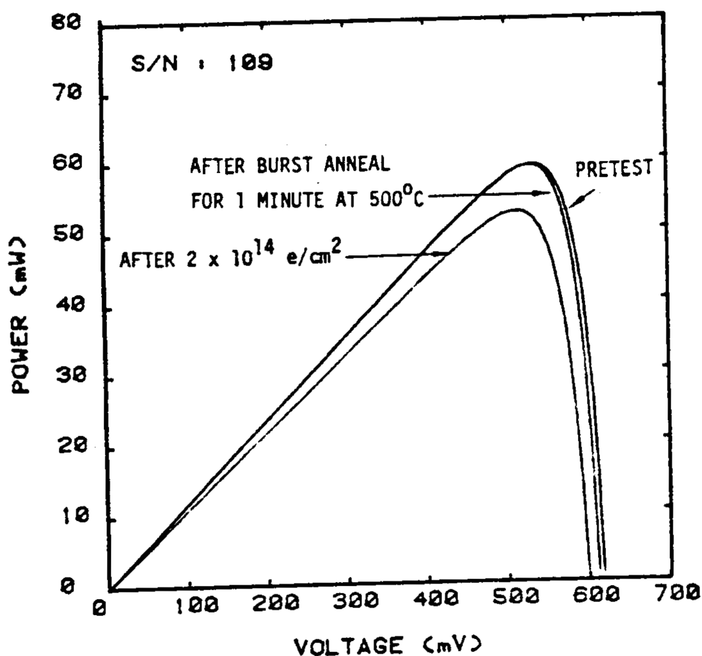

Figure 10. Burst Annealing of 0.3 ohm-cm Cell #109 After Low Electron Fluence

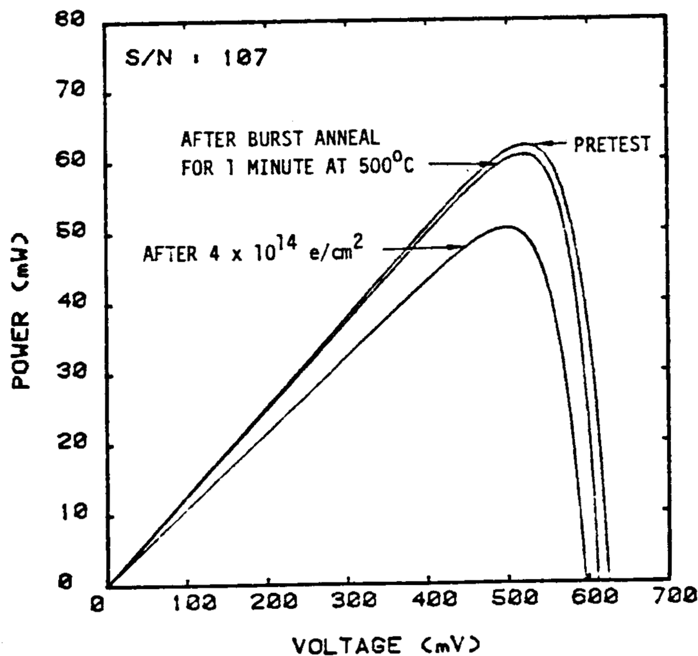

Figure 11. Burst Annealing of 0.3 ohm-cm Cell #107 After Intermediate Electron Fluence

N86-17854

I-V-T ANALYSIS OF RADIATION DAMAGE IN HIGH EFFICIENCY Si SOLAR CELLS*

S. Banerjee, W. A. Anderson, and B. B. Rao
State University of New York at Buffalo
Buffalo, New York

High efficiency surface passivated N^+-P junction solar cells show deterioration in photovoltaic performance when subjected to 1 MeV electron irradiation. This change could be attributed to an increase in the dark saturation current after irradiation. A detailed analysis of the excess current using a thermal spectroscopic method reveals that the recombination mechanisms responsible for this effect can be identified as bulk recombination and space charge recombination through shallow traps. The former of these two mechanisms has a more severe effect and should be taken into account in the design.

INTRODUCTION

High efficiency silicon solar cells are widely used for space applications. Presently, silicon solar cells with efficiency ∿ 16% can be obtained routinely and finely tuned designs can yield even higher efficiencies (ref. 1,2). From time to time, various studies, both in-flight and on ground, are conducted to evaluate the stability of solar cells in a space environment. As a result of extensive research it is now understood that deterioration in photovoltaic performance is caused by a drastic increase in dark saturation current (ref. 3,4) which is evident from the following relationship,

$$V_{oc} = \frac{nkT}{q} [\ell n \frac{J_{sc}}{J_o}] \quad (1)$$

where V_{oc} is the open circuit voltage, J_{sc} is the short circuit current density, J_o is the dark saturation current density, n is the diode ideality factor of the solar cell, and other symbols have their usual meanings. Following this lead, much research is being addressed towards understanding the mechanisms causing enhancement in J_o values in crystalline silicon solar cells (ref. 3).

It is well accepted that the current-voltage characteristics of a solar cell can be in general expressed as a double exponential behavior given by the simple relationship (ref. 3)

$$J = J_{DO} [\exp \frac{qV}{n_1 kT} - 1] + J_{RO} [\exp \frac{qV}{n_2 kT} - 1] \quad (2)$$

where symbols have their usual meanings. The first term on the right is the diffusion current according to the theory developed by Shockley (ref. 5) and the second term on the right is the space charge recombination current given by Sah, et. al. (ref. 6). Equation (2) can be easily modified to incorporate the effect of series resistance (R_s) and shunt reistance (R_{sh}) of the solar cell. Results from different experiments (ref. 4) on N^+/P-P (passivated n^+-p junction) silicon solar cells indicate that it is the first term in eq. (2) which is changed after the cells were subjected to 1 MeV e^- irradiations at room temperature.

To investigate this effect further, dark and illuminated current-voltage characteristics of the aforementioned solar cells were studied as a function of temperature from 100 °K - 375 °K for which a marked increase in dark current was observed after the cells were irradiated. Activation energy plots indicate that under-illumination, diffusion current is the dominant component over much of the temperature range whereas under dark there is an excess current component besides the diffusion current. A simple analysis described elsewhere (ref. 7) was performed to extract this excess current component and the results will be discussed herein.

EXPERIMENTAL CONSIDERATIONS

Device Structure

Devices studied here have been supplied by Dr. Mark Spitzer of Spire Corp., Boston, and are fabricated on 0.3 Ω-cm boron doped silicon obtained from Wacker Chemtronics (standard WASO-grade). An n^+-p junction has been formed by 5 keV $^{31}P^+$ ion-implantation with an average dose of $\sim 2.5 \times 10^{15}$ ions/cm^2 resulting in a junction depth $\lesssim 0.5$ μm and emitter surface concentration $\sim 10^{20}$ cm^{-3}. The entire processing sequence and a schematic of the finished device are shown in reference 8.

Measurement Techniques

Solar cells were initially evaluated for their photovoltaic performance by measuring V_{oc}, J_{sc}, fill-factor (FF) and efficiency (η) at AM1 and AM0 intensity. However, only AM0 intensity parameters have been monitored after successive irradiation steps. Other measurements that were used to assess the cells include spectral response and diffusion length following the method developed by Stokes, et. al. (ref. 9).

Current-voltage characteristics have been measured in dark and under illumination as a function of temperature from 100 °K - 375 °K. Shunt resistance (R_{sh}) has been obtained from the slope of V_{oc}-I_{sc} measurements with very low illumination (ref. 10) performed at different temperatures in the aforementioned range. The series resistance R_s values at different temperatures have been obtained from the dark J-V characteristics using conventional techniques. The results obtained were quite consistent for different cells.

Irradiation Technique

After an initial assessment of the devices, some were subjected to 1 MeV e^- irradiation using a Van de Graff type electron accelerator. Devices were placed on a water-cooled sample holder to avoid any heating during irradiation. The electron beam was rastered across the entire sample holder in order to ensure a uniform irradiation. Irradiation dose was varied from 1×10^{14} e^-/cm^2 - 1×10^{16} e^-/cm^2 increased by an order each time. All the devices were tested for their photovoltaic performance after successive irradiations.

DATA ANALYSIS

The photovoltaic measurements are used as a performance check at different stages of irradiation. The major emphasis is on the current-voltage characteristics in dark and under illumination for which a simple method of analysis will be described. From the dark and illuminated current-voltage characteristics, dark and light ideality factors (n_d and n_ℓ, respectively) and saturation current densities (J_{do} and $J_{\ell o}$, respectively) have been extracted using the straight line portions of the curves at a bias voltage approximately equal to the V_{oc} at each temperature. Using J_{do} and $J_{\ell o}$ values at different temperatures, Arrhenius plots were made to obtain the activation energy.

The analysis of experimental current-voltage behavior is based on a model which can be expressed as (ref. 7),

$$J_{Total} = J_{od} \left[\exp \frac{qV_d}{n_D kT} - 1\right] + J_{Excess} \qquad (3)$$

where J_{Total} is the total measured diode current density, J_{od} is the saturation current density for the diffusion component, V_d is the diode bias voltage, n_D is the ideality factor for diffusion mechanism, and J_{Excess} is the excess current component responsibe for enhancement of J_{Total} from its ideal value. The only assumption made here, to be justified later, is that ideally the total current should have only a diffusion component. Furthermore, J_{Excess} is not given any functional form as in some earlier works (refs. 3,11). Voltage and temperature dependences of J_{Excess} have been studied to obtain the nature of J_{Excess}.

To extract J_{Excess} from the experimental data eq. (3) is modified to incorporate the effect of R_s and R_{sh}. Thus,

$$I_{Total} = I_{od} \left[\exp \frac{q(V - I_{Total} R_s)}{n_D kT} - 1\right] + I_{Excess} + \frac{V - I_{Total} R_s}{R_{sh}} \qquad (4)$$

where V is the terminal voltage and

$$V = V_d + I_{Total} R_s \qquad (5)$$

To calculate I_{Excess} from the experimental data, I_{od} and n_D in eq. (4) were replaced by $J_{\ell o}$ x A and n_ℓ, respectively, where A is the area of the cell. The reason for this change will become aparent in the next section. Finally, J_{Excess} is calculated as I_{Excess}/A. The J_{Excess} thus obtained is plotted as a function of voltage with temperature as a parameter. The results of this analysis will be discussed in the next section.

RESULTS AND DISCUSSION

Typical current-voltage characteristics (in dark) for N^+-P/P silicon solar cells before and after e^- irradiation are shown in Figures 1 and 2, respectively. It is clear from the graphs that the total current density is higher in the latter case. Also, the shape of the curve for low temperatures and intermediate voltage range is different in the two cases due to the fact that in this particular voltage regime, shunt current given by the last term in eq. (4) is the dominant component of the total current especially at the lower temperatures. Therefore, the remaining two terms are masked by this effect. However, after the cells were irradiated by 1 MeV e^- to a dose of 1×10^{16} e^-/cm^2, this particular component is not affected as much as the other two terms i.e., the diffusion and the excess current, hence the slope of the ℓn J vs V is slightly higher than those in Figure 1 for the same voltage regime. As the temperature is raised, the first two terms in eq. (4) become larger than the shunt resistance current and the flat region in the ℓn J vs V curves disappear. The straight line region of these curves near the V_{oc} values at each temperature is used to extract the J_{do} and n_d values. The n_d values obtained vary typically between 1.27 - 1.43 and 1.21 - 2.08 before and after irradiation, respectively, indicating the presence of a mechanism(s) other than diffusion. The J_{do} values obtained from the dark J-V characteristics before and after irradiation show a two orders difference due to a change expected in the diffusion length values. Independent measurements of diffusion length and spectral response support this result. Using the J_{do} values, Arrhenius plots were drawn as shown in Figures 3 and 4 from which activation energies* were typically 0.95 eV and 0.85 eV, respectively. This further suggests that there is a deviation from a purely diffusion mechanism, where activation energy should equal 1.12 eV, which is larger after irradiation.

A similar analysis for the illuminated current-voltage (J_{sc} - V_{oc}) characteristics with a typical plot shown in Figure 5, gives n_ℓ values of 1.04 - 1.10 and 1.04 - 1.12 before and after irradiation, respectively. However a two orders of magnitude difference in $J_{\ell o}$ values were also observed in this case. Following the same arguments as in the case of J_{do}, it is suggested that a bulk recombination current component is responsible for the enhancement of J_{do} and $J_{\ell o}$ values after e^- irradiation. Arrhenius plots using $J_{\ell o}$ values shown in Figures 3 and 4 yield activation energies of 1.18 eV and 1.14 eV before and after irradiation, respectively, suggesting that a diffusion current is the dominant component. It should be noticed that in the latter case this diffusion current is a combination of ideal diode current and the bulk recombination current which has a same temperature and bandgap energy (E_g) dependence as the ideal diode current (ref. 3). Furthermore, it can be inferred that under illumination these solar cells show a near ideal diode behavior due to the fact that photo-carriers fill the traps responsible for space charge recombination mechanism(s), however, it is not possible to identify these mechanisms at this stage of analysis.

* Values obtained are not corrected for the temperature dependence of bandgap energy (E_g).

Figures 6 and 7 show typical excess-current $\ell n\ J_e$ vs V characteristics before and after irradiation, respectively, where excess current components were obtained from eq. (4), and represent recombination current components. From Figure 6 it is obvious that there are two regions with different slopes for each temperature whereas in the case of the cells after irradiation (Figure 7) there are two different temperature regions for which the slopes are entirely different. In the former case the ideality factors in the low slope region are calculated to be closer to 2 while the ideality factors are calculated to be closer to 1 for the higher slope region. Furthermore, the ideality factors increase with decrease in temperature. The J_{eo} (excess saturation current density) obtained for the different regions were used to make Arrhenius plots shown in Figure 8. The lower slope region gives an activation energy of 0.565 eV indicating a recombination through deep traps (ref. 6), whereas the upper slope region yields an activation energy of 0.763 eV indicating a recombination mechanism through shallow traps in the space charge region which corresponds to a trap level approximately equal to 0.706 eV (ref. 3) after correcting for the temperature effect of E_g and the energy difference between $E_g/2$ and intrinsic level E_i. This behavior differs from what has been observed in the previous work (ref. 3) using diffused junctions and can be attributed to incomplete annealing of ion-implantation damage.

A typical Arrhenius plot for the cells after irradiation is also shown in Figure 8. Unlike in the previous case, there are two distinct slopes in different temperature regions. In the higher temperature region, 250 °K - 375 °K, an activation energy of 0.763 eV has been obtained, following the previous procedure, which correspond to a trap level of 0.706 eV. A very low activation energy of 0.124 eV is obtained between 110 - 280 °K. The ideality factors obtained from the $\ell n\ J_e$ vs V plots in this case is closer to 1 at higher temperatures and increases to more than 2 as the temperature is decreased. Variation of ideality factor in N^+-P junction solar cells can be explained by a distribution of traps in the space charge region rather than a single trap level (ref. 11,6). The reoccurrance of the 0.706 eV level as the dominant shallow trap further makes one believe that this is inherent to the implantation. It is possible that there are other shallow traps developed after irradiation, however, if the trap-levels are very closely spaced, it is difficult to identify each of those using such a simple approach.

CONCLUSION

A detailed analysis of current-voltage characteristics of N^+-P/P solar cells indicate that there is a combination of different mechanisms which results in an enhancement in the dark current and in turn deteriorates the photovoltaic performance of the solar cells after 1 MeV e^- irradiation. The increase in the dark current is due to three effects i.e., bulk recombination, space charge recombination by deep traps and space charge recombination through shallow traps. It is shown that the increase in bulk recombination current is about 2 - 3 orders of magnitude whereas space charge recombination current due to shallow traps increases only by an order or so and no space charge recombination through deep traps was observed after irradiation. Thus, in order to improve the radiation hardness of these devices, bulk properties should be preserved.

REFERENCES

1. Spitzer, M. B.; Keaveny, C. J.; Tobin, S. P.; and Milstein, J. E.; "Ion Implanted Silicon Solar Cells with 18% Conversion Efficiency," Proc. 17th Photovoltaic Specialists Conference, Kissimmee, Florida 398-402, 1984.

2. Green, M. A.; Blakers, A. W.; Jiqun, S.; Keller, E. M.; Wenham, S. R.; Godfrey, R. B.; Szpitalak, T.; and Willison, M. R.; "Towards A 20% Efficient Silicon Solar Cell," Proc. 17th Photovoltaic Specialists Conference, Kissimmee, Florida, 386-389, 1984.

3. Wolf, M.; Noel, G. T.; and Stirn, R. J.; "Investigation of the Double Exponential in the Current-Voltage Characteristics of Silicon Solar Cells," IEEE Trans. Electron Dev., ED-24, #4, 419-428, 1977.

4. Anderson, W. A.; Solaun, S.; Rao, B. B.; and Banerjee, S.; "Influence of Design Variables on Radiation Hardness of MINP Solar Cells," Space Photovoltaic Research and Technology Conf., Cleveland, Ohio, 1985.

5. Shockley, W.; "The Theory of P-N Junctions in Semiconductors and P-N Junction Transistors," Bell Syst. Tech. J., 28, 435-489, 1949.

6. Sah, C. T.; Noyce, R. N.; and Shockley, W.; "Carrier Generation and Recombination in P-N Junctions and P-N Junction Characteristics," Proc. IRE, 45, 1228-1243, 1957.

7. Rao, B. B.; Banerjee, S.; Anderson, W. A.; and Han, M. K.; "Excess Currents in MINP Type Solar Cells," IEEE Trans. Electron Dev., ED-32, #4, 817-821, 1985.

8. Spitzer, M. B.; Tobin, S. B.; and Keavney, C. J.; "High Efficiency Ion-Implanted Solar Cells," IEEE Trans. Electron Dev., ED-31, #5, 546-550, 1984.

9. Stokes, E. D.; and Chu, T. L.; "Diffusion Lengths in Solar Cells from Short Circuit Current Measurement," Appl. Phys. Lett., 30, #8, 425-426, 1977.

10. Chan, D. S. H.; and Phang, J. C. H.; "A Method for the Direct Measurement of Solar Cell Shunt Resistance," IEEE Trans. Electron Dev., ED-31, #3, 381-383, 1984.

11. Stirn, R. J.; "Junction Characteristics of Silicon Solar Cells," Proc. 9th Photovoltaic Specialists Conference, Silver Springs, Maryland, 72-82, 1972.

* The work described in this paper was performed in part under the sponsorship and technical direction of International Telecommunications Satellite Organization (INTELSAT). Any views expressed are not necessarily those of INTELSAT.

ORIGINAL PAGE IS
OF POOR QUALITY

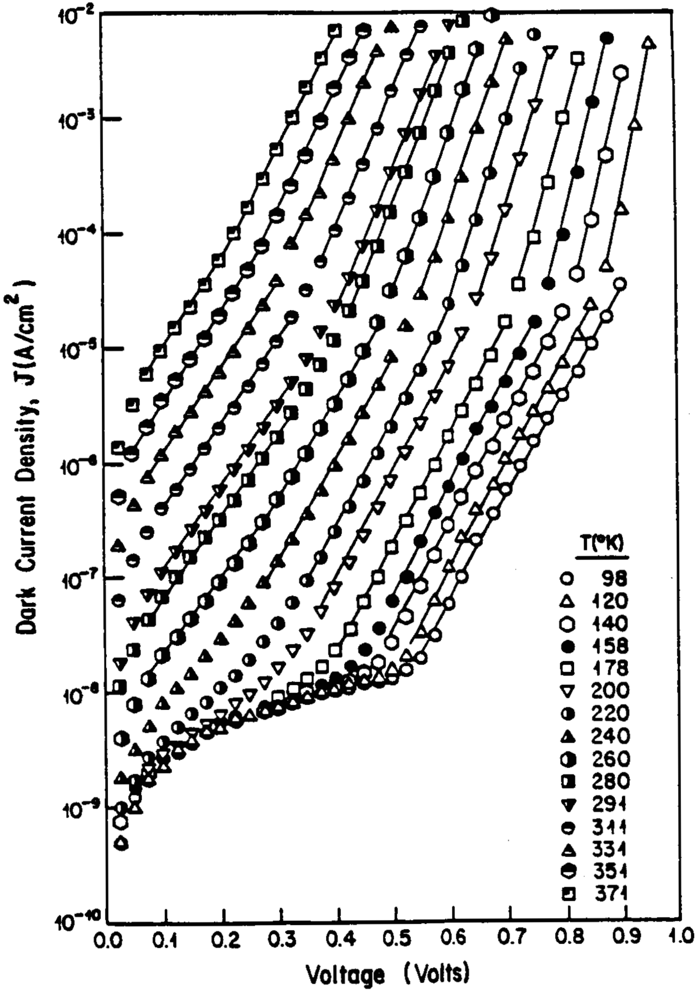

Figure 1. Typical Dark J-V curves before irradiation.

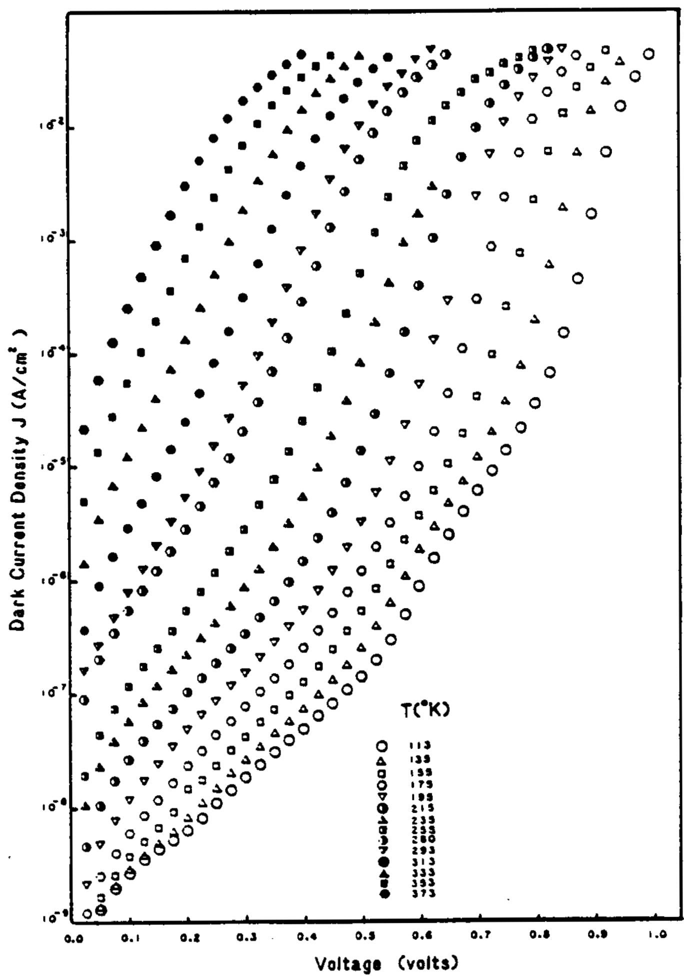

Figure 2. Typical Dark J-V curves after irradiation

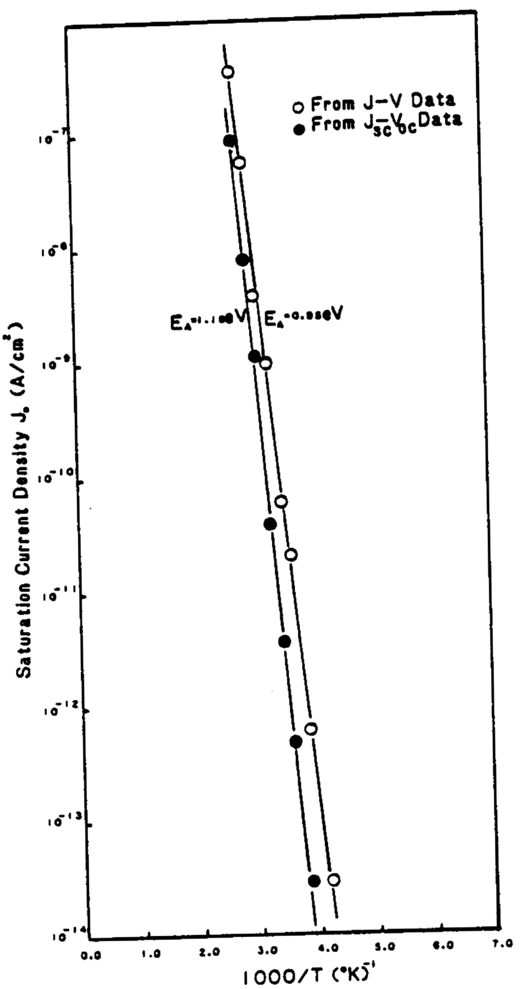

Figure 3. Arrhenius plots before irradiation

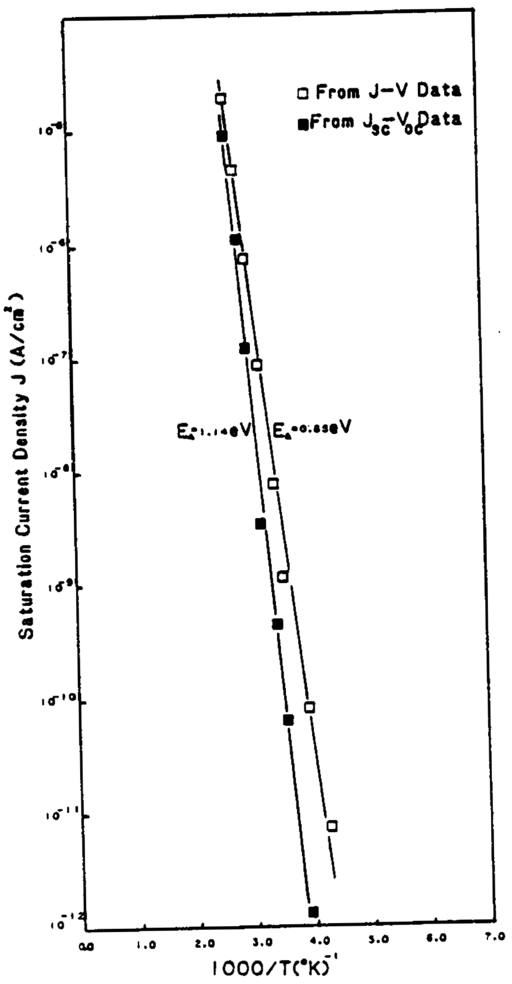

Figure 4. Arrhenius plots after irradiation

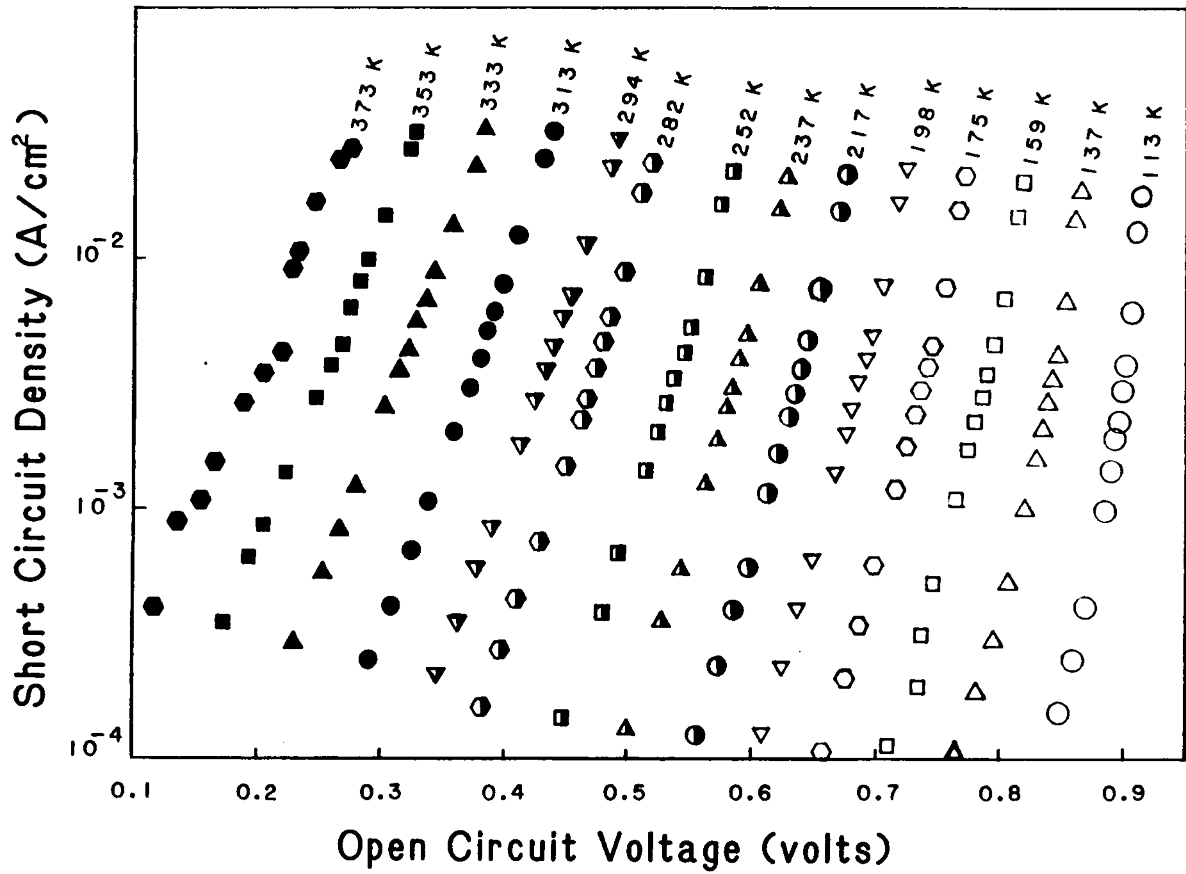

Figure 5. Typical Illuminated Current-Voltage (J_{sc}-V_{oc}) Curves

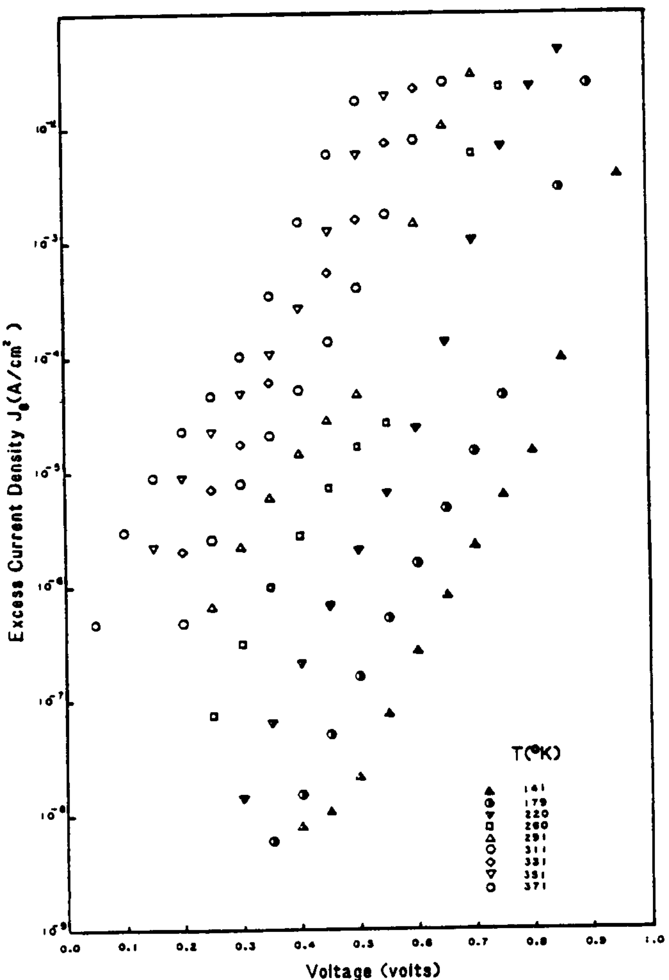

Figure 6. Typical Excess-Current J_e-V Curves Before Irradiation

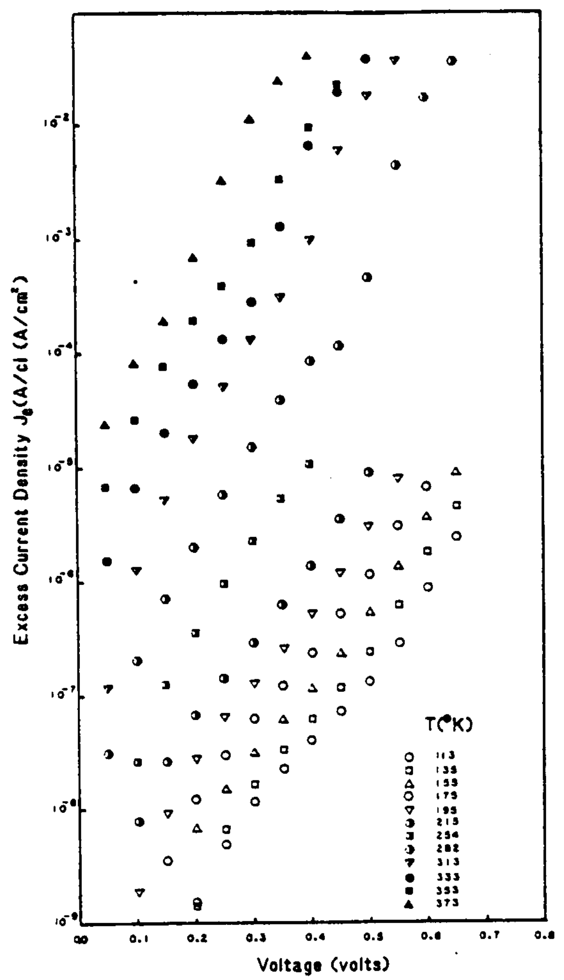

Figure 7. Typical Excess-Current J_e-V Curves After Irradiation

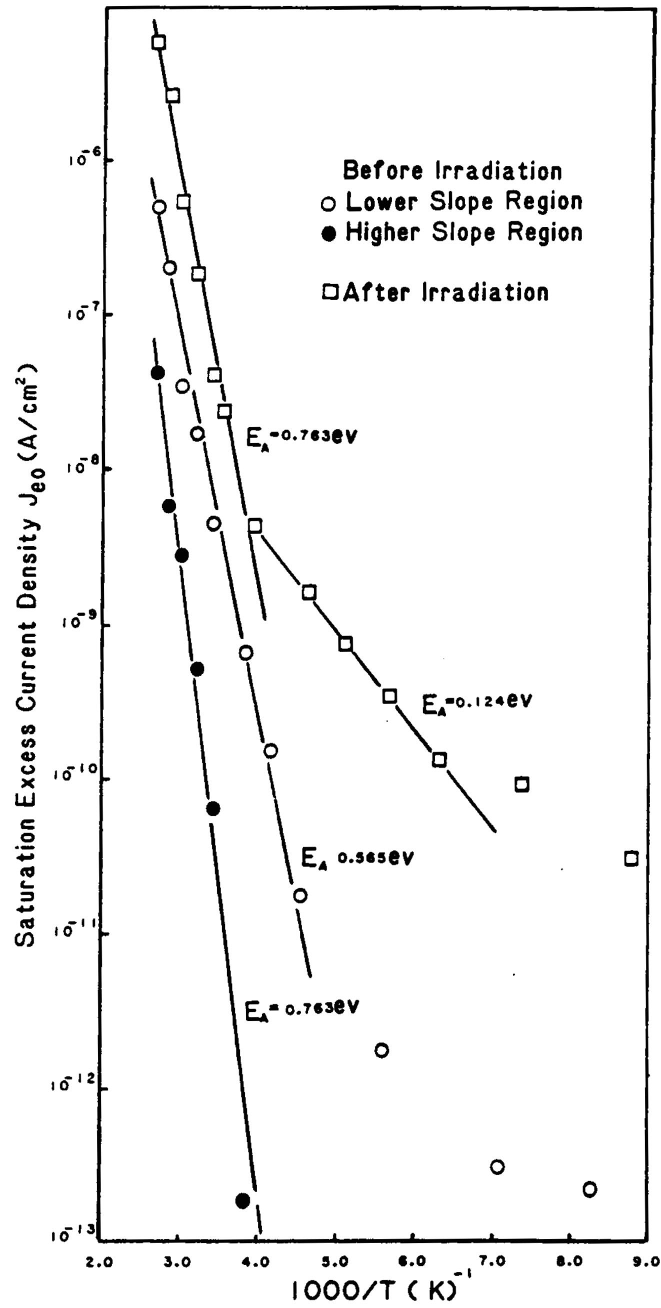

Figure 8. Arrhenius plots for saturation value of Excess-Current Density (J_{eo}).

N86-17855

INFLUENCE OF DESIGN VARIABLES ON RADIATION HARDNESS OF SILICON MINP SOLAR CELLS*

W. A. Anderson, S. Solaun, B. B. Rao, and S. Banerjee
State University of New York at Buffalo
Buffalo, New York

Metal-insulator-N/P silicon (MINP) solar cells were fabricated using different substrate resistivity values, different N-layer designs, and different I-layer designs. A shallow junction into an 0.3 Ω-cm substrate gave best efficiency whereas a deeper junction into a 1-4 Ω-cm substrate gave improved radiation hardness. I-layer design variation did little to influence radiation hardness.

INTRODUCTION

Recent trends in silicon solar cell research point towards increased efficiency. Shallow junction N/P solar cells have been reported with efficiency in the 16 - 18% range (ref. 1,2). The MINP solar cell was introduced by M. A. Green because of the high open circuit voltage. This type of cell utilizes an insulator layer over the shallow N^+ region followed by a low work function metal grid. This combination reduces surface recombination and dark current, while providing an electric field to increase ultraviolet response and efficiency.

Solar cells for extraterrestrial applications must withstand electron, proton, and U.V. radiation while being designed for high efficiency and light weight. Many aspects of space radiation effects and solar cell performance are discussed in the Solar Cell Radiation Handbook published by Jet Propulsion Laboratory and NASA (ref. 3). A preliminary report on MINP solar cells was published in IEEE Transactions on electron Devices (ref. 4). The work reported herein is an extension of the preliminary work in considering different MINP solar cell designs and the resultant influence of 1.0 MeV electron irradiation.

THEORETICAL CONSIDERATIONS

On a theoretical basis, high efficiency cells should have a shallow junction depth (x_j) to minimize recombination of photo-generated carriers, high emitter doping (N_D) to give a favorable electric field profile, and base doping (N_A) of about $7 \times 10^{17}/cm^3$ to give a low value of reverse saturation current (J_{ob}) while perserving a large diffusion length (L_n). These requirements are illustrated by using several rather fundamental equations. The basic dark current density equation is

* The work described in this paper was performed in part under the sponsorship and technical direction of International Telecommunications Satellite Organization (INTELSAT). Any views expressed are not necessarily those of INTELSAT.

PRECEDING PAGE BLANK NOT FILMED

$$J = (J_{oe} + J_{ob})\,(e^{qV/kT}-1) + J_{or}\,(e^{qV/2kT}-1) \qquad (1)$$

$$\text{where } J_{ob} = \frac{qn_i^2 D_n}{N_A L_n} \qquad (2)$$

$$J_{oe} \simeq \frac{qn_i^2 S_p}{N_D} << J_{ob} \qquad (3)$$

$$J_{or} = \frac{qn_i x'}{\tau_o} << J_{ob} \qquad (4)$$

In these equations J_{ob} = base current contribution, J_{oe} = emitter current contribution, J_{or} = space charge layer recombination current contribution, N_A = substrate doping density, L_n = diffusion length in the substrate, S_p = surface recombination velocity, N_D = doping in the emitter assuming a uniform doping profile, x' = space charge layer width, and τ_o = carrier lifetime. The other terms have their usual meaning. Open circuit voltage may also be calculated using

$$V_{oc} = \frac{nkT}{q} \ln \left(\frac{J_{sc}}{J_o}\right) \qquad (5)$$

If $J_{ob} > J_{oe}$ for substrate control, then

$$V_{oc} = \frac{nkT}{q} \ln \left(\frac{J_{sc} N_A L_n}{qn_i^2 D_n}\right) \qquad (6)$$

and with $J_{oe} > J_{ob}$ for emitter control,

$$V_{oc} = \frac{nkT}{q} \ln \left(\frac{J_{sc} N_D}{qn_i^2 S_p}\right) \qquad (7)$$

Equations 3 and 7 clearly show the importance of low surface recombination velocity (S_p) which is achieved in MINP and MNP-P cells by oxide passivation.

EXPERIMENTAL METHODS

The ion-implanted cells were fabricated by implanting ^{31}P at 5 KeV, 2.5 x 10^{15}/cm^2 onto 0.3 Ω-cm p-type silicon substrates. The samples were annealed at 850 °C (30 minutes, N_2 flow) followed by 550 °C for 1 hour to remove the implantation damage. The back ohmic contact was formed by thermally evaporating Al which was sintered at 500 - 600 °C during which time a thin oxide layer was allowed to grow over the entire n-surface for the fabrication of MINP solar cells. Ytterbium, a low work function metal, followed by Cr and Al, was used for the grid contact.

Thermally evaporated SiO_x served as the antireflection coating. In the case of the MNP-P solar cell, a thick (≈ 300 Å) SiO_2 layer was grown over the entire n-surface. Photolithography techniques were used to remove the oxide in regions where the grid contact was to be formed. Examples of these cells are given in Figure 1.

Several values of implantation energy and substrate resistivity were chosen to examine the theoretical predictions and evaluate radiation effects as well which may not have an obvious result. Thus, implant energies of 5, 10 and 30 kV were used with substrate resistivities of 0.1-0.3, 0.3 and 1-4 Ω-cm as shown in Table I. Also, some MNP-P cells were fabricated by bubbling O_2 through trichloroethylene (TCE) (ref. 5) which produces a Cl-containing oxide for improved surface passivation. This should reduce S_p to improve photovoltaic response as predicted by equations 3 and 7.

Completed cells were tested for photovoltaic performance and spectral response after edge isolation by a diamond saw. An ELH quartz halogen lamp was calibrated for AM0 illumination by a p/n junction cell previously tested at the NASA-Lewis Research Center. Spectral response was measured using a Schoeffel GM-100 monochromator from 0.4 μm - 1.0 μm. Samples were irradiated at 1.0 MeV using a Model GS High Voltage Engineering Van de Graff accelerator with a water cooled stage to prevent thermal damage during irradiation. Samples were irradiated at fluence levels of $1.0 \times 10^{14}/cm^2$, $1.0 \times 10^{15}/cm^2$ and $1.0 \times 10^{16}/cm^2$ after which the previously mentioned measurements were conducted.

EXPERIMENTAL DATA

Resistivity and Implant Energy

Two MINP solar cells were fabricated from each of four pairs of the design variables, substrate resistivity (ρ_s) and implant energy (E). These four conditions are clearly listed in Tables I and II. Table I considers diode factor and reverse saturation current density from dark and illuminated I-V curves. Lower n-values and J_o-values are seen when using lower values of ρ_s as predicted by eq. (2). A lower implant energy is also advantageous since lattice damage is reduced and a sharper electric field profile exists to reduce carrier recombination. Spectral response at λ = 0.4 μm is improved for shallow junctions since collection of U.V. photons would be more efficient.

Radiation effects on the subject samples are listed in Table II indicating a greater stability for higher ρ_s. This is not surprising since less dopant reduces radiation interaction with the dopant atom to create fewer recombination centers.

MINP vs MNP-P-O vs MNP-P-T

Cells with a ≈ 22 Å I-layer over the entire surface (MINP) were compared with those having a ≈ 150 Å standard SiO_2 I-layer between grid lines (MNP-P-O) or those having a ≈ 150 Å Cl-containing SiO_2 I-layer between grid lines (MNP-P-T). Table I indicates reduced values of n-factor and J_o for the MNP-P variety since tunneling

through the thin I-layer is eliminated. A statistical comparison of photovoltaic (PV) data for the three kinds of cells, in Table III, indicates the MINP cell to be more efficient due to increased J_{sc} and V_{oc}. This is attributed to perhaps less optical absorption in the I-layer and to reduced recombination under the grid lines in MINP cells. The MNP-P-T cells are slightly more efficient than the MNP-P-O variety which we attribute to reduced surface recombination from Cl in the oxide.

Spectral response data of Figure 2 indicate the relative order of superiority from MINP to MNP-P-T to MNP-P-O which agrees with data in Table III. Effects of 1.0 MeV irradiation, shown in Table IV, do not indicate a significant difference on radiation hardness between these 3 kinds of cells. This points to the substrate as the main point of degradation whereas the surface damage is minimal.

Effects of irradiation on dark I-V data for MINP compared to MNP-P-T cells is given in Figures 3 and 4. At low voltages, MINP cells exhibit an increased current component, which may be due to tunneling and which is quite insensitive to irradiation. The MNP-P-T cell current was sensitive to radiation at low voltages and more sensitive at higher voltages than was the MINP cell. Irradiation effects on spectral response were quite similar for all 3 designs with an example given for the MNP-P-T cell in Figure 5. All cells exhibited a trend towards increased U.V. response after $10^{16} e^-/cm^2$ irradiation which at this time is unexplained. The trend was most prevalent for the pictured MNP-P-T variety.

DISCUSSION

MINP-type cells are quite insensitive to 1.0 MeV e^- irradiation in the U.V. response meaning that the surface damage is minimal. Most reduction in performance is due to bulk damage as evidenced by spectral response data, increased J_o, decreased V_{oc}, and decreased J_{sc}. Diffusion length typically decreases to 8-10 μm at 10^{16} e^-/cm^2 regardless of the starting value. There is a trend in cell efficiency to decrease to a certain value even though original efficiency values may vary. The measured value of L_n in equation (2) accurately predicts the increased J_{ob} which accurately predicts the reduced V_{oc} using equation (5). For example, equation (2) predicts $J_{ob} = 3 \times 10^{-13}$ A/cm^2 before irradiation with $L_n = 250$ μm and 1.2×10^{-11} A/cm^2 after irradiation with $L_n = 6$ μm. This corresponds to a change in V_{oc} from 669 mV to 554 mV which is 115 mV or 17% whereas experimentally we observed an average change of about 105 mV which is 17%. The good agreement between experiment and theory is evidence that bulk damage and not surface damage is the controlling factor in degradation. MINP cell efficiency is maximized for $\rho_s = 0.3$ Ω-cm whereas the radiation tolerance is improved for $\rho_s > 1.0$ Ω-cm. A design trade-off is thus suggested to obtain both high efficiency and radiation hardness. Figure 6 gives a comparison of V_{oc} and efficiency loss due to irradiation for the MINP cell, conventional, and advanced N/P Si cells. The MINP cell is clearly superior in V_{oc} and in efficiency for electron fluence $< 10^{15}$ e^-/cm^2. The proposed new goals for surface passivated cells would predict a performance superior to existing silicon cells. Use of Ga-doped Si (ref. 6) or Li counterdoping (ref. 7) may give an MINP cell with even better performance at high fluence levels.

REFERENCES

1. Young, R. T.; Van der Leeden, G. A.; Sanstrom, R. L.; Wood, R. F.; and Westbrook, R. D.; "High Efficiency Si Solar Cells by Beam Processing," Appl. Phys. Lett., 43, pp. 666-668, 1983.

2. Blakers, A. W.; Green, M. A.; Jiqun, S.; Keller, E. M.; Wenham, S. R.: Godfrey, R. B.; Szpitalak, T.; and Willison, M. R.; "18 - Percent Efficient Terrestrial Silicon Solar Cells," IEEE Electron Device Letters, EDL-5, pp. 12-14, January 1984.

3. Tada, H. Y.; Carter, Jr., J. R.; Anspaugh, B. E.; and Downing, R. G.; Solar Cell Radiation Handbook, Third Edition, JPL Publication, 82-69, 1982.

4. Thayer, M.; Anderson, W. A.; and Rao, B. B.; "Reliability of MINP Compared to MIS, SIS and N/P Silicon Solar Cells Under 1.0 MeV Electron and Environmental Effects," IEEE Trans. on Elec. Dev., ED-31, pp. 619-621, May 1984.

5. Jackson, M. A.; Rao, B. B.; and Anderson, W. A.; "Improved Performance of Surface-Passivated Solar Cells by Chlorine-Containing Oxides," J. Appl. Phys., to appear May 15, 1985.

6. Minahan, J. A.; and Trumble, T. M.; "Electron Irradiated Solar Cells: Cold Crucible (Ga), Float Zone (Ga, B), and Czochralski (Ga, B), Proc. 17th IEEE Photovoltaic Specialists Conference, Orlando, p. 144, 1984.

7. Weinburg, J.; Mehta, S.; and Swartz, C. K.; "Radiation Damage and Defect Behavior in Ion-Implanted Lithium Counterdoped Silicon Solar Cells," Proc. 17th IEEE Photovoltaic Specialists Conference, Orlando, p. 1088, 1984.

TABLE I

INFLUENCE OF FABRICATION CONDITION ON COMPONENTS OF I-V EQUATION

Substrate Resistivity (Ω-cm)	Implant Energy (kV)	Diode Factor		Reverse Saturation Current Density		Spectral Response @ 0.4 μm (mA/mW)
		Dark n_d	Light n_ℓ	J_{od} (mA/cm^2)	$J_{o\ell}$ (mA/cm^2)	
1 - 4	30	1.69	1.28	4.5×10^{-8}	2.5×10^{-9}	0.19
0.1 - 0.3	30	1.80	1.33	1.8×10^{-7}	2.0×10^{-9}	0.20
0.3	10	1.58	1.15	3.0×10^{-9}	4.0×10^{-11}	0.22
0.3	5	1.58	1.17	4.0×10^{-9}	5.0×10^{-11}	0.24
0.3	5*	1.42	1.05	1.2×10^{-9}	9.8×10^{-12}	
0.3	5**	1.39	1.05	7.9×10^{-10}	8.0×10^{-12}	

* MNP-P-O

** MNP-P-T

TABLE II

EFFECT OF 1.0 MeV e^- RADIATION UPON AVERAGE PHOTOVOLTAIC OUTPUT OF MINP CELLS HAVING DIFFERENT SUBSTRATE RESISTIVITY AND IMPLANTATION ENERGY*

OPEN CIRCUIT VOLTAGE, V_{oc}

Cell Numbers	Substrate Resistivity (Ω-cm)	Implant Energy (kV)	Initial Value (V)	After $10^{15} e^-/cm^2$ (V)	After $10^{15} e^-/cm^2$ (% dec.)	After $10^{16} e^-/cm^2$ (V)	After $10^{16} e^-/cm^2$ (% dec.)
694, 697	1 - 4	30	0.575	0.527	8.4	0.490	14.6
714, 716	0.1 - 0.3	30	0.585	0.556	4.9	0.516	11.9
745, 746	0.3	10	0.600	0.563	6.2	0.516	14.0
776, 784	0.3	5	0.618	0.569	7.9	0.516	16.5

SHORT CIRCUIT CURRENT DENSITY, J_{sc}

Cell Numbers	Substrate Resistivity (Ω-cm)	Implant Energy (kV)	Initial Value (mA/cm^2)	After $10^{15} e^-/cm^2$ (mA/cm^2)	After $10^{15} e^-/cm^2$ (% dec.)	After $10^{16} e^-/cm^2$ (mA/cm^2)	After $10^{16} e^-/cm^2$ (% dec.)
694, 697	1 - 4	30	46.2	36.0	22.0	28.6	38.2
714, 716	0.1 - 0.3	30	42.2	30.6	27.4	20.7	51.0
745, 746	0.3	10	42.7	30.5	28.6	21.5	44.6
776, 784	0.3	5	45.7	34.0	25.6	23.4	48.0

EFFICIENCY, η

Cell Numbers	Substrate Resistivity (Ω-cm)	Implant Energy (kV)	Initial Value (%)	After $10^{15} e^-/cm^2$ (%)	After $10^{15} e^-/cm^2$ (% dec.)	After $10^{16} e^-/cm^2$ (%)	After $10^{16} e^-/cm^2$ (% dec.)
694, 697	1 - 4	30	13.5	9.3	30.9	7.1	47.6
714, 716	0.1 - 0.3	30	12.5	8.2	34.2	5.2	57.6
745, 746	0.3	10	14.2	9.4	34.2	5.0	64.3
776, 784	0.3	5	15.6	9.9	36.6	4.8	69.2

* Simulated AMO illumination. All J_{sc} and η-values are based on active area. Total area is about 10% more.

TABLE III

STATISTICAL DATA FOR PHOTOVOLTAIC PERFORMANCE OF MINP, MNP-P-O AND MNP-P-T SOLAR CELLS*

	Cell #	V_{oc} (mV)	J_{sc} (mA/cm^2)	FF	η(%)	Type of Cell
	737	630	35.1	0.70	15.5	MINP
	703	617	36.9	0.72	16.4	MINP
	765	631	36.7	0.80	18.5	MINP
	769	626	35.1	0.80	17.5	MINP
	730	624	35.9	0.72	16.2	MINP
	784	615	35.1	0.77	16.6	MINP
Average		624	35.8	0.75	16.8	
Standard Deviation		6.04	0.76	0.04	0.97	
	720	610	34.8	0.74	15.8	MNP-P-O
	735	624	34.5	0.74	16.0	MNP-P-O
	731	611	32.1	0.73	14.4	MNP-P-O
Average		615	33.8	0.74	15.4	
Standard Deviation		6.38	1.21	0.005	0.71	
	756	622	34.3	0.78	16.6	MNP-P-T
	783	606	34.5	0.78	16.4	
	750	615	31.8	0.74	14.5	
Average		614	33.5	0.77	15.8	
Standard Deviation		6.55	1.22	0.02	0.94	

* Tested with simulated AM1 illumination

TABLE IV

PHOTOVOLTAIC DATA COMPARING MNP-P-O, MNP-P-T, AND MINP

	Open Circuit Voltage			Short Circuit Current Density**			Efficiency**		
	Initial Value (mV)	Change (mV)	% Change (%)	Initial Value (mA/cm^2)	Change (mA/cm^2)	% Change (%)	Initial Value (%)	Change (%)	% Change (%)
	632			47.0			16.3		
735[a] Rad 1*		37	5.8		6.6	14.0		3.0	18.4
Rad 2		72	11.4		13.5	29.0		6.1	37.4
Rad 3		120	19.0		22.6	48.1		9.9	60.8
	604			44.4			14.7		
782[a] Rad 1		20	3.3		5.1	11.5		2.1	14.3
Rad 2		44	7.3		11.9	26.8		5.0	34.0
Rad 3		99	16.4		21.4	48.2		8.9	60.8
	608			46.7			16.4		
783[b] Rad 1		15	2.5		5.1	10.9		2.5	15.2
Rad 2		43	7.1		12.1	25.9		5.7	34.8
Rad 3		97	16.0		22.1	47.3		10.0	60.9
	626			45.7			15.7		
756[b] Rad 1		31	4.9		6.5	14.2		2.9	18.5
Rad 2		61	9.7		12.8	28.0		5.8	36.9
Rad 3		116	18.5		22.5	49.2		9.5	60.4
	602			48.2			15.5		
768[c] Rad 1		22	3.6		7.4	15.4		2.9	18.7
Rad 2		52	8.6		14.4	29.9		6.0	38.7
Rad 3		98	16.3		24.3	50.4		9.4	60.8
	608			43.2			15.0		
785[c] Rad 1		19	3.1		0.8	1.8		1.1	7.3
Rad 2		51	8.4		8.6	19.9		4.7	31.3
Rad 3		102	16.8		18.0	41.7		8.6	57.2

* Rad 1 = 1×10^{14} e^-/cm^2, Rad 2 = 1×10^{15} e^-/cm^2, Rad 3 = 1×10^{16} e^-/cm^2.

** Tested at simulated AMO using a GE-ELH lamp.

(a) MNP-P-O, (b) MNP-P-T, (c) MINP

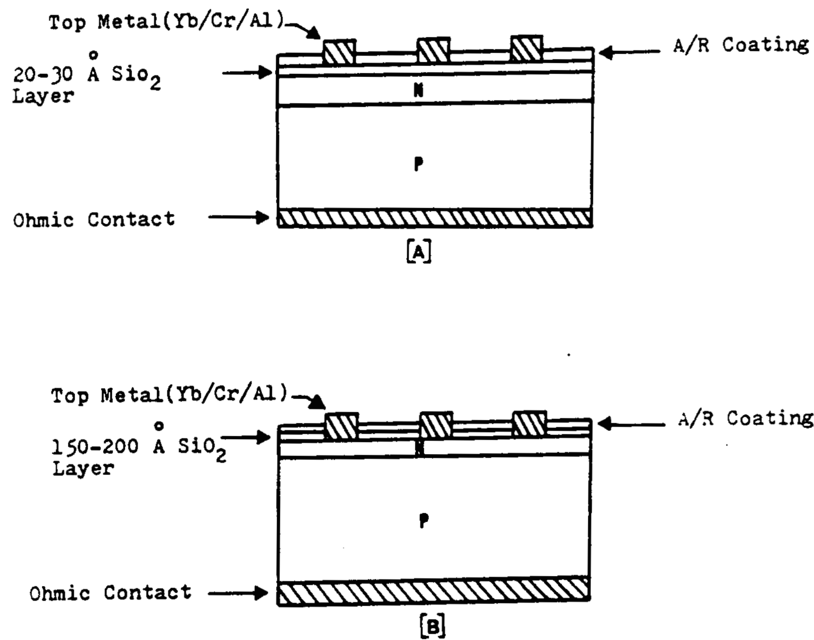

Figure 1: Diagram of [A] MINP and [B] MNP-P cells.

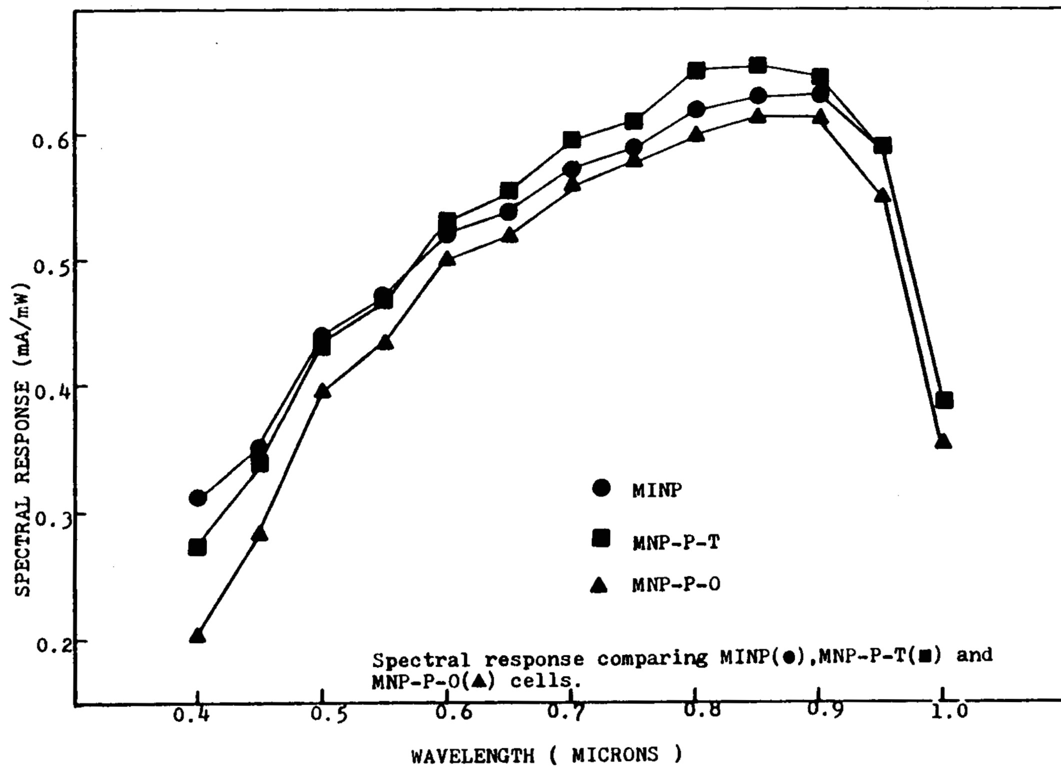

Figure 2: Spectral response of MINP, MNP-P-O, and MNP-P-T cells.

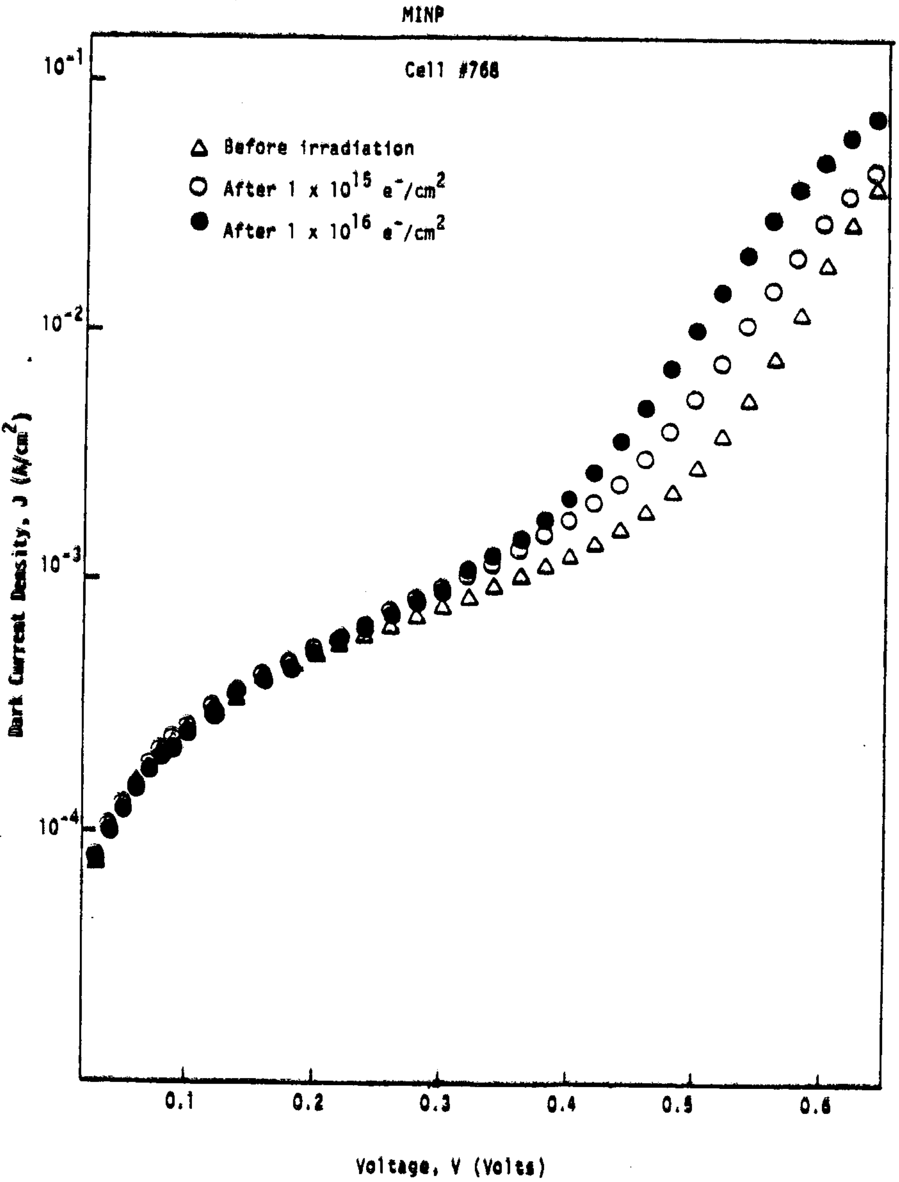

Figure 3: Dark J-V for a MINP cell as a function of e^- irradiation.

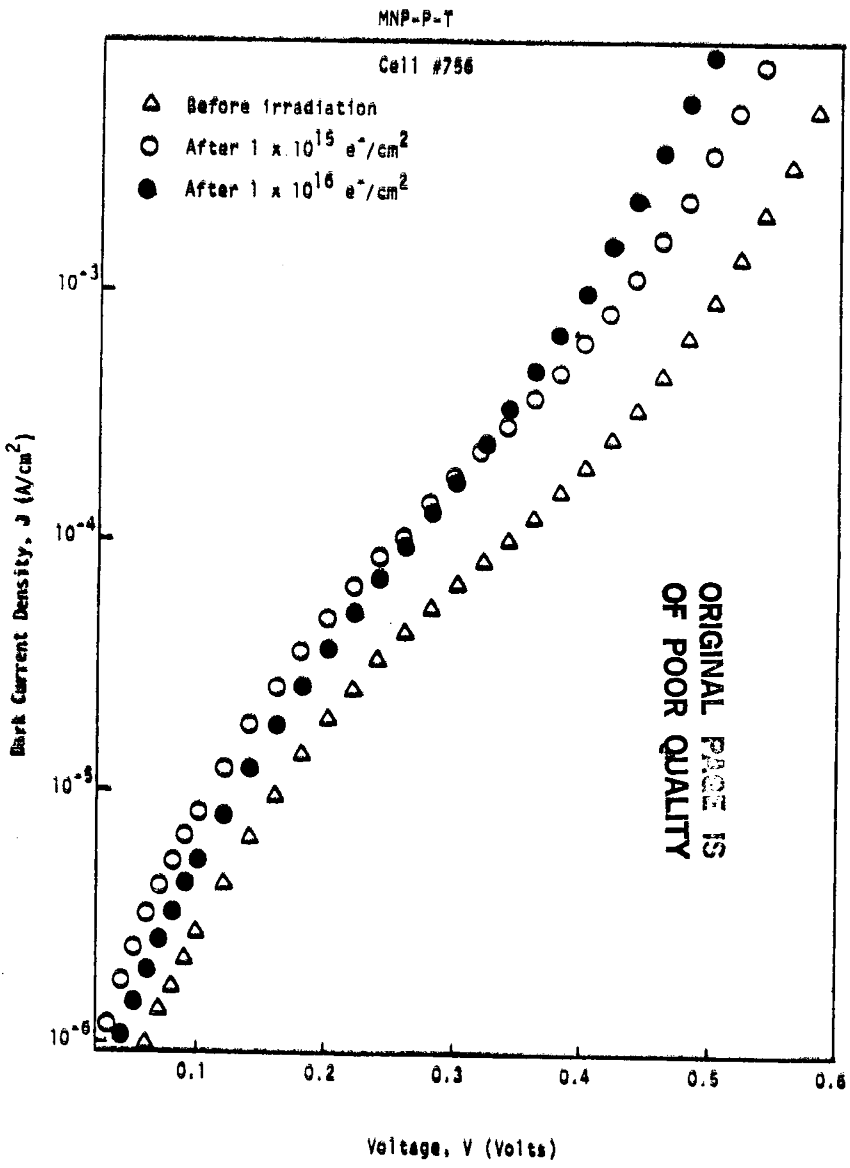

ORIGINAL PAGE IS
OF POOR QUALITY

Figure 4: Dark J-V for a MNP-P-T cell as a function of e^- irradiation.

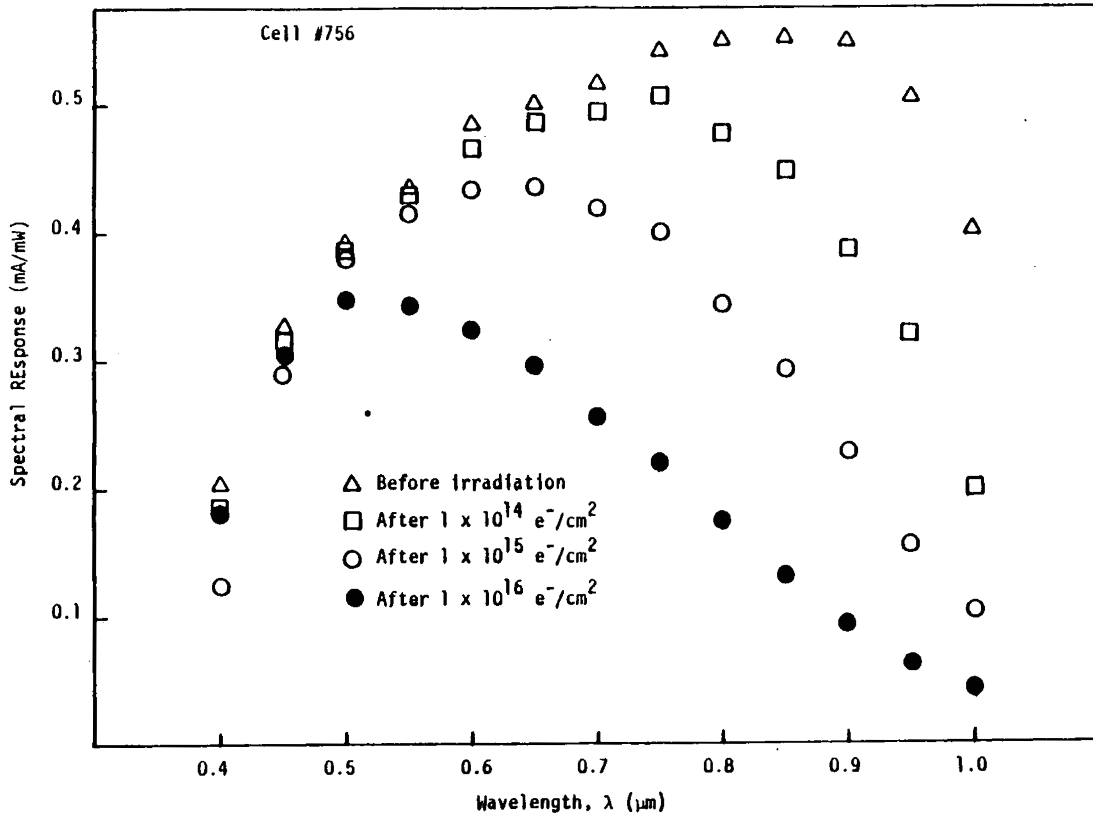

Figure 5: Spectral response of a MNP-P-T cell as a function of e^- irradiation.

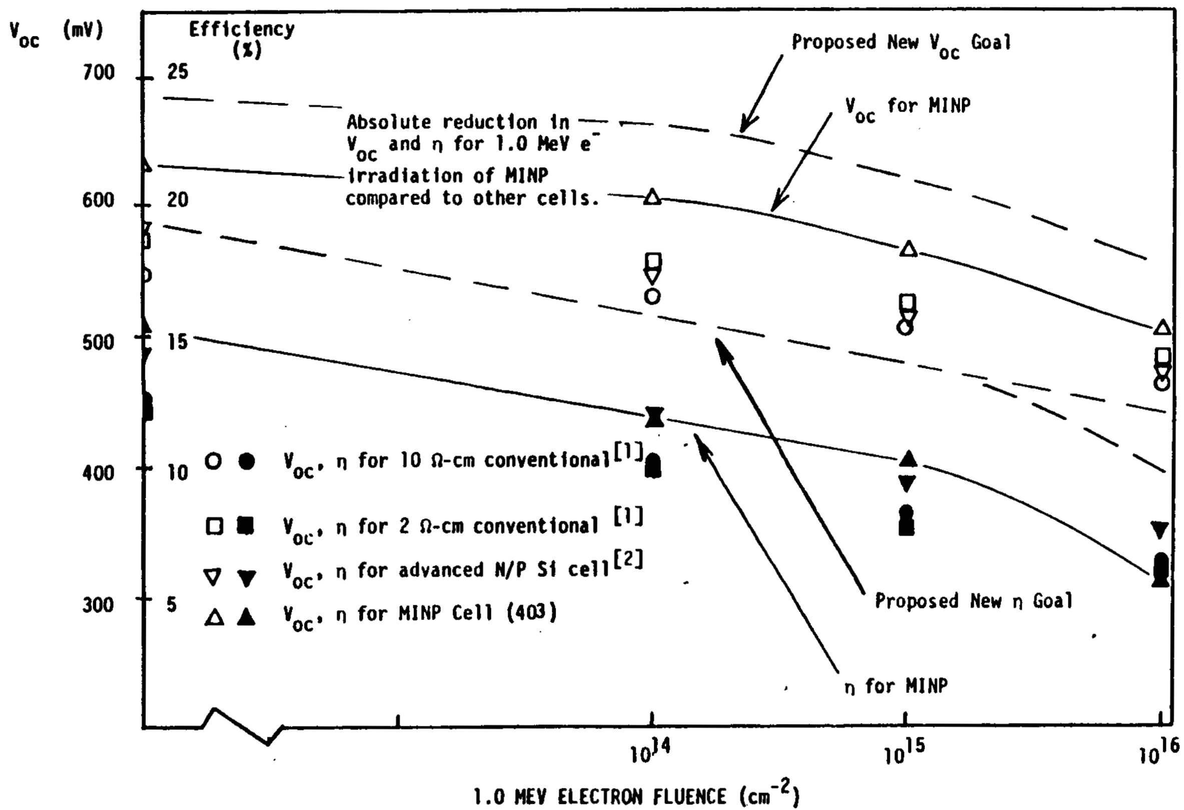

Figure 6: Photovoltaic data variation with e^- fluence for several cells.

N86-17856

E-2706-18

RADIATION DAMAGE IN HIGH-RESISTIVITY SILICON SOLAR CELLS

I. Weinberg, C.K. Swartz, and C. Goradia*
NASA Lewis Research Center
Cleveland, Ohio

High-resistivity silicon solar cells exhibit reduced radiation damage when light is incident on the gridded back surface. Under back illumination, radiation damage decreases as cell resistivity increases; under front illumination, radiation damage increases as cell resistivity increases. Thin (50 μm) back-illuminated cells outperform conventional 10-Ω-cm 50 and 200 μm cells at low 1-MeV electron fluences. However, at higher fluences, the conventional cells exhibit superior radiation resistance. This is attributed to the low BOL diffusion lengths observed in the thin, back-illuminated cell. These results are discussed in terms of injected charge distributions, electric fields in the cell base, and the effects of a dominant boron-oxygen defect.

INTRODUCTION

The motivation for investigating radiation-damage effects in high-resistivity silicon cells stems from the fact that, at low resistivities ($\rho < 20$ Ω-cm), radiation damage decreases as cell resistivity increases. Thus, it was our initial expectation that the effects of radiation could be decreased by increasing the p-base resistivity of n^+pp^+ silicon solar cells. Unfortunately, when, after electron irradiation, the cells were illuminated in the conventional way (light incident on the n^+ side, or front illuminated), the opposite effect occurred (fig. 1). Since the cells were provided with gridded metallic contacts on both the n^+ and p^+ faces, light could be incident on either the front or back. In this respect, for high enough cell resistivities, radiation damage decreased when the cell was back illuminated (ref. 1). This effect was demonstrated previously for a 1250-Ω-cm cell (ref. 1). In the present study, these results are extended to 800- and 8000-Ω-cm, 250-μm thick cells, and performance data are presented for a back-illuminated, 8000-Ω-cm, 50-μm-thick cell. The mechanisms responsible for the observed effects are discussed.

EXPERIMENTAL RESULTS

All cells were n^+pp^+ with gridded front and back contacts and p-base resistivities of 84, 800, 1250, and 8000 Ω-cm, respectively. Details of cell fabrication are contained in reference 1. The behavior of P_{max} after irradiation by 1-MeV electrons is seen in figure 2 for the 84- and 8000-Ω-cm cells. When the difference between front and back illumination is considered, the 84-Ω-cm cell is less degraded when it is front illuminated. However, for the 8000-Ω-cm cell, the degradation is less under back illumination. The data for all cell resistivities, including a 10-Ω-cm conventional cell, are summarized in figure 3. In general, for front-illuminated cells in the resistivity range shown, the radiation-induced degradation increases with cell resistivity. However, for cells with resistivities

*Department of Electrical Engineering, Cleveland State University

above several hundred Ω-cm, the degradation decreases with increasing resistivity when the cells are back illuminated.

DISCUSSION

In order to understand these effects, we first examined the injected minority carrier charge distribution in the cell base. Figure 4 shows the calculated injected charge distribution for a 1250-Ω-cm cell. The charge distributions show that the total injected minority carrier charge is greater when the cell is back illuminated. For the present cells, the increase in carrier concentration varies as much as an order of magnitude. This implies that the cell base resistivity and therefore the ohmic voltage drops are less when the cell is back illuminated, a fact which is confirmed by detailed calculations (ref. 1). The increased charge concentration results essentially from an increase in charge at the pp^+ junction. Schwartz (ref. 2) has shown that an electric field in the cell base tends to draw minority carriers away from the pp^+ junction. We have calculated the electric field using the expression

$$E = \left[q(n\mu_n + p\mu_p)\right]^{-1} \left[J - kT(\mu_n - \mu_p)\left(\frac{d\Delta n}{dx}\right)\right] \qquad (1)$$

where J is total cell current, μ_n and μ_p the electron and hole mobilities, n and p the carrier concentrations in the cells p-base, and Δn the injected minority carrier concentration in the p region. Since $d\Delta n/dx$ changes sign, it is obvious that the second term in brackets will have opposite signs under front and back illumination. Figure 5 shows the results of a calculation of E using the data of figure 4 in equation (1). The field is considerably decreased in the back-illuminated condition. This results in a decreased tendency for the field to draw charge away from the pp^+ junction. The net result is an increased injected charge in the p region and, consequently, a decreased ohmic drop in the cell base under back illumination.

As shown in figure 3, the ohmic drop is the dominant loss mechanism for all but the 10- and 84-Ω-cm cells. Although ohmic effects are nontrivial in the 84-Ω-cm cell, loss in collection efficiency is the dominant cell-degradation mechanism. Hence, this cell performs better under front illumination. For the higher-resistivity cells, the ohmic voltage drop in the p-base, which is the dominant loss mechanism, decreases under back illumination, and less degradation occurs than when the cell is front illuminated. On the other hand, under front illumination, the decrease in cell output with increased resistivity is due to the increased ohmic drop.

The decreased degradation, with increased resistivity, observed under back illumination is due to the decreasing boron concentration in the cell as resistivity increases. Previous results have shown that a radiation-induced boron-oxygen defect is the principal cause of cell degradation (ref. 3) and that the concentration of this defect decreases with decreasing boron concentration (ref. 4). Since ohmic drops are less significant under back illumination, the effects of decreasing boron concentration result in decreased degradation as resistivity increases. Figure 3 shows that this effect begins to saturate at the highest resistivities. Thus, it appears unlikely that the degradation will decrease significantly above 8000 Ω-cm. Obviously, however, for the present cells, as resistivity increases, radiation resistance increases under back illumination.

To optimize this latter effect, we have utilized thin, high-resistivity, back-illuminated cells. The results for an 8000-Ω-cm, 50-μm-thick, back-illuminated cell are presented in figure 6. This figure also shows, for comparison, performanc data for conventional, front-illuminated, thin and relatively thick 10-Ω-cm cells (ref. 5). At the lower fluences, the thin, back-illuminated cell shows improved performance over the conventional cells. At the higher fluences, however, the base diffusion length becomes comparable to cell thickness and degradation occurs. It is noted here that the BOL diffusion length in the thin, 8000-Ω-cm, back-illuminated cell was 120 μm. This length is much lower than the diffusion length (450 μm) we observed at BOL for the thicker high-resistivity cells. Hence, increases in diffusion length for the thin high-resistivity cell should result in superior performance over a greater portion of the fluence range than that shown in figure 6.

CONCLUSIONS

By considering the effects of electric fields in the cell base, and their effect on the ohmic voltage drop, we have contributed to an understanding of the decreased degradation encountered by back-illuminated, high-resistivity cells. Thi effect occurs for cell resistivities above several hundred Ω-cm. Below this resistivity range, loss in collection efficiency begins to dominate and the back illuminated cells show more degradation. The increased degradation for front illumination, with increasing cell resistivity, is attributable to the ohmic voltage drop in the cell base. For the back-illuminated, high-resistivity cells, the decreased degradation with increasing resistivity is attributed to the decreasing importance of the ohmic drop and the decreasing boron content.

From these results, it appears unlikely that one can increase indefinitely the radiation resistance of thick silicon solar cells by increasing the base resistivit above 8000 Ω-cm. However, the present results for the thin, 8000-Ω-cm, back-illuminated cell indicate that, with improved processing, this cell should outperform the conventional cells at higher fluences.

REFERENCES

1. Weinberg, I., Goradia, C., Swartz, C.K., and Brandhorst Jr., H.W., "Radiation damage in front and back illuminated high resistivity silicon solar cells," 16th IEEE Photovoltaic Specialists Conf. pp. 216-221, (1982).

2. Schwartz, R.J., Lundstrom, M.S., and Nasby, R.D., "The degradation of high intensity BSF solar cell fill factors due to a loss of conductivity modulation," IEEE Trans. on Electron Devices, Vol. ED-28, pp. 264-269 (1981).

3. Weinberg, I., Mehta, S., and Swartz, C.K., "Increased radiation resistance in lithium-counterdoped silicon solar cells," Appl. Phys. Lett. 44, pp. 1071-1073, (1984).

4. Mooney, P.M., Cheng, L.J., Suli, M., Gerson, J.D., and Corbett, J.W., "Defect energy levels in boron-doped silicon irradiated with 1 MeV electrons," Phys. Rev. B, pp. 3836-3843, (1977).

5. Tada, H.Y.; Carter, Jr., Anspaugh, B.E.; and Downing, R.G.: Solar cell radiation handbook. 3rd Edition, JPL-PUB-82-69, Jet Propulsion Laboratory, 1982.

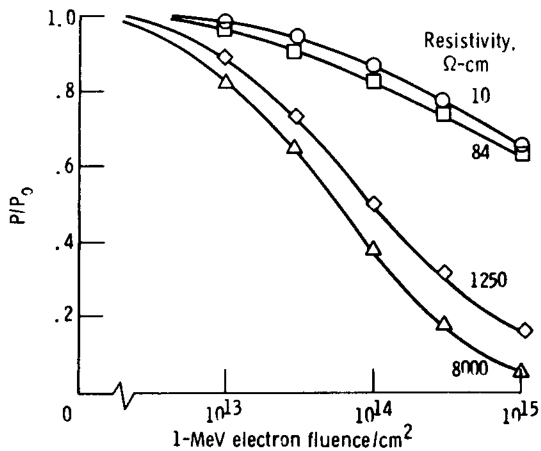

Figure 1. - Normalized maximum power for front-illuminated cells. Thickness, 250 μm.

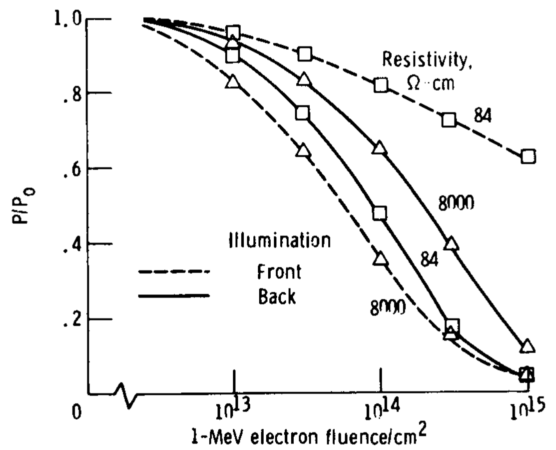

Figure 2. - Normalized maximum power for front- and back-illuminated high-resistivity cells.

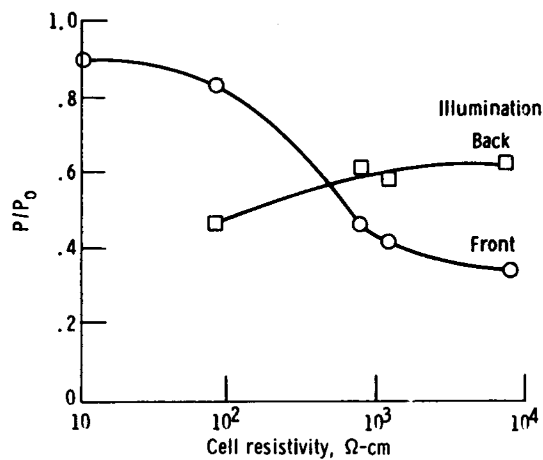

Figure 3. - Normalized maximum power for n^+pp^+ back- and front-illuminated cells after 1-MeV electron irradiation. Fluence, 10^{14}/cm^2; thickness, 250 μm.

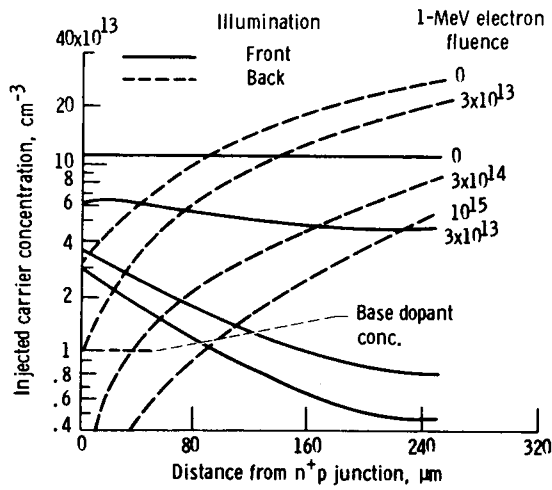

Figure 4. - Injected minority carrier concentration in p region of 1250 Ω-cm cell.

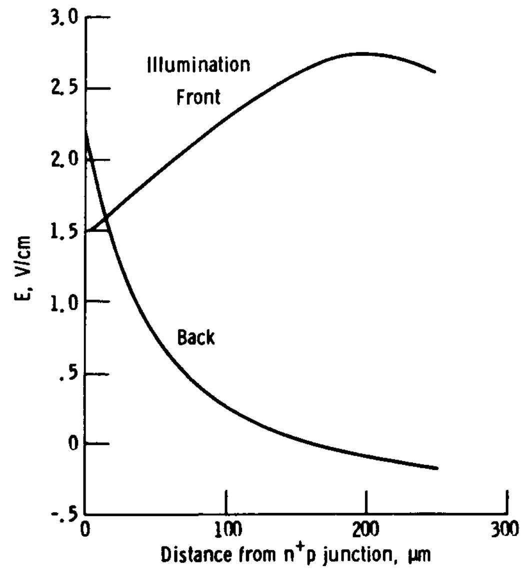

Figure 5. - Calculated electric fields in cells p region Resistivity, 1250 Ω-cm; thickness; 250 µm.

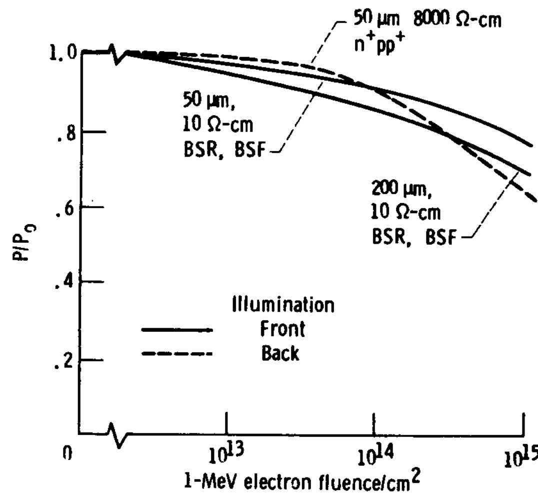

Figure 6. - Comparison of thin, back-illuminated, high-resistivity silicon cell with conventional cells.

N86-17857

PROTON RADIATION EFFECTS ON $CdS/CuInSe_2$ THIN FILM SOLAR CELLS

H. Dursch, W. Chen, and D. Russell
Boeing Aerospace Company
Seattle, Washington

Previous studies have shown that $CdS/CuInSe_2$ solar cells have an inherent tolerance to irradiation by 1 MeV electrons up to at least 2×10^{16} electrons/cm^2. Because of the unknown tolerance of $CuInSe_2$ cells to proton irradiation, the following test was performed at Boeing Radiation Effects Laboratory.

Eleven, unencapsulated, 1 cm^2 cells deposited on alumina substrates were irradiated with 1 MeV protons at normal incidence. The cells were exposed to six fluences ranging from 2.5×10^{10} protons/cm^2 to 5.0×10^{13} protons/cm^2. After each interval of exposure, the cells were removed from the radiation chamber to undergo current/voltage (I-V) characterization. Results show that none of the cells' electrical characteristics exhibited any degradation up to and including a fluence of 1×10^{11} protons/cm^2. At fluences greater than this, the damage to the $CuInSe_2$ cells' V_{OC} and fill factor (FF) was more severe than that exhibited by the I_{SC}. The $CuInSe_2$ cells proved to be approximately a factor of 50 more resistant to 1 MeV proton irradiation than silicon or gallium arsenide cells previously reported (reference 1). Annealing of a $CuInSe_2$ cell at 225°C for six minutes restored it to within 95% of its initial efficiency.

INTRODUCTION

Polycrystalline thin film $CdS/CuInSe_2$ solar cells have been undergoing development in our laboratory since 1976. Air mass-1 (AM 1) photovoltaic conversion efficiencies of 11% have been achieved on 1 cm^2 cells with anti-reflection coating. Monolithic modules of 20 cm^2 area comprised of two series connected cells and 91 cm^2 area comprised of four series connected cells have exhibited AM 1 efficiencies of 8.0% and 6.1% respectively without anti-reflection coating. The 20 cm^2 modules have been encapsulated with ethylene vinyl acetate (EVA) and glass, and efficiencies of 9.2% have been achieved. These cells require such small amounts of material that with the use of lightweight substrates and superstrates, power-to-weight ratios of over 350 W/kg can be achieved.

Because of the potential for space power application, studies to characterize the $CuInSe_2$ cell in the space environment were performed. Cells were irradiated by 1 MeV electrons up to a fluence of 2×10^{16} electrons/cm^2 with no loss of efficiency. Reference 2 describes the results of a similar effort conducted at JPL on $CuInSe_2$ cells with the same results. To further characterize the $CuInSe_2$ cells, 1 MeV proton radiation testing was performed in our laboratories. This paper describes the results of that test.

PRECEDING PAGE BLANK NOT FILMED

EXPERIMENTAL

Cell Description - Figure 1 shows a schematic cross-section of the completed $CuInSe_2$ cell structure. The alumina substrate is metalized with a molybdenum conductor film. A $CuInSe_2$ film of 3-4 μm is deposited by simultaneous elemental evaporation onto the substrate which is heated to 350°C and 450°C. Following the selenide deposition, a 3 μm film of CdS is evaporated onto the substrate which is heated to 200°C. The semiconductor films are then patterned and an aluminum grid deposited to complete the cell structure. The details of the film properties and deposition processes have been discussed in greater detail elsewhere (reference 3).

To provide a good statistical sampling, eleven 1 cm^2 cells with efficiences ranging between 7.7-9.6% (AM 1) were irradiated. Two other cells with equivalent efficiencies were used as control cells. One cell was kept in the laboratory and the other cell was placed in the radiation chamber, but shielded from the proton beam. These two cells were used to determine if there were effects other than proton irradiation causing changes in cell performance. Both cells were characterized at the same intervals as the other eleven. These two cells retained their initial I-V characteristics throughout the duration of the proton test.

Proton Irradiation Techniques - The proton radiation testing was performed using a Dynamitron accelerator as the source of 1 MeV protons. The proton beam is directed into the vacuum chamber by a beam handling system that includes 90° momentum analysis and quadrupole beam focusing. The proton beam passes through a high purity aluminum foil after entering the vacuum chamber. The scattering by this foil improves the beam uniformity and provides the desired beam profile at the sample plane.

The beam uniformity is determined by rotating a Faraday cup across the sample plane and recording the output vs. position (figure 2). The variation of proton flux across the mounted cells was less than 4%. The required current from the accelerator is controlled by a second Faraday cup mounted in the sample plane.

The cells were exposed to 1 MeV proton fluences of 2.5×10^{10}, 1.0×10^{11}, 1.0×10^{12}, 5.0×10^{12}, 1.0×10^{13} and 5.0×10^{13} protons/cm^2. All cells were irradiated at normal incidence. After each interval of exposure the cells were removed from the vacuum chamber to undergo I-V characterization. All characterization tests were performed within three hours of irradiation.

RESULTS AND DISCUSSION

Figure 3 shows the effects of 1 MeV proton radiation averaged over the eleven $CuInSe_2$ cells. Also shown are silicon and gallium arsenide cells that were previously reported (reference 1). The silicon cells were 10 ohm-cm, 200 microns thick with dual anti-reflection coatings and aluminum back-surface reflectors. The GaAs cells were made with the liquid phase epitaxy process incorporating GaAlAs windows. From figure 3 it is determined that $CuInSe_2$ cells are approximately a factor of 50 more resistant to 1 MeV protons than GaAs and Si cells.

Figure 4 shows the I-V characteristics of an individual cell before and after irradiation at fluences of 1.0×10^{13} and 5.0×10^{13} protons/cm^2. Figure 5 shows the average degradation of the I_{sc}, V_{oc} and FF for the eleven cells vs. increasing proton fluence. The main cause of the cells' degradation was decreasing V_{oc} and

FF. This indicates that the damage to $CuInSe_2$ cells occurs near the junction of the cell and, therefore, raises the dark current which lowers the V_{OC} and FF. In contrast, the main cause of degradation of the Si and GaAs cells is the decreasing I_{SC} which tends to be a bulk material problem.

Initial spectral response measurements were taken, but due to negligible degradation of the I_{SC}, no follow up measurements were taken. Annealing experiments were performed at 225°C. After a short duration of 6 minutes, cell efficiency was restored from 13% to 95% of its initial value. No attempt was made to optimize the annealing parameters.

CONCLUSIONS

The $CuInSe_2$ cell proved to be approximately a factor of 50 more resistant to 1 MeV protons than Si or GaAs cells. The cell had previously been proven to be inherently stable to 1 MeV electrons up to a fluence of $2 \times 10^{16} e/cm^2$. Combined with potential of high specific power, $CuInSe_2$ cells show an excellent potential for generating electric power in space applications.

Detailed characterization of the proton damage as a function of proton energy and fluence is needed to determine the damage mechanism. Because the damage appears to take place at the junction, redesigning the cell window layer by changing thickness or material could lead to further enhancement of the cell radiation hardness.

REFERENCES

1. Anspaugh, B. E. and Downing, R. G.: Radiation Effects in Silicon and Gallium Arsenide Solar Cells using Isotropic and Normally Incident Radiation, Proc. 17th IEEE Photovoltaic Specialist Conference, 1984, p. 23.

2. Gay, C. F. et al: Radiation Effects on Thin Film Solar Cells, Proc. 17th IEEE Photovoltaic Specialist Conference, 1984, p. 151.

3. Mickelsen, R. A. and Chen, W. S.: Development of a 9.4% Efficient Thin Film $CuInSe_2$/CdS Solar Cell, Proc. 15th IEEE Photovoltaic Specialist Conference, 1981, p. 800.

ORIGINAL PAGE IS
OF POOR QUALITY

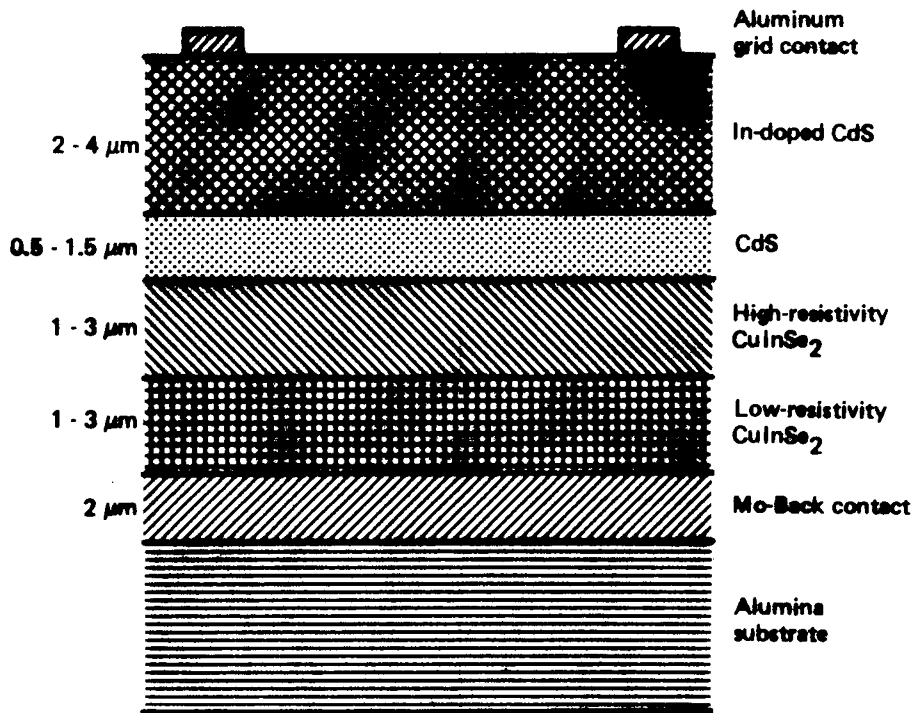

Figure 1. CdS/$CuInSe_2$ Thin-Film Cell Structure

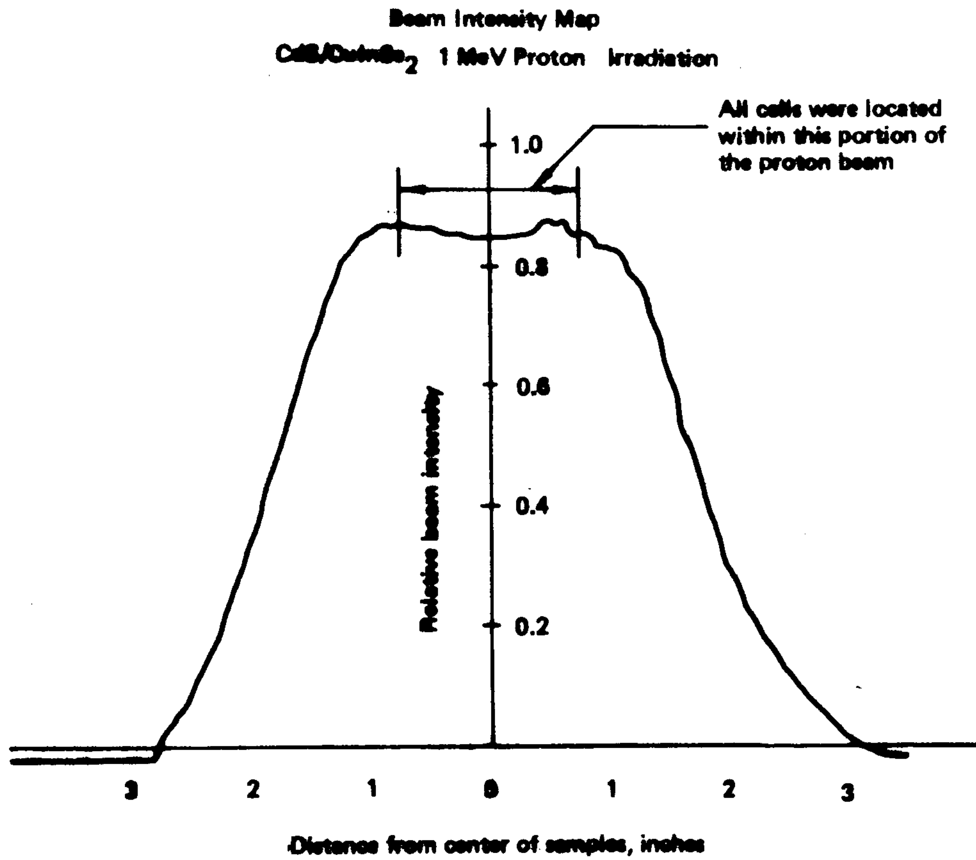

Figure 2. Proton Beam Intensity Map

ORIGINAL PAGE IS
OF POOR QUALITY

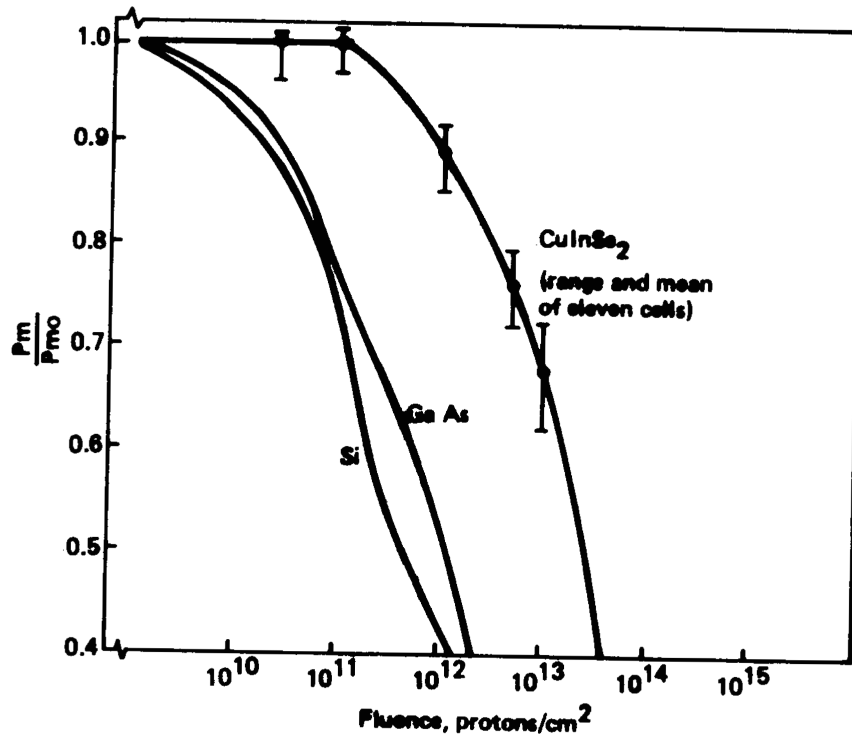

Figure 3. Degradation of Thin-Film $CdS/CuInSe_2$ Solar Cells as Function of 1 MeV Proton Fluence

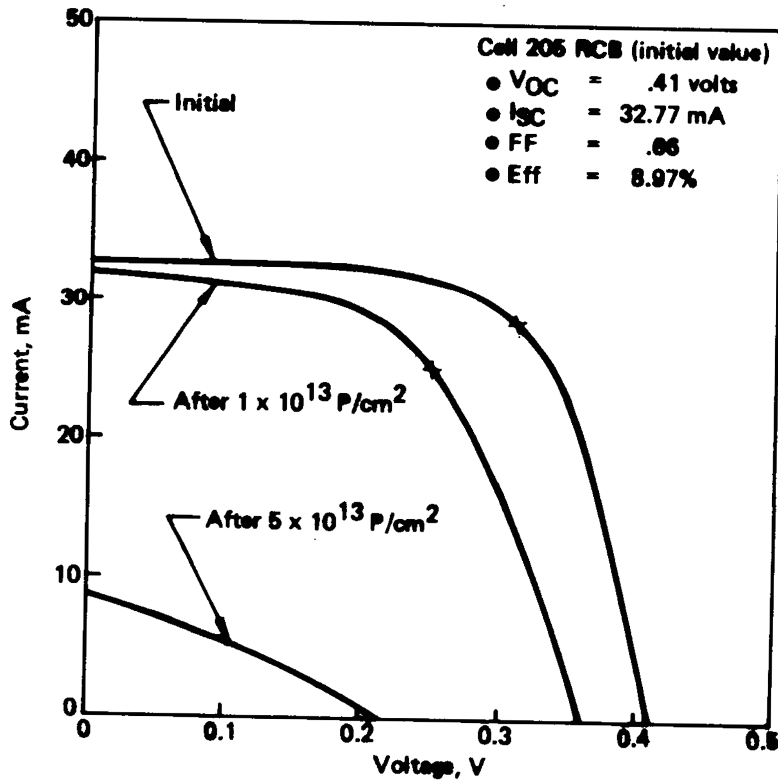

Figure 4. Degradation of a $CdS/CuInSe_2$ Solar Cell Under 1 MeV Proton Irradiation

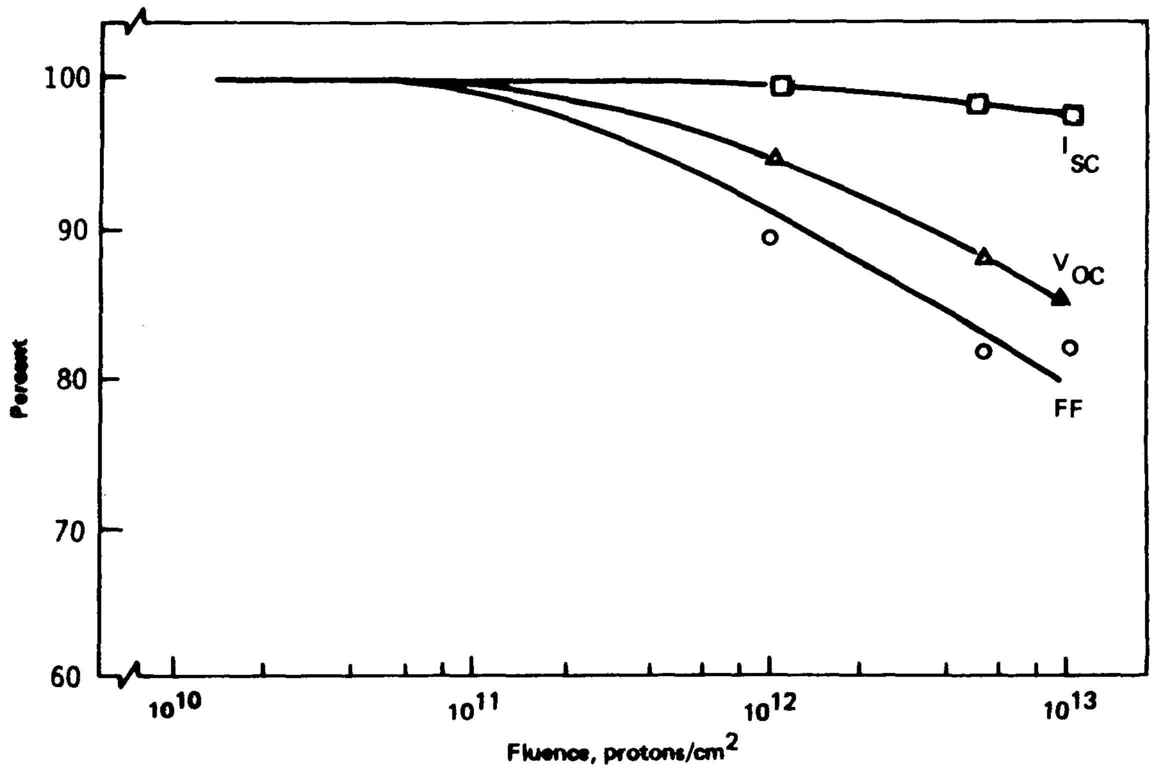

Figure 5. Degradation of Photovoltaic Parameters of Thin-Film CdS/CuInSe$_2$ Solar Cells as Function of 1 MeV Proton Fluence

N86-17858

DLTS ANALYSIS OF RADIATION-INDUCED DEFECTS IN ONE-MEV ELECTRON IRRADIATED GERMANIUM AND $AL_{0.17}GA_{0.83}AS$ SOLAR CELLS*

Sheng S. Li and C. G. Choi
University of Florida
Gainesville, Florida

R. Y. Loo
Hughes Research Laboratories
Malibu, California

The purpose of this paper is to investigate the radiation-induced deep-level defects in one-MeV electron-irradiated germanium and $Al_xGa_{1-x}As$ (with x = 0.05 and 0.17) solar cell materials using the Deep-level Transient Spectroscopy (DLTS) and C-V techniques. Defect and recombination parameters such as defect density and energy levels, capture cross sections and lifetimes for both electron and hole traps were determined from these measurements. In this study, both the germanium and AlGaAs p/n junction cells were irradiated by one-MeV electrons with fluences of 10^{14}, 10^{15}, and 10^{16} e/cm^2. DLTS, I-V, and C-V measurements were then performed on these cells. The results are summarized as follows: (1) For the irradiated germanium samples, the dominant electron trap was due to the E_c - 0.24 eV level with density around $4x10^{14}$ cm^{-3}, independent of electron fluence; its origin was attributed to the vacancy-donor complex defect formed during the electron irradiation. In addition two new hole traps with activation energies of E_v + 0.10 and 0.16 eV were observed in the irradiated samples; these two hole traps were attributed to the divacancy-donor complex defects with densities varying from 1.5 to $4x10^{14}$ cm^{-3}. (2) As for the one-MeV electron irradiated $Al_{0.17}Ga_{0.83}As$ sample, two dominant electron traps with energies of E_c-0.19 and -0.29 eV were observed; the density for both electron traps was also found to remain nearly constant, independent of electron fluence. The results of this study show that one-MeV electron irradiation creates very few or no new deep-level traps in both the germanium and $Al_xGa_{1-x}As$ cells, and as such they are suitable for fabricating the radiation-hard high efficiency multijunction solar cells for space applications.

INTRODUCTION

Considerable interests in developing high efficiency cascade junction solar cell using materials such as $Al_xGa_{1-x}As$, GaAs, and germanium or $In_xGa_{1-x}As$ have been reported recently [1-5]. The cascade junction solar cell is particularly attractive for space power generation since it has potential to achieve AMO efficiency of 30 % or higher by using a triple junction structure. To design a

* Research supported by Air Force Aeropropulsion Lab., WPAFB, through Universal Energy Systems Inc., under subcontract No.F33615-81-C-2058.

radiation-hard triple junction solar cell for space power generation, the radiation induced defects in materials to be used for the cascade solar cell fabrication should be studied. Although extensive studies of the radiation damage in GaAs irradiated by one-MeV electrons and low energy protons have been reported in theliterature [6-10], only limited information concerning the radiation induced defects in $Al_xGa_{1-x}As$, $In_xGa_{1-x}As$ and germanium is available at present [11-16]. In order to obtain a detailed information concerning the radiation induced defects in germanium and $Al_xGa_{1-x}As$ for cascade junction solar cell applications, a systematic study of the deep-level defects vs electron or proton fluence must be conducted. In this paper we report the results of our DLTS analysis of the one-MeV electron irradiation induced deep-level traps in germanium and $Al_{0.17}Ga_{0.83}As$ p-n junction cells for different electron fluences. In addition the I-V and C-V measurements were also performed to determine the recombination mechanisms in these electron irradiated samples. From the results of our C-V and DLTS analysis and those reported in the literature, the possible physical origins for the observed electron and hole traps in both germanium and $Al_{0.17}Ga_{0.83}As$ materials are discussed.

EXPERIMENTAL

The $Al_xGa_{1-x}As$ p-n junction solar cells used in this study were fabricated by using infinite solution melt liquid phase epitaxial (LPE) technique for two different aluminum compositions (x = 0.05 and 0.17), while the germanium p-n junction cells were fabricated by using alloying process. The background dopant density for the AlGaAs cells is around 10^{17} cm^{-3}, and is about 10^{15} cm^{-3} for the germanium cells. The one-MeV electron irradiation was performed at room temperature on these cells using three different electron fluences. The I-V, C-V, and DLTS measurements were performed on both germanium and AlGaAs samples before and after electron irradiation, and the results are presented next.

RESULTS AND DISCUSSION

The arsenic-doped germanium p-n junction cells were irradiated by one-MeV electrons with fluences of 10^{14}, 10^{15} and 10^{16} cm^{-2} in the room temperature. DLTS and C-V measurements were made on these samples to determine the defect parameters such as activation energy, defect density, capture cross sections and the lifetimes for both the electron and hole traps. The results are summarized in table 1. Fig. 1 and Fig. 2 show respectively the DLTS scans of electron and hole trap in the unirradiated germanium cells. The E_c - 0.26 eV electron trap and the E_v + 0.33 eV hole trap observed in the unirradiated cells were attributed to the copper impurity related defect [15], and the density for both trap levels is nearly identical (3.8×10^{14} cm^{-3}). Fig. 3 shows the DLTS scan of the E_v + 0.26 eV hole trap observed in the 10^{15} e/cm^2 irradiated sample. The annealing experiments were performed on these germanium samples, and the results are shown in Fig. 4 through Fig. 6. Fig.4 shows the effect of thermal annealing on the E_c - 0.27 eV electron trap observed in the 10^{15} cm^{-2} electron irradiated cell. In this sample, the thermal annealing was carried out by repeating the DLTS scans between 77 and 435 K. Significant reduction in defect density was observed in the first three annealing cycles, and showed little or no reduction in defect density after the fifth annealing cycle. Fig. 5 shows the DLTS scans of E_c - 0.26 eV electron trap observed in the unirradiated germanium sample. The effect of thermal annealing (annealed at 162 ^{o}C for 12 hours) is negligibly

small in this case, indicating that this electron trap is indeed the impurity (Cu^{3-}) related defect. Fig.6 shows the effect of thermal annealing on the hole traps observed in the 10^{14} cm^{-3} electron irradiated sample. The E_v + 0.10 eV hole trap level was disappeared after 45 min. of annealing at 162 °C. The results of our DLTS measurements on the irradiated germanium samples clearly show that one-MeV electron irradiation induced defects can be reduced drastically via low temperature (less than 200 °) thermal annealing process. The results show that germanium possesses good radiation resistance; this is consistent with our I-V data and those reported by others in the literature. Fig. 7 shows the current-voltage relationship under the forward bias conditon for four germanium cells irradiated by different electron fluences. The results show little or no correlation between the dark forward current and the electron fluence in these irradiated germanium samples.

The DLTS analysis of deep-level defects in one-MeV electron irradiated $Al_x Ga_{1-x}As$ with x=0.05 and 0.17 was also carried out in this study. Fig.8 shows a typical DLTS scan of electron traps observed in the one-MeV electron irradiated AlGaAs cell. Defect parameters deduced from our C-V and DLTS measurements for the $Al_{0.17}Ga_{0.83}As$ samples irradiated by one-MeV electrons with 10^{15} and 10^{16} e/cm^2 fluences are summarized in table 2. No deep-level defects were detected by our DLTS measurements in the $Al_{0.05}Ga_{0.95}As$ sample, while two electron traps with energies of E_c-0.19 eV and E_c-0.29 eV were observed in the $Al_{0.17}Ga_{0.83}$ samples. It is interesting to note that both electron traps observed in the one-MeV electron irradiated $Al_{0.17}Ga_{0.83}As$ sample have also been observed in the unirradiated AlGaAs specimen with x > 0.15. This result clearly indicates that no new defect levels were introduced in the $Al_xGa_{1-x}As$ specimen by the one-MeV electron irradiation.

In summary, the results of our DLTS and C-V analysis on the one-MeV electron irradiation induced defects in germanium and $Al_{0.17}Ga_{0.83}As$ materials clearly show that both of these two materials possess good radiation resistance characteristics, and may be suitable for use as the top and bottom cell materials in a triple junction structure with GaAs as the middle cell material. The possible physical origins for the observed deep-level traps in the germanium samples are also listed in table.1.

REFERENCES

1. C. R. Lewis, W. T. Dietze, and M. J. Ludowise, "Development of a 30 % Efficient 3 - Junction Monolithic Cascade Solar Cell," Proc. of NASA Space Photovoltaic Research and Technology Conference, p.140 (1983).

2. John C. C. Fan and B. J. Palm, "Optimal Design of High Efficiency Single-Junction and Tandem Concentration Space Cells At 80 °C and 100 Suns," Proc. of NASA Space Photovoltaic Research and Technology Conference, p.120 (1983).

3. V. L. Dalal, Realistic Design of Monolithic, Multijunction Amorphors Solar Cells," Proc. IEEE Photovoltaic Special. Conf., p. 86 (1984).

4. M. E. Lamorte and D. H. Abbott, "Cascade Solar Cell Design for High-Temperature Operation," IEEE Trans. Elec. Devices, vol. ED-27, p. 831 (1980).

5. S. M. Bedair, J. A. Hutchby, J. Chiang, M. Simons and J. R. Hauser, "AlGaAs/GaAs High Efficiency Cascade Solar Cells," Proc IEEE Photovoltaic Specialists Conf., p.21 (1981).

6. S. S. Li, W. L. Wang, P. W. Lai, R. Y. Loo, G. S. Kamath, and R. C. Knechtli, "Deep-Level Defects, Recombination Mechanisms, and Their Correlation to the Performance of Low Energy Proton Irradiated GaAs Solar Cells," IEEE Trans. Elec. Devices, vol.ED-27, p.857 (1980).

7. B. E. Anspaugh and R. G. Downing,"Radiation effects in Silicon and GaAs Solar Cells Using Isotropic and Normally Incident Radiation," Proc. IEEE Photovoltaic Spec. Conf., p.23 (1984).

8. R. Y. Loo, R. C. Knechtli, and G. S. Kamath, "Enhanced Annealing of GaAs Solar Cell Radiation Damage," Proc. IEEE Photovoltaic Spec. Conf., p.33 (1981).

9. S. S. Li, W. L. Wang, R. Y. Loo and W. P. Rahilly, Proc. of the 16th IEEE Photovoltaic Specialists Conf., p.211, (1982).

10. W. L. Wang and S. S. Li, Proc. of the 17th IEEE Photovoltaic Specialists Conf., p.161, (1984).

11. J. C. Pigg and S. H. Crawford, Jr., Phy. Rev., vol. 135, No. 4A, p. A1141, (1964).

12. T. V. Mashovets, Inst. Phys. Conf. Ser., No. 31, p.30, (1977).

13. H. Saito, J. C. Pigg and J. H. Crawford, Jr., Phy. Rev., vol. 144, No. 2, p.725, (1966).

14. N. Fukuoka, H. Saito and Y. Tatsumi, Inst. Phys. Conf. Ser., No. 23, P.206, (1975).

15. Y. Kamiara, F. Hashimoto, T. Nobusoda, and S. Yoneyama, J. Appl. Phys. 56(4), p.936, (1984).

16. O. L. Curtis, Jr., and J. H. Crawford, Jr., Phy. Rev., vol.126, p.1342, (1962).

Table 1. Defect parameters in one-MeV electron irradiated germanium.

Samples	Φ_e (e/cm^2)	E_T (eV)	N_D (cm^{-3})	N_t (cm^{-3})	σ_n (cm^2)	σ_p (cm^2)	τ_n	τ_p	Defect origin
GE-B	0	E_c-0.26	1×10^{15}	3.73×10^{14}	4.23×10^{-16}		6.33×10^{-7}		Cu^{3-}
A=2.65×10^{-5} cm^2		E_v+0.33		3.89×10^{14}		8.52×10^{-15}		3.02×10^{-8}	Cu^{2-}
GE13	10^{14}	E_c-0.24	7.45×10^{14}	3.55×10^{14}	5.55×10^{-16}		5.10×10^{-7}		VD Complex
		E_v+0.10		3.51×10^{14}		3.6×10^{-17}		7.91×10^{-6}	VVD Complex
		E_v+0.17		1.33×10^{14}		1.22×10^{-16}		6.16×10^{-6}	VVD Complex
GE12	10^{15}	E_c-0.27	8.9×10^{14}	4.51×10^{14}	4.47×10^{-15}		4.96×10^{-8}		VD Complex
		E_v+0.26		2.92×10^{14}		4.24×10^{-14}		8.08×10^{-9}	VVD Complex
GE11	10^{16}	E_c-0.24	7.46×10^{14}	3.54×10^{14}	5.55×10^{-16}		5.09×10^{-7}		VD Complex
		E_v+0.10		2.69×10^{14}		3.60×10^{-17}		1.03×10^{-5}	VVD Complex
		E_v+0.17		1.72×10^{14}		1.22×10^{-16}		4.77×10^{-6}	VVD Complex

Table 2. One-MeV Electron Irradiation Induced Defects in $Al_{0.17}Ga_{0.83}As$ Materials.

Electron Fluence (e/cm^2)	N_d (cm^{-3})	E_T(eV)	N_T (cm^{-3})	σ_n (cm^{-2})
$\phi_e = 10^{15}$	3.7×10^{17}	E_c- 0.19	1.12×10^{16}	6.99×10^{-14}
		E_c- 0.29	1.3×10^{16}	5.14×10^{-14}
$\phi_e = 10^{16}$	2.9×10^{17}	E_c- 0.19	1.08×10^{16}	6.99×10^{-14}
		E_c- 0.29	1.13×10^{16}	5.14×10^{-14}

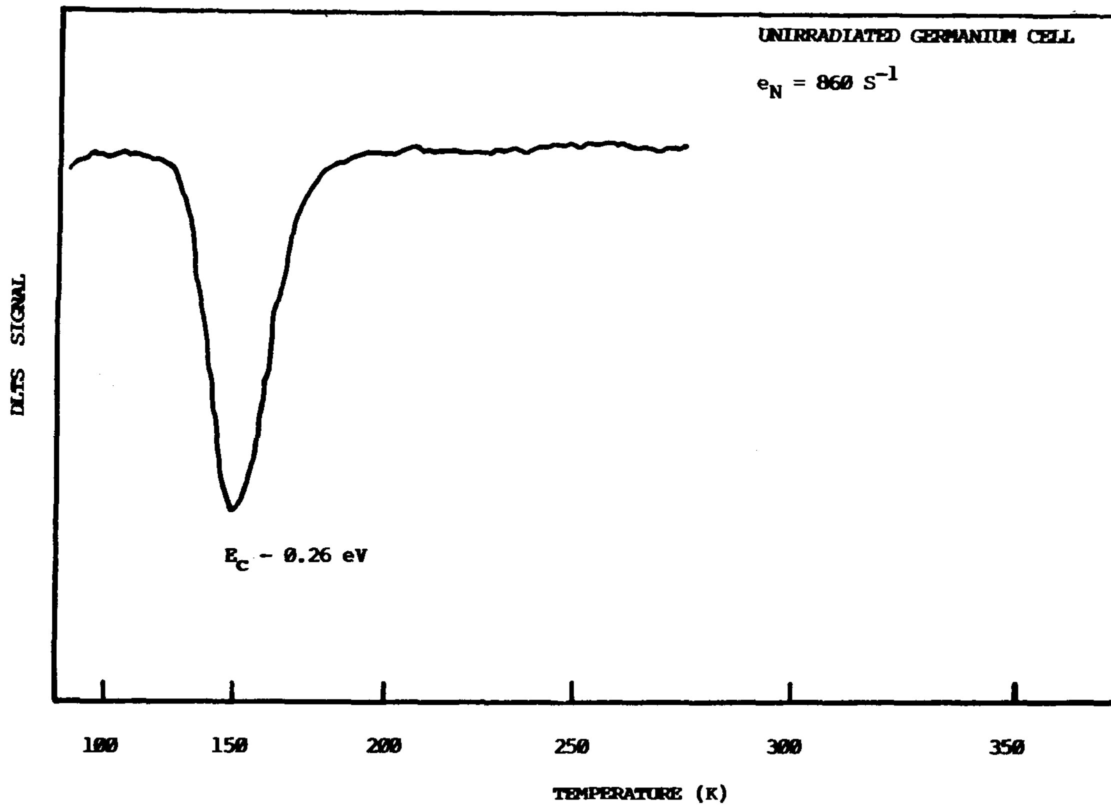

Fig. 1 DLTS scan of electron trap in unirradiated germanium cell.

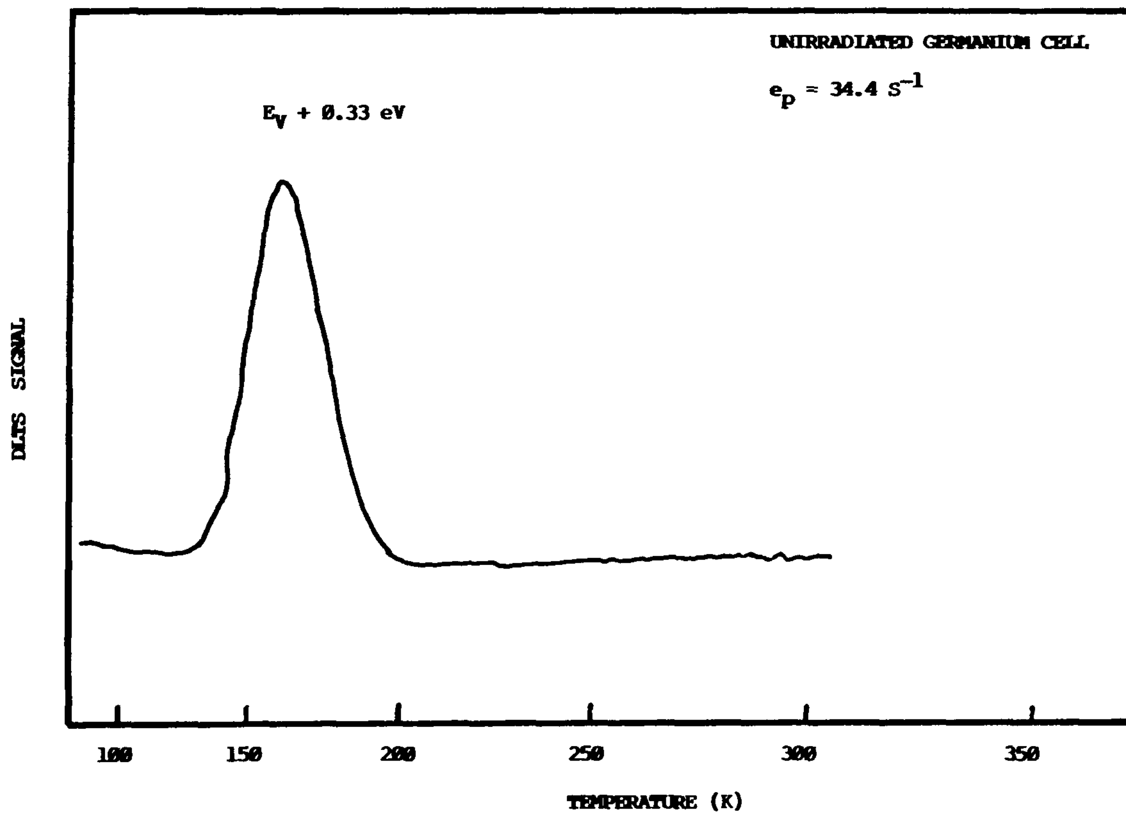

Fig.2 DLTS scan of hole trap for the unirradiated germanium cell.

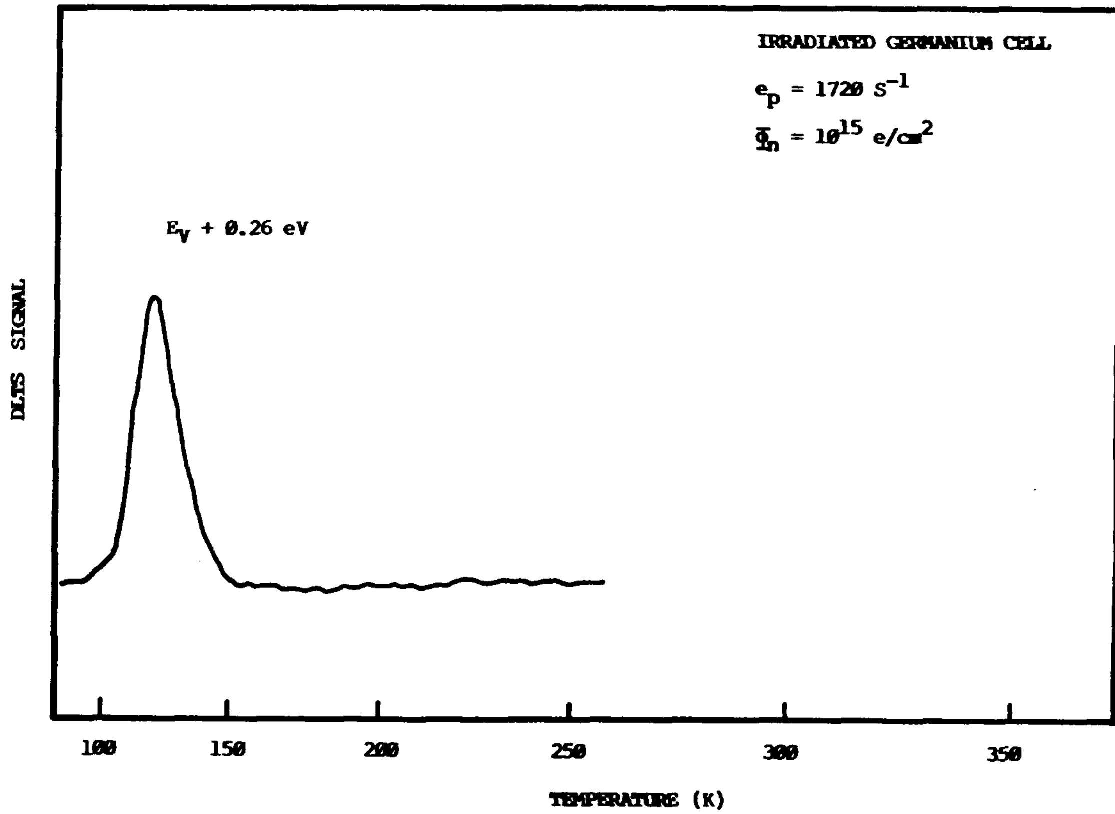

Fig.3 DLTS scan of hole trap for the irradiated germanium cell.

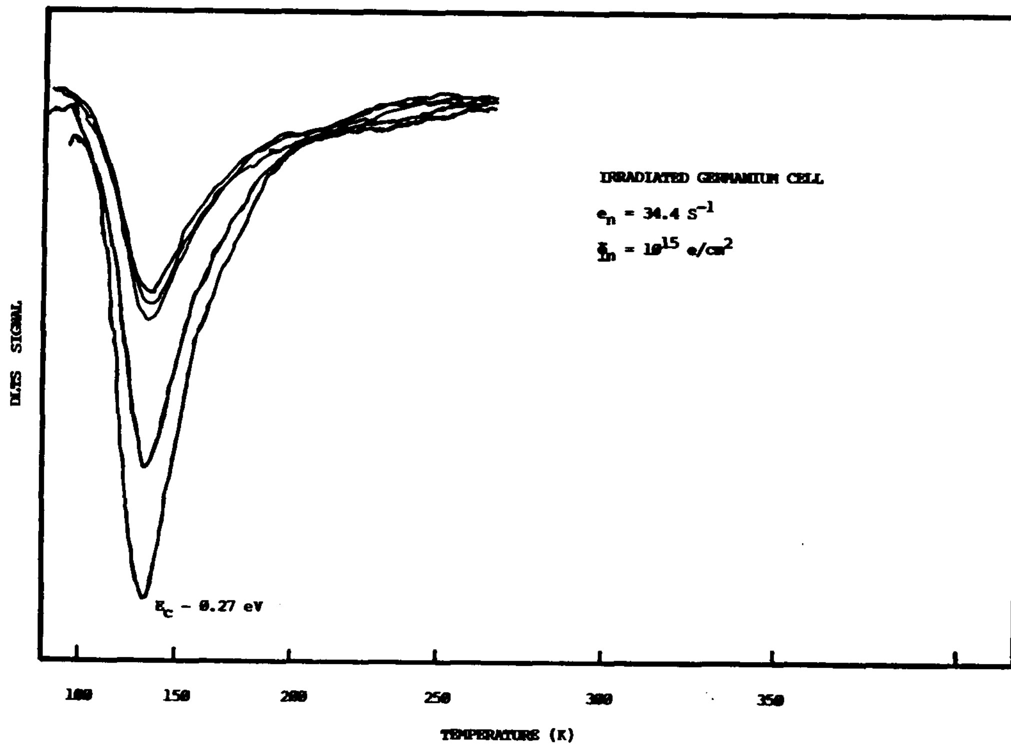

Fig.4 DLTS scans of electron trap for the irradiated germanium cell by repeating thermal scan between 77 and 435 K, showing the effect of thermal annealing.

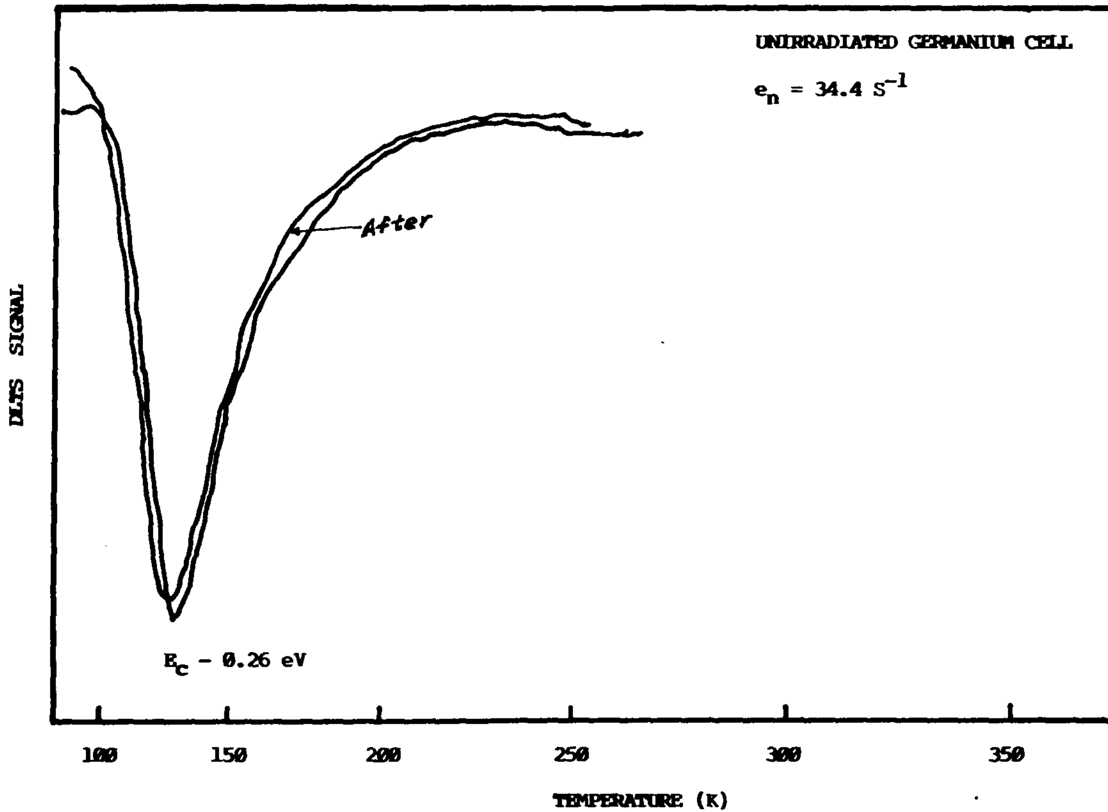

Fig.5 DLTS scans of electron trap for the unirradiated germanium cell by thermal annealing at 162 C for 12 hours.

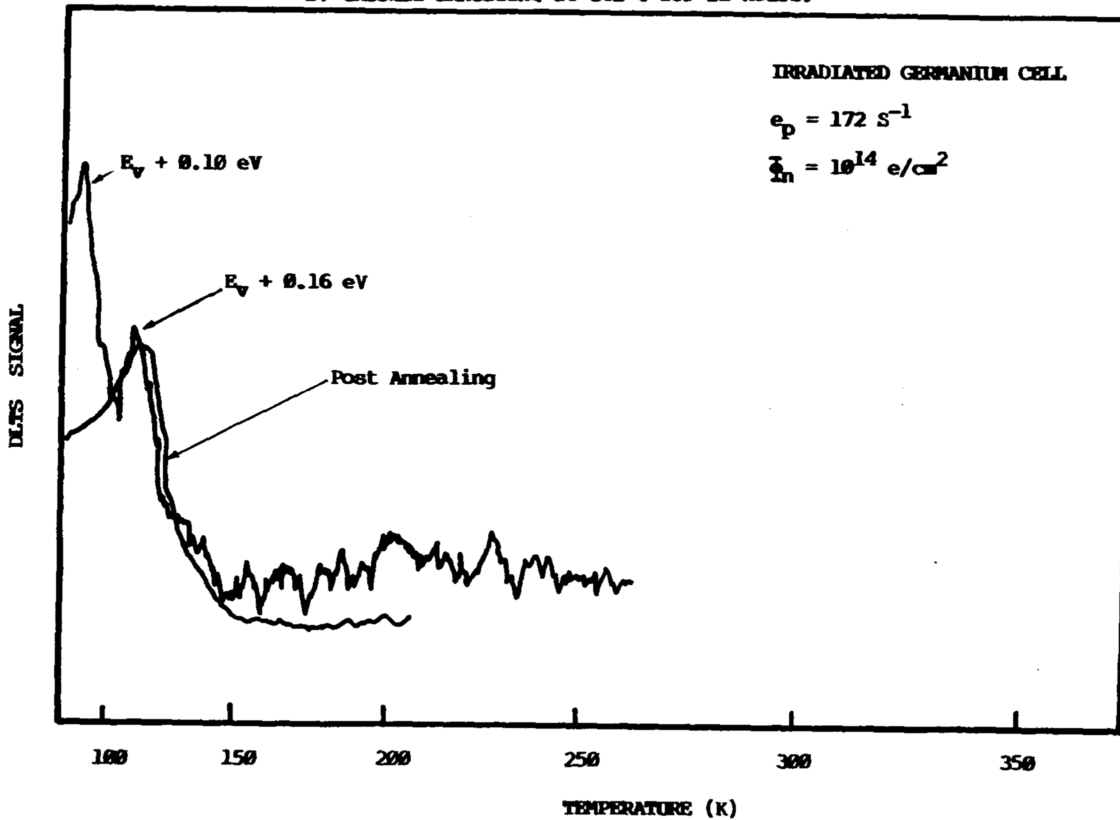

Fig.6 DLTS scans of hole traps for the irradiated germanium cell before and after thermal annealing at 162 C for 45 min.

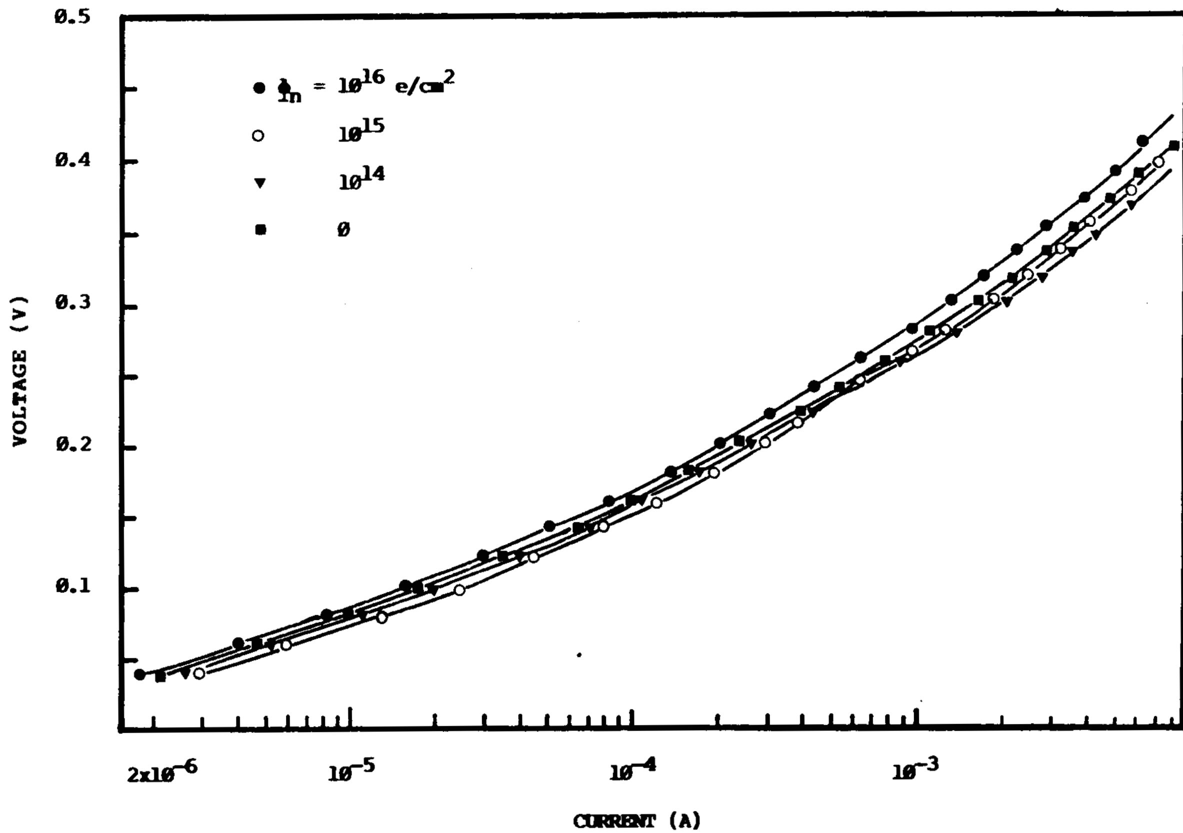

Fig. 7 Forward I-V curves in germanium p/n junction cells irradiated by one-MeV electrons of different fluences.

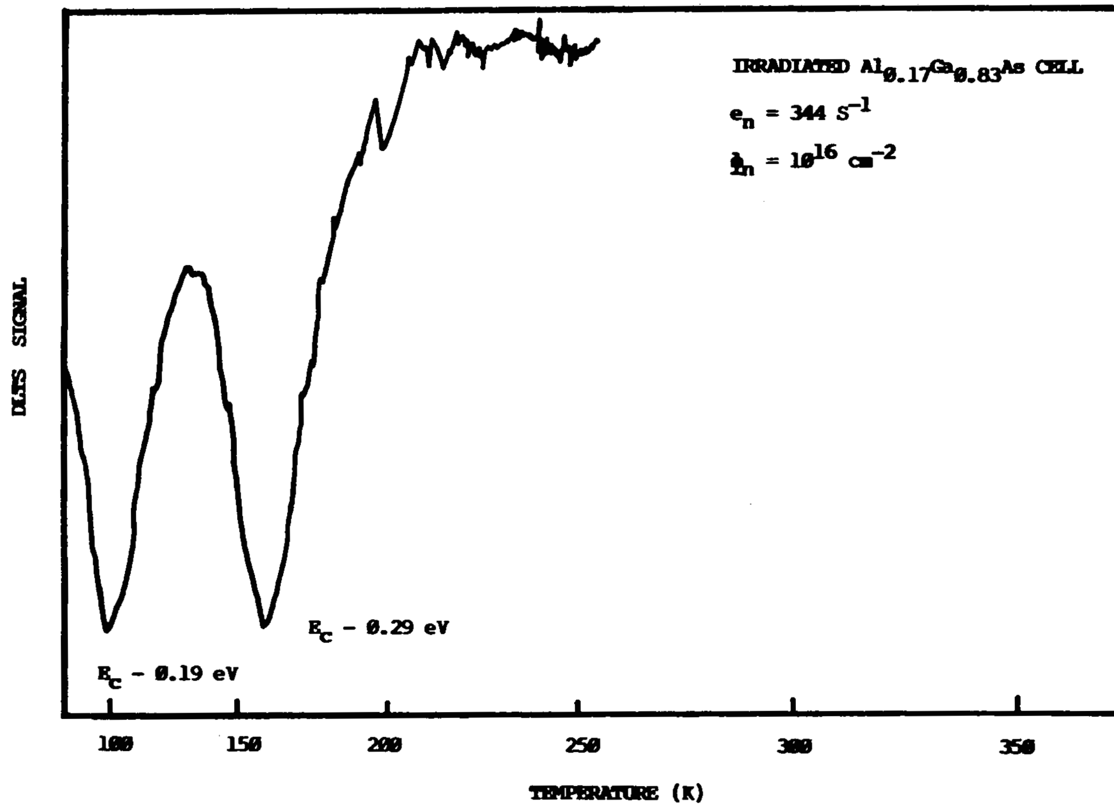

Fig.8 DLTS scan of electron traps for the one-MeV electron irradiated $Al_{0.17}Ga_{0.83}As$ solar cell.

N86-17859

DEPLETION LAYER RECOMBINATION EFFECTS ON THE RADIATION DAMAGE HARDNESS OF GALLIUM ARSENIDE CELLS

G. F. J. Garlick
Spectrolab, Inc.
Sylmar, California

In 1973 Hovel (ref. 1) demonstrated the significant effect of junction depletion layer recombination on the efficiency of 'windowed' GaAs cells. The effect becomes more pronounced as radiation damage occurs and is included in the analyses of later workers. In this paper it is more explicitly considered for 1 MeV electron fluences up to 10^{16} e/cm^2. The cell modeling separates damage in emitter and base or buffer layers using different damage coefficients recently reported by Yamaguchi et al (refs. 2 and 3). The lower coefficient for the emitter predicts less loss of performance at fluences greater than 10^{15} e/cm^2. A method for obtaining information on junction recombination effects as damage proceeds is described; this enables a more complete diagnosis of damage to be made.

INTRODUCTION

In 1973 Hovel (ref. 1) analyzed the effect of junction depletion layer recombination in AlGaAs windowed GaAs cells showing that it could account for a few percent loss of cell efficiency (AMO). Later Loo et al (ref. 2) and Knechtli et al (ref. 3) carried out analyses of electron radiation damage in this type of cell using models which included the junction effects. Their models, which are similar to those of Hovel and Woodall (ref. 4), have been the basis of our analysis. In addition we have looked at the effects of different damage coefficients for the emitter and buffer (or base) regions. We have used the information on these given in the work of Yamaguchi et al (refs. 5 and 6). Compared with the assumption of equal damage coefficients in emitter and buffer (about 10^{-7}/e) the emitter damage coefficient is $3.5 \cdot 10^{-8}$ for a P doping of 10^{18}/cm^2 and the buffer damage coefficient is $1.8 \cdot 10^{-7}$ for N doping of $2 \cdot 10^{17}$/cm^3. Using the separate values shows significant differences in cell damage from that using equal damage coefficients.

It is clear that in order to use the modeling for damage in gallium arsenide to explain experimental data, measurements have to be sufficiently comprehensive at each fluence level to give information on the junction depletion region. One can include a complete dark current characteristic measurement at each fluence but we describe below a simple way to obtain sufficient information by using the variation of V_{OC} and I_{SC} with solar flux.

Our modeling uses a computer code developed here for the HP/3000 'in house' computer. Short circuit current (I_{SC}) is obtained by using the solar AMO spectrum and the absorption data for the cell window and for the underlying GaAs. Open circuit voltage (V_{OC}), power maximum, efficiency (η), etc. are obtained as in previous models using of course the derived I_{SC} values. The junction effects are found by using the relations of Sah, Noyce and Shockley (ref. 7 as modified by Choo (ref.8)).

PRECEDING PAGE BLANK NOT FILMED

C-3

Cell parameters such as thickness of the various layers, doping concentrations, surface and interface recombination velocities, diffusion lengths and coefficients etc. are taken for typical production cells from Hughes Research Laboratories made by the LPE method.

DAMAGE ANALYSIS MODELING

It is assumed that diffusion lengths decrease with fluence of electrons in the following way:

$$1/L^2 = 1/L_o^2 + K.\emptyset \qquad (1)$$

where $\emptyset$ is the fluence (e/cm^2), L_o is the BOL (beginning of life) value and L the diffusion length value at $\emptyset$, K being the damage coefficient (usually quoted for L values in cm).

The analytical relations for I_{sc}, V_{oc}, etc. will not be requoted here but it is useful to note that I_{sc} will depend on L values and on absorption spectra for the cell layers as well as on the layer thicknesses, etc.

The open circuit voltage depends on the above factors, including I_{sc} but is also strongly dependent on the resulting saturation currents for the NP GaAs diode system. The so called first diode saturation current I_{01} is the sum of the components due to the emitter and the buffer (Iol_e and Iol_b) while I_{02} is the saturation current for the 'second diode' arising from the depletion layer recombination. The relation determining their effect on V_{oc} is:

$$I_{sc} = I_{01}.\exp(qV_{oc}/kT) + I_{02}.\exp(qV_{oc}/2kT \qquad (2)$$

q being the electronic charge, k Bȯltzmann's constant and T the absolute temperature. This relation forms the basis for analyzing experimental data on cell damage. It is not usual to include the junction term when calculating V_{oc} but as gallium arsenide cell modelers show it is too significant to be neglected. However, past experimental data for high fluences cannot be analyzed properly because measurements of a kind giving I_{02} are missing. We show how this can be remedied below.

We now look at results of modeling with respect to saturation currents. Figure 1 gives the saturation currents for a cell as functions of 1 MeV electron fluence for a typical cell specification, which is:

Window and emitter thickness = .5 micron. Buffer thickness 10 micron.
Window is Al(86%)Ga(14%)-As, buffer and base are GaAs.
Window diffusion length .2 micron, emitter diffusion length 5 micron, buffer diffusion length 2 micron.
Window diffusion coefficient .7, emitter value 90, buffer value 5 each in cm^2/s.
Window surface recombination velocity 10^6, emitter interface recombination velocity 10^4 cm/s respectively; buffer assumed 'thick' in cell theory.
Window and emitter doping concentrations $10^{18}/cm^3$ and buffer doping concentration $2.10^{17}/cm^3$. Emitter damage coefficient is $3.5.10^{-8}$/e, buffer damage coefficient is $1.8.10^{-7}$.

(It should be remembered that the formula for I_{02} contains a V_{oc} dependent term in equation (2) and this makes the equation transcendental. However, it is easily solved by a Newton Raphson method.)

Figure 1 shows that the dominating influence in I_{01} for moderate fluences is that of the buffer component. However, at fluences of 10^{15} e/cm^2 or more the emitter contribution becomes significant and at 10^{16} e/cm^2 overtakes that of the buffer. In addition the effect of I_{02} which is almost constant up to 10^{15} e/cm^2 becomes an important factor at higher fluences. The combined effect of these three saturation currents makes the change of cell parameters with damage rather different from that predicted from 'base only' damage (see e.g. JPL Radiation Damage Handbook, ref. 9) usually assumed for silicon cells.

Figure 2 shows the effect of the saturation current behavior on the open circuit voltage, V_{oc}. Curve A is when no effect of I_{02} is included while Curve B shows the effect of its inclusion. The broken curve, C, is for equal damage coefficients in emitter and base of $10^{-7}/e$. The % changes for the effect are listed in Table 1 below.

Figure 3 shows the effect of the I_{02} component on the cell maximum power fall off with fluence. Curve A is when no I_{02} term is present, Curve B that when it is there; as in Figure 1, curve C shows the case of equal damage coefficients in emitter and base ($10^{-7}/e$). Again, % changes are given in Table 1.

It is well established by previous workers that there is a great advantage in making cells with thinner window and emitter layers. We have not given the plots for a 'thin' cell but have included a summary of our modeling in Table 1 for a cell with .2 micron window and .2 micron emitter but keeping all other specifications the same. The improvement in I_{sc}, V_{oc} and maximum power and efficiency is evident. The difference in efficiency at end of life (10^{16} e/cm^2) is .6% when the damage coefficients are assumed different in the emitter and buffer. However, the effect of the I_{02} component of saturation currents is still similar to that for equal damage coefficients.

ANALYSIS OF EXPERIMENTAL DATA

We have already shown that diagnosis of damage in gallium arsenide cells needs a knowledge of the second diode (I_{02}) behavior as electron fluence is increased. We have developed a simple measurement for the same purpose in looking at silicon cells. In addition to the usual measurements of spectral response, V_{oc}, I_{sc} and maximum power (from current voltage load curves) we take an extra pair of readings of I_{sc} and V_{oc} at an illumination less than that at AMO (about 3 times less). Then using the AMO values and these new values we can apply Equation 2 to get I_{01} and I_{02} values. As a simple example for an undamaged cell we give measurements of I_{01} and I_{02} for a cell of efficiency 17.5% at AMO flux from a production run (HRL).

Io1 (A/cm^2)	Io2 (A/cm^2)	I_{sc} mA/cm^2	V_{oc} mV	Effy %
$8.53.10^{-20}$	$4.11.10^{-11}$	29.0	1026	17.5

It is thus possible to obtain quantitative measurements of first and second diode saturation currents I_{01} (total) and I_{02} for gallium arsenide cells and to compare them with theoretical curves like those in Figure 1 to test the efficacy of the modeling. It is also possible to introduce a constant contribution to I_{02} arising from junction contamination levels into the model.

CONCLUSIONS

(a) The significant effects of junction depletion layer recombination on the radiation hardness of 'windowed' gallium arsenide cells have been explicitly demonstrated. They represent a basic limit to cell hardness especially at high fluence levels. It would appear that improvement in hardness will have to come from an 'offsetting' of damage processes in cell emitter and buffer layers. This might be helped by a greater fundamental understanding of the nature of recombination centers induced by the high energy radiation.

(b) The advantages of thinner window and emitter layers are obvious but they do not alleviate the second diode effects.

(c) It is possible to estimate the second diode effects experimentally at various stages of damage by adding a simple I_{sc}-V_{oc} test at lower light flux levels. Of course more detailed information can be included if dark current voltage measurements are also made at each stage of damage.

(d) In the course of similar modeling for silicon cells we have found that the second diode effects are not insignificant at the high fluence levels. In this case we have considerable experimental evidence from damaged cells. Similar experimental evidence will be obtained for gallium arsenide when damaged samples are available.

REFERENCES

1. Hovel, H. J.; IEEE 10th Photovoltaic Specialists Conf. p. 34 (1973).

2. Loo, R.; Kamath, G. S.; and Knechtli, R. C.; 14th Photovoltaic Specialists Conf. p. 1090 (1980).

3. Knechtli, R. C.; Loo, R. Y.; and Kamath, G. S.; IEEE Trans. Electronic Dev. ED-31, 577 (1984).

4. Hovel, H. J. and Woodall, J. M.; IEEE 10th Photovoltaic Specialists Conf. p. 288 (1973).

5. Yamaguchi, M. and Amano, C.; J. Appl. Phys. 57, 537 (1985).

6. Yamaguchi, M. and Uemura, C.; J. Appl. Phys., 57, 604 (1985).

7. Sah, C. T.; Noyce, R. N.; and Shockley, W.; Proc. I.R.E., 45, 1228, (1957).

8. Choo, S. C., Solid State Electronics, 11, 1069 (1968).

ORIGINAL PAGE IS
OF POOR QUALITY

Table 1

Comparison of performance of thick (.5 micron) and thin (.2 micron) windowed gallium arsenide cells with equal and unequal radiation damage coefficients in the emitter and buffer layers.

(K(emit) = K(buff) = 10^{-7}/e or K(emit) = $3.5 \cdot 10^{-8}$/e and K(buff) = $1.8 \cdot 10^{-7}$/e)

(Emitter layer thickness is same as that of window for each cell as given in text.)

	K(emitter) ≠ K(buffer)				K(emitter) = K(buffer)			
	Thick Cell		Thin Cell		Thick Cell		Thin Cell	
Fluence e/cm	With I_{02}	No I_{02}	With I_{02}	No I_{02}	With I_{02}	No I_{02}	With I_{02}	No I_{02}
	Open Circuit Voltage (mV)							
0	1016.4	1038.7	1018.7	1041.5	1016.4	1038.7	1018.7	1041.5
10^{14}	997.7	1030.3	1000.3	1033.7	991.0	102.9	994.3	1034.6
10^{15}	929.6	1003.7	931.4	1008.7	916.5	995.2	921.2	1008.2
10^{16}	809.6	958.0	818.6	970.9	783.2	940.0	805.5	960.9
	Short Circuit Current (mA/cm^2)							
0	30.23	-	31.36	-	30.23	-	31.36	-
10^{14}	29.72	-	30.69	-	29.73	-	30.93	-
10^{15}	27.63	-	28.41	-	26.69	-	28.95	-
10^{16}	20.47	-	24.52	-	15.14	-	23.76	-
	Maximum Power (mW/cm^2)							
0	25.13	25.84	26.11	26.88	25.13	25.84	26.11	26.88
10^{14}	23.93	25.20	24.74	26.11	23.66	25.17	24.65	26.33
10^{15}	20.16	22.82	20.76	23.61	19.15	21.86	20.85	24.02
10^{16}	12.64	16.13	15.32	19.60	9.01	11.71	14.56	18.79
	% Efficiency at AM0							
0	18.58	19.10	19.30	19.87	18.58	19.10	19.30	19.37
10^{14}	17.68	18.63	18.28	19.30	17.49	18.61	18.22	19.46
10^{15}	14.90	16.87	15.35	17.45	14.15	16.16	15.41	17.76
10^{16}	9.34	11.93	11.32	14.88	6.66	8.66	10.76	13.80
	(21.7%)	(-)	(21.8%)	(-)	(23.1%)	(-)	(22.5%)	(-)
	Cell Fill Factor							
0	.818	.821	.817	.823	.818	.823	.817	.823
10^{14}	.807	.823	.806	.823	.803	.823	.802	.823
10^{15}	.785	.823	.784	.823	.783	.823	.782	.823
10^{16}	.763	.823	.763	.823	.760	.823	.761	.823
	(7.3%)		(7.3%)		(7.65%)		(7.5%)	

(% in brackets give loss in cell efficiency and fill factor due to second diode I_{02}.)

ORIGINAL PAGE IS
OF POOR QUALITY

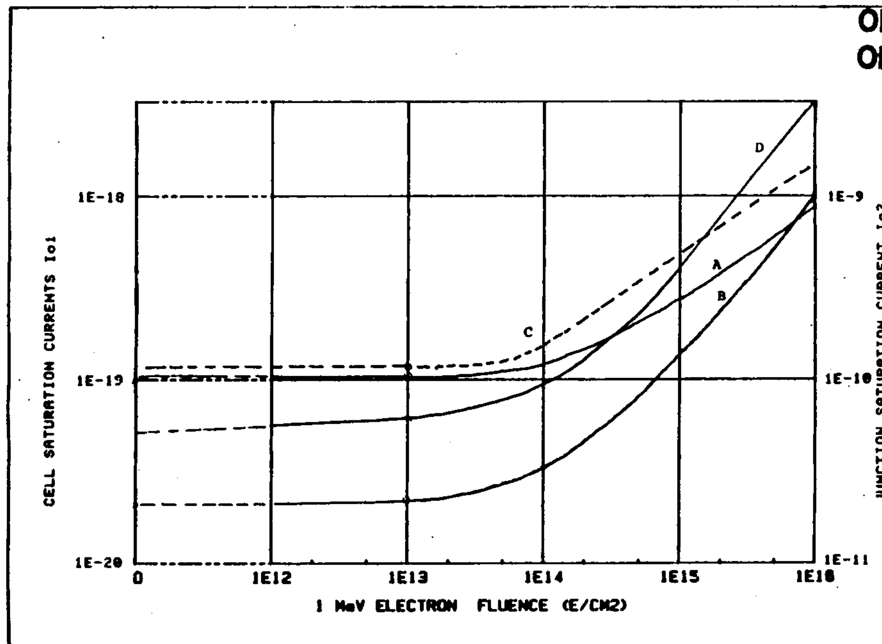

Figure 1. Dependence of diode saturation currents on 1 MeV electron fluence for a 'windowed' gallium arsenide cell with specification and damage coefficients as in text.

A. Saturation current I_{01} for buffer layer

B. Satuation current I_{01} for emitter layer

C. Total I_{01} (curve A + curve B)

D. Second diode saturation current I_{02} for junction

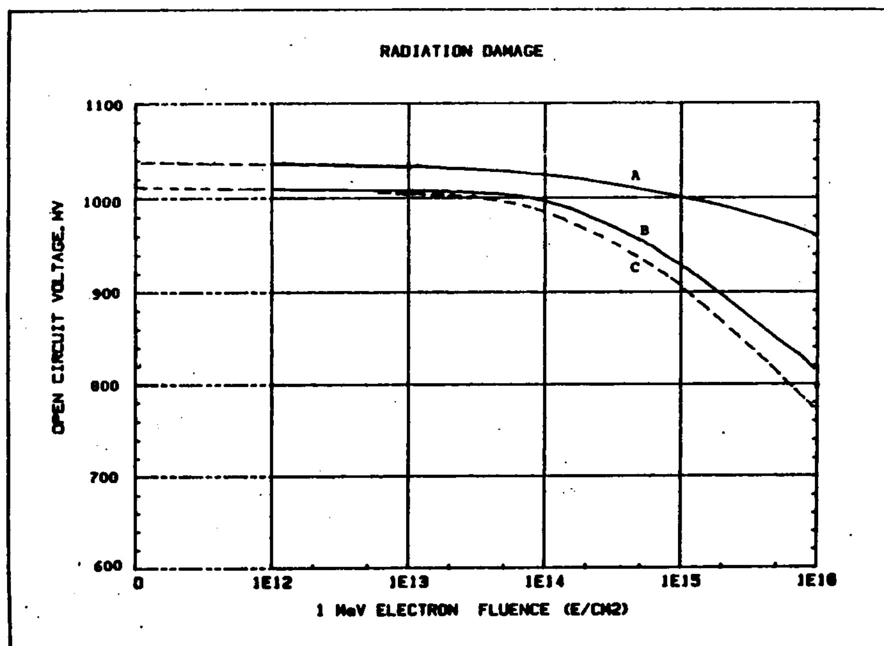

Figure 2. Dependence of open circuit voltage V_{oc} on 1 MeV electron fluence for a 'windowed' gallium arsenide cell with specification and damage coefficients as in text.

A. Variation of V_{oc} when no second diode current is present

B. Variation of V_{oc} when second diode current is present

C. Variation of V_{oc} when second diode current is present and same damage coefficients for emitter and buffer $(10^{-7}/e)$

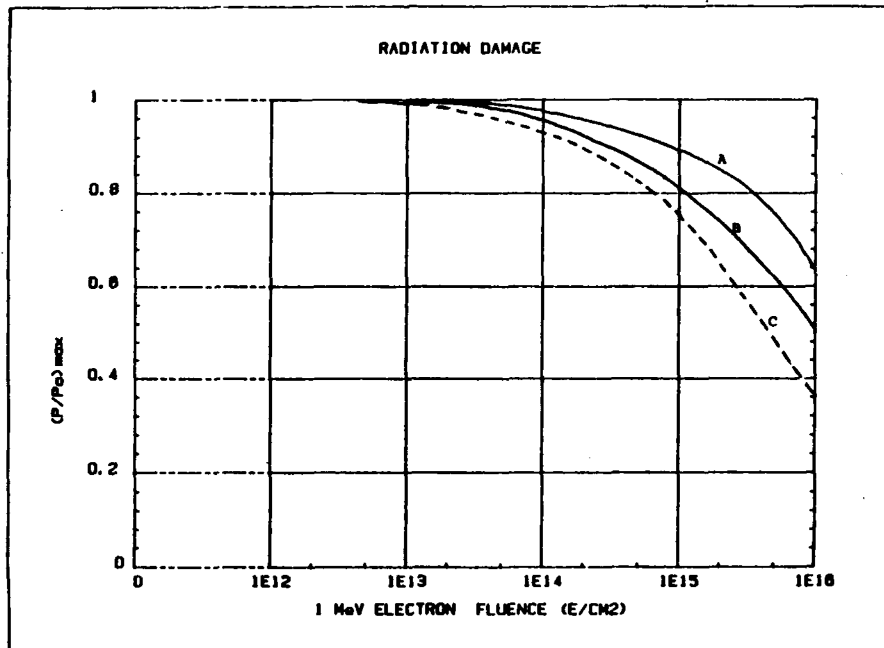

Figure 3. Dependence of ratio (power max. at given fluence/initial power max.) as a function of 1 MeV electron fluence for a 'windowed' gallium arsenide cell with specification and damage coefficients as in text.

A. Variation of ration when no second diode is present

B. Variation of ratio when second diode is present

C. Variation of ratio when second diode is present and for equal damage coefficients in emitter and buffer (10^{-7}/e)

N86-17860

PERFORMANCE OF HUGHES GaAs CONCENTRATOR CELLS

UNDER 1-MeV ELECTRON IRRADIATION

Henry B. Curtis and Clifford K. Swartz
NASA Lewis Research Center
Cleveland, Ohio

Several Hughes gallium arsenide (GaAs) concentrator cells were exposed to 1-MeV electrons at fluences up to 1×10^{15} electrons/cm^2. Performance data were taken after several fluences, at two temperatures (25 and 80 °C), and at concentration levels from 1 to ~150x AM0. Data at 1 sun and 25 °C were taken with an X-25 xenon-lamp solar simulator. Data at concentration were taken using a pulsed solar simulator with the assumption of a linear relationship between short-circuit current and irradiance. The cells are 5 by 5 mm with a 4-mm-diameter illuminated area.

INTRODUCTION

The use of concentrating optics for space photovoltaic power generation has been under consideration for some time. The potential advantages of concentrators include higher cell efficiency, better radiation resistance, and lower cost. One possible optical design out of several is the miniature Cassegrainian concept developed by TRW (ref. 1). This design involves small GaAs cells operating at a concentration level of 100 to 130x AM0. The cells are 5 by 5 mm with a 4-mm-diameter illuminated area which leaves about half the cell area covered with outer bus-bar.

One of the unanswered questions involving concentrator cells is their performance degradation at concentrated light levels after electron irradiation. As part of an ongoing concentrator-cell program at NASA Lewis, several Hughes concentrator GaAs cells were irradiated with 1-MeV electrons. The data presented here are intended to be a first look at the performance of concentrator cells after electron bombardment.

EXPERIMENTAL DESCRIPTION

Five Hughes GaAs small-area concentrator cells were individually mounted in separate cell holders. The holders consist of a small bottom metal base and a washerlike metal top with a beveled hole slightly larger than the illuminated area of the cell. These two pieces supply both a permanent support for the cell and an area for the four-wire electrical attachment. The cells remained in their holders throughout all electron irradiations and performance measurements. There were no cover glasses attached to the cells nor was there any shielding by optical elements during the irradiations.

Electron irradiations using 1-MeV electrons were performed at the NASA Lewis dynamitron and at the Naval Research Laboratory Van de Graff generator. (The electron irradiation facilities at NRL were made available through the cooperation of Richard Statler and Robert Farr.) The cells were irradiated to a total fluence of

PRECEDING PAGE BLANK NOT FILMED

1×10^{15} electrons/cm^2, with performance measurements made at several intermediate fluence levels. The performance measurements consisted of the following:

(1) I-V data at 25 °C and 1 AMO using an X-25 xenon solar simulator and a reference cell

(2) I-V data at 25 °C at several concentrations up to 100 times AMO and above using a pulsed xenon solar simulator and the linear assumption between irradiance and short-circuit current

(3) Short-circuit current data at one fixed concentration at both 25 and 80 °C in order to set the current scale at the elevated temperature

(4) I-V data at 80 °C at several concentrations as in step (2)

During I-V measurements the cells in their holders are mounted to a temperature-controlled block. The concentration level on the cell is varied by a combination of changing the distance from the light source and using and not using a fresnel lens. Since the duration of the light pulse from the flash simulator is just 2 msec, there is no heating effect from the concentrated light. The elapsed time at 80 °C was about 90 min for each cell. Several repeat measurements were made at 1 sun and 25 °C after the elevated temperature measurements in order to determine if any annealing had taken place.

RESULTS AND DISCUSSIONS

The data presented in the tables and figures are the average of the five cells which were carried throughout the electron irradiations. Table I shows the initial I-V parameters before irradiation. One cell was somewhat lower in current and efficiency than the others and therefore lowered the averages. Two cells had an efficiency of 19 percent at 100x AMO and 80 °C.

Figure 1 is a plot of cell efficiency versus concentration level for the unirradiated case and two irradiated cases for data taken at 25 °C. One common factor among the three curves is that they get flatter with increasing electron fluence. This indicates that there is more power loss due to electron irradiation at concentrated levels than at 1 sun. This can be seen more clearly in figure 2, which shows the ratio of maximum power P_{max} after irradiation to the initial value as a function of electron fluence for both AMO and 100x at 25 °C.

Table II shows the ratios of short-circuit current I_{SC}, open-circuit voltage V_{OC}, fill factor, and P_{max} after irradiation to the unirradiated values for several fluence levels at 25 °C and at 1 and 100x AMO. At 1 sun the power degrades to 78.9 percent of the unirradiated value while it drops to 74.1 percent at 100x AMO. Both the voltage and fill-factor changes contribute to the greater power loss after irradiation at concentration. Note that the fill factor increases by 3 percent at 1 sun after irradiation while it decreases by 1.6 percent at 100x AMO. The ratios for short-circuit current are the same for both solar irradiation levels due to the linear current-irradiance assumption.

There is somewhat more V_{OC} degradation at 100x AMO than at 1 sun (0.91 versus 0.925). This indicates that even though the unirradiated V_{OC} is larger at 100x AMO than at 1 sun, it is still taking a larger percentage drop after

irradiation. This can be seen more clearly in table III, which lists the differences in V_{OC} between 100x AM0 and 1 sun measured after different fluence levels. The initial V_{OC} difference of 180 mV drops to about 150 mV after irradiation to 1×10^{14} electrons/cm^2 and then remains fairly constant for the final two electron fluences.

The decrease in the V_{OC} difference indicates that the cell is becoming more diffusion current dominated and less space-charge recombination current dominated, as the electron fluence increases. A difference of about 120 mV (60 mV/decade for 2 decades) would be expected for a cell with an n value of 1. At present, we have no good explanation for the change in V_{OC} differences.

Figure 3 shows the degradation in P_{max} at 100x AM0 for both 25 and 80 °C. The curves are nearly identical indicating that the effects on cell performance due to electron irradiation are essentially the same at the two temperatures.

Performance data were also taken at 25 °C after the 60 to 90 min spent at 80 °C for measurement purposes in order to determine if there were any annealing effects. In all cases, there was no annealing due to the time spent at 80 °C.

CONCLUDING REMARKS

Five small Hughes GaAs concentrator cells were irradiated with 1-MeV electrons to a total fluence of 1×10^{15} electrons/cm^2. After several different intermediate fluences, performance measurements were made at both 25 and 80 °C at different irradiance levels. The major conclusions are as follows:

1. The drop in P_{max} after irradiation was larger at 100x AM0 than at 1 sun.

2. There was no significant difference in the degradation of cell performance when measured at 25 or 80 °C.

3. There was no annealing due to about 90 min spent at 80 °C for measurements.

REFERENCE

1. Patterson, Robert E.: Preliminary Concept of a 100-Kilowatt Miniaturized Cassegrainian Concentrator Solar Array. Space Photovoltaic Research and Technology 1983, NASA CP-2314, Oct. 1983, pp. 157-162.

TABLE I. - I-V PARAMETERS FOR UNIRRADIATED CELLS

Concentration	1	100
Temperature, °C	25	80
Short-circuit current, I_{sc}, mA	3.46	365.5
Open-circuit current, V_{oc}, V	0.947	1.041
Fill	0.755	0.815
Efficiency, percent	14.5	18.3

TABLE II. - RATIOS OF IRRADIATED TO INITIAL VALUES FOR SEVERAL FLUENCES

Irradiation, electrons/cm^2	Short-circuit current, I_{sc}	Open-circuit current, V_{oc}	Fill	Maximum power, P_{max}
1 sun				
$1x10^{13}$	0.982	0.990	1.010	0.982
$3x10^{13}$	.965	.980	1.007	.954
$1x10^{14}$	.925	.964	1.019	.908
$3x10^{14}$	.893	.947	1.024	.866
$1x10^{15}$	.828	.925	1.030	.789
100x AMO				
$1x10^{13}$	0.982	0.978	0.997	0.957
$3x10^{13}$	.965	.962	.994	.924
$1x10^{14}$	.925	.941	.992	.863
$3x10^{14}$	.893	.932	.988	.822
$1x10^{15}$	.828	.910	.984	.741

TABLE III. - DIFFERENCES IN CURRENT V_{oc} BETWEEN 100x AMO AND 1 SUN AT 25 °C

Electron irradiation, electrons/cm²	V_{oc} difference, mV
Unirradiated	180
1×10^{13}	165
3×10^{13}	157
1×10^{14}	149
3×10^{14}	152
1×10^{15}	150

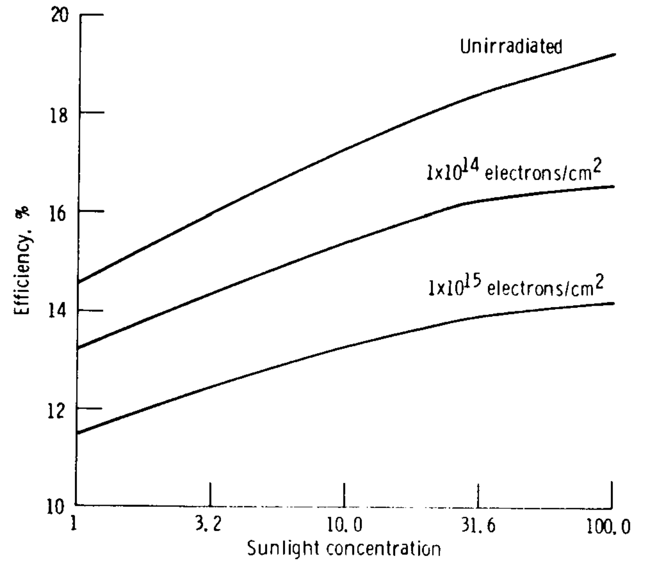

Figure 1. - Cell efficiency versus sunlight concentration for different electron fluences.

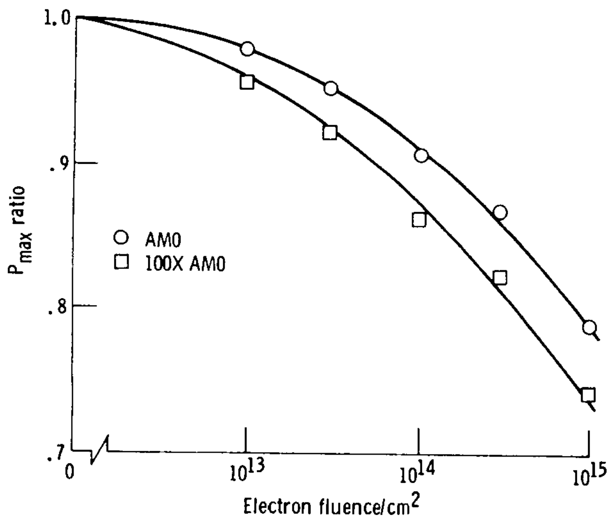

Figure 2. - P_{max} ratio versus electron fluence for 1 sun and 100X AM0 at 25 °C.

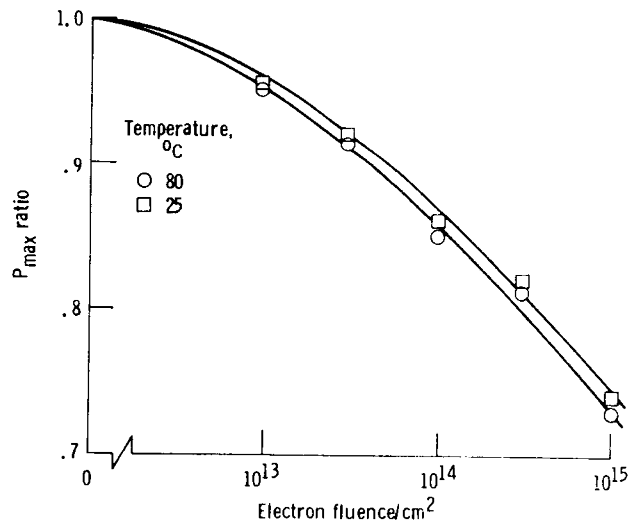

Figure 3. - P_{max} ratio versus electron fluence for 100X AM0 at 25 and 80 °C.

N86-17861

INTERPLANETARY EXPLORATION-A CHALLENGE FOR PHOTOVOLTAICS*

Paul M. Stella
Jet Propulsion Laboratory
California Institute of Technology
Pasadena, California

Future U.S. interplanetary missions will be less complex and costly than past missions such as Voyager and the soon to be launched, Galileo. This will be required in order to achieve a balanced exploration program that can be sustained within the context of a limited budget.

Radioisotope Thermoelectric Generators (RTGs) have served as the power source for missions beyond the orbit of Mars. Recent government costing practices have indicated that the cost to the user of these power sources will significantly increase. Solar arrays can provide a low cost alternative for a number of missions. Potential missions are identified along with concerns for implementation, and some array configurations under present investigation are reviewed.

INTRODUCTION

During the first decade of planetary exploration, spacecraft were launched as often as every few months, first to the moon, then the nearby planets, and finally to the outer planets. By the end of the second decade the intervals between launches lengthened to years as a result of budgetary constraints and increased mission complexity. This change has strained the nation's ability to conduct an effective interplanetary exploration effort. Technologies and talents required for various aspects of the spacecraft were required only at sporadic intervals and as a result maintenance of interplanetary spacecraft and scientific capabilities has become difficult.

In 1980 the Solar System Exploration Committee (SSEC), an ad hoc committee of the NASA Advisary Council, was established to examine and review the planetary exploration program. From this review, the SSEC defined an overall program that presented a number of features including a balance of missions between near earth planets, small bodies (asteroids and comets) and the outer planets (ref. 1). Of major importance, the program established a critical level of activity consistent with a realistic sustainable budget, in order to provide for stability. In implementing this, the approach specified highly focussed, less complex mission that could rely heavily on existing technology and hardware inheritance to reduce costs. Whereas the cost of some early missions such as Viking 1 and 2 had exceeded two billion dollars total, the new plan would be based on a total annual funding level of ~$300 M (FY '84). Of this total approximately $60 M/year would be available for the planetary observer program (near earth missions), ~$100 M/year for Mariner Mark II

---

*The research described in this paper presents the results of one phase of research carried out by the Jet Propulsion Laboratory, California Institute of Technology, under contract with the National Aeronautics and Space Administration.

PRECEDING PAGE BLANK NOT FILMED

program (missions beyond the inner solar system), and the remainder available for mission operations and scientific analysis. (These numbers can be compared with previous years funding levels for interplanetary exploration. For the years 1964-66 and 1972-74, annual funding exceeded $800 M in FY '84$. For 1978, and 1981-84, funding fell below $250 M in FY '84$.)

A critical item in any of these missions is the power source. For missions such as the planetary observers (Venus Radar Mapper, Mars Observer, Mars Aeronomy Orbiter, Venus Atmosphere Probe, Mars Surface Probe, Lunar Geoscience Orbiter) previous planetary experience has demonstrated the suitability of photovoltaics as the primary power source. For missions within the Mariner Mark II program (Comet Rendezvous/-Asteroid Flyby, Comet Sample Return, Multiple Mainbelt Asteroid Orbiter/Flyby, Earth Approaching Asteroid Rendezvous, Saturn Orbiter, etc.) past experience would point to the use of RTGs. However, within the past few years the cost of RTGs has come under examination. Historically, the cost of the fuel for an RTG power source has been "subsidized" by DOE, resulting in a relatively low RTG cost to NASA. This policy is presently under review and not yet resolved. Existing estimates of the RTG fuel costs range up to ~$3500 per thermal watt. If NASA is required to assume these costs or a significant portion of them, the RTG cost per mission could be prohibitive within the context of a constrained budget. This is especially so when qualification and spare unit article costs are included. For this reason a number of missions which normally might be RTG powered are potentially open to photovoltaic power. As shown in figure 1, the solar array cost is a function of the solar distance at which the power is required. Allowing for uncertainties in RTG costs, and array performance, array applications out to 6 AU can be considered as cost effective. With this in mind Mariner Mark II missions can be examined for solar suitability.

MARINER MARK II

A number of the Mariner Mark II missions present challenging opportunities for photovoltaics. As shown in figure 2 the solar range of these missions extends well beyond the range of present solar array experience. In addition, array operation is required over a wide variation of solar intensity resulting in a correspondingly large variation in array output. A major concern for photovoltaics under these circumstances is that for conditions of low intensity low temperature (LILT), various losses in cell output can occur. These losses are very irregular and can lead to an unacceptable degree of nonpredictability in array design and operation. Consequently, when LILT losses become appreciable the use of solar arrays may be impractical. As shown in figure 2, the onset of such conditions can be moved to increasing distances by means of solar concentration, although at an increase in structural complexity and array pointing requirements.

Even without the LILT degradation solar arrays present a number of difficulties for interplanetary acceptance. Since solar intensity drops off with the square of distance, a rapidly increasing array area is required to meet power needs at increasing solar distance. With typical interplanetary spacecraft power requirements of a few hundred watts, many tens of square meters of array can be required. This large area impacts launch packaging and deployment, and ultimately leads to a requirement for low array mass density. Additionally, large arrays will compete for limited available spacecraft area with scientific experiments and with required fields of view. Consideration must also be given to spacecraft maneuvering during

encounters, to ensure simultaneous array sun pointing, antenna earth pointing, and experiment target viewing. Unlike typical earth orbiting missions, these maneuvers may involve very rapid movements due to high approach velocities.

Since array area must be sized for the worst case, the variation in solar distance means that available power not only will vary widely but for much of the mission will greatly exceed the requirements. Handling such a power variation, and yet maintaining the highest efficiency at critical conditions will not be a trivial matter. Removal of excess power, due to widely varying circuit currents and voltages, needs to be effectively handled in the design of the solar array power system. In some cases combinations of separate and discrete circuits might be utilized at various solar distances and in other cases it may be more effective to allow for circuit reconfiguration during flight or to consider the use of maximum power tracking.

The first planned use of solar power for a Mariner Mark II mission will be unique in that an array will be combined with an RTG. As mentioned earlier the cost of an RTG is quite high. At the same time the present RTG power supply provides for a fixed unit of power, ~250 W. Scaleable RTGs have been proposed but are not presently available. For the Comet Rendezvous/Asteroid Flyby (CRAF) mission present planning indicates that slightly more than 250 W will be required. For this mission, a spare RTG from the Galileo program will be used. Acquiring a second RTG to meet an additional power need cannot be justified on a cost basis. Hence, the idea was proposed of using an add on solar array to make up the difference.

Such an array was initially envisioned to be on the order of 6 m^2, located at a fixed angle on the spacecraft side (fig. 3). After analysis of the array performance, including LILT effects, possible off sun pointing (up to 45°) and potential shadowing, it was apparent that greater area was required to meet the mission power requirements. Packaging a larger array on the configuration was difficult but resolved by changing the array shape to that of a washer and locating it colinearly with the earth pointing high gain antenna. The maximum size of the array was then established by the shuttle bay. As shown in figure 4, a considerable increase in array area was achieved, although the washer shape will reduce the cell packing density. As an additional benefit the array will maintain close to normal incidence sun-pointing, particularly as the solar distance is increased. This is due to the near coincidence of sun and earth locations for outbound viewing. Thus as array output decreases with increasing solar distance, any off angle pointing loses will also be reduced, maximizing output for the critical power situations. The array/RTG combination provides an interesting fusion of techologies that can meet technical and cost requirements. The tie in of antenna and array functions also provides a way of avoiding the complexity of a separate fully articulated array orientation system. Although the CRAF array is of good size by conventional array standards (~10 m^2), it is useful to consider what a fully photovoltaic powered spacecraft might require. Figure 5 is a schematic for such an array. The spacecraft is dwarfed in comparison. Yet with the trend to larger area arrays for planetary spacecraft and the NASA-OAST funded development of large area deployable arrays such a configuration may not seem unusual within a decade.

As mentioned earlier, one problem for the CRAF mission (and other MMII missions) that needed to be addressed was the LILT degradation. The array performance analysis for CRAF included an amount of LILT loss. However, as many have observed, the magnitude of LILT degradation for any single cell is quite unspecified and can vary

considerably from cell to cell or for different LILT conditions (ref. 2). Possible mechanisms for LILT losses have been discussed. Some causes, such as low shunt resistance, or non-ohmic contact behavior have been convincingly identified and their incidence can be avoided. Others, such as the "broken knee" (softening of knee of cell I-V curve) phenomenon have not been demonstrably corrected. Since a LILT degradation-free cell does not exist, the initial MMII approach to this problem will be to select cells based on both air mass zero and LILT behavior. Although requirements have not been defined, it is assumed that a certain amount of LILT degradation will be tolerated and included in the array performance design analysis. Although excluding cells with high LILT degradation will reduce the yield of acceptable cells it is presently assumed that a reasonable yield can be achieved. At present, insufficient data is available to determine the accuracy of this assumption. Clearly failure to achieve this will significantly jeopardize use of solar arrays for MMII type missions. A far better solution would be to correct the LILT degradation phenomenon at the cell level. Until that can be demonstrated, a cell selection process is felt to offer the best alternative.

SOLAR ELECTRIC PROPULSION

The use of photovoltaics to power electric/magnetic engines for spacecraft has been evaluated for many years. Recent advances in thruster technology have lead to performance improvements renewing interest in outer planetary mission applications. Advantages of solar electric propulsion (SEP) systems include those of reduced flight time and enhanced spacecraft mass allowance. In order to use solar arrays for thruster power a number of concerns must be addressed, some of which are common to any deep space mission. First is the need for large area arrays. Typical SEP applications are based on the availability of multikilowatt power sources, between 25 and 30 kW at beginning of life. RTGs are not competitive at these levels. Obviously, high specific power (W/kg) becomes important for these power levels. In addition because of the very large size of these arrays methods for achieving lower specific cost ($/watt) will be very important. Although primary thrust performance is achieved near earth it is advantageous to maintain a high power output as long as possible. Consequently maintaining maximum solar array output requires accommodations of cell voltage variation with solar distance and avoidance of severe LILT degradation.

Although arrays of this size are not state-of-the-art, experience gained with the shuttle flown solar array flight experiment (SAFE), and present NASA-OAST programs for large area high performance arrays development are all applicable to SEP.

CONCLUSION

The need to provide for stability in the U.S. planetary exploration program has been addressed by NASA. The means for achieving this relies on the use of less complex, yet scientifically high priority, low cost missions. The potentially high cost of RTG power sources may jeopardize the viability of this approach. Photovoltaic solar arrays offer a low cost solution for powering a number of far earth missions. In order to achieve this it will be necessary to overcome a number of

obstacles. Due to reduced solar intensity large area arrays will be required, even for modest power outputs. These large sizes will in turn impact available mass allowances and spacecraft fields of view. The variation in array performance with solar distance must be accommodated in a manner that effectively meets the spacecraft power needs under all circumstances. The degradation in power output due to LILT conditions must be handled in a practical manner, if an outright solution is not feasible. Predictable power output is as important for a mission as is the quantity of that output. Although none of the above obstacles is considered insurmountable it will be necessary to address them during the next few years to establish technology readiness.

As an initial step in using solar arrays at far AU conditions, the Mariner Mark II Comet Rendezvous mission is examining the combined use of an RTG and a solar array. In this case the array is used to provide a modest augmentation in power, avoiding the costly addition of another complete RTG.

As a method of eliminating orientation mechanisms and controls, the array will be a washer shaped structure located colinear with the earth pointing high gain antenna. Use of this concept is dependent on a predictable and minimal LILT array power loss. Its success will provide a demonstration of the suitability of photovoltaic power systems for other interplanetary missions beyond the orbit of Mars.

REFERENCES

1. Planetary Exploration Through Year 2000, part one of a report by the Solar Exploration Committee of the NASA Advisory Council, U.S. Government Printing Office, Washington, DC 1983.

2. Luft, W., "Silicon Solar Cells at Low Temperature," Proceedings of the Eighth IEEE Photovoltaic Specialists Conference, Aug., 1970, pp. 161-168.

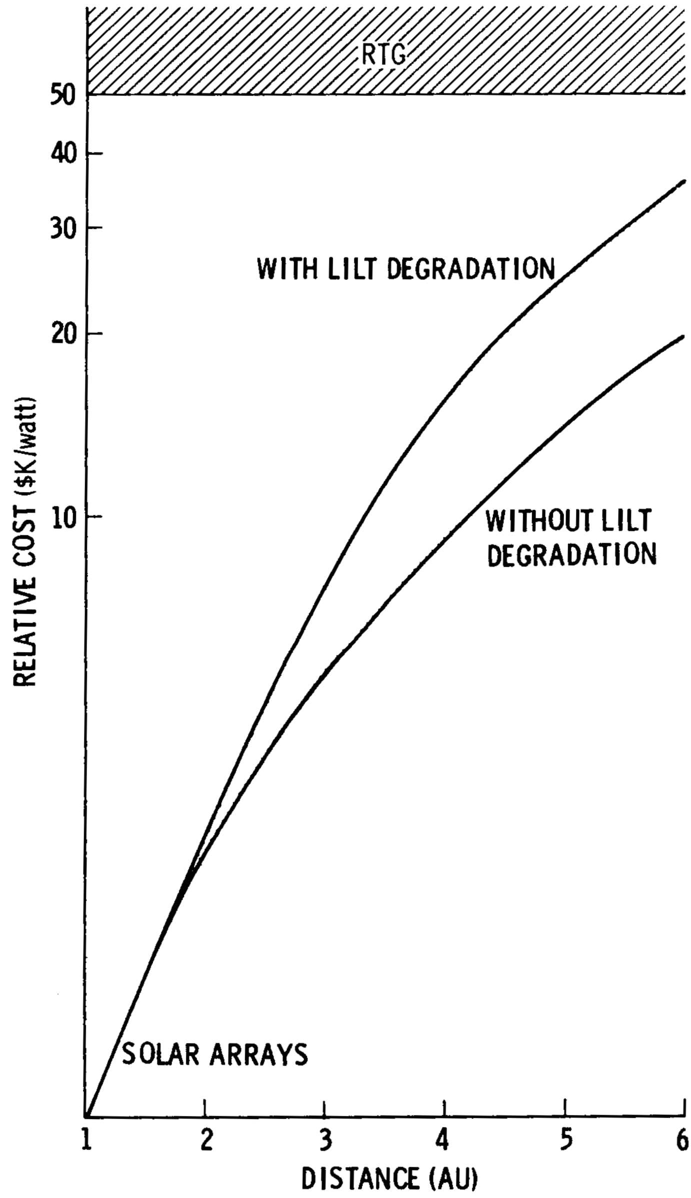

FIGURE 1. SOLAR ARRAY COST vs SOLAR DISTANCE

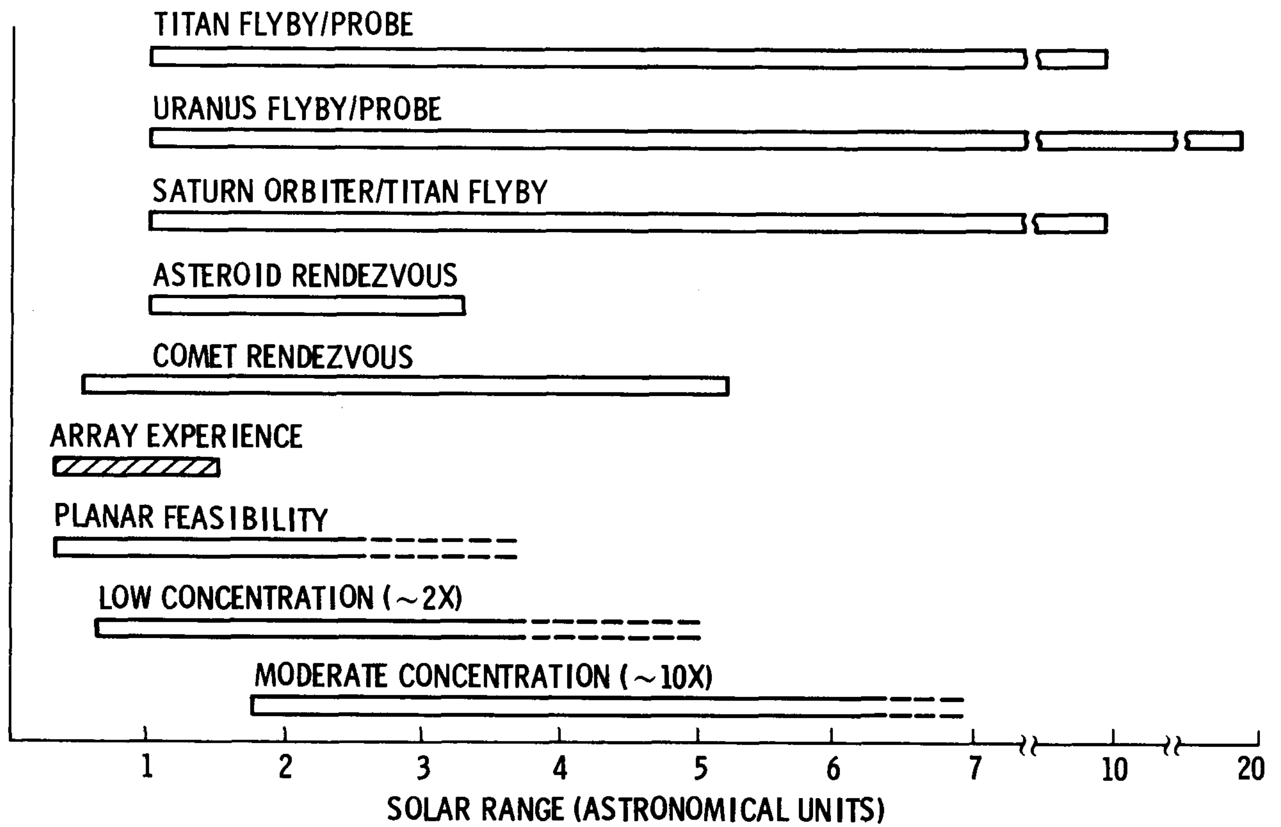

FIGURE 2. MARINER MARK II MISSIONS vs SOLAR DISTANCE

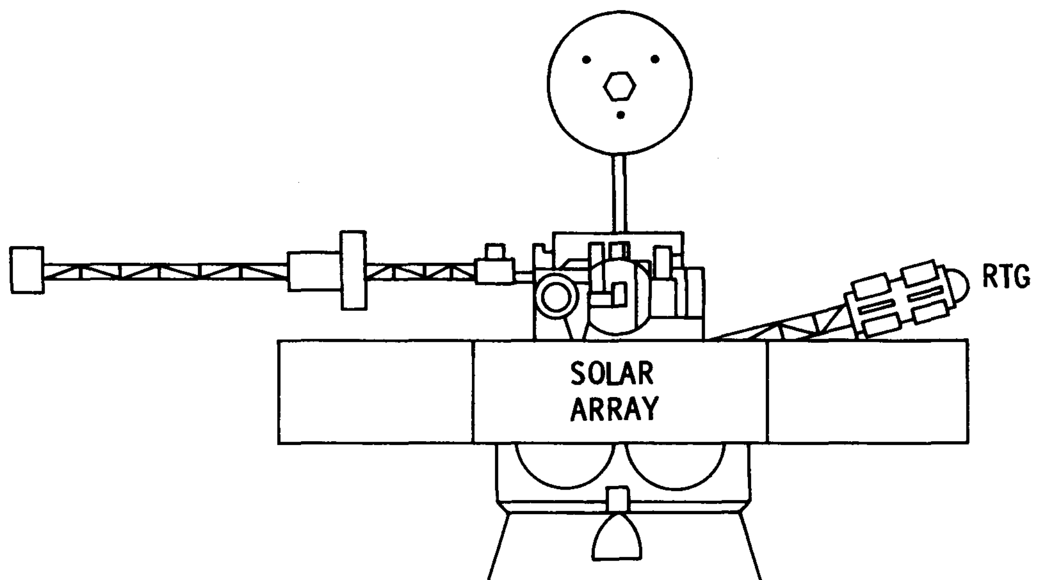

FIGURE 3. INITIAL MMII CRAF SPACECRAFT SOLAR ARRAY CONFIGURATION

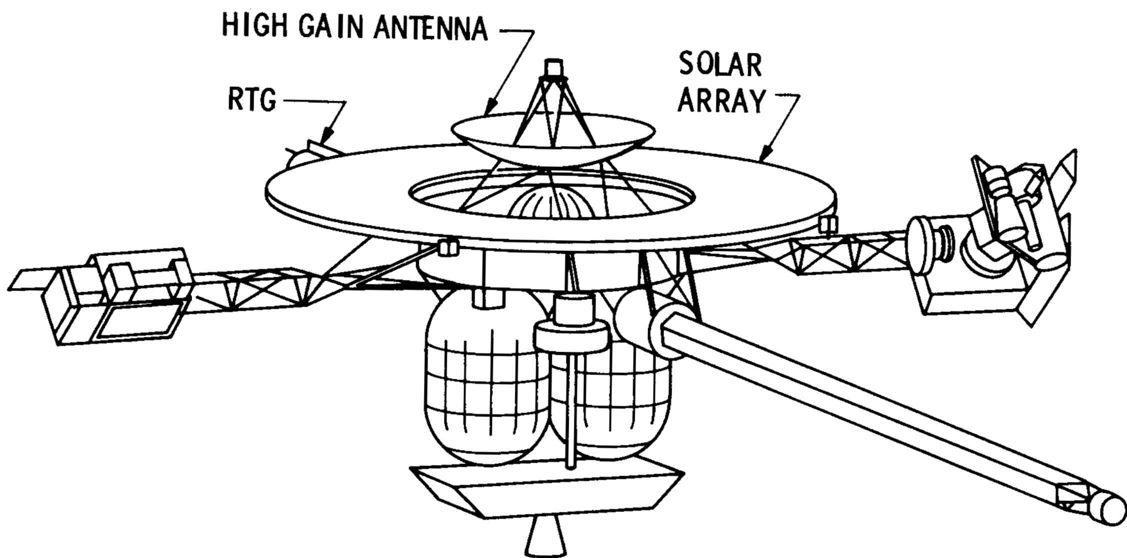

FIGURE 4. ADVANCED CONCEPT SPACECRAFT SOLAR ARRAY CONFIGURATON

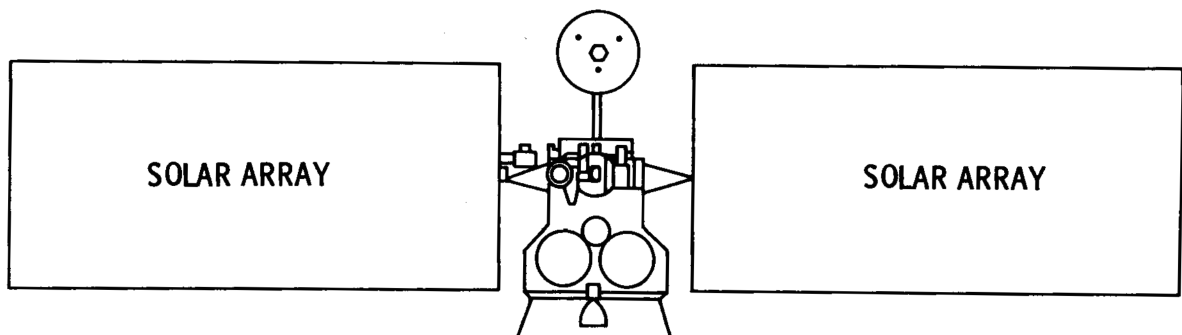

FIGURE 5. CONCEPTUAL MMII CRAF SPACECRAFT FULLY SOLAR POWERED

N86-17862

TWO YEARS OF ON-ORBIT GALLIUM ARSENIDE PERFORMANCE FROM THE LIPS SOLAR CELL PANEL EXPERIMENT

R. W. Francis
The Aerospace Corporation
Los Angeles, California

and

F. E. Betz
U. S. Naval Research Laboratory
Washington, D.C.

An analysis of the LIPS on-orbit performance of the gallium arsenide panel experiment is presented from flight operation telemetry data. Raw data, obtained from the NRL, was culled to preclude spurious results from large sun angles, shadowing, and measurements made on a cold array. Algorithms were developed by; and computerized at The Aerospace Corporation to calculate the daily maximum power and associated solar array parameters by two independent methods. The first technique utilizes a least mean square polynomial fit to the power curve obtained with intensity and temperature corrected currents and voltages; whereas, the second incorporates an empirical expression for fill factor based on an open circuit voltage and the calculated series resistance. Maximum power, fill factor, open circuit voltage, short circuit current and series resistance of the solar cell array are examined as a function of flight time. Trends are analyzed with respect to possible mechanisms which may affect successive periods of output power during two years of flight operation. Degradation factors responsible for the on-orbit performance characteristics of gallium arsenide are evaluated and discussed in relation to the calculated solar cell parameters. Performance trends and the potential degradation mechanisms are correlated with existing laboratory and flight data on both gallium arsenide and silicon solar cells for similar environments.

INTRODUCTION

The normally passive plume shield for a spacecraft upper stage rocket has been modified to incorporate an active payload by the Naval Research Laboratory. Partly in humor, the resulting satellite was named "Living Plume Shield," and the acronym "LIPS-II" has been widely embraced. An artist's rendition of the satellite is shown in Figure 1. The outer diameter of the body is 188cm (74 in.), and the inner diameter 142cm (56 in.). Maximum body thickness is 10cm (4 in.) at the inner ring and tapering to 38mm (1.5 in.) at the outer edge. The three solar array panels have solar cells mounted on both

sides and these provide the power generation capability to the spacecraft. One side of one panel contains 300 (2cm x 2cm) gallium arsenide (GaAs) solar cells while each of the other five sides contain 104 (2cm x 6cm) silicon (Si) solar cells. The U. S. Air Force developed GaAs cells were donated to the Navy in a cooperative program to build, test, qualify, and fly a GaAs solar panel.

The solar panels are stowed on the same surface as the antenna and gravity gradient boom, (which are also stowed) during launch and upper stage burn, and therefore protected from the rocket plume impingement. Shortly after the upper stage burn, LIPS-II is separated and is a free satellite in approximately circular orbit at 600nm with a 63° inclination. Antennas and solar panels are deployed and the satellite is subsequently despun and gravity gradient stabilized. As shown in Figure 1, the antenna and gravity gradient boom are earth pointing, providing stability in pitch and roll, but allowing freedom in yaw, damped only by hysterisis rods, which couple to the earth's magnetic field.

GaAs Panel Design

The GaAs solar cells were designed and fabricated by the liquid phase epitaxy (LPE) process developed by Hughes Research Laboratory, Malibu, under contract to the Aero Propulsion Laboratory, Air Force Wright Aeronautical Laboratories. The cells were transferred form the Air Force and assembled into a flight panel by Spectrolab under contract to the Naval Research Laboratory.

The orbit and experimental description is given in Table 1. Three circuits in parallel each consists of 25 cells in series by four cells in parallel for a total of 100 cells per circuit. The total of 300 GaAs cells has less active area than one Si cell panel surface each consisting of 52 cells in series by two cells in parallel. Both the GaAs and the Si cell panels were designed to produce similar voltages to power the LIPS-II. Figure 2 is a pictoral diagram of the GaAs panel layout.

A sun sensor is deployed diametrically opposite to the GaAs panel on the satellite. It is designed to quantify the deviation between the perpendicular to the GaAs panel and the sun line. This information is needed to accurately evaluate the panel output at other than nominal conditions. Additionally, a thermistor has been imbedded in the aluminum honeycomb panel substrate to sense the temperature of the back of a centrally located GaAs cell. Panel temperature, as indicted by this thermistor, together with the angle of solar incidence from the sun sensor, and intensity variations in the solar constant due to the earth orbit ecliptic are used to normalize GaAs panel data parameters.

EXPERIMENT DESIGN

An electronic experiment control package was designed and fabricated which allows the GaAs panel to contribute its power to the LIPS-II bus under normal conditions, and be commanded into an experiment mode to evaluate the GaAs performance. When activated, the entire 300 cell panel is disconnected from

the bus and electrically cycled through a simulated load sequence. The dwell at each step is approximately one second, during which time, ten data samples are transmitted to the ground station. The first step is an open circuit voltage (V_{OC}) measurement. The second step obtains short circuit current (I_{SC}). In actuality, the value is slightly off true Isc due to diode and line voltage drops. The third returns to V_{OC}. The fourth through seventh steps measure both current and actual voltage at approximately 22, 20, 18, and 16 volts. These step points were chosen to permit close evaluation of the current-voltage curve from beginning to end of life and under varying intensity conditions where voltage variations are second order effects. The eighth and final step of the experiment, returns the panel to the bus.

It is noted that the angle from the panel normal to the sun line and panel temperature are also in the telemetry with the panel electrical parameters.

DATA ACQUISITION AND REDUCTION

Once LIPS-II was in orbit, all telemetry and data are acquired in real time at NRL's Blossom Point Satellite Tracking and Command Station in Maryland. Typically the station "sees" LIPS-II for seven passes each day with varying pass duration up to about 20 minutes long. During those times, the sun angle is monitored, and if the sun line is within 45° of normal to the GaAs panel, the experiment is activated. Up to three activations of the experiment per pass are commanded if the sun conditions are acceptable. On many passes, no data at all is taken, since the satellite is free in yaw and its position relative to the sun cannot be controlled. Further, the ground station position relative to the satellite orbit may be unfavorable for an extended period, with passes occurring predominately at night when satellite eclipsing is likely. This condition may last for days until the satellite orbit precession and earth movement around the sun again produce favorable conditions for the experiment. Unfortunately, one of these extended data outages occurred for the first 30 days after launch, and beginning of life data was therefore lost.

Once data is acquired by the tracking station, it is converted to report form by an off-line data reduction and correction program. Current, temperature, and sun angle information are reported as received; voltages are corrected for diode and line drops and then reported as a raw value. A second data set is then generated by the Aerospace Computer Program, correcting the raw currents and voltages for intensity and temperature. The cosine of the angle to the sun and the solar constant correction as well as the appropriate temperature coefficient corrections are used to modify both current and voltage values. The temperature coefficients, α and β, used for current and voltage correction (Ref. 1) are 3.9×10^{-5} Ampere/°C and -2.04×10^{-3} Volt/°C, respectively. Raw telemetry data is normalized to 28°C and a solar insolation of 135.3×10^{-3} Watts/cm^2 (AMØ) normal to the panel surface.

Algorithms and a computer program (Ref. 2) were developed to obtain the normalized daily maximum power by two independent techniques (Ref. 3). The computer program discriminates against telemetry requiring large corrections for data normalization. This minimizes mathematical error from raw telemetry requiring large extrapolation. Therefore, temperature

correction is limited to between 0° and 50°C; sun angle between 0° and 25°; and percent allowable deviation from the ten previous calculated power data points to less than 15%.

After the telemetry voltages and currents are normalized, the two algorithms separately calculate the maximum power output for each revolution which, in turn, are statistically averaged on a daily basis. The LMS-Method incorporates a fifth order polynomial to approximate the power curve which is then maximized as a function of voltage. The order of the polynomial is excessive, but was used to maintain small deviations in curve fitting.

The FF-Method is based on parametric equations developed from solar cell empirical characteristics (Ref. 4). The pertinent input parameters for this method are open circuit voltage, short circuit current, and the calculated series and shunt resistances. The general equation is,

$$FF = \left(\frac{v_{OC} - \ln(v_{OC} + 0.72)}{v_{OC} + 1}\right)\left(1 - r_S\right) -$$

$$\left(\frac{v_{OC} + 0.7}{v_{OC}\, r_{SH}}\right)\left(\frac{v_{OC} - \ln(v_{OC} + 0.72)}{v_{OC} + 1}\right)^2 \left(1 - r_S\right)^2$$

v_{OC} ≡ open circuit voltage (V_{oc}) divided by (nkT/q)

r_{SH} ≡ shunt resistance (R_{sh}) divided by (V_{oc}/I_{sc})

r_S ≡ series resistance (R_s) divided by (V_{oc}/I_{sc})

For the LIPS-II experiment, calculated panel shunt resistances range between 600-1200 ohms. Therefore, the second term in the above equation is negligible. The fill factor is affected more by the series resistance, however, whose panel values are between 2 and 3 ohms. The above equation for fill factor reduces to:

$$FF = \left(\frac{v_{OC} - \ln(v_{OC} + 0.72)}{v_{OC} + 1}\right)\left(1 - r_S\right)$$

This value combined with the corrected I_{sc} and V_{OC} allows the maximum output power to be calculated.

Results and Analysis

Measurements taken at Spectrolab with an uncollimated xenon lamp prior to shipment of the LIPS-II GaAs solar cell panel gave 24.5 watts at 1 sun (AMØ) intensity and values for I_{sc} of 1.29A, V_{oc} of 25.2V, and FF (fill factor) of 0.76. This beginning-of-life (BOL) power equates to a 15.1% in panel cell efficiency. Figures 3 and 4 show on-orbit panel output power vs. time. BOL

data was not available after panel deployment in orbit, since the ground station position relative to the satellite orbit was unfavorable and eclipsing occurred during satellite monitoring for the first 30 days after launch. On day 32 after launch the GaAs panel's measured power output degraded 6.9% from the value at Spectrolab's facility. Most of the power loss is a result of the I_{sc} degrading by 6.2% (Fig. 5). V_{oc}, FF, and R_s (Figs. 6 through 8) are relatively unchanged during the first 32 days in orbit. It is only conjecture as to the cause, since the actual loss mechanism has not been identified. From day 32 to 550 the power degrades an additional 12.2% and again there is good correlation with it being attributed to the loss in I_{sc}. Again, there is little, if any, change in V_{oc}, FF, and R_s. After day 550, the trend appears to plateau and the power output degrades less. Power has degraded only 0.2 watts (0.8%) from a 2nd order smoothing curve through the daily averaged power measured up to 765 days after launch. Short circuit current has also degraded approximately the same amount with no change in the other parameters (Figs. 6 through 8). Power performance data and the corresponding solar array parameter values for I_{sc}, V_{oc}, and FF are listed in Table 2 for the three successive time periods discussed.

Data in Table 3 give the equivalent electron and proton 1-MeV electron fluences for both Si and GaAs solar cells (Ref. 5) in the 600 nmi/63° space radiation environment. The latter is based on damage coefficients obtained from JPL publication 84-61 (Ref. 6). The total 1-MeV electron fluences calculated for GaAs after 550 and 765 days are 1.82×10^{13} and $2.53 \times 10^{13} e \cdot cm^{-2}$, respectively; whereas, for Si they are 5.48×10^{13} and $7.62 \times 10^{13} e \cdot cm^{-2}$, respectively. According to the "Solar Cell Radiation Handbook" (Ref. 7), Si solar cells with both BSF and BSR will degrade 11-14% and those with only a BSR will degrade 2-4% after a total fluence of $5.48 \times 10^{13} e \cdot cm^{-2}$ (550 days) and a respective 13-16% and 3-6% after a 1-MeV fluence of $7.62 \times 10^{13} e \cdot cm^{-2}$ (765 days). On the other hand, p/n GaAs solar cells with an AlGaAs window layer will degrade 2.0% after $1.82 \times 10^{13} e \cdot cm^{-2}$ (550 days) and 2.5% in power output after $2.53 \times 10^{13} e \cdot cm^{-2}$ (765 days).

Due to the large discrepancy between the observed on-orbit and calculated irradiated GaAs power losses, anomalous power loss factors other than electron and proton radiation can account for such a discrepancy and still maintain a constant fill factor as shown in Fig. 7. These are listed in Table 4 with the observed degraded panel parameters that can account for each. The Air Force Wright Aeronautical Labs (AFWAL), Aero Propulsion Laboratory (APL), has undertaken the investigation of an equivalent GaAs solar cell panel, LIPS-I, that has not flown. The issues raised by the anomalous power loss mechanisms in Table 4 will be addressed as shown in Table 5 by mechanical and thermal stress testing the LIPS-1 panel and special irradiation tests on GaAs and Si solar cells.

Referring back to Table 3, one sees that Si will degrade approximately 2% from day 550 to day 765 after launch (i.e., an incremental $2.14 \times 10^{13} e \cdot cm^{-2}$ at 1-MeV after 550 days of irradiation exposure in low earth orbit). GaAs, how-

ever, will degrade only 0.5% after an additional increment of 7.10 x $10^{12} e \cdot cm^{-2}$ equivalent 1-MeV fluence after 550 days in orbit. This calculated power loss of 0.5% using the 1-MeV equivalent electron fluence model for GaAs incorporating GaAs damage coefficients is very close to the observed 0.8% power loss (see Table 2) between day 550 and 765 after launch. Apparently the anomalous power loss factors contributing to the large loss in output power from the GaAs panel from launch up to around day 550 after launch have subsided and/or the re-connecting of electrical interconnects and/or thermal annealing of GaAs is starting to take place.

The experimental results of the LIPS-II panel are beginning to look encouraging. Only more orbital telemetry after more exposure to the geomagnetically trapped radiation of space will demonstrate and confirm the projected advantages of GaAs solar cells for primary power applications in a space environment.

Summary and Conclusions

The first two years of on-orbit telemetry from the LIPS II gallium arsenide solar cell panel experiment was evaluated to determine power output performance and degradation vs. time in orbit. The power loss associated with decreasing short circuit current but constant fill factor, open circuit voltage and series resistance during the first 550 days after launch is excessive. The loss is attributed to anomalous optical and/or mechanical panel degradation factors which overwhelm the power output loss due to the electron and proton omni-irradiation environment in free space. During the period following 550 days, a decreasing trend in the power loss rate is observed. This region of power output decay can be described by the 1-MeV equivalent electron fluence model with GaAs damage coefficients inputed for the Si damage coefficients.

ACKNOWLEDGMENTS

The authors wish to give special thanks to Dr. B. E. Anspaugh of the Jet Propulsion Laboratory for his helpful discussions and valuable technical input. In addition, much appreciation is extended to my colleague L.T. Bavaro for his guidance and consultation in the development and use of the computer software.

References

1. "A Method for Predicting Solar Cell Current-Voltage Curve Characteristics as a Function of Incident Solar Intensity and Cell Temperature," by J. D. Sandstrom, JPL Technical Report 32-1142, July 15, 1967.

2. "LIPS Gallium Aresnide Solar Array," by M. P. Pennell, The Aerospace Corporation, ATM-83(3524-03)-1, August 10, 1983.

3. "On-Orbit Performance of LIPS Gallium Arsenide Solar Cell Experiment," by T. Bavaro, R. W. Francis, and M. Pennell, Proceedings of the Space Photovoltaic Research and Technology Conference, NASA Publication 2314, pp. 81-89, 1983.

4. "Solar Cell Fill Factors: General Graph and Empirical Expressions," by M. A. Green, Solid-State Electronics, Vol. 24, No. 8, pp. 788-789, 1981.

5. "Solar Cell Radiation Model Computer Program," Aerospace Corporation Power Sources Section, 1985.

6. "Radiation Effects in Silicon and Gallium Arsenide Solar Cells Using Isotropic and Normally Incident Radiation," by B. E. Auspaugh and R. G. Downing, JPL Publication 84-61, September 1, 1984.

7. "Solar Cell Radiation Handbook," by H. Y. Tada, J. R. Carter, B. E. Anspaugh, and R. G. Downing, JPL Publication 82-69, November 1, 1982.

8. Private communication with B. E. Anspaugh, JPL, Pasadena, CA, July, 1984.

LIPS II

LAUNCH DATE:	10 FEB 83
ORBIT:	CIRCULAR
ALTITUDE:	600 nmi
INCLINATION:	63°
ORBITAL PERIOD:	1.8 hr

GaAs Experiment

1-PANEL:	4P x 25S x 3 CKTS
CELLS:	300 EACH (2 x 2 x 0.036 cm), 15.5%
COVERGLASS:	0.03 cm (0.012 in.) FS/UV-FILTER
POWER (BOL):	24.5W AT 30°C

Table 1

Observed GaAs Panel Power Loss

DAYS FROM LAUNCH	P_{MAX} (W)	I_{SC} (A)	V_{OC} (V)	FF
0 - 32	24.5 - 22.8 -6.9%	1.29 - 1.21 -6.2%	25.2 - 24.7 -2.0%	0.76 - 0.78 +2.5%
32 - 550	22.8 - 19.8 -12.2%	1.21 - 1.07 -10.8%	24.7 - 24.1 -2.4%	0.78 - 0.78 0.0%
550 - 765	19.8 - 19.6 -0.8%	1.07 - 1.06 -0.8%	24.1 - 24.1 0.0%	0.78 - 0.78 0.0%
TOTAL	-19.9%	-17.8%	-4.4%	+2.5%

Table 2

Calculated Space Radiation Environment

	FLUENCE-Si (equiv 1-MeV e/cm^2)	FLUENCE-GaAs (equiv 1-MeV e/cm^2)	%PMAX AFTER 550 DAYS	%PMAX AFTER 765 DAYS
ELECTRONS	7.57×10^{11} /yr	6.80×10^{11} /yr	Si 11 - 14%	Si 13 - 16%
PROTONS	3.56×10^{13} /yr	1.14×10^{13} /yr	GaAs 2.0%	GaAs 2.5%

Table 3

Anomalous Power Loss Factors which Maintain Constant Fill Factor

I. SPECTRAL TRANSMISSION LOSS

- DECREASING I_{SC}

II. FAILED-OPEN CELL INTERCONNECTS OR CRACKED/BROKEN CELLS, LEAD TO REVERSE-BIASED PARALLEL CELLS

- PROMINENT I_{SC} DECREASE (reverse cell characteristics control)
- SMALL V_{OC} LOSS

III. LOW ENERGY PROTON OMNI IRRADIATION ON UNFILTERED GaAs CELL AREAS (bus edges and lifted metal contacts)

- DECREASING I_{SC} WITH FLUENCE
- SMALL V_{OC} LOSS WITH FLUENCE

Table 4

LIPS-I Investigation

- ISSUES TO BE RESOLVED AT AFWAL/APL
  - MECHANICAL DEGRADATION STRESS FACTORS
  - THERMAL CYCLING TO STIMULATE ORBITAL CONDITIONS
  - SPECIAL RADIATION EDGE EFFECTS ON GaAs vs Si SOLAR CELLS

Table 5

LIPS II Living Plume Shield

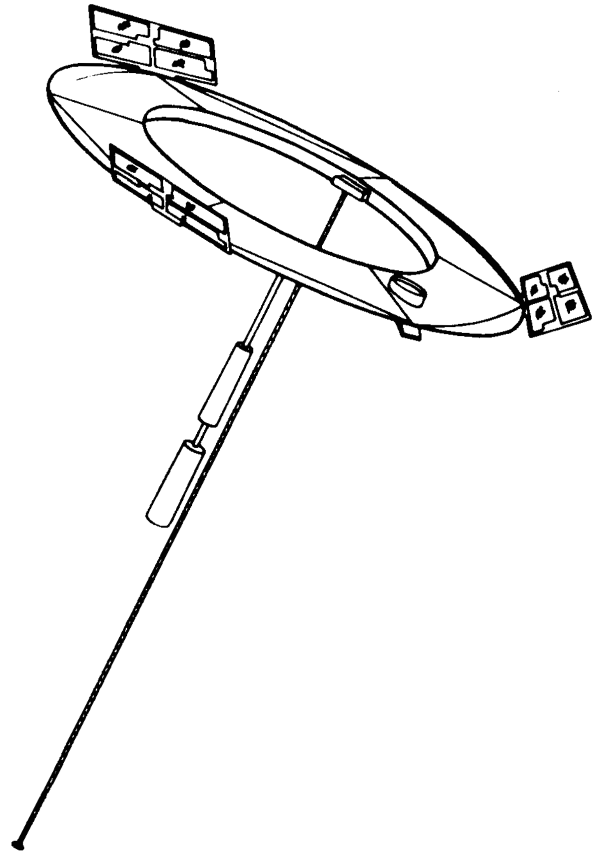

Figure 1

LIPS II Gallium Arsenide Solar Panel Layout

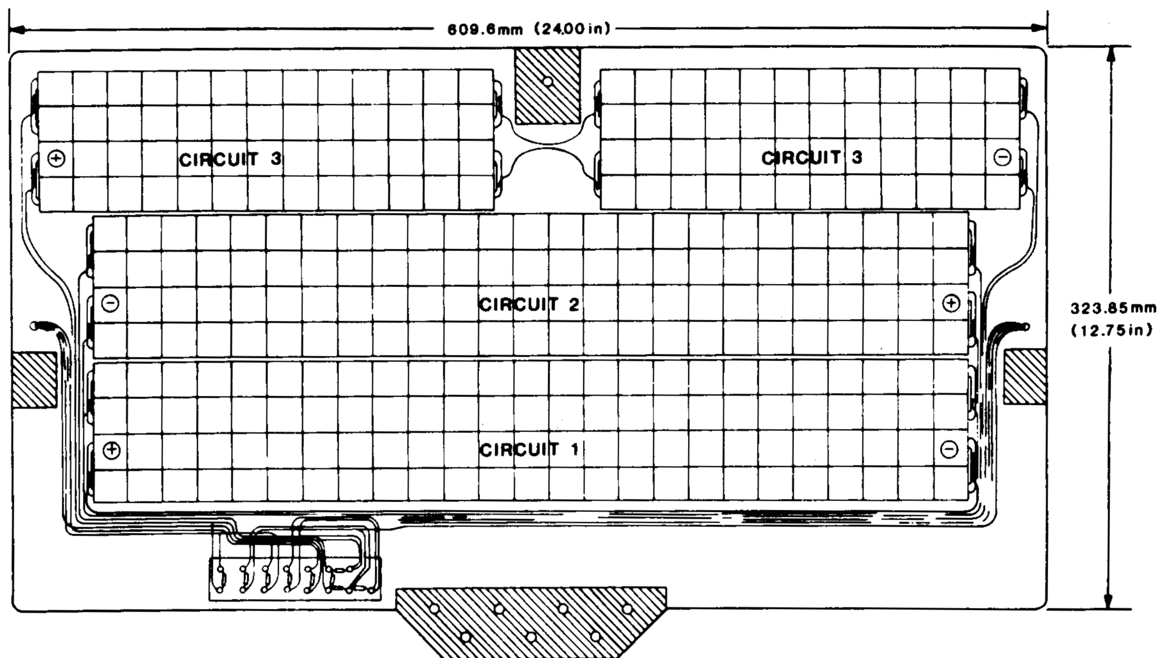

Figure 2

Maximum Power (LMS Method) with Second Order Smoothing Curve vs Days from Launch

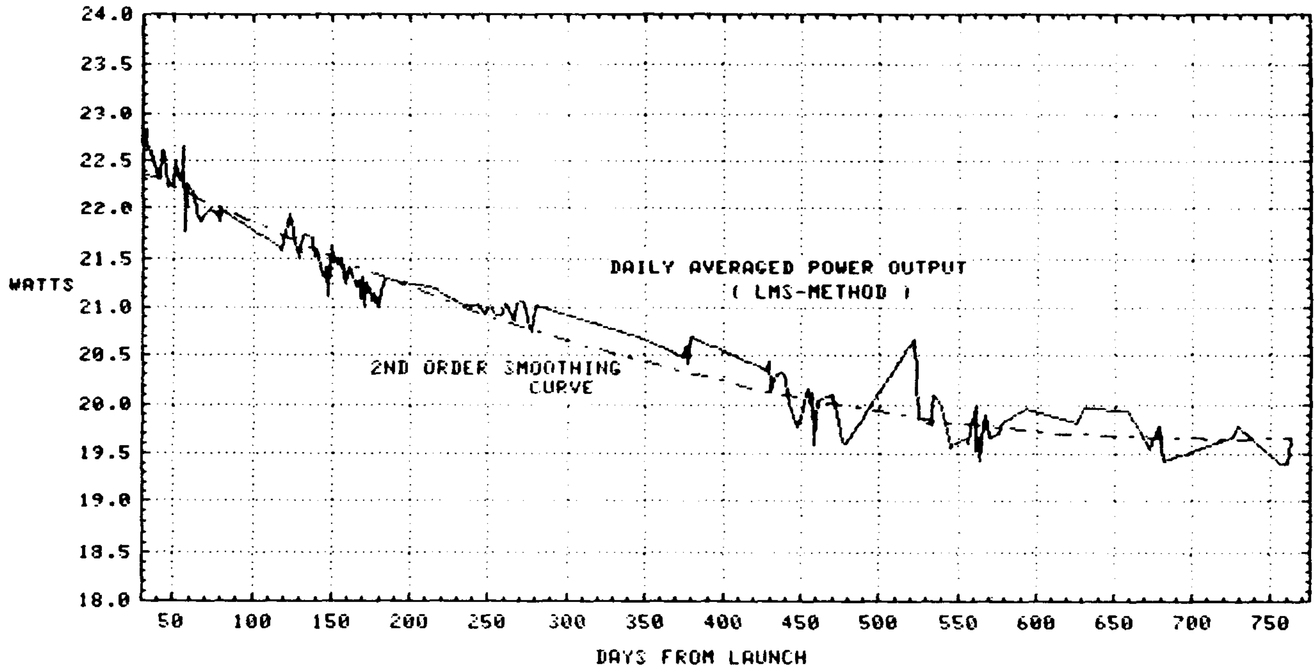

Figure 3

Maximum Power (FF-Method) with Second Order Smoothing Curve vs Days from Launch

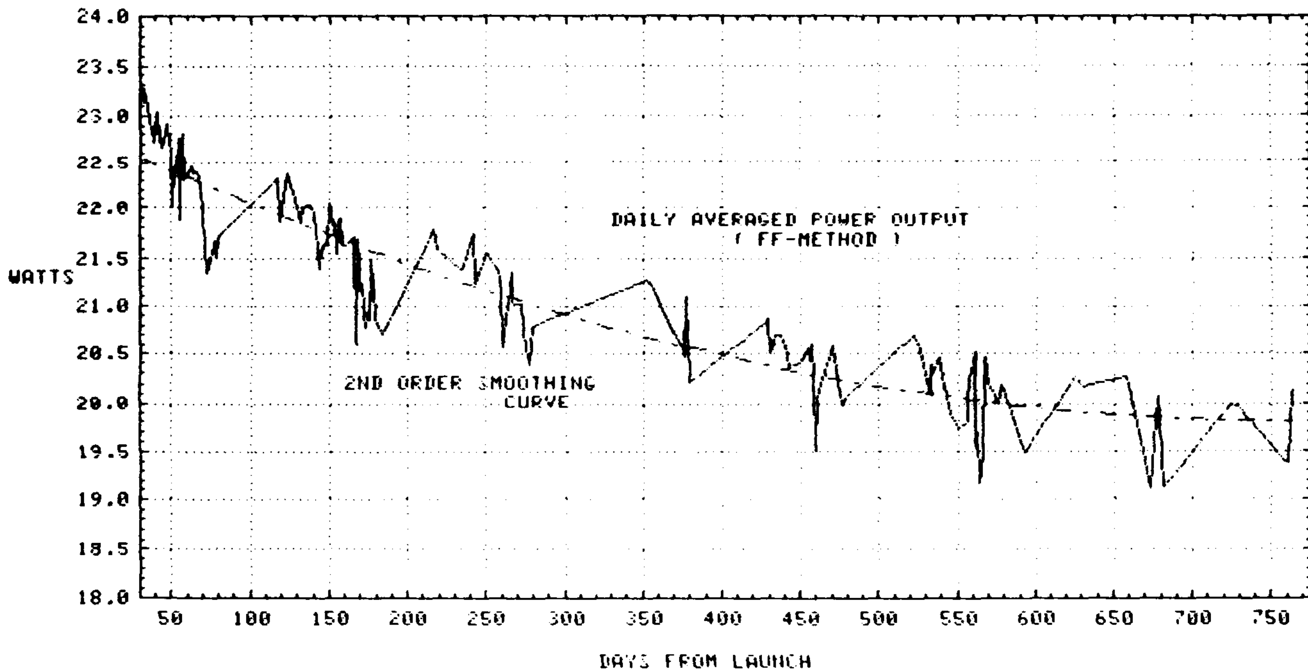

Figure 4

Short Circuit Current vs Days from Launch

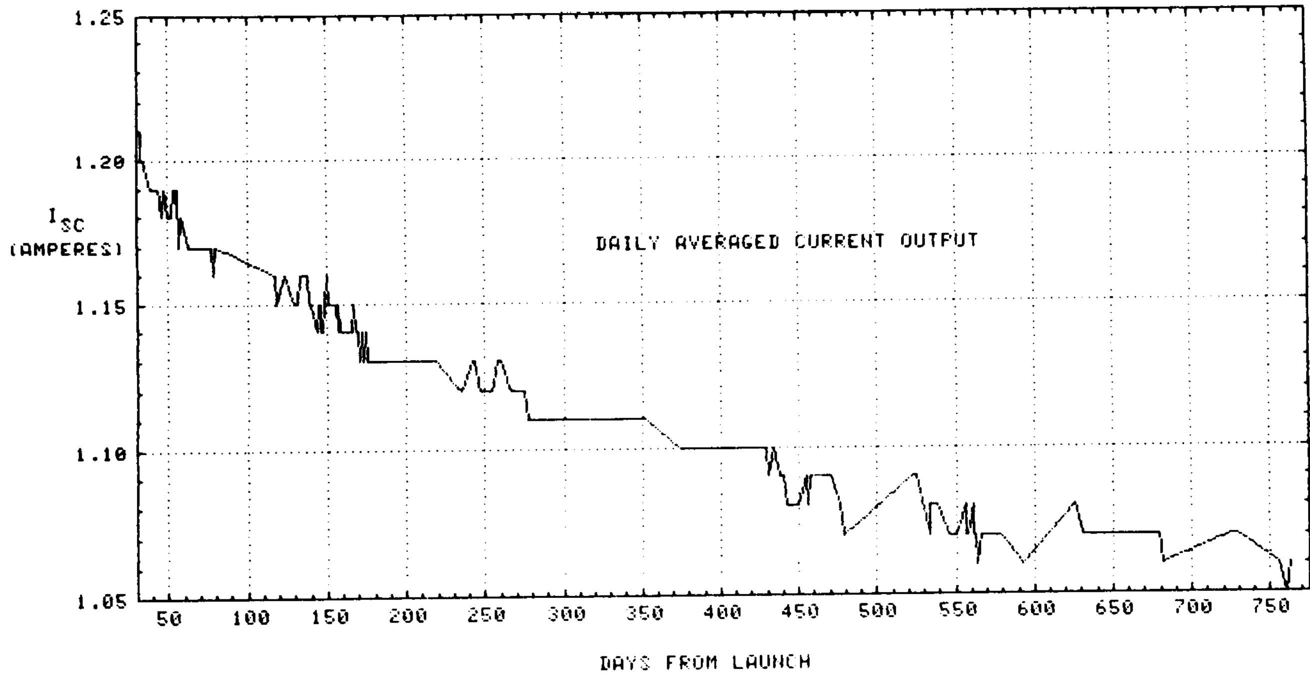

Figure 5

Open Circuit Voltage vs Days from Launch

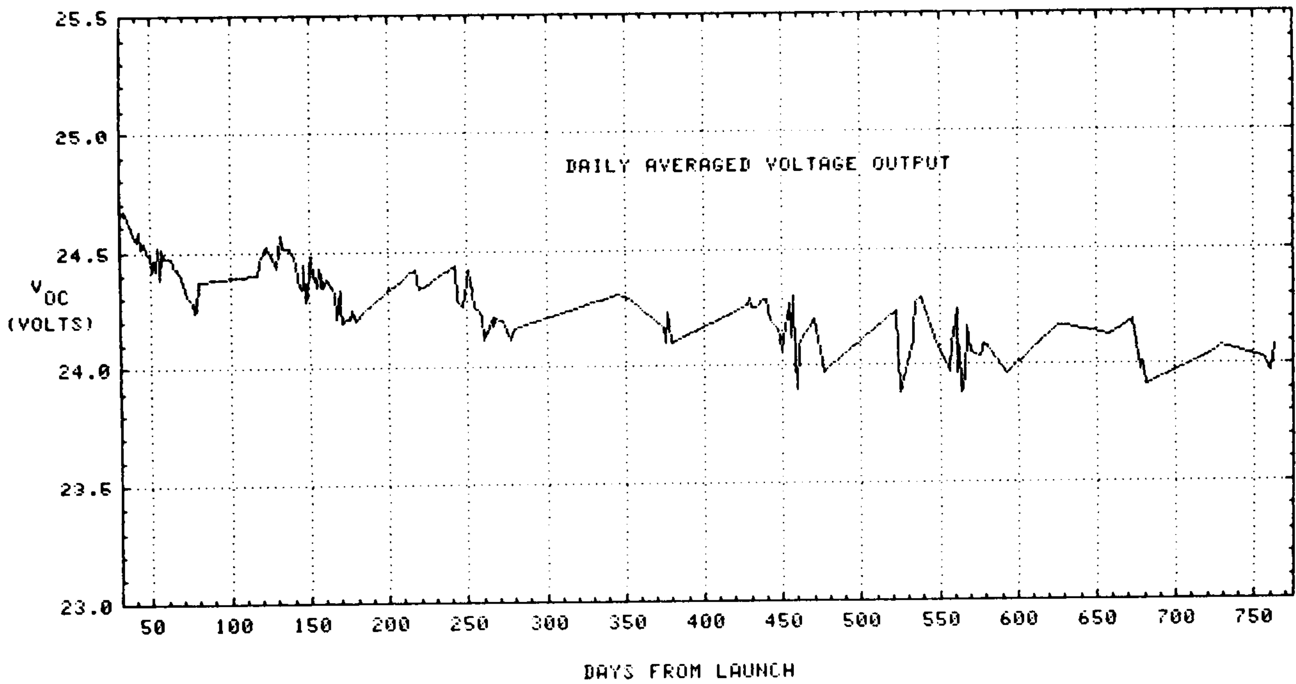

Figure 6

Fill Factor vs Days from Launch

ORIGINAL PAGE IS
OF POOR QUALITY

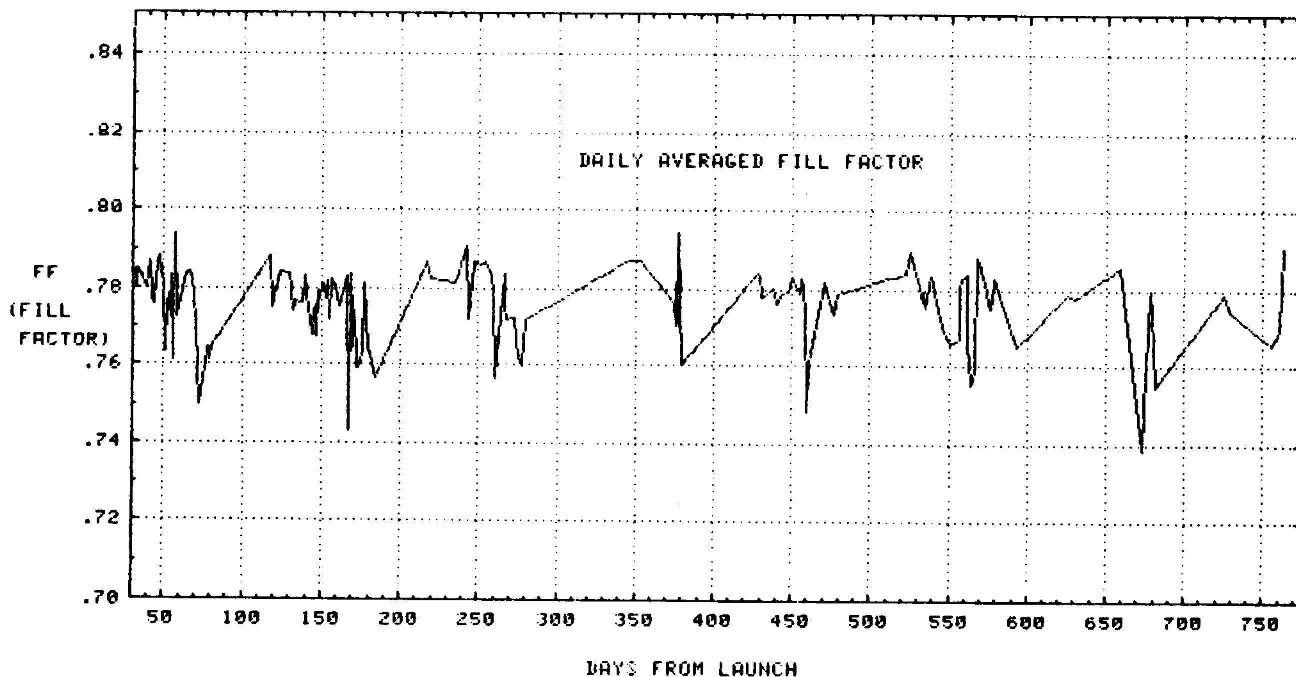

Figure 7

Series Resistance vs Days from Launch

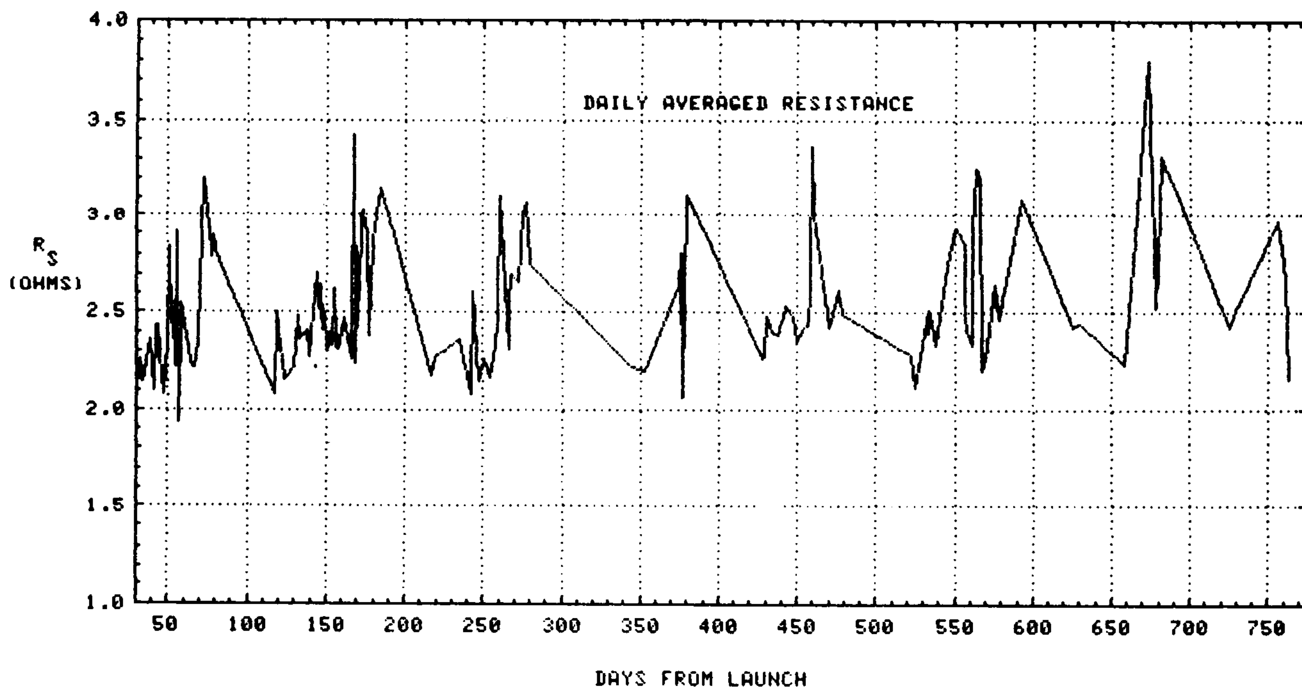

Figure 8

N86-17869

PASP - A HIGH VOLTAGE ARRAY EXPERIMENT

John Scott-Monck
Jet Propulsion Laboratory
California Institute of Technology
Pasadena, California

Robert Morris
Air Force Wright Aeronautical Laboratories
Aero Propulsion Laboratory
Wright Patterson AFB, Ohio

In the near future, Air Force mission payloads will require significant increases in power. Sophisticated sensing systems such as infrared focal plane detector arrays and radar will be employed by the Air Force to fulfill its strategic objectives. Such payloads will demand that the power subsystem provide up to 50 kW at the end of mission life, more than an order of magnitude greater than is currently required. Some of these payloads must be flown in low-earth (<600 km) polar orbits in order to satisfy mission objectives, thus it is likely that large (500-600 m^2) solar photovoltaic arrays will have to operate in the low-earth polar environment.

The "standard" 28 volt power subsystem is not weight efficient for the array power levels (~50 kW) being considered. Figure 1 illustrates the impact of the solar array operating voltage on the total weight of the array and the subsystem power conditioning and distribution components. Therefore, in the interest of reducing power subsystem weight, higher array operating voltages must be considered. This, however, introduces new problems for the array designer, as will be discussed.

In order to provide a maximum return on the tremendous investment of resources (many hundreds of million dollars) required to develop and place these assets in orbit, they must be designed to operate effectively for extended periods of time (up to 10 years). To achieve this capability, the system must be able to function in the threat-induced and natural space environment.

Traditionally, the major natural threat to Air Force assets has been the relatively high energy (>100 keV) portion of the space radiation environment. A tremendous accumulation of flight data plus characterization of the radiation environment has allowed ground test methods to be developed that adequately simulate the effect of this environment on the performance of solar arrays.

However, within less than a decade, a large body of evidence has been accumulated that powerfully argues that the low-energy space plasma (<100 keV) environment will be the major natural threat to the next generation of Air Force systems, regardless of orbit. The SCATHA and PIX-1 flight experiments (Ref. 1, 2) have clearly indicated that plasma-induced events are capable of producing catastrophic effects on the spacecraft's operational capabilities, including failure of the spacecraft.

PRECEDING PAGE BLANK NOT FILMED

Although the space plasma environment has been fairly well characterized, it can easily be perturbed by natural changes in the earth's magnetosphere or the presence of a relatively large (>100 m^2) spacecraft subsystem or payload such as a solar array or radar. The interaction of the perturbed plasma with such a body can lead to conditions that produce high voltage discharges, current leakage to the plasma, and electromagnetic interference. Plasma-induced arcing can lead to sudden significant losses in array power or in the worst case, total loss of power. Electromagnetic interference can compromise the operations of other subsystems or the payload in a completely random fashion. Array current drain to the plasma is a situation that may prove to be a threat to the performance of the solar array.

The PIX-1 experiment verified laboratory experiments conducted on small (~100 cm^2) array samples. Also, the PIX data confirmed the observation that for positive bias voltage, the plasma coupling current changes from being proportional to the amount of exposed array interconnect area at below 100 volts to being proportional to the total array area at above 250 volts. The magnitude of the post transition (>250 volts) plasma coupling current was also shown to be related to the space plasma density. Of even greater significance, array discharge (arcing) was produced at negative voltage levels which agreed with ground-based experiments.

The present view, based on the PIX results plus NASCAP computer modeling studies, is that the effect of high positive array bias voltage is of minor concern compared to the effect of high negative voltage which is more likely to be predominant over most of the area of large solar arrays operating in the space plasma environment. However, it should be pointed out that PIX-1 only confirmed the results obtained in laboratory tests of small array samples. PIX-1 did not use an array test sample that was operating in sunlight, nor was data obtained on photoelectrically-generated plasma interactions that may occur when the array enters sunlight from occultation. Finally, PIX-1 did not experience the effects of an auroral substorm-induced plasma environment. The proposed Photovoltaic Array Space Power (PASP) experiment is aimed at providing this kind of data as well as acting as a check on the PIX data.

The PASP experiment, which is being sponsored by the Air Force Wright Aeronautical Laboratories, Aero Propulsion Lab, (AFWAL/APL) has been designated to be one of the elements comprising the Interaction Measurement Payload for Shuttle (IMPS) multiprobe experiment package scheduled to be flown in late calendar year 87 or early 88. IMPS will be a free-flier experiment, released from a Vandenburg launched Shuttle and planned to function in a noon/midnight, low-earth polar orbit, for up to eight days. The carrier for the IMPS package is to be the Shuttle Pallet Satellite (SPAS), which was built by MBB and has flown from previous NASA shuttle missions.

The IMPS multi-probe will consist of a complex environmental measurements experiment being developed by the Air Force Geophysics Laboratory (AFGL), the PASP experiment, and at least two other instrument packages designed to assess the influence of the low-earth polar space environment on materials and components essential for the success of future Air Force missions. Due to the limitations associated with the amount of attitude control gas carried by the SPAS, the critical portions of the PASP experiment are being sequenced to obtain the essential data during four consecutive orbits. Since the PASP requirements have to be coordinated with those of other IMPS experiments, it is not yet possible to accurately describe the PASP experiment sequence.

PASP OBJECTIVES

The objective of the PASP experiment is to develop an instrument package that, operating in conjunction with a number of conventional and potentially survivable Air Force array designs, will provide engineering and scientific information concerning the influence of the low-earth polar orbit plasma environment on solar array performance.

There are six main data objectives for the PASP experiment. The first, and most important from an engineering sense, is to determine how much the array samples discharge or arc as a function of negative bias voltage, space plasma density, and plasma temperature, since these measurements will be made in both polar regions and the equatorial (higher plasma density) portion of the orbit. The second objective is to measure electromagnetic interference (amplitude, rise-time, polarity, etc.) generated by the array samples when they arc. This will hopefully be done for both hard-wire and radiated components.

The third objective is to measure the array samples' current leakage to the space plasma, a potential power loss factor, as a function of positive bias voltage and plasma environment. The fourth objective is to measure the plasma density and temperature in the vicinity (<50 cm) of the test arrays. The fifth objective is to measure the power output and temperature of each array under actual (illuminated) operating conditions. This measurement is very important since it will likely be the first time that certain array designs (concentrator) are flown in space. The final objective is to verify or modify more cost-effective ground simulation techniques, including computer modeling and plasma-chamber testing, particularly for the as yet untested concentrator designs.

PASP INSTRUMENT DESCRIPTION

The experiment is planned on the assumption that the PASP instrument package will contain: (1) a Langmuir probe to measure the plasma environment in the very near (<50 cm) vicinity of the test array modules, (2) an I-V curve tracer to measure the power output of each test array, (3) a sun sensor to assure proper array test conditions, (4) a high voltage power supply to negatively and positively bias the test arrays to a maximum of 500 V in controlled steps, (5) a wide dynamic range electrometer to measure coupling currents over the range of 1×10^{-6} to 1 A, and (6) temperature sensors (thermistors) on each array module. Electromagnetic interference will be measured by a transient pulse monitor included in the IMPS environmental measurements experiment.

There will be five different types of solar array modules tested. Each module will be mounted as an electrically isolated entity from spacecraft common. There will basically be three types of measurements performed on each module: (1) current-voltage (I-V) characteristic curves, (2) DC plasma coupling current as a function of positive and negative bias voltage with the module in an open-circuit voltage mode, and (3) AC "noise" as a function of positive and negative voltage in the open-circuit mode. In this open-circuit mode, the modules will actually be loaded with a very high impedence, allowing a minute current flow, thus insuring proper voltage gradients across the modules. Any "noise" generated by the arrays

due to interactions with the space plasma will be measured and recorded by a companion experiment also on the SPAS. A sixth advanced technology cell design module may also be included for I-V curve testing, depending on availability in time for the flight. A complete description of the proposed test modules will be provided in a subsequent section of this paper.

Both of the above-described measurements will be performed when the modules are oriented normal to the sun within plus or minus one and one-half degrees. Sun orientation will be performed by gas thrusters on the SPAS controlled by commands from the Shuttle, based on signals received from the sun sensor mounted on the PASP panel.

This tight sun pointing requirement is necessary to obtain accurate I-V data on the power output of the concentrator test modules. Slight deviations in the acquisition of the sun by the concentrator optics will cause the amount of energy focused on the solar cells to be substantially reduced. For example, the mini-Cassegrainian module will lose almost seven percent of the incoming solar energy if the misalignment to true sun normal is only about two degrees (Ref. 3). The sun angle tolerance for the Survivable Low Aperature Trough System (SLATS) concentrator design is equally stringent (Ref. 4), thus requiring the plus or minus one and one-half degrees sun pointing. The data acquisition described above is planned to be performed during four successive Earth orbits after the SPAS has been released from the shuttle bay and placed in a free flier mode.

During any orbits in excess of the four in which attitude control is available, the PASP will be put into a drift mode. In this mode, the silicon array module will be biased by a "constant" voltage (probably about -300 V) and the leakage currents, arc discharges and sun incidence angle will be monitored regularly; about every second for the plasma interaction events and every five to ten minutes for the sun angle. Also during this time, the Langmuir probe will be acquiring information about the plasma environment around the test module. The information obtained during this drift mode will provide a sort of "map" of the entire low-earth polar orbit and how the array module interacts with it while at a high negative voltage.

Figure 2 shows a block diagram of the proposed PASP instrument. It is assumed that the SPAS vehicle will provide the battery power and data recording capability to support the PASP instrument during the free-flight portion of the IMPS mission.

PASP TEST MODULES

Five solar array modules will be tested as part of the PASP measurements package. Module 1 will consist of 100 series-connected silicon solar cell assemblies (covered solar cells) mounted on an insulated aluminum honeycomb substrate. The cells will be nominal 2 cm x 4 cm in size and are representative of the type now used for Air Force missions. Module 2 will consist of 100 series-connected by two parallel-connected gallium arsenide (GaAs) solar cell assemblies, 2 cm x 2 cm in size, mounted on the same type of substrate as the silicon array module. The cover glass and adhesive will be the same as that used for the silicon module.

Modules 1 and 2 are representative of the standard configuration now used for arrays and will act as benchmarks for the other three test modules and as a basis of comparison to previous flight data from the PIX-1 experiment. Modules 3, 4 and 5 represent advanced Air Force array designs that show high potential for survivability. Their unique configurations also make them well suited to significantly expand the existing scientific data base on the subject of plasma interactions.

Module 3 will be composed of an eight element concentrator using GaAs solar cells. This design, known as the mini-Cassegrainian concentrator (Ref. 3), is capable of providing an effective solar concentration of approximately 80 times normal.

Module 4 is another concentrator configuration, SLATS (Ref. 4). The baseline design consists of a semi-parabolic primary reflector which also serves as a thermal radiator; compound elliptical second-stage optics for gathering off-axis rays, and in-line GaAs solar cell assemblies mounted at the exit aperture of the second stage optics. The module will be approximately three times the size of the mini-Cassegrainian, or about 0.75 ft^2.

Module 5, designated Integral Cover Array (ICA), is a conventional silicon solar cell module, except that it will be totally encapsulated using a deposited dielectric coating composed of silicon dioxide (SiO_2) and aluminum oxide (Al_2O_3). The thickness of the deposited layer will be between 3 and 5 mils since it is required to offer adequate protection to the solar cell from the low energy proton environment of space. The module will be approximately the same size as the mini-Cassegrainian.

A sixth module may be included for the purpose of measuring its I-V characteristics. This module will consist of 10 to 25 AlGaAs/GaAs stacked multi-bandgap solar cells. Inclusion of this module, however, depends on the availability of MBG cells. At the present time, the prospects for including this sixth module in the PASP package look rather dim.

GROUND TESTS AND MODELING

As previously mentioned, an important part of the PASP objective is to verify existing ground test techniques for solar array performance in the low-earth polar environment. This verification is particularly important for the advanced design modules which have not yet been flown in space. To achieve this goal, the PASP experiment will be "simulated" in two ways; computer modeling and plasma-chamber exposure. The flight-data will be compared to the ground tests which can then be verified for accuracy or modified using the flight-data as a basis.

Preliminary computer modeling of PASP has been performed at NASA-LeRC by an Air Force Institute of Technology (AFIT) student, Capt. Karl Reichle, for AFWAL/APL using the NASCAP/LEO code. The objective of this preliminary modeling was to define the plasma environment around the SPAS vehicle during execution of the PASP experiment sequence and to establish what effects PASP-induced potentials have on the remainder of the SPAS. Initial results indicate that biasing the largest PASP array modules (Si or GaAs) to high voltages drives the SPAS ground

potential much less than expected. A complete report on this modeling is expected in June 1985, at which time more concise quantitative information will be available.

Future modeling using the NASCAP/LEO code will incorporate more accurate information on other experiments aboard the SPAS vehicle (as it becomes available) and will involve investigating widely varying array potentials, plasma environments, and resulting plasma-coupling interactions. Similar computer modeling will be performed using the POLAR code at AFGL, which is designed specifically for analyzing the polar orbit environment, as opposed to LEO, which is designed for general low-earth orbits.

Plasma-chamber simulations will be performed by NASA-LeRC on sample modules representative of the actual PASP flight array modules. These simulations will be composed of exposing the array samples to different plasma environments under different bias voltages and monitoring any interactions. It should be interesting to see how the flight data compares with these results, particularly for the concentrator designs with their inherently large exposed metal surfaces and the ICA module which has very little exposed conductor area due to the interconnects being covered.

CONCLUSIONS

The PASP experiment has the potential of providing a great deal of significant information on both the low-earth polar plasma environment and its influence on the performance of advanced survivable arrays that will be necessary to support future Air Force missions operating in this challenging environment. It is also likely that the initial flight will generate new questions that may require additional flight experiments. Anticipating this, the PASP experiment is being designed to be easily modified and reflown.

It is worth observing that the current status of our understanding and appreciation of the major impact that the plasma environment can have on photovoltaic power systems is akin to the situation faced by array designers in the early 1960s when it became obvious that the natural high-energy space radiation environment had been badly underestimated. The PASP and the NASA-Lewis VOLT (voltage-operating-limit-test) experiments are examples of the growing appreciation that DOD and NASA are now attaching to understanding the space plasma environment.

REFERENCES

1. D.A. McPherson and W.R. Schober, "Spacecraft Charging at High Altitudes: The SCATHA Satellite Program," Progress in Astronautics and Aeronautics: Spacecraft Charging by Magnetospheric Plasmas, Vol. 47, edited by A. Rosen, AIAA, New York, 1976.

2. N.T. Grier and N.J. Stevens, "Plasma Interaction Experiment (PIX) Flight Results," Proceedings of the Spacecraft Charging Technology Conference, Air Force Academy, Colorado Springs, CO, Oct. 1978.

3. R.E. Patterson and W.L. Crabtree, "Cassegrainian Concentrator Solar Array Exploratory Development Module," Proceedings 17th IECEC, Los Angeles, CA, Aug. 1982, p. 1589.

4. T.G. Stern and E.W. Hayes, "Structural Design for High-Power Parabolic Trough Concentrator Arrays in Space," Proceedings 17th IEEE Photovoltaic Specialists Conference, Kissimmee, FL, May 1984, p. 326.

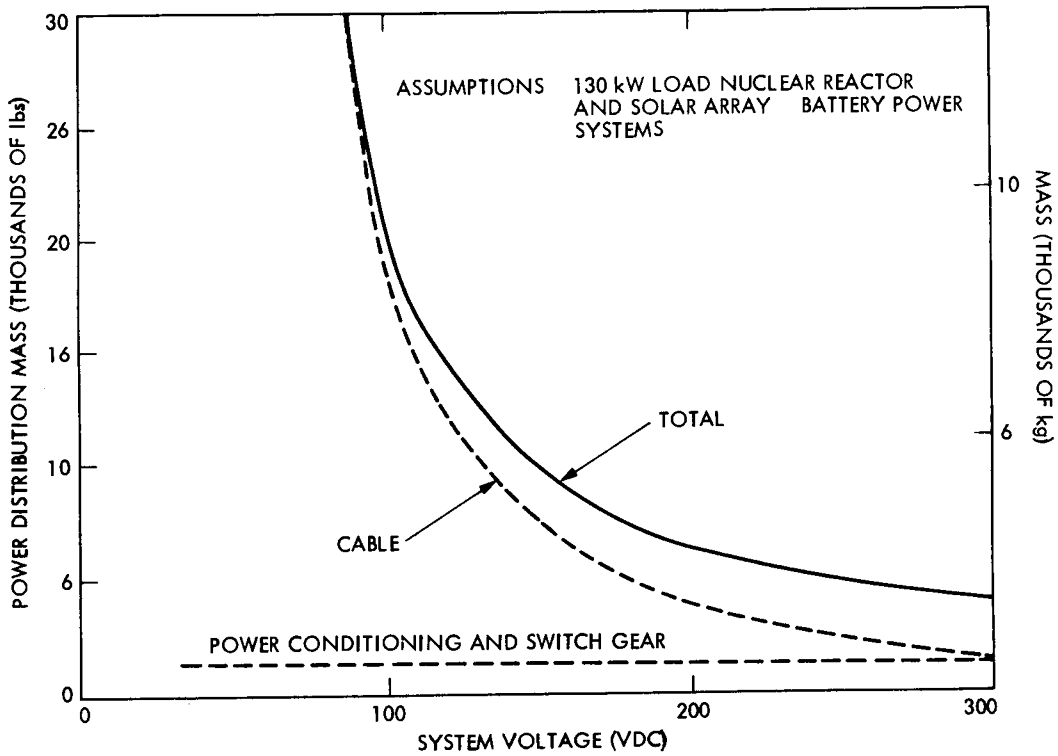

Figure 1. Effect of Array Operating-Voltage on Power System Weight

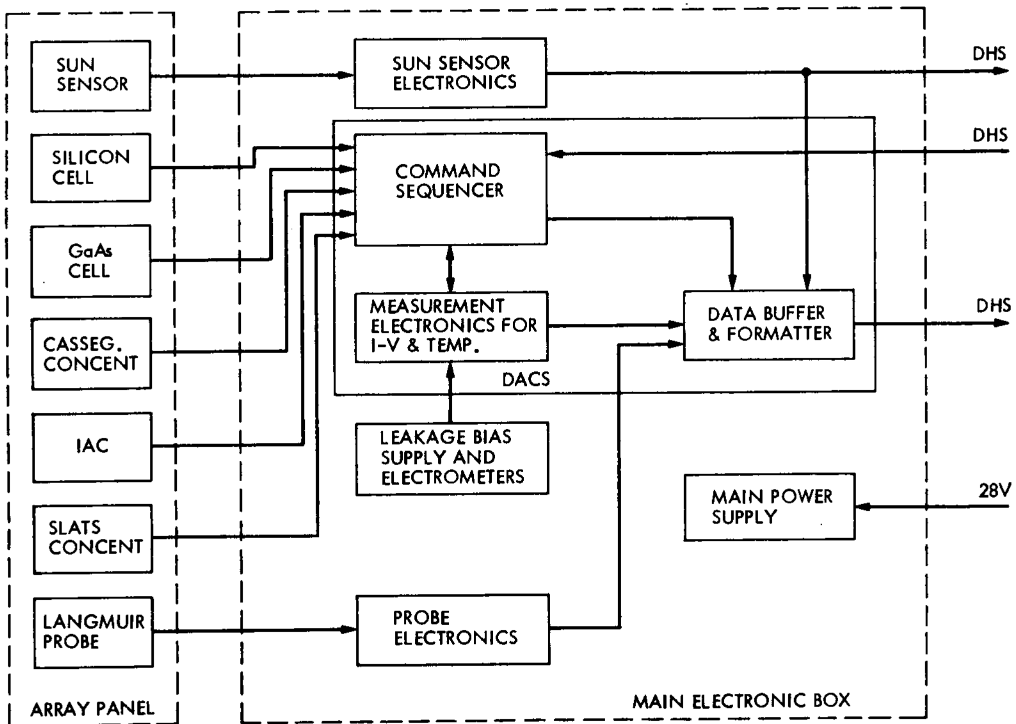

Figure 2. PASP Instrument Block Diagram

N86-17864

TESTING OF GALLIUM ARSENIDE SOLAR CELLS ON THE CRRES VEHICLE*

Terry M. Trumble
Air Force Wright Aeronautical Laboratories
Aero Propulsion Laboratory
Wright Patterson AFB, Ohio

A flight experiment has been designed to determine the optimum design for gallium arsenide (GaAs) solar cell panels in a radiation environment. Elements of the experiment design include, different coverglass material and thicknesses, welded and soldered interconnects, different solar cell efficiencies, different solar cell types, and measurement of annealing properties. This experiment, designated AFAPL-801, is scheduled to fly on the Combined Release and Radiation Effects Satellite (CRRES) to be launched in July of 1987 (Fig. 1). This satellite will simultaneously measure the radiation environment and thus, for the first time, provide engineering data on solar cell degradation that can be directly related to radiation damage.

INTRODUCTION

The initial portion of this flight will be in low earth orbit (LEO). The LEO portion of the flight will be a circular orbit at an altitude of 358 km inclined at an angle of about 28.5 degrees. During this ninety day orbit NASA will conduct their experiments and the AFAPL-801 experiment will be turned on. The CRRES vehicle will then be boosted into geosynchronous transfer orbit (GTO) for a 3 year mission. The GTO will be elliptical with an apogee of 35,000 km and a perigee of 400 km. The angle of inclination will be about 18 degrees. It is in this orbit that both the AFAPL-801 experiment and the SPACERAD experiments will be conducted. The SPACERAD experiments are a group of experiments designed to accurately measure the earth's trapped radiation belts (Fig. 2).

EXPERIMENT DESIGN

The design of an experiment of this type will take into account the different types and ranges of efficiencies of GaAs solar cells available. It will also provide a fiducial from which to judge the state-of-the-art of radiation resistance in solar cells. To accommodate these requirements, both liquid phase epitaxy (LPE) and metal organic chemical vapor deposition (MOCVD) GaAs solar cells will be used. Additionally, a string of K 4 3/4 silicon solar cells will be used as a reference. The K 4 3/4 silicon cells have been the workhorse of the industry and the wealth of data on these cells provides an excellent data base for comparisons. Finally, to round out the experiment one string of the thin silicon cells has been included on the test panel.

* Development of this experiment is being accomplished under AF Contract #F33615-79-C-2039 by the Space and Communications Group of Hughes Aircraft Co., Los Angeles CA.

The AFAPL-801 experiment consists of two flight panels, an ambient panel (Fig. 3), and an annealing panel (Fig. 4). Each panel is 6" x 12". The ambient panel will be aluminum honeycomb and will have 12 cell strings mounted on it. Different cell strings will use welded and soldered interconnects. Coverglass thickness will vary from about 2.5 mils to about 30 mils. Both microsheet and quartz coverglasses will be used. The LPE GaAs solar cells will have 16%, 17% and 18% beginning of life (BOL) efficiencies. The MOCVD GaAs cell string will be 16% efficient, BOL. The thin silicon solar cell string, A K 7 3/4 cell will also be about 13.5% BOL. All of these efficiencies are quoted at a temperature of 25°C.

The annealing panel is a glasscloth polyimide core honeycomb. This panel will only use the LPE GaAs solar cells. There are four pairs of cell strings. The first pair of cell strings are for temperature reference and to evaluate the effect coverglass thickness on annealed versus unannealed cells. These cell strings are designed to run at 70°C. The second pair of cell strings will be continuously heated at 150°C to evaluate the advantages of continuously annealing in space. A special heater has been designed to provide a continuous 150°C temperature over the lifetime of the flight experiment. The third pair of cell strings will be heated to 150°C for two hours a week to evaluate intermittent annealing properties of cell strings. The fourth and final pair of cells will be forward biased once a week and also will be run at 250°C for two hours a week. This experiment will complement the intermittent experiment and will determine the practicality of using intermittent heating to anneal radiation damage in space.

DATA MATRIXING

The unique feature of the design of this experiment is to matrix the data from different cell strings. Each of the total of twenty cell strings can be compared to each of the other cell strings. Of course some of the comparisons are of more value than others. The following is a list of the cell strings and the variations associated with each cell string. The cell strings are given in no particular order.

<u>Ambient panel</u>

Cell Type	Efficiency	Interconnect	Coverglass Thickness	Material
1. GaAs	16%	Solder	2.5 mils**	Quartz
2. GaAs (MOCVD)	16%	Solder	6 mils	Quartz
3. GaAs	16%	Welded	4 mils	Quartz
4. GaAs	17%	Solder	4 mils	Microsheet
5. GaAs	16%	Solder	6 mils	Quartz
6. Si (Thin)	13.5%	Solder	12 mils	Quartz
7. GaAs	16%	Welded	12 mils	Microsheet
8. GaAs	18%	Solder	12 mils	Quartz
9. Si (ref)	13.5%	Solder	12 mils	Microsheet
10. GaAs	16%	Solder	20 mils	Quartz
11. GaAs	16%	Welded	20 mils	Quartz
12. GaAs	16%	Welded	30 mils	Quartz

Annealing Panel

13. GaAs	16%	Welded	6 mils	Quartz
14. GaAs	16%	Welded	12 mils	Quartz
15. GaAs	16%	Welded	6 mils	Quartz
16. GaAs	16%	Welded	12 mils	Quartz
17. GaAs	16%	Welded	6 mils	Quartz
18. GaAs	16%	Welded	12 mils	Quartz
19. GaAs	16%	Welded	6 mils	Quartz
20. GaAs	16%	Welded	12 mils	Quartz

**Note: 1 mil = .001 inch
Note: All GaAs solar cells are made by the LPE process unless noted otherwise.

The current (I) and the voltage (V) will be measured at 16 loads and an IV curve generated. The temperature of the ambient panel will be taken and the temperature of each string on the annealing panel will be taken. The IV curves will be taken at a relatively slow data rate thus there will probably be some data slewing, requiring that several data sets be taken for analysis to ensure accuracies of at least 3% or better. There are two different load banks, one for the silicon cells and the other for the gallium arsenide solar cells. This ensures accurate measurements of both types of cells at the knee of the curve even after three years of operation.

A few examples of how the matrix will be used are as follows. If cell string #7 is used as a reference, the matrix is based upon the use of a 12 mil coverglass on a 16% efficient cell. The temperature of the cell is monitored and the IV points taken. The string is now compared to cell string #14 on the annealing panel. A correction for temperature is made and the data from the 16% cells compared. The only difference between the two strings is that string #7 has a microsheet cover and strings #14 has a quartz cover. A better example is what effect coverglass thickness has on the degradation of the cells. The comparison uses strings #1, #5, #10, #13 and #14. All cells are 16% efficient, use soldered interconnects and have different coverglass thicknesses. The thicknesses in mils; 2.5, 6.0, 20, 6.0 and 12 makes it possible to generate a radiation damage curve after a single data pass from the CRRES satellite.

DESIGN CONCERNS

Experiments conducted in the past on the NTS-2 and the LIPS-2 satellites have left a number of things unanswered. The NTS-2 used the older LPE GaAs solar cells. These cells were deep junction cells (1 micron) which were apoxied down. Although their performance was very good, opening the door for further development work, the degradation of the cells in the first 30 days of flight time was unexplainable. The LIPS-2 used the newer half micron junction depth cells, however, in a less than optimum fashion. This was due to the very short time period allotted between the initiation of the program, the production of GaAs solar cells and the subsequent panel fabrication. Cell selection was from

a limited number of cells and the procedures for cell laydown had to be developed. Both flight experiments, however experienced the same type of power losses in the first 30 days of their flights. It is during this infancy period that we want to identify the cause of the problem. The CRRES flight will begin in low earth orbit (LEO) where the anticipated radiation environment will be low. The AFAP:-801 will be turned on in this orbit as soon as possible to measure the infancy problem. This requirement, as well as several others, mandated that a data matrix type of experiment be established. This ensures that data taken on as little as one pass will provide valid radiation damage data to aid in the identification and quantification of the source of cell degradation.

EXPERIMENT HARDWARE

The design of the experiment has been completed. Prototypical panels have been built and laboratory tested under contract. The electronics portion of the experiment has been breadboarded and tested and the final printed circuit boards are being delivered for assembly into the housing.

CONCLUSIONS

The results of this experiment will provide much needed information on the performance of solar cells in a high radiation environment with radiation measurements that are traceable recognized laboratory standards. The comparison of the four key types of solar cells either in use or planned for use in the near future will make it possible for satellite designers to have a high degree of confidence in their design margins and will make it possible for them to design with a high degree of accuracy. These four key types; GaAs (MOCVD), GaAs (LPE), Si (K4 3/4) and the Si (thin cell) will be responsible for providing the major portion of space electrical power for several years to come. The optimum hardware configuration for this particular orbit can be chosen from the results of the flight and the optimum combination of coverglass, adhesive, cell efficiency and interconnects can be projected for uses in other orbits. It is possible, that as a result of this experiment, that it can be proven that a thinner coverglass may be used to afford the level of radiation protection required for orbits lasting between 5 and 10 years.

ORIGINAL PAGE IS
OF POOR QUALITY

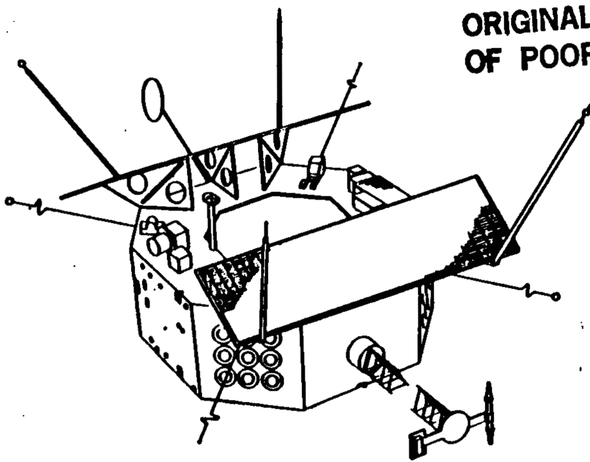

Figure 1 - CRRES Vehicle

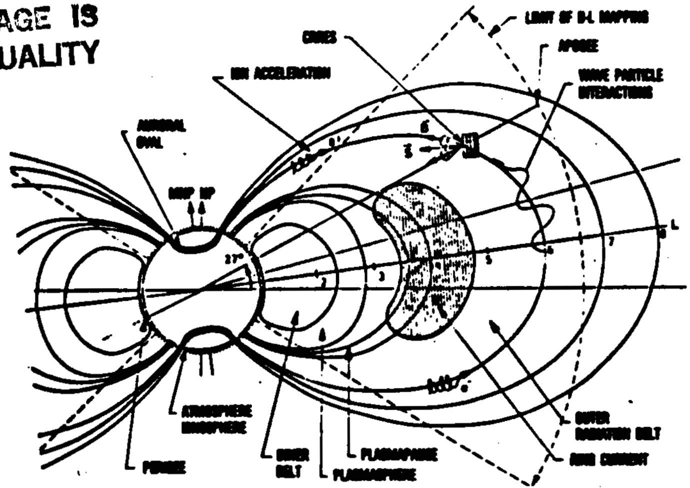

Figure 2 - Space Radiation

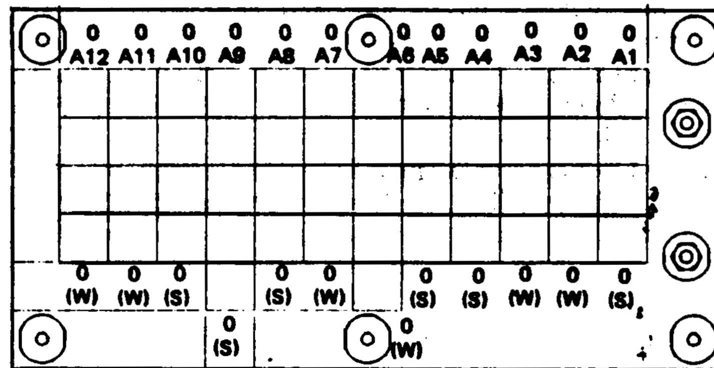

Figure 3 - Ambient Panel

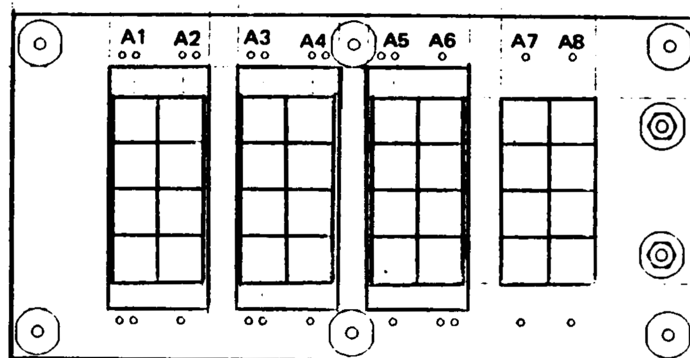

Figure 4 - Annealing Panel

N86-17865

THERMAL STRESS CYCLING OF GaAs SOLAR CELLS

Bruce K. Janousek, Robert W. Francis, and Jerry P. Wendt[1]
The Aerospace Corporation
Los Angeles, California

I. Introduction

A thermal cycling experiment is being performed on GaAs solar cells to establish the electrical and structural integrity of these cells under the temperature conditions of a simulated low-earth orbit of 3-year duration (15,000 cycles from -80°C to +80°C). Thirty single junction GaAs cells were obtained (ten each from Applied Solar Energy Corporation, Hughes Research Laboratories, and Varian Associates) and tests were performed to establish the beginning-of-life characteristics of these cells. These tests consisted of cell I-V power output curves, from which were obtained short-circuit current, open circuit voltage, fill factor, and cell efficiency, as well as optical micrographs, spectral response, and ion microprobe mass analysis (IMMA) depth profiles on both the front surfaces and the front metallic contacts of the cells. Following 5,000 thermal cycles, the performance of the cells was re-examined in addition to any factors which might contribute to performance degradation. The results presented here establish that, after 5,000 thermal cycles, the cells have retained their power output with no loss of structural integrity or change in physical appearance.

II. Beginning of Life Cell Characteristics

The thirty GaAs solar cells obtained for this experiment were 2 x 2 cm, p-on-n, unglassed, single-junction cells with thicknesses of either 12 or 15 mils. To fully characterize these cells the following tests were carried out: 1) I-V measurements, 2) spectral response, 3) IMMA depth profiles, and 4) optical microscopy.

A. Cell I-V Curves

The cell I-V curves were measured at the Jet Propulsion Laboratory (JPL) using a Spectrolab X-25 solar simulator in conjunction with a balloon-flown GaAs standard cell to establish beginning-of-life efficiency and to

PRECEDING PAGE BLANK NOT FILMED

confirm the efficiencies reported by the vendors. All cells loaded into the temperature cycler had a beginning-of-life AM0 efficiency greater than 16% aside from one cell with a measured efficiency of 15.95%. The average efficiency of the combined thirty cells was 16.66% with a standard deviation of 0.53%.

B. Cell Spectral Response

Absolute spectral response measurements were obtained at JPL on two solar cells from each of the three vendors. These curves allow one to follow the factors which might contribute to loss in performance by determining which region of the cell is degrading. The beginning-of-life cell spectral response curves all show the classical behavior exhibited by GaAs solar cells - a sharp rise near the bandgap wavelength (~ 900 nm) to a maximum response of ~ 0.55 mA/mW followed by a gradual decrease in response at shorter wavelengths and a sharp drop at wavelengths less than 450 nm.

C. Ion Microprobe Mass Analysis

One of the possible degradation mechanisms in GaAs solar cells is the diffusion of the front contact metallization into the junction region of the cell with subsequent cell shorting. Thus, elemental depth profiles were obtained employing an ARL ion microprobe mass analyzer (IMMA) on the front of one each of the vendors' cells both on and between the grid lines. By obtaining IMMA depth profiles before and after temperature cycling, one can determine whether metal diffusion is occurring.

IMMA sputtering was carried out on the tip of a grid line furthest from the cell bus bar to minimize the possibility of degrading the cell output. The investigated cells demonstrated both well-behaved graded metallization profiles and semiconductor interface regions.

D. Optical Micrographs

Color photographs at a magnification of 4X were taken of all 30 cells in order to compare the cell surface morphology, optical properties, and possible grid line delamination before and after thermal cycling.

III. Temperature Cycling

Temperature cycling is being performed in The Aerospace Corporation's

Aerophysics Laboratory. The cycle period is 30 minutes, and the temperature extremes are -80°C and +80°C with a sinusoidal temperature vs. time relationship. During cycling, the cells are maintained at a pressure less than 10^{-6} Torr. The cycler includes fail safe features which prohibit the solar cell from experiencing temperatures above +100°C and below -100°C. In the event of a loss of vacuum, the cells are returned to room temperature.

During cycling, the solar cells sit in an aluminum "picture frame" which is bolted to the temperature-controlled cooling/heating block. The picture frame has 36-1.0 inch square openings to accommodate the cells. Three 2 x 2 cm silicon solar cells are included in the thermal cycling test to provide an internal standard for comparison to the GaAs thermal stress results. The remaining three openings are filled with electrically-inactive GaAs cells with thermocouples attached with conductive epoxy to allow temperature monitoring inside the cell block. In addition, three thermocouples are epoxied to the outside of the temperature block to provide control and monitoring of the temperature and thermal gradients. A cover plate over the solar cells encloses the cells while they are in thermal contact with the cooling/heating block such that no light reaches the cells during the temperature cycling.

Table 1 describes the monitored thermal data for the initial 497 thermal cycles; this data is indicative of the thermal environment for the subsequent 4,503 cycles. T6 and T8 are thermocouples affixed to the outside of the cooling/heating block on each end and T7 is attached to the outside middle of the block. The thermocouples attached to the GaAs blanks inside the block were not employed for temperature control or monitoring since the thermocouples became disconnected from the GaAs surface during cycling, resulting in anomalous temperature readings. Prior to this, however, it was established that the temperatures measured inside the block on the GaAs blanks were representative of the temperatures measured on the outside surface of the block. The maximum low temperature (-112.4°C) was achieved at T8 when a solenoid valve temporarily stuck open, allowing liquid nitrogen to enter the cooling/heating block from both sides.

IV. Temperature Cycling Results

A. Cell I-V Curves

Data comparing cell performance before and after the 5,000 thermal

cycles are presented in Table 2. The solar cells are listed in descending order of beginning-of-life efficiency. Two cells, #9 and #19, were damaged during IMMA analysis, resulting in a performance degradation. Thus, the averages listed at the bottom of Table 2 reflect those taken on the beginning-of-life performance and the 5,000 thermal cycle performance excluding cells #9 and #19.

The data in Table 2 indicate that the performance change of the GaAs solar cells after 5,000 thermal stress cycles is very small and within the experimental error of the measurement (± 0.20%). The small decrease in efficiency observed (16.67% to 16.60%) was largely due to a decrease in average cell fill factor from 0.781 to 0.777. The small decrease in average V_{oc} was almost identical, on a percentage basis, to the small increase in average I_{sc}. The average efficiency of the three Si cells included for comparison in the temperature cycling test increased from 13.44% to 13.50% after 5,000 cycles, an increase which is again within the experimental error of the efficiency measurement.

B. Cell Spectral Response

Absolute spectral response curves after 5,000 thermal cycles for the six cells on which spectral response measurements were obtained before cycling showed negligible changes due to the thermal stress.

C. Ion Microprobe Mass Analysis

Ion Microprobe Mass Analysis depth profiles obtained after the 5,000 thermal cycles between and on the metal grid lines on one each of the vendors' cells showed no interface redistribution or enhanced penetration of sintered metal contacts due to the thermal stress.

D. Optical Micrographs

Optical micrographs taken after 5,000 thermal cycles showed no change in the surface morphology or optical properties of the solar cells. The grid line of one cell peeled along a short section (~ 0.7 mm) furthest from the bus bar; this may have caused the fill factor decrease for this cell from 0.814 to 0.799.

V. Summary/Conclusions

Temperature cycling of single junction GaAs solar cells to simulate the temperature conditions of a low-earth orbit of 3-year duration has been initiated. The change in cell electrical performance after 5,000 thermal stress cycles was found to be negligible. Furthermore, there were no observed changes in the cell spectral response, metallization and interface profiles, surface morphology, and optical characteristics. These results should enhance the overall confidence in GaAs solar cells for space applications since the cells tested in this experiment represent different crystal growth and metallization schemes. The cells are currently undergoing the second set of 5,000 thermal cycles, and performance will again be evaluated after 10,000 and 15,000 thermal cycles.

VI. References

1. The authors gratefully acknowledge the cooperation of Applied Solar Energy Corporation, Hughes Research Laboratories, and Varian Associates for supplying solar cells for this experiment. We would also like to thank Bruce Anspaugh and Bob Weiss of the Jet Propulsion Laboratory for their assistance in carrying out the cell efficiency and spectral response measurements, Martin Lundquist and Tim Wall for the design and operation of the temperature cycler, and Nick Marquez for carrying out the Ion Microprobe Mass Analysis experiments.

Table 1. Temperature Cycling Data for the Initial 497 Thermal Cycles

Minimum Temperatures (°C)

	T6	T7	T8
Average	-87.1	-87.6	-93.5
σ	3.6	1.7	4.5
Minimum Minimum	-69.1	-85.0	-82.1
Maximum Minimum	-96.7	-95.0	-112.4

Maximum Temperatures (°C)

	T6	T7	T8
Average	79.7	85.0	87.2
σ	2.4	2.4	3.9
Minimum Maximum	70.7	70.9	70.2
Maximum Maximum	90.9	95.3	99.4

Table 2. Comparison of Solar Cell Electrical Performance Before and After 5,000 Thermal Cycles

Cell#	$V_{oc}(0)$ volts	$V_{oc}(5,000)$ volts	$I_{sc}(0)$ mA	$I_{sc}(5,000)$ mA	ff(0)	ff(5,000)	η(0) %	η(5,000) %
1	1.015	1.012	116.8	116.8	0.814	0.799	17.82	17.45
2	1.038	1.035	118.9	119.6	0.774	0.772	17.66	17.74
3	1.031	1.029	119.4	119.8	0.776	0.775	17.65	17.64
4	1.001	0.998	116.5	116.5	0.818	0.816	17.64	17.54
5	1.017	1.016	112.7	113.2	0.814	0.800	17.24	17.00
6	1.034	1.032	118.9	119.4	0.750	0.750	17.04	17.06
7	1.030	1.028	117.8	118.0	0.759	0.758	17.03	17.00
8	1.005	1.009	114.1	114.1	0.800	0.788	16.96	16.77
9*	1.018	0.996	119.8	89.1	0.750	0.710	16.90	15.83
10	1.018	1.016	113.7	113.3	0.788	0.789	16.86	16.78
11	0.993	0.991	114.3	115.6	0.804	0.798	16.86	16.90
12	0.976	0.974	117.1	116.7	0.793	0.794	16.74	16.67
13	1.013	1.011	111.3	112.0	0.803	0.798	16.73	16.69
14	0.974	0.969	117.1	117.7	0.787	0.783	16.58	16.50
15	1.033	1.031	117.1	117.9	0.740	0.736	16.55	16.53

Cell #	$V_{oc}(0)$ volts	$V_{oc}(5,000)$ volts	$I_{sc}(0)$ mA	$I_{sc}(5,000)$ mA	ff(0)	ff(5,000)	$\eta(0)$ %	$\eta(5,000)$ %
16	0.952	0.950	117.4	117.7	0.800	0.794	16.52	16.41
17	1.018	1.015	118.0	118.6	0.743	0.738	16.50	16.40
18	1.021	1.018	112.0	112.4	0.778	0.772	16.44	16.33
19*	0.950	0.961	115.2	115.3	0.808	0.676	16.34	13.84
20	1.024	1.021	119.1	119.8	0.725	0.719	16.33	16.25
21	0.987	0.984	111.6	111.7	0.802	0.798	16.32	16.20
22	0.968	0.966	115.0	115.7	0.793	0.792	16.31	16.37
23	1.005	1.003	110.6	110.8	0.793	0.781	16.29	16.03
24	1.006	1.004	115.6	115.3	0.752	0.757	16.16	16.19
25	1.009	1.006	113.0	113.5	0.766	0.761	16.14	16.05
26	0.982	0.979	114.5	115.0	0.777	0.776	16.14	16.14
27	1.006	1.004	111.2	111.1	0.780	0.776	16.11	16.00
28	1.000	0.998	109.1	109.3	0.798	0.792	16.08	15.97
29	0.989	0.986	113.7	113.6	0.773	0.778	16.07	16.09
30	1.012	1.009	111.4	111.2	0.766	0.772	15.95	15.99
Averages	1.006V	1.003V	114.9mA	115.2mA	0.781	0.777	16.67% σ= 0.54%	16.60% σ= 0.53%

* Cells damaged during IMMA analysis. Data on these cells not included in averages.

N86-17866

DEMONSTRATED RESULTS OF WELDED AND SOLDERED INTERCONNECTIONS

Russell E. Hart, Jr.
NASA Lewis Research Center
Cleveland, Ohio

Solar cell modules with welded and soldered interconnections were constructed using a flexible substrate material. These modules were thermally cycled between ±80 °C at rates >100 cycles/day to demonstrate survivability under simulated low Earth orbit (LEO) temperature conditions. The modules, cycled in an inert atmosphere, showed durability for >36 000 cycles (6 yr LEO).

INTRODUCTION

In April 1982, NASA embarked on a demonstration to compare the ability of state-of-the-art interconnections on welded and soldered silicon solar cells to withstand simulated low Earth orbit (LEO) thermal-cycle conditions. It was believed that soldered contacts would last little more than 5 years in a space station LEO. If welded contacts could be made reliably, the problems associated with soldered contacts would be eliminated and longer lifetimes in orbit could be achieved. Lewis Research Center began a joint effort with the Jet Propulsion Laboratory (JPL), as the prime contractor, and four subcontractors - Lockheed Missiles & Space Corporation (LMSC), TRW, Hughes Aircraft Company, and Hughes/Spectrolab. These groups were joined together in a common interest to demonstrate the durability of soldered and welded interconnections on silicon solar cells mounted on flexible substrates.

SOLAR CELL MODULE CONSTRUCTION

Five welded and three soldered modules were fabricated by each subcontractor. Each module consisted of 0.02 cm thick, silicon solar cells. Of these modules, one soldered and three welded were selected for cycling. All module materials were to be capable of withstanding the space environment and were to be readily available in production, in pilot production, or in advanced development. The module substrate materials were to be flexible materials such as Kapton, fiberglass, cloth, etc. All modules were to provide at least 140 W/m^2 when measured at 28 °C under AMO illumination. Welded modules were to be capable of at least 90 W/kg. State-of-the-art fabrication processes including welding and soldering were to be used to produce the modules.

Because of facility limitations associated with the 5.9 cm by 5.9 cm wraparound (W/A) solar cell, LMSC constructed their nine cell modules into three series strings using both soldering and parallel-gap welding to interconnect the 0.0036 cm thick, rolled copper, integrated circuit to the cells (table I). TRW used 2 cm by 4 cm conventional cells with front and rear contacts, but they elected to build a module of 3 by 6 series-parallel configuration. TRW's solar cell interconnects were 0.0049 cm, silver clad Invar which were soldered and parallel-gap welded. Both LMSC and TRW used Kapton for the substrate material. Hughes and Hughes/Spectrolab constructed their modules with conventional 2 cm by 4 cm solar cells in a series-parallel configuration. The substrate material was a Kevlar fabric rigidized with epoxy. The Hughes/Spectrolab solar cell interconnects were 0.0049 cm thick, silver plated Invar which were soldered or parallel-gap welded. Hughes solar cells were soldered or ultrasonic welded with a silver, 0.0127 cm thick mesh, interconnection.

TEST ENVIRONMENTS

Because there were no standards for thermal-cycling modules for a LEO orbit condition, the following conditions were used for this test. The temperature cycle was to be ±80 °C, with a variance of <5 °C, and cycling was to be in an inert atmosphere. TRW elected to cycle in a vacuum, while the other contractors elected to cycle in dry nitrogen. Cycling times were to be accelerated to about 15 min/cycle. The goal of 5 years in LEO or 30 000 cycles was set as a minimum test. Nondestructive inspections consisted of visual inspections (10x magnification) as well as electrical measurements (current/voltage (I-V) at 28 °C in an AMO solar simulator). These tests were to be performed at 0, 500, 1000, 2000, 4000, 8000, 12 000, 18 000, 24 000, and 30 000 thermal cycles.

TEST RESULTS

Figure 1 shows plots of P/PO and FF/FFO versus thermal cycles. Since the Hughes and Hughes/Spectrolab test results were exactly the same, just one plot is necessary. In this case, where one plots only the fill factors, the problems in solar simulation tend to fall out leaving a more ideal plot. Although the data for the four Hughes and four Hughes/Spectrolab were averaged together for the plot, the range of differences was little more than 1 percent. They also cycled their cells an additional 6000 cycles to a 6 year LEO (36 000) with no apparent degrading based on fill factor. The three welded TRW modules (whose cells were cycled in a vacuum) showed little power degradation. Any differences could have resulted from testing inaccuracy. LMSC had two starts in their test. The first cells failed rapidly because of poor adhesion of the silver coating. This fault was verified by pull tests. New cells were made using silver which was specially prepared to have less oxygen. Pull tests showed them to be much stronger, so they proceeded with another test, which is also plotted. The plot is an average of nine, three cell series strings mounted in three modules. The average power for these strings degraded 4 percent, with a variation from the average of 4 percent. This test was concluded early (12 000 thermal cycles) because of a previous commitment for the cycling facility. LMSC believes that the loss in power was caused by oxygen in the system. This oxygen caused microcrack creep at the welds. Solar cells (2 cm by 4 cm) being cycled in vacuum in another facility are showing little or no failure.

CONCLUSIONS

Soldered or welded interconnects have survived equally well for a simulated 6 years in LEO. Survivability of welded contacts, both parallel-gap welded and ultrasonic welded, were demonstrated during this test. Further cycling of these modules should be conducted to the expected requirements of the space station (now believed to be 10 yr in LEO). Further development of the 5.9 cm by 5.9 cm solar cells with wraparound contacts and integrated printed circuit contacts should be conducted to advance them to the level demonstrated by the conventional (2 cm by 4 cm) solar cells.

TABLE I. - FINAL MODULE DESIGN

Experimenter	Cell size, cm	Inter-connections	Module matrix	Number of modules	Atmosphere
LMSC	5.9 x 5.9 silver (W/A) contacts	0.0036 cm rolled copper	9 Cell module 3 Cell series 3 Cell strings	3 Welded 1 Soldered	Nitrogen
Hughes	2.11 x 4.03 conventional silver contacts	0.0011 cm silver foil mesh	9 Cell module 3 by 3 Series-parallel	4 Ultra-sonic welded 2 Soldered	Nitrogen
Hughes/ Spectrolab	2.11 x 4.03 conventional silver contacts	0.0049 cm silver plated Invar	9 Cell module 3 by 3 Series-parallel	4 Parallel-gap welded 2 Soldered	Nitrogen
TRW	0.11 x 4.03 conventional silver contacts	0.0049 cm silver clad Invar	18 Cell module 3 by 6 Series-parallel	3 Parallel-gap welded 2 Soldered	Vacuum

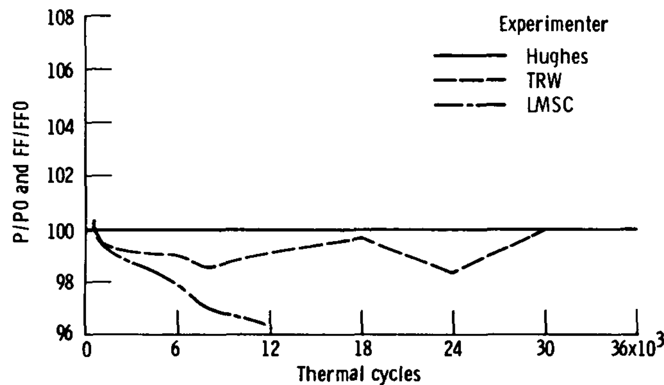

Figure 1. - Welded modules.

N86-17867

THIN FILM COATINGS FOR IMPROVED α/ϵ RATIOS

M. Eric Krisl and I. M. Sachs
OCLI
Santa Rosa, California

New thin film coatings have been developed for fused silica, ceria doped glass, and Corning 0211 microsheet which provide increased emissivity and/or decreased solar absorption.

Emissivity is enhanced by suppression of the reststrahlen reflectance and solar absorption is reduced by externally reflecting the ultraviolet portion of the solar spectrum.

Optical properties of these coatings make them suitable for both solar cell cover and thermal control mirror applications. Measurements indicate equivalent environmental performance to conventional solar cell cover and thermal control mirror products.

INTRODUCTION

Increased system requirements on next generation spacecraft have stimulated interest in methods for obtaining more power from solar arrays. One potential method involves lowering the operating temperature of conventional solar arrays either by decreasing the unusable solar energy absorbed or by increasing the energy re-radiated into space. Estimates based on simple assumptions (Reference 1) indicate that 1% power gains can be achieved for each 0.02 decrease in array solar absorption. Power gains of 1% can also be achieved for each 0.04 increase in front side emissivity on a two-sided array and for each 0.02 increase in emissivity on a one-sided body mounted array.

Thin film coatings have been developed for solar cell coverglass materials which increase emissivity and decrease solar absorption of the solar cell assembly. Coverglass materials considered include fused silica, ceria doped glass (CMX), and microsheet. Additional gains may be possible by application of these coatings to the thermal control mirror (TCM) surfaces of spacecraft; further lowering operating temperature.

Figure 1 illustrates a conventional solar cell assembly. Coverglasses for conventional cells usually have thin film coatings applied to both their internal and external surfaces. External coatings have most often been single layer MgF_2 anti-reflection (AR) coatings. Internal coatings are normally ultraviolet reflecting coatings (UVR) which protect the adhesive from ultraviolet light exposure which causes darkening.

PRECEDING PAGE BLANK NOT FILMED

ENHANCED EMISSIVITY COATINGS

Coverglass emissivity, ε, is related to spectral reflectivity $R(\lambda)$ as follows from Reference 1,

$$\varepsilon = 1 - \frac{\int_{\lambda_1}^{\lambda_2} R(\lambda) BB_T(\lambda) d\lambda}{\int_{\lambda_1}^{\lambda_2} BB_T(\lambda) d\lambda} \qquad (1)$$

where λ is the radiation wavelength, and $BB_T(\lambda)$ is the blackbody spectral distribution function for a blackbody at temperature T. For spacecraft applications, T is near 300 Kelvin and 96% of the distribution is contained between 5.0µm (λ_1) and 50.0µm (λ_2). Equation 1 indicates that surfaces with low reflectance between 5µm and 50µm will have high emissivities.

Figure 2 shows infrared spectral reflectance data for conventional AR coated fused silica. Overlaid on this data is the 300 Kelvin blackbody radiance distribution function. Notice that fused silica has a high reststrahlen reflectance near the peak of the blackbody distribution at 9.6µm. An external coating which reduces this reflectance will be effective in increasing the emissivity of the coverglass. Of course, this coating should neither significantly reduce transmittance of the coverglass in the silicon solar cell response band, nor degrade the environmental durability. As will be shown, the enhanced emissivity coatings developed have these desirable properties.

REDUCED SOLAR ABSORPTION COATINGS

Solar absorption, α, of a solar cell assembly is related to the spectral absorption, $A(\lambda)$, by

$$\alpha = \frac{\int_{\lambda_1}^{\lambda_2} A(\lambda) S(\lambda) d\lambda}{\int_{\lambda_1}^{\lambda_2} S(\lambda) d\lambda} \qquad (2)$$

where $S(\lambda)$ is the solar irradiance spectral distribution function. Since only 0.2% of solar radiation is below 0.25µm and only 3.7% is above 2.5µm, these values were selected for λ_1 and λ_2 respectively for purposes of discussion.

Although lower α will reduce operating temperatures thereby improving conversion efficiencies, methods to decrease α are beneficial if they decrease $A(\lambda)$ only in the region outside the spectral response band of the solar cell. Figure 3 shows the spectral absorption from 0.25µm to 2.5µm for ceria doped glass. Overlaid on this data is an approximate solar spectral distribution function. It can be seen from the figure that the coverglass will contribute to $A(\lambda)$ of the assembly only in the ultra-

violet region. This region is outside the response band of the solar cell. An external coating which reflects rather than absorbs the ultraviolet energy will be effective in beneficially reducing the α of the solar cell assembly. As with the enhanced emissivity coating, this coating must neither significantly reduce transmittance of the coverglass in the spectral response band, nor degrade the environmental durability. Coatings have been developed which meet these requirements.

APPLICATION TO FUSED SILICA

Enhanced emissivity coatings can be very beneficial to the performance of fused silica. Figure 4 shows infrared reflectance data for a conventional fused silica coverglass (MgF_2 coated) and for a coverglass coated with an enhanced emissivity coating. Note that the reststrahlen reflectance at 8.85µm near the peak of the blackbody distribution has been substantially reduced. Reflectance has been slightly increased at longer wavelengths, but this has minimal effect since the blackbody distribution has a low weighting factor in this region.

Table I gives performance data for this enhanced emissivity coating. The conventional fused silica coverglass is labeled AR/BR in that table where the AR is a single layer MgF_2 coating and the BR is an internal ultraviolet reflecting coating. BR stands for "blue" reflector to differentiate this conventional internal coating from the new external UVR coating. The emissivity listed in the table is normal emissivity, ϵ_N, which is the emissivity calculated from Equation (1) using specular reflectance data measured at near normal angle of incidence. Weighted average transmittance, $\bar{T}$, is the transmittance of the coverglass weighted by the cell spectral response and the solar spectral distribution function. Values of $\bar{T}$ given assume the internal side of the coverglass is adjacent to an adhesive with refractive index 1.43. Measurements were made on 0.3mm thick substrates. Environmental tests were performed in MIL SPEC test equipment except for radiation exposure. Radiation exposures were conducted by Boeing Radiation Effects Laboratory.

Since conventional fused silica coverglass is non-absorbing in the ultraviolet and has an internal ultraviolet reflecting coating, no technical advantage can be obtained with the use of an external UVR coating. However, an external UVR coating was deposited and tested on fused silica because it has potential for cost reduction. Manufacturing costs would be reduced since one external coating would replace both the internal and external coatings on conventional fused silica coverglass. The data in Table I shows that this approach yields equivalent technical performance to conventional coverglass.

APPLICATION TO CERIA DOPED GLASS

Although uncoated CMX has a higher emissivity than uncoated fused silica, emissivity coatings are still effective. The infrared reflectance of both MgF_2 coated and enhanced emissivity coated CMX is shown in Figure 5. As with fused silica, the reflectance near the peak of the 300 Kelvin blackbody curve has been reduced by the enhanced emissivity coating. Performance data for this coating is shown in Table II. Ceria doped glass does not require an internal ultraviolet reflecting coating because it absorbs sufficiently in that spectral region to protect the adhesive. This high absorption below 0.35µm increases the overall solar absorption of a CMX covered solar cell assembly. The absorption of MgF_2 coated CMX is compared to external UVR coated CMX in Figure 6. The comparison shows substantially reduced absorption between

0.27µm and 0.35µm. This spectral region contains 4% of the solar energy output. By proper design, the UVR coating can also serve as an AR coating. Table II lists the performance data for this coating. The data indicates equivalent or better performance in all categories to the MgF_2 coated CMX coverglass.

APPLICATIONS TO MICROSHEET

The physical properties of Corning 0211 microsheet are very similar to CMX glass except that ultraviolet absorption begins at 0.315µm instead of 0.35µm. This cutoff wavelength is too low to adequately protect the adhesive and therefore conventional microsheet coverglass has an internal ultraviolet reflecting coating (BR), as well as an external MgF_2 AR. In the infrared, the reflectance properties of microsheet are identical to CMX. Figure 7 shows the infrared reflectance of conventional microsheet coverglass as well as enhanced emissivity coated microsheet. Performance data is given in Table III.

The lower ultraviolet absorption cutoff wavelength of microsheet as compared to CMX means that conventional microsheet coverglass will have less solar absorption than CMX. However, there is still improvement possible with the use of an external UVR coating. The ultraviolet absorption of coventional (AR/BR) coated microsheet and external UVR coated microsheet is shown in Figure 8. Substantially reduced absorption occurs between 0.27µm and 0.32µm, a band which contains 1.8% of the sun's energy. Table III shows a reduction in α of 1.8% with the external UVR coating along with other relevant performance data.

One drawback to microsheet as a coverglass substrate is its slightly lower resistance to high energy electron radiation. The transmission loss indicated in Table III is substrate related, not coating related, as confirmed by identical coatings on different substrate materials and by Reference 2. Selection of microsheet as a coverglass material must therefore be limited to missions which will not receive high radiation dosage.

APPLICATION TO THERMAL CONTROL MIRRORS

A conventional thermal control mirror is a fused silica coverglass uncoated on the external surface and internally coated with a broadband metallic reflector. The metal strongly absorbs the ultraviolet so no additional adhesive protection is required.

Uncoated fused silica has essentially identical infrared reflectance to MgF_2 coated fused silica. Therefore, the data given for enhanced emissivity coatings on fused silica coverglass will apply directly to thermal control mirrors. (See Figure 4 and Table I).

The absorption of thermal control mirrors is low everywhere except in the ultraviolet where metals stop reflecting. An external UVR coating will be beneficial to TCM's by lowering absorption in this region. Figure 9 shows a comparison of the absorption from 0.28µm to 0.50µm of uncoated and UVR coated thermal control mirrors. Solar absorption is reduced by 2.3%. Environmental data is identical to that given in Table I for a UVR coating on fused silica.

CONCLUSION AND WORK IN PROGRESS

It has been shown that enhanced emissivity coatings and external ultraviolet reflecting coatings can improve the α/ε ratio for solar cell coverglass materials, as well as thermal control mirrors. Table IV is a comparison table giving,

1) Normal emissivity values achievable for each coverglass material,
2) Reduction in solar absorption possible with external UVR coatings, and
3) Estimated percentage power increases achievable from a fixed planar array if both enhanced emissivity and external UVR coatings are employed.

Although data presented in this paper applied to the independent application of either an enhanced emissivity coating or an external UVR coating, preliminary development results indicate that both can be simultaneously utilized. Effort is ongoing to optimize transmittance in the cell response band for the combined designs. Final $\bar{T}$ values greater than 96% are anticipated with no loss in environmental durability.

REFERENCES

1. Rauschenbach, H.S.; Solar Cell Array Design Handbook; Pgs. 132, 175 and 394; Von Norstrand Reinhold, New York 1980.

2. Crabb, R.L.; "Evaluation of Cerium Stablized Microsheet Coverslips for Higher Solar Cell Outputs"; Conference Records of the 9th IEEE Photovoltaic Specialists Conference, Silver Springs, Maryland 1972.

3. Rancourt, J. et al.; "Emissivity Enhancement of Fused Silica for Space Applications"; Proc. 4th European Symp. 'Photovoltaic Generators in Space', Cannes, France 1984.

TABLE I. Performance Data on Fused Silica Coverglass

Performance Parameter	Conventional AR/BR	Enhanced Emissivity	External UVR
Normal Emissivity ϵ_N	0.82	0.89	0.82
Coverglass Solar Absorption α	<.01	<.01	<.01
Weighted Average % Transmittance $\bar{T}$	97.1	97.0	97.7
Environmental Durability			
Humidity per MIL-C-675	Pass	Pass	Pass
Adhesion per MIL-M-13508	Pass	Pass	Pass
Abrasion per MIL-C-675	Pass	Pass	Pass
Salt Fog per MIL-STD-810B	Pass	Pass	Pass
Temperature Cycle (-320°F to 350°F)	Pass	Pass	Pass
Radiation Damage			
0.56 Mev protons to $5 \times 10^{13}/cm^2$	None	None	None
1.0 Mev electrons to $2 \times 10^{15}/cm^2$	None	None	None

TABLE II. Performance Data on Ceria Doped Glass

Performance Parameter	Coating Type: Conventional MgF_2	Enhanced Emissivity	External UVR
Normal Emissivity ε_N	0.86	0.90	0.86
Coverglass Solar Absorption α	.048	.048	.011
Weighted Average % Transmittance $\bar{T}$	97.0	96.3	96.8
Environmental Durability			
Humidity per MIL-C-675	Pass	Pass	Pass
Adhesion per MIL-M-13508	Pass	Pass	Pass
Abrasion per MIL-C-675	Pass	Pass	Pass
Salt Fog per MIL-STD-810B	Pass	Pass	Pass
Temperature Cycle (-320°F to 350°F)	Pass	Pass	Pass
Radiation Damage			
0.56 Mev protons to $5 \times 10^{13}/cm^2$	$<1\%$ $\bar{T}$ loss	$<1\%$ $\bar{T}$ loss	$<1\%$ $\bar{T}$ loss
1.0 Mev electrons to $2 \times 10^{15}/cm^2$	$<1\%$ $\bar{T}$ loss	$<1\%$ $\bar{T}$ loss	$<1\%$ $\bar{T}$ loss

TABLE III. Performance Data on Microsheet

Performance Parameter	Coating Type: Conventional AR/BR	Coating Type: Enhanced Emissivity	Coating Type: External UVR
Normal Emissivity ϵ_N	0.86	0.90	0.86
Coverglass Solar Absorption α	.023	.023	.005
Weighted Average % Transmittance $\overline{T}$	97.3	96.8	97.8
Environmental Durability			
Humidity per MIL-C-675	Pass	Pass	Pass
Adhesion per MIL-M-13508	Pass	Pass	Pass
Abrasion per MIL-C-675	Pass	Pass	Pass
Salt Fog per MIL-STD-810B	Pass	Pass	Pass
Temperature Cycle ($-320^{\circ}F$ to $350^{\circ}F$)	Pass	Pass	Pass
Radiation Damage			
0.56 Mev protons to $5 \times 10^{13}/cm^2$	$<1\%$ $\overline{T}$ loss	$<1\%$ $\overline{T}$ loss	$<1\%$ $\overline{T}$ loss
1.0 Mev electrons to $2 \times 10^{15}/cm^2$	3% $\overline{T}$ loss	3% $\overline{T}$ loss	3% $\overline{T}$ loss

TABLE IV. Improvement Potential from Coverglass Coatings

Performance Parameter	Coverglass Material: Fused Silica	CMX	Microsheet
ϵ_N	0.89	0.90	0.90
α Decrease	None	0.037	0.018
Estimated % Power Increase	1.8	2.9	1.9

SOLAR CELL COVER CONFIGURATION

Figure 1: Coverglass components in a conventional solar cell assembly.

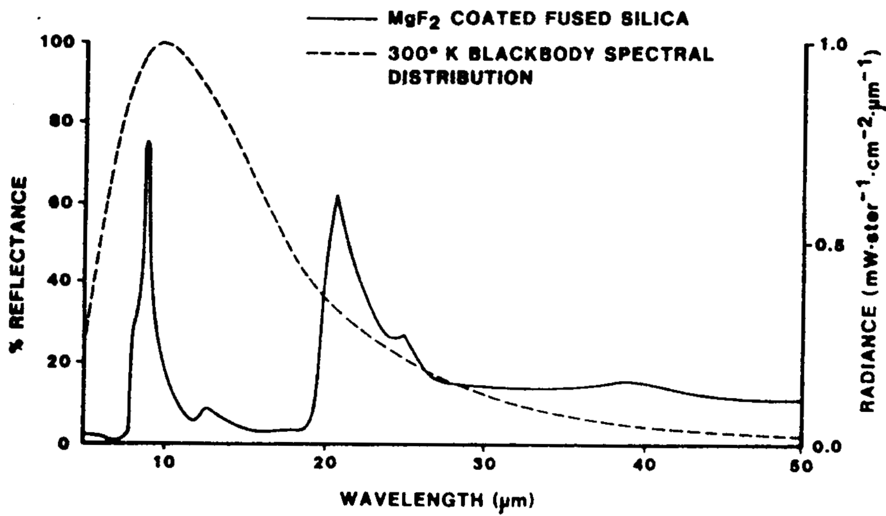

Figure 2: Infrared reflectance of fused silica coverglass showing high reflectance near the peak of a 300 Kelvin blackbody spectral distribution.

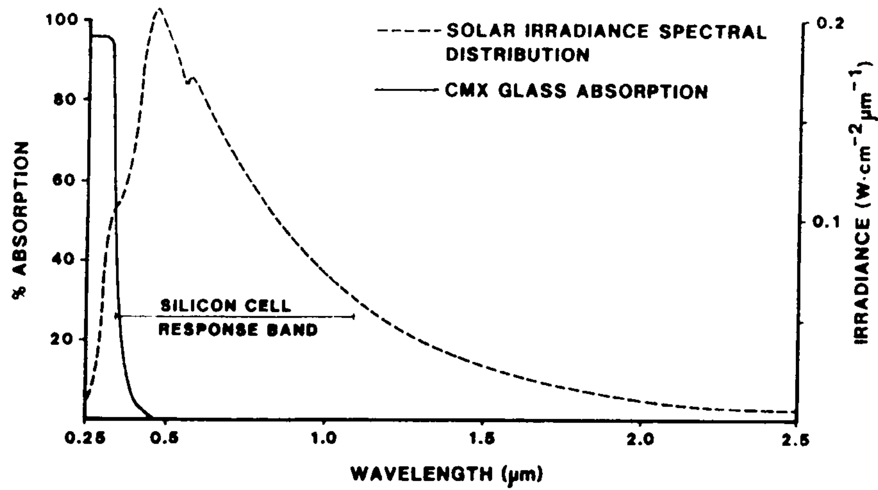

Figure 3: Absorption in ceria doped glass relative to the solar irradiance spectral distribution.

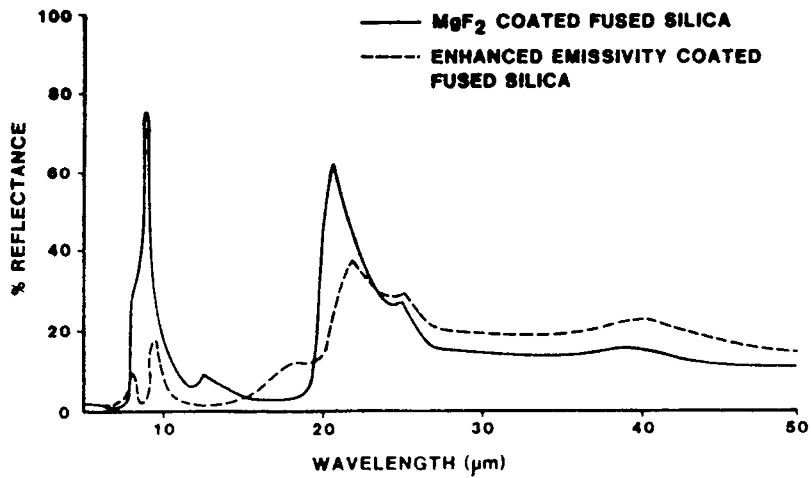

Figure 4: Infrared reflectance of MgF_2 coated and enhanced emissivity coated fused silica showing reflectance suppression near 10µm.

ORIGINAL PAGE IS
OF POOR QUALITY

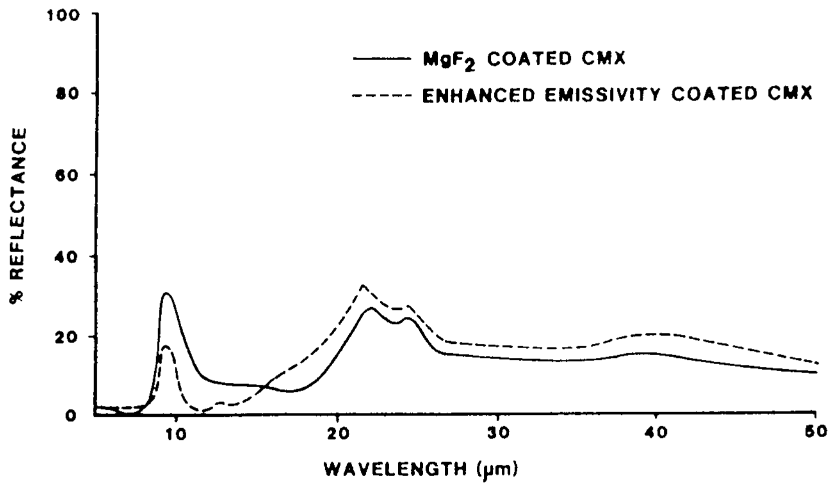

Figure 5: Infrared reflectance of CMX glass showing redistribution of reflectance produced by the enhanced emissivity coating.

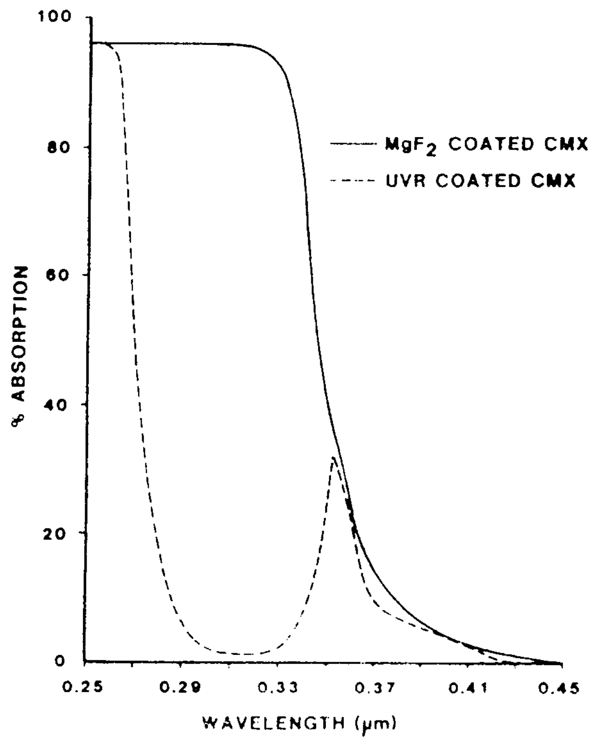

Figure 6: Ultraviolet absorption of MgF_2 and UVR coated CMX. UVR coating decreases UV absorption.

ORIGINAL PAGE IS
OF POOR QUALITY

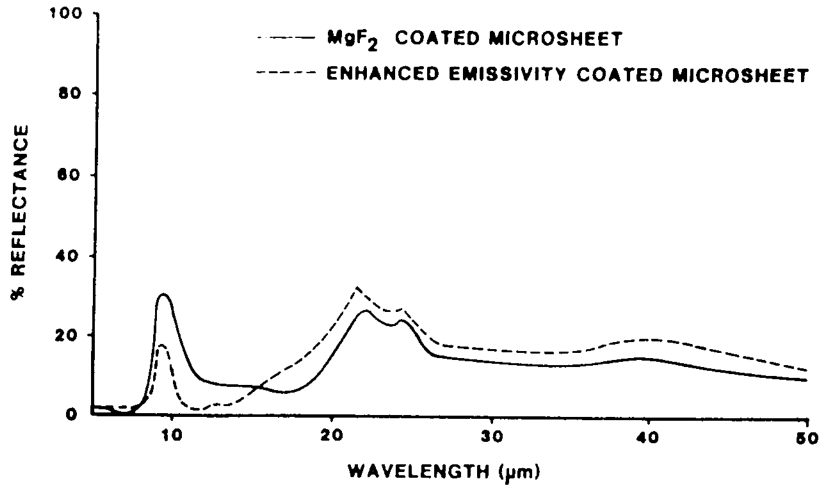

Figure 7: Infrared reflectance of microsheet with and without enhanced emissivity coating.

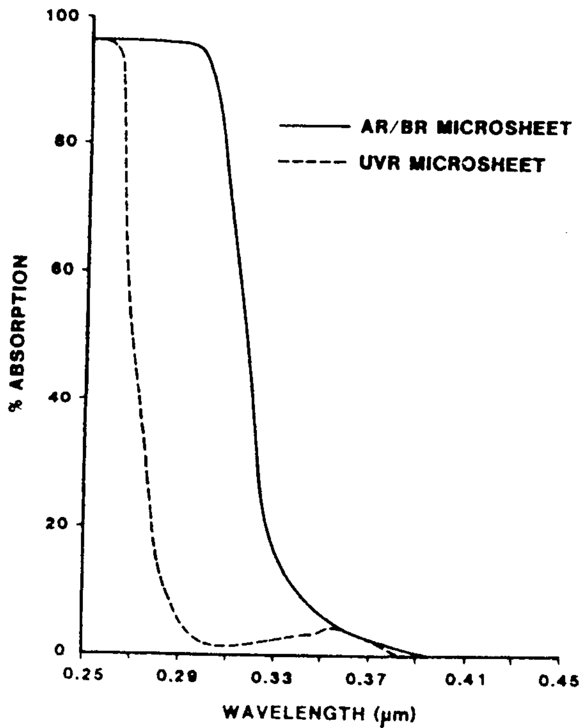

Figure 8: Ultraviolet absorption of conventional and UVR coated microsheet.

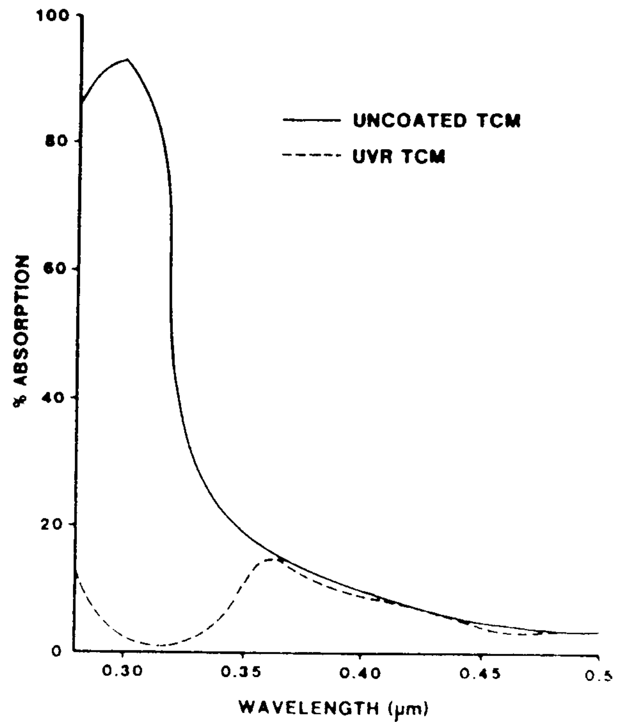

Figure 9: Ultraviolet absorption of thermal control mirror with and without UVR coating.

N86-17868

POWER REQUIREMENTS FOR COMMERCIAL COMMUNICATIONS SPACECRAFT*

W. J. Billerbeck
COMSAT Laboratories
Clarksburg, Maryland

This paper presents historical data on commercial spacecraft power systems and relates their power requirements to the growth of satellite communications channel usage. On the basis of these data as well as input from other sources, some approaches for estimating future power requirements of this class of spacecraft through the year 2000 are proposed. The key technology drivers in satellite power systems are also addressed. The paper concludes with a description of several technological trends in such systems, focusing on the most useful areas for research and development of major subsystems, including solar arrays, energy storage, and power electronics equipment.

INTRODUCTION

Commercial communications satellites have become a significant portion of the total U.S. spacecraft market, with sales to both domestic and foreign entities. Their importance can be measured in several ways, including level of engineering design effort, number of projects, and construction costs, to name a few. An interesting illustration of their market potential can be seen in a recent NASA flight manifest (ref. 1), which shows that 36 percent of the assigned shuttle payloads for the 1984 to 1987 period consist of commercial communications spacecraft.

The prominence of this class of spacecraft requires that future NASA research and development programs be aimed at improving the technology to produce increasingly sophisticated U.S. engineering and commercial efforts in this area.

GROWTH IN TELECOMMUNICATIONS TRAFFIC

Active repeater satellites have become a routinely accepted means of relaying electronic communications for commercial purposes. Although television is perhaps the form of international communications most widely recognized by the general public, voice communications far exceeds the international satellite-borne traffic volume represented by television. This growth in service (ref. 2), characterized by 4-kHz bandwidth 2-way links currently in service within the INTELSAT system, is shown in figure 1. The continuing growth of this traffic undoubtedly is the result of several factors, including the rapid growth of international trade, as well as the reductions in rates, as shown in figure 2.

Basic data on the characteristics of the INTELSAT geosynchronous spacecraft, an enabling element in the INTELSAT communications systems, are shown in table 1. Each of the INTELSAT satellite series listed consists of a group of similar spacecraft, typically numbering between four and eight. The INTELSAT I through IV series are now

*This paper is based on work performed at COMSAT Laboratories under the sponsorship of the Communications Satellite Corporation.

PRECEDING PAGE BLANK NOT FILMED

deactivated; the INTELSAT IV-A, V, and the first V-A now provide all international operational service. Additional INTELSAT V and V-A series are being prepared for flight, and the INTELSAT VI series of spacecraft is currently in the construction and testing phases.

In recent years, much attention has been given to increasing satellite communications capacities through sophisticated techniques such as digital modulation, narrower antenna beams, and polarization diversity to allow for frequency reuse.

An analysis of the DC power required at the spacecraft's main bus terminals for each 2-way telephone channel (two half-circuits in communications parlance) is plotted versus time, as shown in figure 3. This decreasing power per channel is indicative of the results of these technological improvements. In addition, effort has been focused on increasing the available electric power for communications equipment. Many spacecraft subsystems typical of those on board current communications satellites have matured so much that changes to the overall system configuration are evolutionary rather than revolutionary. However, new devices and techniques are continually being introduced to improve their performance. To a large degree, electric power subsystems for communications satellites fit this category.

TRENDS IN POWER REQUIREMENTS

An interesting example of the growth of DC power requirements for commercial satellites is again provided by the INTELSAT spacecraft series. The proportions of primary power distributed to various loads on a typical spacecraft are shown in figure 4, taken from reference 3. All earlier designs used microwave-repeater-type devices in which most of the power goes to traveling wave tubes with a DC-to-RF conversion efficiency of 30 to 40 percent. More recently, solid-state RF power amplifiers, with longer life and higher reliability, are being introduced in the lower frequency bands. These amplifiers presently have a DC-to-RF conversion efficiency of about 30 percent.

A historical survey of overall DC power requirements for the INTELSAT spacecraft reveals continual and reasonably predictable growth over time. These data are presented in figure 5, with plotted points showing the total DC power load on the main bus vs the date of actual or anticipated launch of each spacecraft.

Several approaches can be taken in estimating future power requirements for this class of microwave relay spacecraft. A simple extrapolation from the historical trend of power vs time would lead one to expect a spacecraft power load of about 12 to 25 kW by the year 2000.

A more elegant approach rests on a number of assumptions. The first of these is the anticipation that international traffic will continue to grow at the same compound rate as that of the last 10 years. A spacecraft average channel occupancy rate of perhaps 60 percent can be selected; then, assuming a DC-power-per-channel that is based on an extrapolation of the historical trend shown in figure 3, and assuming the number of satellites in the constellation, the DC power required per spacecraft can be calculated.

For example, in the year 2000, if the present rate of international satellite communications traffic growth continues unabated, the number of half-circuits in use worldwide might be extrapolated to be 900,000 to 1,330,000. A more detailed formal study of expected satellite channel requirements developed from a communications point of view (ref. 4) anticipates international satellite traffic of between 752,000 and 1,140,000 channels by the year 2000. Thus, the simple traffic extrapolation seems reasonable. Assuming an extrapolated ratio of 19 telephone circuits per DC watt of spacecraft bus power, and a 60-percent channel usage rate, the total in-orbit power required for the whole constellation might be about 70 to 117 kW.

Various scenarios can be developed, to determine the number of satellites in the constellation. These scenarios must involve complex tradeoffs related to orbital slot availability, launch vehicle capabilities, and launching costs, as well as questions about the operational complexities of operating a large number of spacecraft. The latter is probably dependent to a large degree upon the amount of automation on the ground and in the spacecraft. Assuming a total of 10 similar operational spacecraft in orbit, each one would have to support a DC load of about 8 to 12 kW, whereas an assumption of 20 operational spacecraft would imply a DC load of about 4 to 6 kW on each one. Based on the present distribution of traffic at the three orbital locations (10-percent Pacific, 20-percent Indian Ocean, 70-percent Atlantic), the constellation of 10 similar satellites probably represents the minimum reasonable number required to fully utilize the Pacific satellite. At the other extreme, 20 satellites is probably a reasonable maximum for control center loading, since some in-orbit spares (probably older spacecraft) must also be operated and maintained.

This series of assumptions leads to an expectation of a requirement for an international communications spacecraft with a DC-load capability in the range of approximately 4 to 12 kW by the year 2000. Allowing some power margin, this translates to an end-of-life (EOL) solar array capability of approximately 5 to 14 kW.

IMPACT OF WEIGHT REDUCTION

It is possible to use already published data to estimate the value of weight and power savings in terms of potential revenue on commercial spacecraft. For instance, if improvements in power system efficiency are made that allow for additional telephone channel capacity, the expected lifetime revenue payback can be calculated from the product of the number of channels per DC watt (table 1), the leasing price per channel-year (fig. 2), the spacecraft design lifetime, and the estimated ratio of channels leased compared to full load. With the first launch of a spacecraft, the channel load is usually low; the size of the load grows with time in operational service. It is considered unwise to operate at 100-percent capacity, since this leaves no reserve for peak communications loads, and might also preclude switching to a backup in case of a transponder failure. Between 70 and 80 percent is considered a conservative maximum operating capacity under normal conditions. Using such assumptions, revenue increases can be calculated to be between $200,000 and $300,000 per watt saved by spacecraft power-system efficiency improvements.

Similar calculations can be performed on the potential revenue increases associated with spacecraft mass savings. In this case, the number of communications circuits can be calculated, divided by the total mass of the spacecraft communications system plus power system, to yield the number of telephone channels per pound. This number can be multiplied by the same revenue and channel occupancy factors as before to come up with the potential revenue increase per pound of spacecraft mass saved. Calculations have produced numbers in the range of $300,000 to $500,000 per pound. Based on his calculations, Raab (ref. 5) cites a value of $500,000 to $1 million per pound. In either case, power or weight reduction, the total amount saved must be large enough to allow for an additional transponder on board, and the additional communications capacity must be marketable to actually realize any additional revenue. Spacecraft life and reliability should not be compromised in any way, since this would have a detrimental effect on the desired result.

It is clear that if the above conditions are realized, there are very strong motivations for minimizing power system mass and maximizing power system efficiency in commercial communications satellites. Therefore, R&D efforts that are successful

in reducing power system mass will provide a large payoff for this class of spacecraft.

SOLAR ELECTRIC GENERATORS

Several important technology changes that significantly affect the mass and conversion efficiency of photovoltaic arrays were pioneered during the last decade. These modifications are gradually being applied on operational spacecraft as they progress through the steps of production process refinement, experimental flight, and finally, after they are fully qualified by testing and certified for operational use.

Solar Cells

In the mid-1960s, the silicon photovoltaic cell had reached a rather stable design status with a conversion efficiency plateau of about 10-1/2 percent. Detailed analyses of the sources of energy loss within the cell (ref. 6) highlighted promising areas for improvements in performance. At the same time, a laboratory development effort at COMSAT produced a new silicon cell called the "violet cell" (ref. 7). This triggered a new burst of silicon cell development (ref. 8) which has produced laboratory cells with conversion efficiencies as high as 15-1/2 percent (see fig. 6).

These laboratory developments on the silicon cell component are now being rapidly exploited in operational programs. The hybrid-type cell has been used in a variety of spacecraft programs, and cells closely approaching a 20-mW/cm^2 level were flown on the NASA International Sun-Earth Explorer spacecraft. The USAF supported an extensive qualification program for the 80-mW, textured cell (sometimes referred to as the K7 cell) which is now in operational use on drum-spinner type arrays in the SBS, INTELSAT VI, and other satellite programs. Of course, the mass and area of solar arrays that use these higher efficiency cells can be reduced almost in proportion to the efficiency ratios. In some cases the gains are slightly less because of higher electron degradation rates or increased operating temperatures.

Another possibility, which is still in the prototype production stage, is the 50-μm (2-mil) thick silicon cell. Development work on this component was originally sponsored by NASA through JPL (ref. 9). Conventional cells have a power-to-mass ratio of about 100 W/kg when they are covered with an equivalent thickness of quartz. By contrast, these new thin cells can produce about 1,000 W/kg bare, and using 50- to 100-μm covers, could possibly achieve something in the vicinity of 300 to 500 W/kg covered. In both cases, the mounting and interconnection provisions are not included in the mass. These thin cells have an additional advantage--they degrade less than the conventional 200- to 250-μm cells in the geosynchronous orbit electron radiation environment (ref. 10).

Efficiency improvements from current research and development on advanced cells (such as GaAlAs and multi-bandgap cells) could also have significant effects on the power-to-mass ratio.

Solar Array Structures

Solar array hardware is gradually incorporating these solar cell improvements into operational spacecraft. The structure of these arrays is also changing in an evolutionary way. Most of the early INTELSAT and U.S. commercial spacecraft have been drum spinners with a honeycomb sandwich panel construction. This structure

consisted of epoxy-bonded glass fiber skins bonded to a vented aluminum honeycomb spacer. In structural design terminology, the face sheets are the load-bearing member, and the honeycomb spaces them apart to increase the structural moment of inertia to provide the desired panel stiffness. In most cases this required stiffness is dictated by the vibration environment encountered during launch.

The simple drum-spinner array has proved quite reliable, but as Barthelemy has pointed out (ref. 11), it has required roughly three times as many solar cells as a sun-oriented array. Their maximum power capability was limited by the volume available within the launch-vehicle heat shield. The weight of these drum-spinner arrays has been approximately 100 to 160 kg/kWe at the end of the mission (see table 2). The early RCA SATCOM sun-oriented arrays with aluminum-faced honeycomb panels were considerably lighter, weighing about half as much as the drum spinner arrays.

As payoffs brought about by a reduction in the mass of these commercial satellites are recognized, the new array of structural designs have begun to reflect aerospace industry advances in lightweight structures. For instance, the SBS and Anik-C drum-spinner designs with extending skirts, built by Hughes Aircraft Co., have an epoxy-bonded Kevlar high-strength-to-weight-ratio fiber in the face skins. The much larger (12-ft diameter) INTELSAT VI arrays (ref. 12), built by Messerschmidt-Buclow-Blohm (MBB) in Europe, are similar to them in design concept and materials (see fig. 7). In another example, the INTELSAT V flat, sun-oriented solar arrays (see fig. 8), which were also designed and built by MBB (ref. 13), use woven graphite fibers in epoxy composite skins. In this case, a Kapton layer is placed under the solar cells to insulate them from the conductive graphite.

The laboratory developments (listed in the lower portion of table 2), in combination with the solar cell advances mentioned above, promise continuing area efficiency and power-density improvements significantly better than present operational designs. Much of this improvement will probably result from improved structural concepts investigated in R&D work. It should be noted that much of the recent R&D work on arrays suitable for use on spacecraft in the 5- to 10-kW range (which is a range of interest for communications spacecraft) is being pursued in Europe (ref. 14). This advance in technology is beginning to result in production contracts.

Current R&D designs of flexible roll-out and flexible fold-out arrays are in the 35- to 60-W/kg (34- to 18-kg/kWe) power-density range, and the future possibility of arrays with power densities of 110 to 200 W/kg has been suggested in conceptual design studies (ref. 15). Lightweight solar concentrators with gallium arsenide cells for photovoltaic conversion also offer some promise for the future (ref. 16). However, no concentrator designs have been described in the literature that are presently weight-competitive with the advanced flat solar arrays.

ENERGY STORAGE

Ni-Cd Batteries

The rechargeable nickel-cadmium (Ni-Cd) alkaline cell has been used to supply primary power during eclipse in all operational U.S. domestic and INTELSAT communications spacecraft launched before 1983. In particular, the backlog of orbital experience, high-rate, deep-discharge capability, and long storage life appear to be key qualifications of this type of cell.

Detailed analyses of a number of these Ni-Cd batteries designed for geosynchronous orbit missions reveal that the total energy density available from new cells at 100 percent depth of discharge is relatively constant at about 26 Wh/kg. The cell weight constitutes about 82 percent of the weight of a typical flight battery, with the wiring, connectors, electronics, and structure making up the remaining 18 percent.

Typically, from one-third to one-half of the power subsystem mass in these spacecraft consists of batteries. The principal variables that determine the delivered energy density are actual depth of discharge used and redundancy strategy.

This is shown graphically in figure 9. Most of the U.S. commercial and INTELSAT craft using Ni-Cd batteries have utilized the series cell-redundancy approach and have been operated in the discharge range of 35 to 55 percent of total electrochemical capacity as a maximum (ref. 17). The energy density, in terms of total mass and actual watt-hours delivered to the load during the longest eclipse, is shown in table 3 for several of these spacecraft.

In-orbit reconditioning allows longer mission life and deeper discharging of the Ni-Cd batteries in the newer designs, resulting in somewhat higher energy densities for more recent spacecraft, as shown in table 3 (ref. 18, 19).

Ni-H_2 Batteries

Rechargeable nickel-hydrogen cells have been under development since the original work began at COMSAT Laboratories in 1970. Under USAF and INTELSAT sponsorship, there has been an extensive parallel development of two different cell designs. The INTELSAT cell design was first flown experimentally on the NTS-2 satellite (ref. 20), with successful results. It was then introduced into operational use as part of the INTELSAT V spacecraft series. Because the battery had to be a direct physical and electrical replacement for a Ni-Cd battery package (ref. 21), the delivered energy density was nearly unchanged at about 17.6 Wh/kg, as shown in table 3. The INTELSAT V-A series, which will have a larger DC load and therefore a greater battery depth of discharge, is expected to produce an improved energy density of about 19.6 Wh/kg. The new G-STAR and RCA SPACENET batteries were initially planned as Ni-H_2 designs, and with these designs engineers have been able to reach energy densities of almost 20 Wh/kg delivered to the load (ref. 22).

Several R&D efforts are also under way on bipolar and common pressure vessel Ni-H_2 designs that may reduce battery size and mass by simplifying the structural design of the pressure vessel (ref. 23). These efforts may eventually prove successful in further improving the energy density of nickel-hydrogen batteries.

One area that might help improve the life and reliability of both Ni-Cd and Ni-H_2 battery systems is research in parameters that control the growth of microcracks in sintered nickel electrodes. This crack growth with cycling, illustrated in reference 24, is not well understood; however, it is one of the key degradation mechanisms found in both types of cells.

ADVANCED ENERGY STORAGE SYSTEMS

Advanced electrochemical energy-storage devices and various other mechanical and thermal energy systems have been studied by many investigators. The key requirements of simplicity, long life expectancy (verifiable by testing), modularized design that allows implementation of redundancy with minimum weight penalty, tend to eliminate many of these candidate energy storage systems.

For instance, an in-depth technical comparison, including hardware development on a high-speed composite-wheel energy storage system, indicated that although the wheels themselves have a high energy density, when all auxiliary equipment such as motor/generators, power conditioners, and redundant wheels and control equipment are included, the overall energy storage system density for a geosynchronous mission with a 2.5-kW load is about 13.5 W/kg (ref. 25). This amount is considerably less than that of existing flight hardware $Ni-H_2$ batteries, and taken together with system complexity and other concerns regarding large, extraneous torques on the vehicle, make it an unlikely candidate for commercial geosynchronous communications applications.

Regenerative H_2-O_2 fuel cells have been studied as a possible spacecraft energy-storage system. These multicell designs with separate fuel cell and electrolysis cell units appear feasible. Both acid and alkaline systems have been studied in the past. Under NASA sponsorship, systems studies and laboratory demonstration testing of alkaline fuel cells with electrolyzers is continuing (ref. 26). Estimates of total energy storage subsystem energy density for this type of system are between 80 and 120 Wh/kg for a 35- to 350-kW load. This may be a very satisfactory system in this high-power range. However, a successful single-cell regenerative H_2-O_2 system has not been developed for spacecraft loads in the 4- to 25-kW power range, and a scale-down of the separate electrolyzer system to that level would probably result in much lower energy densities.

Surveys of the advanced secondary electrochemical systems, which are candidates for the next major leap forward in energy density beyond nickel-hydrogen, indicate that the high-temperature sodium-sulfur cell is probably the most attractive one to consider for development (ref. 27). This cell, which has a theoretical energy density of 790 Wh/kg and uses a beta-alumina solid material to separate the electrodes, was invented in the 1960s. Research efforts have been pursued by several U.S. organizations, including Ford and General Electric, and work has also been conducted in the U.K. and in Japan. The work has moved beyond the basic research stage, and prototype rechargeable cells have been developed for several transportation and terrestrial power-topping cycle applications.

These sodium-sulfur cells, as shown in figure 10, have demonstrated good performance in high rate discharge, efficient recharge, and reasonable discharge regulation. Safety issues have also been addressed. In the sizes and charge/discharge rates of interest for these satellites, cell energy densities of 100 to 120 Wh/kg have already been successfully demonstrated (ref. 28), and some cells with twice that amount of energy density have also been reported (ref. 29).

For development and testing aimed at specific NaS battery applications in spacecraft, several battery system studies have been reported (ref. 30), and others are under way. Laboratory testing that simulates the cyclic conditions anticipated in orbital applications (ref. 31) is also being conducted.

One fundamental technical question that constitutes a barrier to future work with NaS cells in geosynchronous applications is related to cell life. The existing Ford cell design has been demonstrated to have a mean lifetime of about 3 years at full operating temperature, with one deep cycle per day (ref. 32). This 1,000-cycle lifetime is probably satisfactory for commercial satellite applications. What is not clear, however, is whether longer calendar lifetimes that approach the desired 7 to 15 years could be expected with these cells in a geosynchronous orbit mode. For instance, it might be possible to place them on standby most of the time, perhaps at a lower temperature in the 225 to 250°C range, and bring them up to full operating temperature for only the 90 days per year when deep discharges are required. Tests of this kind would demonstrate whether the cell is ready for engineering development into a flight design, or whether further R&D on corrosion or other failure mechanisms is needed. Since all other attributes of the NaS cell appear quite attractive, this seems to be a question worthy of investigation.

POWER CONDITIONING EQUIPMENT

Most of the power used on board communications spacecraft flows through electronic power conditioners (EPCs) into the RF transmitting devices, as shown in figure 4. When traveling wave tubes (TWTs) are used, each high-voltage EPC unit typically weighs about the same as the TWT. An EPC unit is dedicated to each TWT, including both operating transponders and back-up units. Thus, the total weight of these units constitute a significant portion of spacecraft in-orbit mass.

Empirical studies of these high-voltage EPC units have shown that over a reasonable range, their mass is a linear function of output power. As shown in figure 11, the mass is strongly affected by the converter switching frequency. Similar trends have also been found in empirical studies of low-voltage DC/DC converters.

This can be explained simply by considering the converter as an "energy ladling" device that stores a certain quantity of energy during each cycle, and then releases it to the load. The physical size and weight of this main energy storage device (which can be an inductor, a transformer, or a capacitor) is related to the amount of energy stored. At a given power level, as the switching frequency is increased, the amount of energy stored per cycle is reduced in inverse proportion, and the mass of the energy storage components can be significantly reduced. The mass of the input and output filters can also be reduced at the higher frequency of operation because they too can be considered to be energy storage components.

The availability of space-qualified, high-voltage field-effect transistor (FET) power devices now makes it possible to operate practical DC/DC converters at much higher frequencies than ever before. For example, a 600-W electronic power conditioner, using a fairly conventional push-pull, current fed topology, was designed for 150-kHz operation and was built to run a high-power, direct broadcast TWT (ref. 33). This reduced the weight of the EPC unit by approximately half, compared to the 50-kHz production design, as shown in figure 11. If implemented throughout the particular spacecraft of interest, it could save a total of 42 pounds.

Much higher operating frequencies are possible by using the FET switches in electronic power converters, and work is under way in several organizations to investigate high-efficiency designs operating in the megahertz region. If these efforts are successful, some very lightweight power converters should result. There are two key background areas that require study to promote a great advance in this technology. First, a firstrate, widely available computer program for the design of high-frequency power transformers and inductors is needed. Such a program would allow rapid iteration and optimization of magnetic component designs on the computer, instead of the repetitive "cut and try" approach that is used almost universally in the industry today.

A second requirement is for more comprehensive research studies and publication of high-efficiency DC/DC power converter and regulator circuit topologies suitable for operation in the megahertz region, with capabilities for power output in the range of 5 to 500 W. This is the region of interest for communications satellites. Many typical tube or solid-state communications transponders require a DC input power of about 10 to 30 W. Some solid-state units are expected to have power requirements as low as 5 W, and the 500-W requirement appears to be at the high end of the current needs for direct broadcast transponders.

Another fundamental requirement is for more efficient power rectifiers with faster recovery times. As DC/DC converters move into higher frequency regimes, the rectification problem becomes much more significant, particularly in supplies for the solid-state RF amplifiers that require voltages in the 4- to 8-V region. If the rectifier forward-conduction drop is a sizeable fraction of 1 V, a significant loss in the overall conversion efficiency results. It appears that more R&D on components

like power FETs optimized for synchronous rectification, or possibly the GaAs Schottky power rectifier (ref. 34), might provide solutions to this problem. If these device developments were brought to fruition, they would have sizable spin-off effects throughout the power processing industry.

CONCLUSIONS AND RECOMMENDATIONS

An analysis of the historical trends in power requirements for commercial communications satellites has been conducted to predict those needs for the year 2000. Several approaches indicate a possible range of 12 to 25 kW, with a more likely DC load in the range of 4 to 12 kW.

Power-system technology drivers for this class of spacecraft have been identified, along with an overview of the development status of major system elements. Specific recommendations for future R&D work in each of these areas are mentioned. One of these recommendations is for the development of a solar array for the 5- to 15-kW range, with a power density greater than 50-W/kg EOL, which provides transfer orbit power and can be conveniently stowed within a launch vehicle. A second recommendation is for R&D to bring the high-energy density, rechargeable, sodium-sulfur battery cell to a technology readiness status for geosynchronous missions as rapidly as possible.

In the area of power electronics components, R&D on special FET switches for synchronous rectification, and possibly the GaAs Schottky power diode, appear to have potentially large payoffs. A good computer program for the design of high-frequency magnetic components that is made available on an industry-wide basis would greatly expedite the design of lightweight, efficient, high-frequency power processors. New studies on DC/DC converter and switching regulator topologies, aimed at utilizing the fast switching capabilities of power FET devices to produce lightweight power conditioners operating in the megahertz region, may also be useful.

REFERENCES

1. Space Shuttle Launch Schedule and Astronaut Flight Assignments--May 1984 Baseline. Morton Thiokol, Inc., Brigham City, UT, 1984.

2. INTELSAT: Annual Report to United Nations. 1983.

3. Slifer, L. W.; Billerbeck, W. J.: Synchronous Orbit Power Technology Needs. Presented at AIAA/NASA Conference on Advanced Technology for Future Space Systems, Hampton, VA, May 1979, AIAA Paper 79-0916.

4. Schnicke, W.; Board, J.; Binckes, J.; Martin, J. E.: Future Global Satellite Systems for INTELSAT. AIAA 9th Communications Satellite Conference, San Diego, CA, March 1982.

5. Raab, B.; Friedrich, S.: Design Optimization for Profit in Commercial Communications Satellites. AIAA 5th Communications Satellite Systems Conference, Los Angeles, CA, April 1974.

6. Wolf, M.: A New Look at Silicon Solar Cell Performance. 8th IEEE Photovoltaic Specialists Conference, Seattle, WA, 1970, Conf. Rec., pp. 360-371.

7. Lindmayer, J.; Allison, J. F.: The Violet Cell: An Improved Silicon Solar Cell. COMSAT Technical Review, Vol. 3, No. 1, Spring 1973, pp. 1-22.

8. Goldsmith, P.; Reppucci, G.: Advanced Photovoltaic Power System. AIAA Paper 77-506, March 1977.

9. Lindmayer, J.; Wrigley, C.Y.: Ultrathin Silicon Solar Cells. IEEE Photovoltaic Specialists Conference, Washington, DC, Conf. Rec., June 1978, pp. 450-453.

10. Miyahira, T.; Ansbaugh, B.: Electron Irradiation of Recent Solar Cell Designs. 13th IEEE Photovoltaic Specialists Conference, Washington, DC, June 1978, Conf. Rec., pp. 463-464.

11. Barthelemy, R., et al.: Aerospace Power Systems--A Building Surge. AIAA Magazine, February 1979.

12. Parker, R. D., et al.: INTELSAT VI Spacecraft Power Subsystem. 19th IECEC, San Francisco, CA, August 1984, Proc., pp. 448-451.

13. Pollard, H.; Baron, W. R.: Technical Aspects of the INTELSAT V Solar Array. 16th IEEE Photovoltaic Specialists Conference, San Diego, CA, 1982, Conf. Rec., pp. 31-35.

14. Bassewitz, H.; Lydorf, J.: Development Status of the Ultralight Solar Array--ULP. 12th IEEE Photovoltaic Specialists Conference, Baton Rouge, LA, 1976, Conf. Rec., pp. 435-442.

15. Scott-Munk, J.; Stella, P.: Recent Developments in High Performance Planar Solar Array Technology. 19th IECEC, San Francisco, CA, August 1984, Proc., pp. 78-84.

16. Patterson, R. E.; Raschenbach, H. S.; Cannady, M. D.: Design and Performance Trades for a Miniaturized Photovoltaic Generator Array. 16th IEEE Photovoltaic Specialists Conference, San Diego, CA, Conf. Rec., 1982, pp. 39-44.

17. Levy, E.; Osugi, F.: Design and Performance of INTELSAT IV Power Subsystem. 7th IECEC, San Diego, CA, August 1972, Proc., p. 677.

18. McKinney, H. N.; Briggs, D. C.: Electrical Power Subsystem for the INTELSAT V Satellite. 13th IECEC, San Diego, CA, August 1978, Proc., pp. 47-53.

19. Gaston, S.: RCA Satcom F1 and F2 NiCd Battery Orbital Performance. 15th IECEC, Seattle, WA, August 1980, Proc., pp. 1623-1626.

20. Betz, F.; Stockel, J. F.; Gaudet, A.: Nickel-Hydrogen Storage Battery for Use on Navigation Technology Satellite--2. 11th IECEC, Lake Tahoe, NV, August 1976, Proc., p. 510.

21. Van Ommering, G.; Stark, R. E.: The INTELSAT V Nickel-- Hydrogen Battery. 17th IECEC, Los Angeles, CA, August 1982, Proc., p. 2203.

22. Gaston, S. J.: The GSTAR and SPACENET Nickel-Hydrogen Batteries for Geosynchronous Orbit Applications. 19th IECEC, San Francisco, CA, August 1984, Proc., p. 258, ANS Paper 849237.

23. Cataldo, R.: Design of a 1-kWh Bipolar Nickel Hydrogen Battery. 19th IECEC, San Francisco, CA, August 1984, Proc., pp. 264-269.

24. Manzo, M., et al.: Teardown Analysis of a Ten-Cell Bipolar Nickel-Hydrogen Battery. 19th IECEC, San Francisco, CA, August 1984, Proc., pp. 270-278.

25. Clermont, M.; Legrand, F.: Wheel Energy Storage Systems for Satellite Power Conditioning and Attitude Control. 33rd IAF Congress, Paris, France, September 1982, IAF Paper A82-47049.

26. Martin, R. E.; Gitlow, B.; Sheilbley, D. W.: Alkaline Regenerative Fuel Cell Energy Storage System for Manned Orbital Satellites. 17th IECEC, Los Angeles, CA, August 1982, IEEE Paper 829361.

27. Knodler, R.: Comparison of Na/S and LiAl/FES Batteries. 17th IECEC, Los Angeles, CA, August 1982, IEEE Paper 829095.

28. Haskins, H. J.; McClanahan, M. L.; Minck, R. W.: Sodium-- Sulfur Cells for High-Power Spacecraft Batteries. 18th IECEC, Orlando, FL, August 1983, ANS Paper 839239.

29. Fuchida, K., et al.: Sodium-Sulfur Battery Program in Japan. 17th IECEC, Los Angeles, CA, August 1982, IEEE Paper 829101.

30. Marcoux, L.; Allen, D. M.: Conceptual Design of a Large Spacecraft Power System Utilizing a Sodium-Sulfur Battery. 18th IECEC, Orlando, FL, August 1983, ANS Paper 839240.

31. Allen, D. M.: Sodium-Sulfur Satellite Batteries: Cell Test Results and Development Plans. 19th IECEC, San Francisco, CA, August 1984, Proc., p. 163, ANS Paper 849142.

32. Bridges, D.; Haskins, H.: Operation of a 100 Kilowatt-Hour Sodium Sulfur Battery. 17th IECEC, Los Angeles, CA, August 1982, Proc., p. 563.

33. Baker, W. E.; Sizemore, W. T.: Design of a Lightweight High-Voltage Spacecraft Power Conditioner. POWERCON 11, Dallas, TX, April 12, 1984.

34. Sears, A. R., et al.: High Voltage, High Speed, GaAs Schottky Power Rectifier. IEDM 83, Proc., pp. 229-232.

Table 1. Growth of INTELSAT Spacecraft

Parameter	INTELSAT Satellite Series							
	I	II	III	IV	IV-A	V	V-A	VI
Year of First Launch	1965	1967	1968	1971	1975	1981	1984	1986-87
Drum Dimensions (cm)								
Diameter	72.1	142	142	238	238	--	--	364
Height	59.6	67.3	104	282	282	--	--	613
Overall Deployed Height (cm)				528	590	1,585	1,585	1,180
Mass (kg)								
At Launch	68	162	293	1,385	1,469	1,870	1,870	--
In Orbit	38	86	152	700	790	1,014	1,014	2,250
Primary Load Power (W)	40	75	120	400	500	975	1,100	1,800
Active Transponders	2	1	2	12	20	23	32	48
Number of Telephones Circuits	240*	240	1,200	4,000	6,000	12,000	~15,000	~30,000
Design Lifetime (yr)	1.5	3	5	7	7	7	7	7

*No multiple access.

Table 2. Solar Array Characteristics

Spacecraft	End-of-Life Power (W)	Array Type	W/m^2	End-of-Life (kg/kWe)	Design Status
NATO III	375	Body-mounted	24.5	127.7	Flight
INTELSAT IV-A	522	Body-mounted	24.5	137.7	Flight
ANIK I-III	219	Body-mounted	23.8	151.6	Flight
ATS-6	600	Rigid, oriented	30	101.3	Flight
Orbital Workshop	12,240	Rigid, oriented	97	188.7	Flight
FilSatCom	1,470	Rigid, oriented	69	62.1	Flight
CTS-Hermes	1,045	Flexible	55.3	45.5	Flight
Hughes FRUSA	1,100	Flexible roll-out	70	28	Flight
SBS (Hughes)	710	Body-extended skirt	29	103	Flight
INTELSAT V (Ford)	1,290	Rigid, oriented	55	50	Flight
ECS (Fokker)	998	Rigid, oriented	75.3	48.5	Flight
MARECS (Fokker)	835	Rigid, oriented	63	58.5	Flight
STC/DBS (RCA)	2,200	Rigid, oriented	104	32.5	Under construction
INTELSAT VI	2,170	Body-extended skirt	35.3	77.2	Under construction
SKYNET 4 (Fokker)	1,400	Rigid, oriented	89.7	38.4	Under construction
TRW Lightweight	1,470	Rigid	75	41	R&D
MBB ULP	1,500	Semirigid	75	30	R&D
Aerospatiale/COMSAT	1,050	Flexible foldout	72	34	R&D
AEG Dora	6,600	Flexible roll-out	77	25	R&D
Lockheed SEPS	12,500	Flexible foldout	83	18	R&D
Fokker ARA MK3	2,000-4,000	Rigid	--	22-25	R&D

Table 3. Battery Energy Density Experience

Spacecraft Battery*	Delivered Wh/kg
INTELSAT III	13.9
INTELSAT IV	13.2
INTELSAT IV-A	13.2
INTELSAT V (F1-5) NiCd	17.6
COMSTAR	15.4
SBS	15.4
RCA SATCOM NiCd	16.5
NTS-2 Experiment Ni-H_2	17.6
INTELSAT V (F6-9) Ni-H_2	17.6
INTELSAT V-A (F10-14) Ni-H_2	19.6
GSTAR Ni-H_2	19.9
RCA SPACENET Ni-H_2	19.7

*Including instrumentation and hardware.

ORIGINAL PAGE IS
OF POOR QUALITY

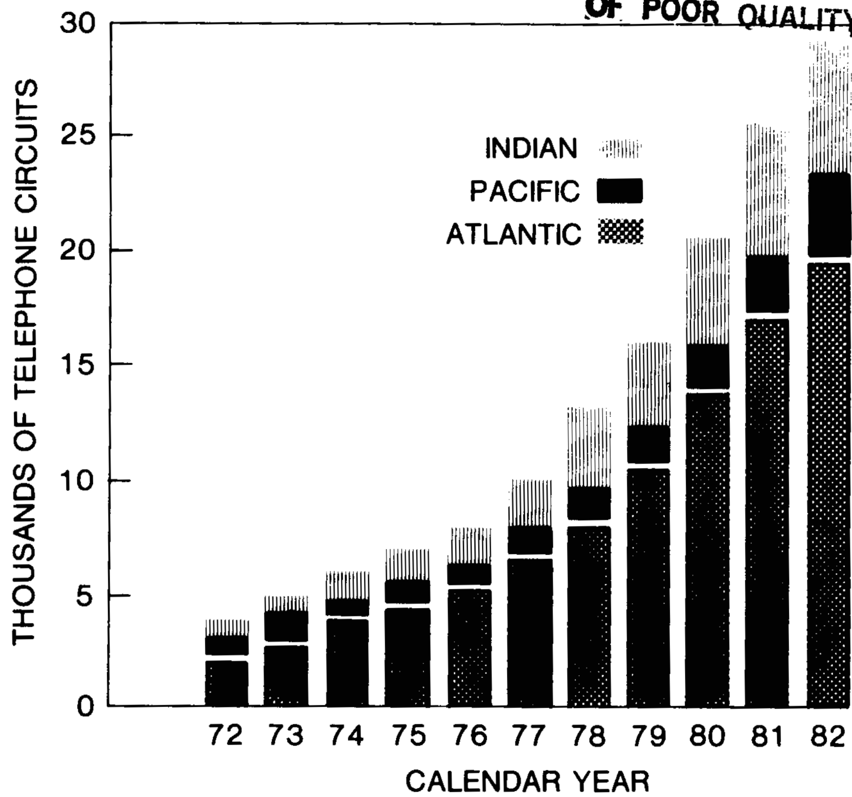

Figure 1. Growth in Full-Time INTELSAT Satellite Use by Region

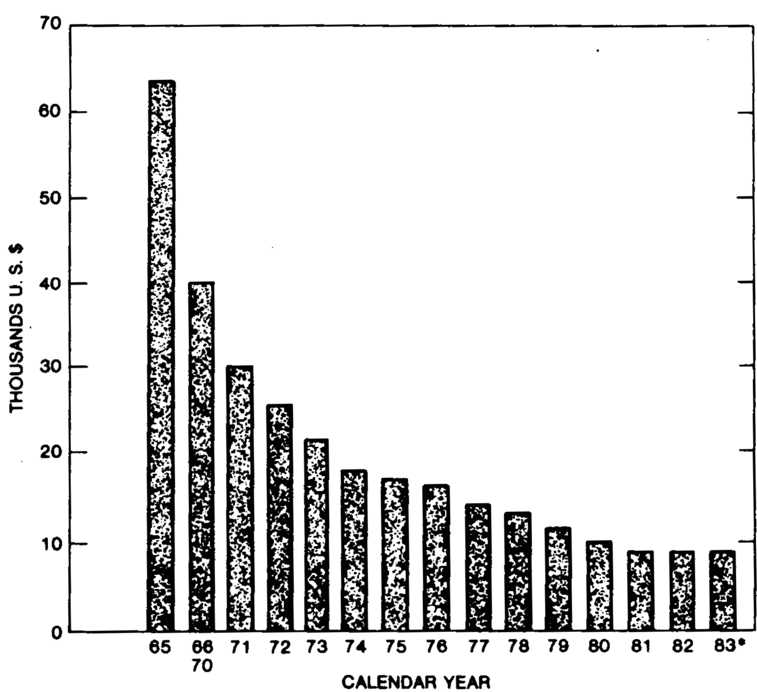

Figure 2. INTELSAT Satellite Utilization Charge

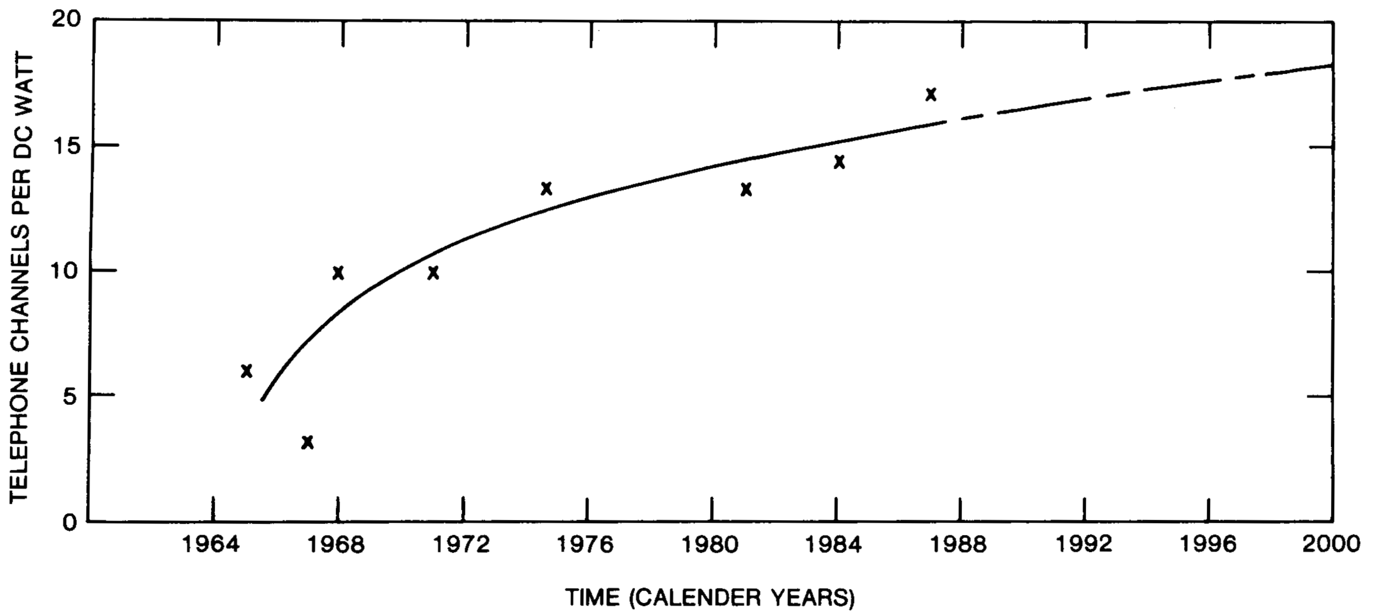

Figure 3. DC Bus Power Required per Two-Way Telephone Circuit

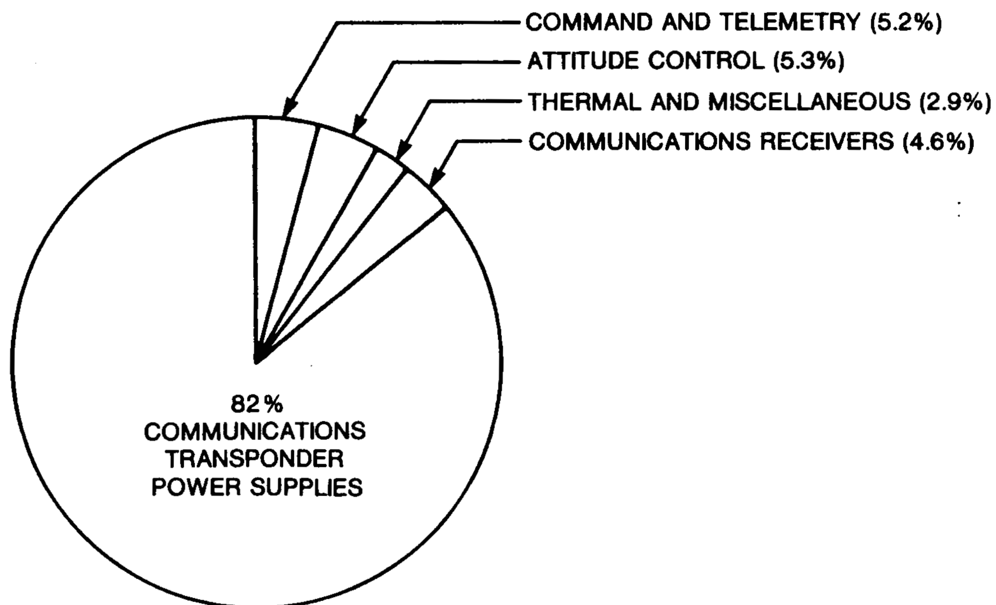

Figure 4. Primary Power Distribution in a Typical Communications Spacecraft

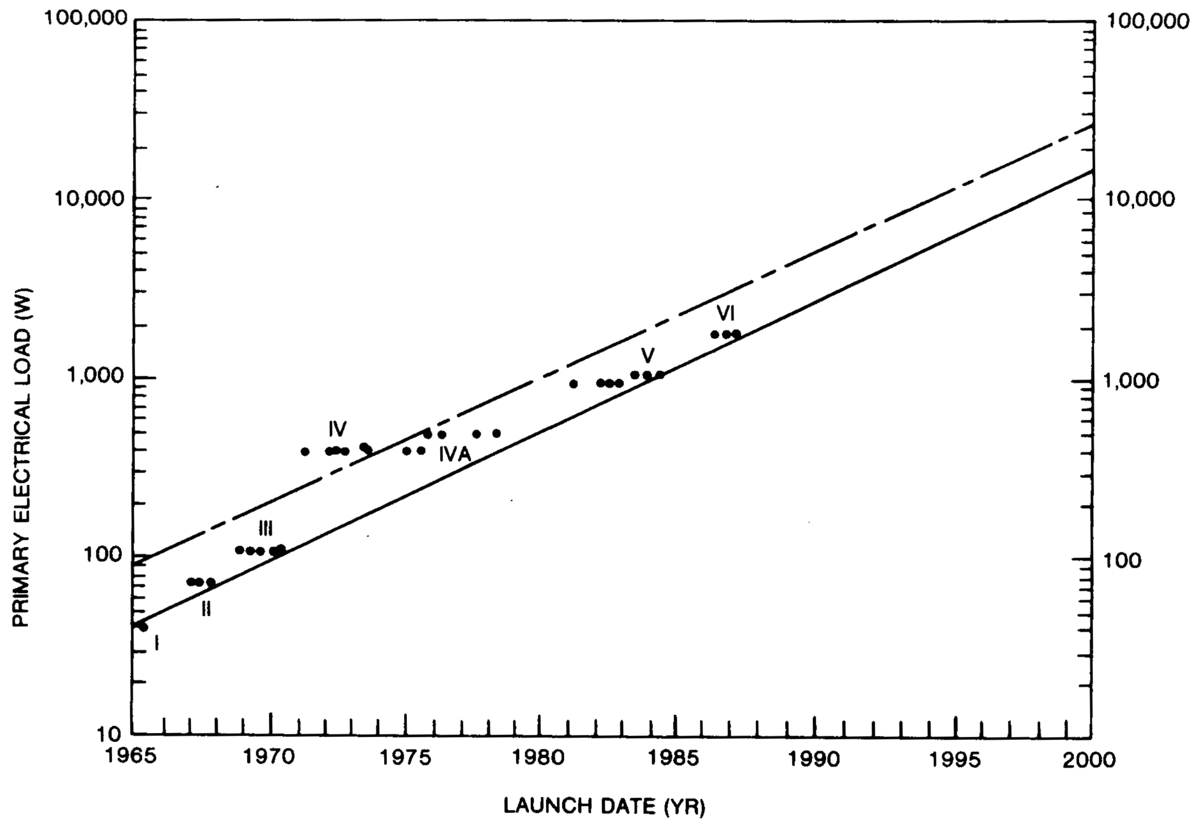

Figure 5. Electrical Load Power for INTELSAT Spacecraft

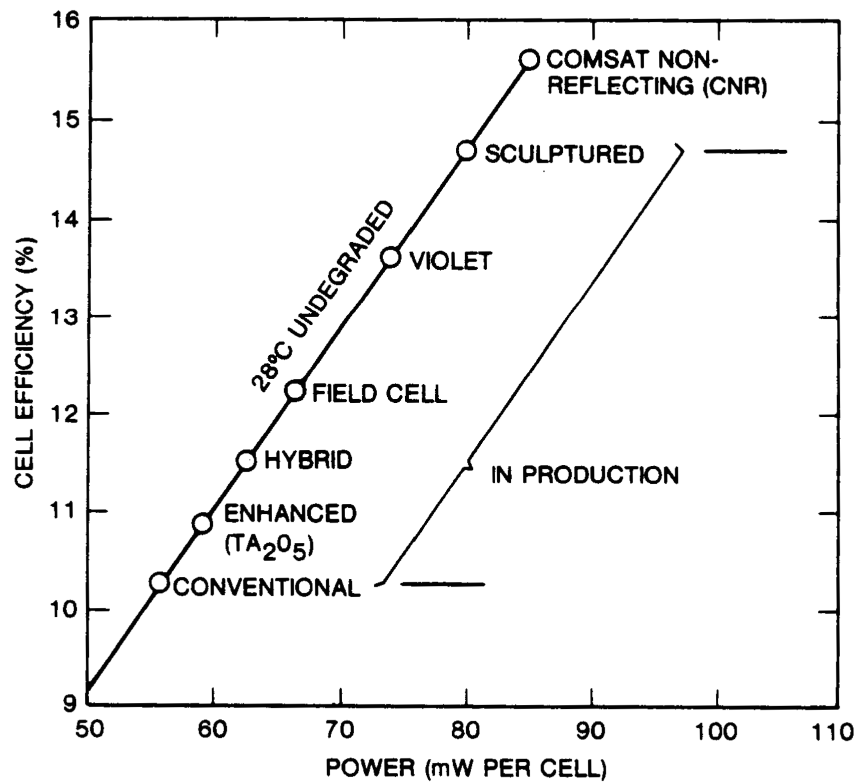

Figure 6. High-Efficiency Solar Cell (2 x 2 cm) Performance

ORIGINAL PAGE IS
OF POOR QUALITY

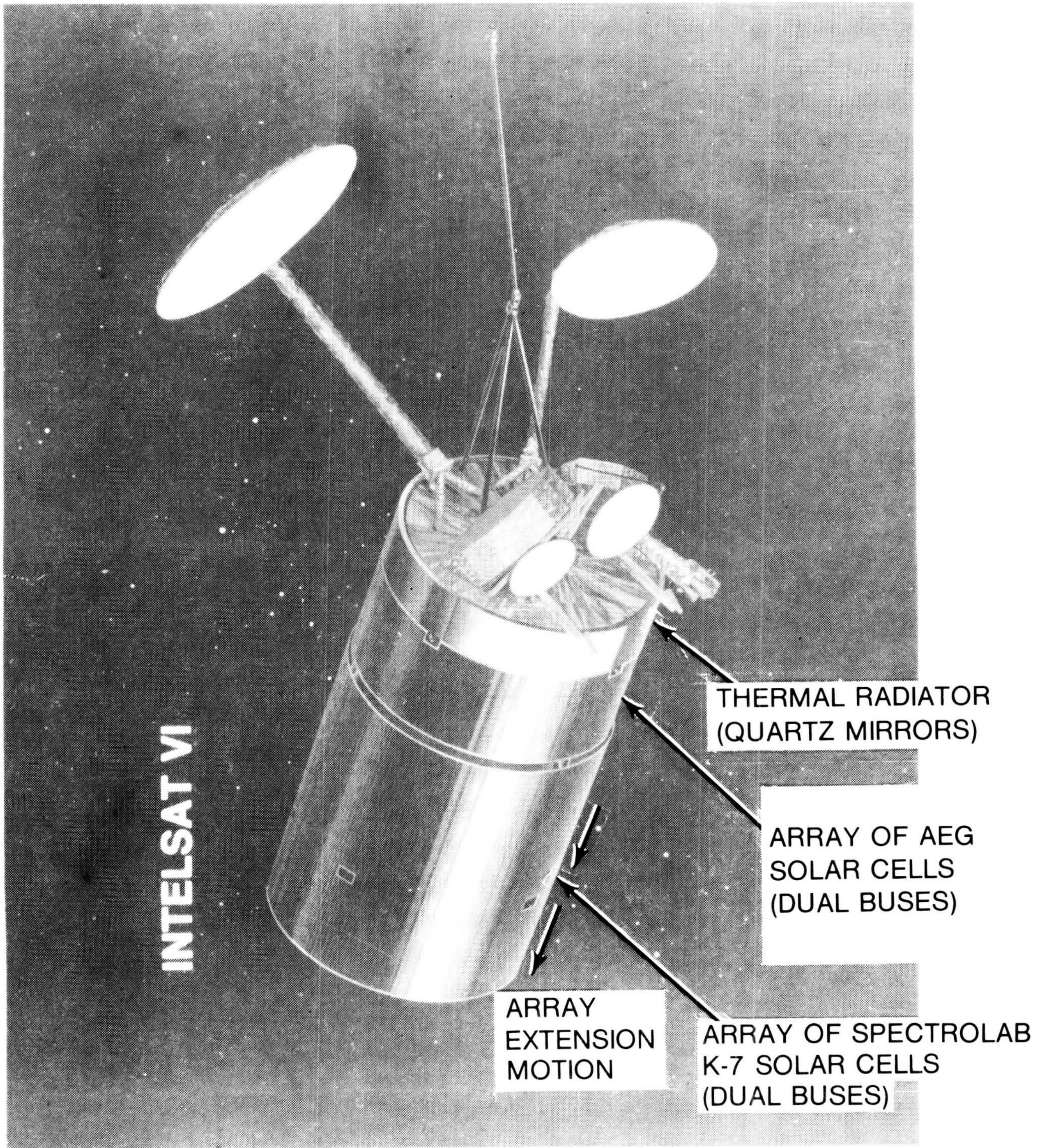

Figure 7. INTELSAT VI Extendable Solar Array

ORIGINAL PAGE IS
OF POOR QUALITY

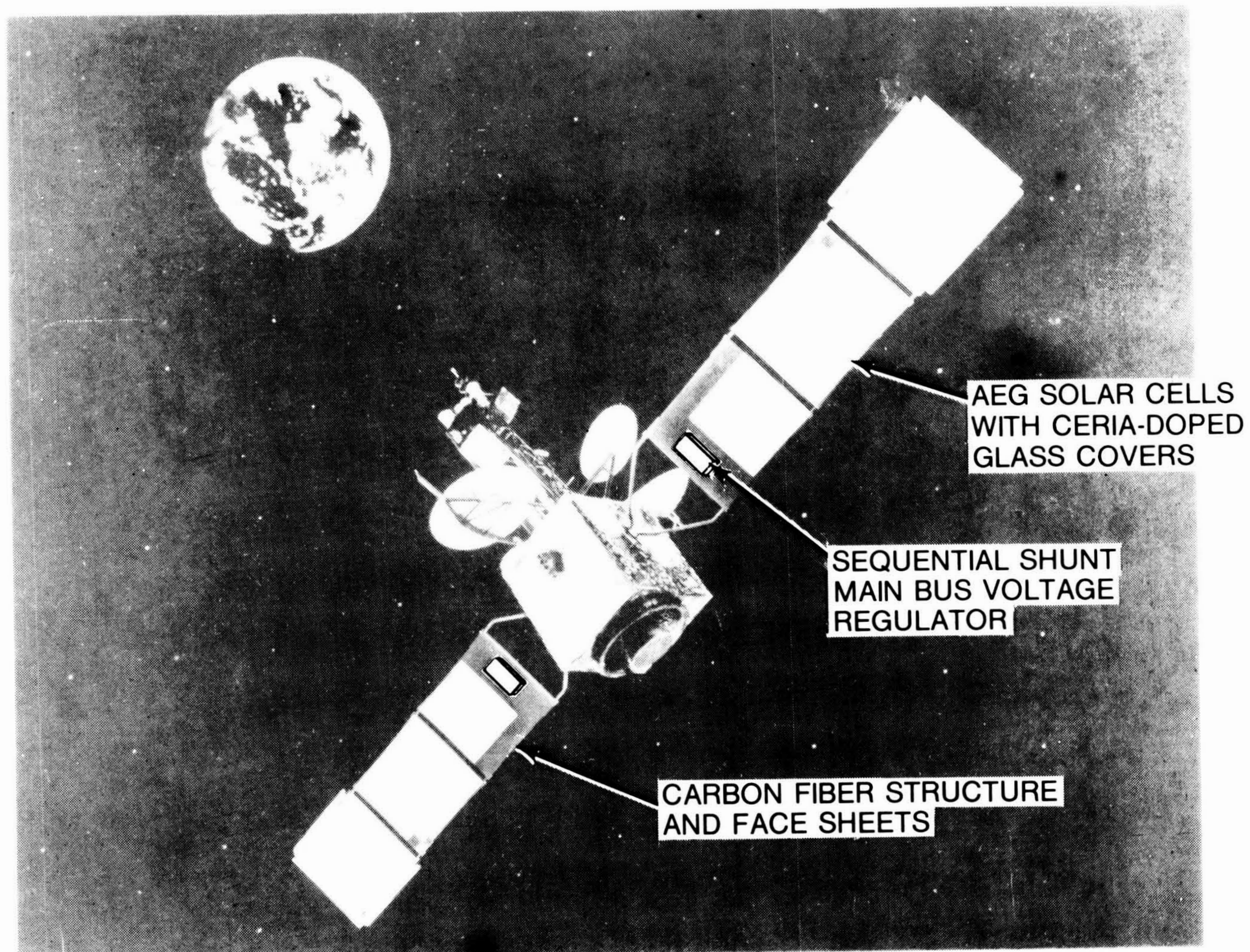

Figure 8. INTELSAT V Solar Arrays

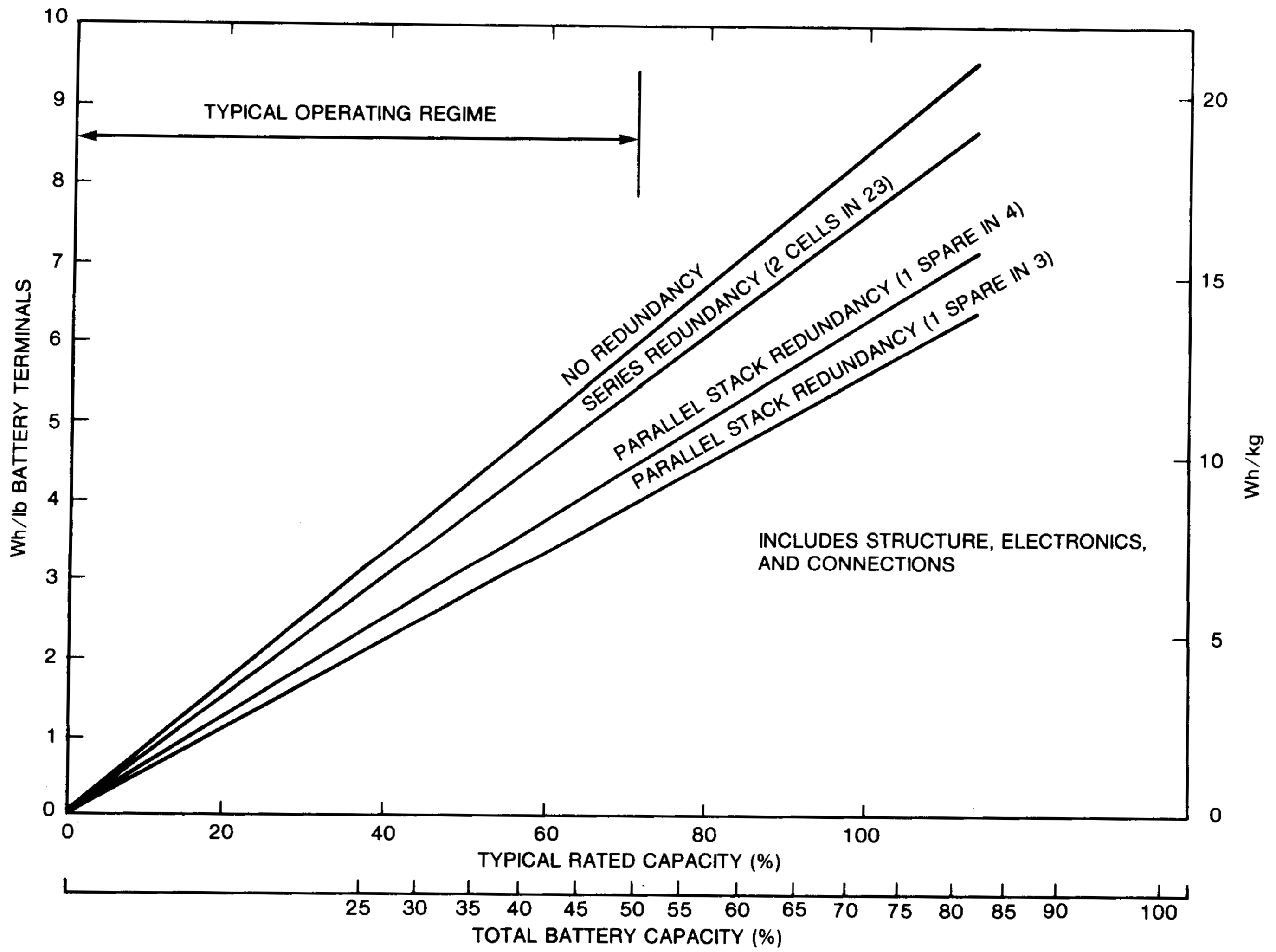

Figure 9. Ni-Cd Battery Energy Density vs Depth of Discharge

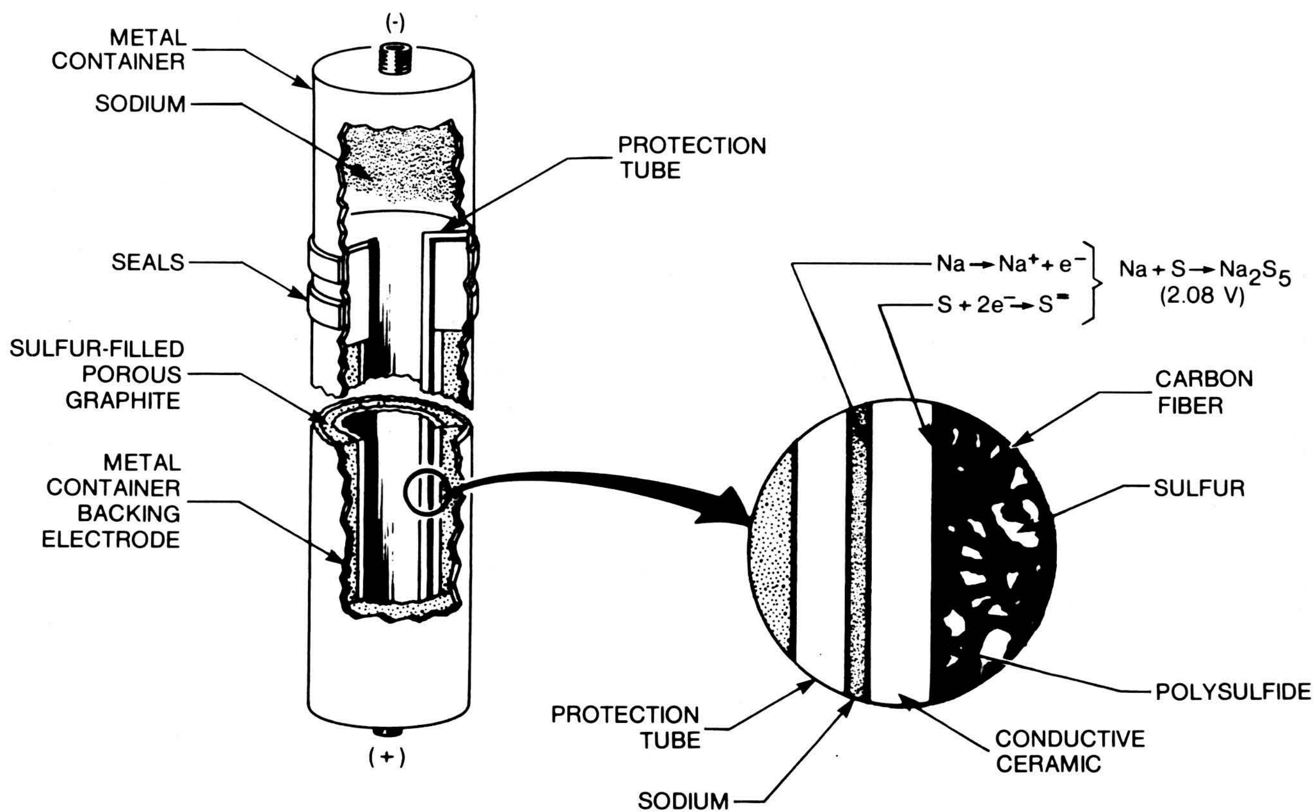

Figure 10. Schematic of Sodium-Sulfur Cell

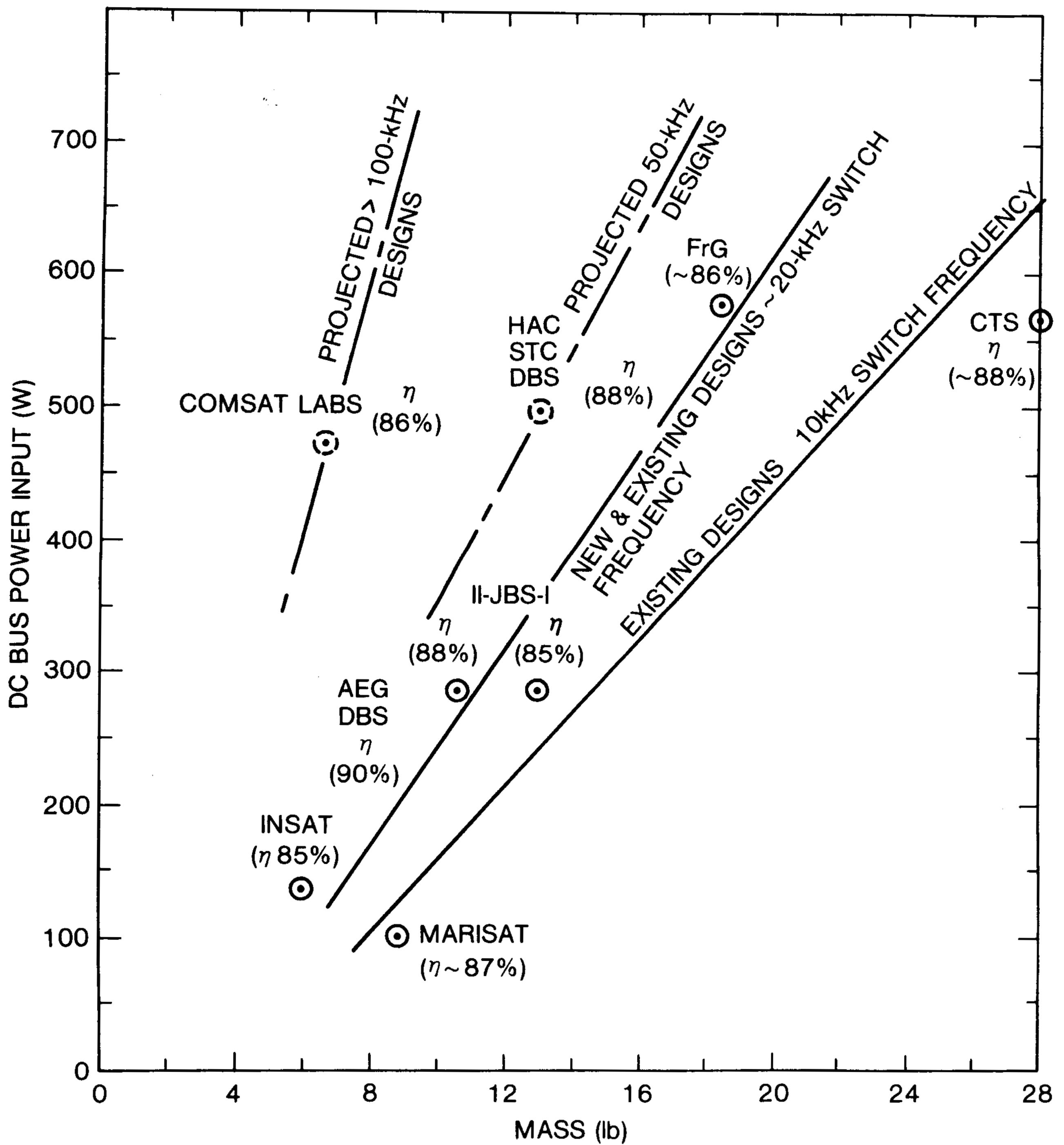

Figure 11. Mass of Electronic Power Conditioners for TWTs at High Power Levels

N86-17869

SPACE STATION POWER MANAGEMENT AND DISTRIBUTION

Fred Teren
NASA Lewis Research Center
Cleveland, Ohio

The power system architecture is presented by a series of schematics which illustrate the PMAD system at the component level, including converters, controllers, switchgear, rotary power transfer devices, power and data cables, remote power controllers, and load converters. Power distribution options, reference power management, and control strategy are also outlined. A summary of advanced development status and plans and an overview of system test plans are given.

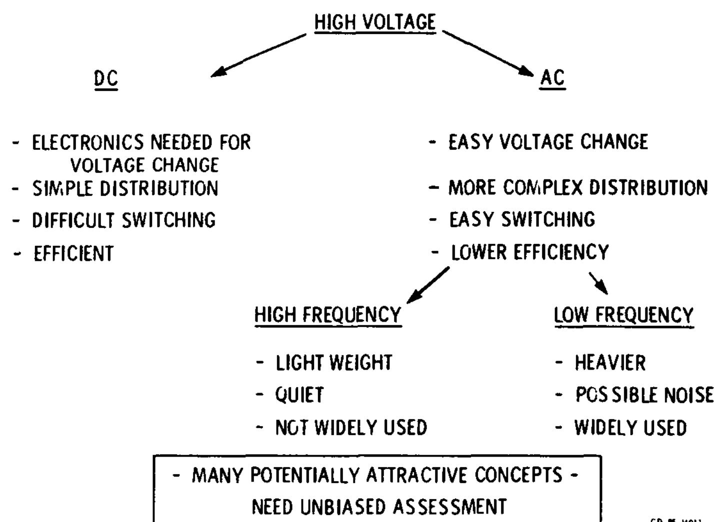

Figure 1.

REFERENCE PHOTOVOLTAIC POWER SYSTEM ARCHITECTURE

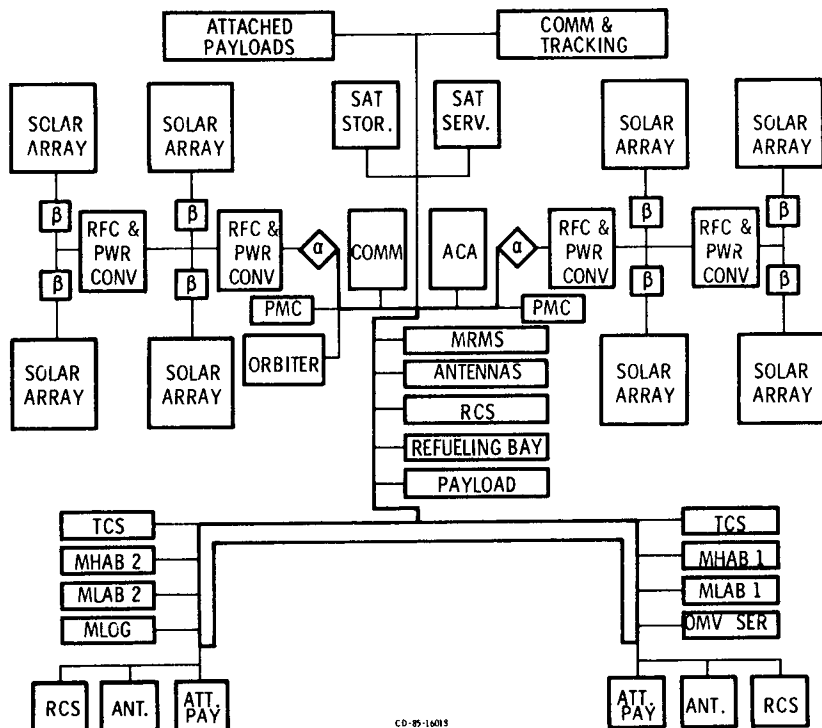

Figure 2.

REFERENCE PHOTOVOLTAIC POWER SYSTEM ARCHITECTURE

OUTBOARD TRANSVERSE BOOM

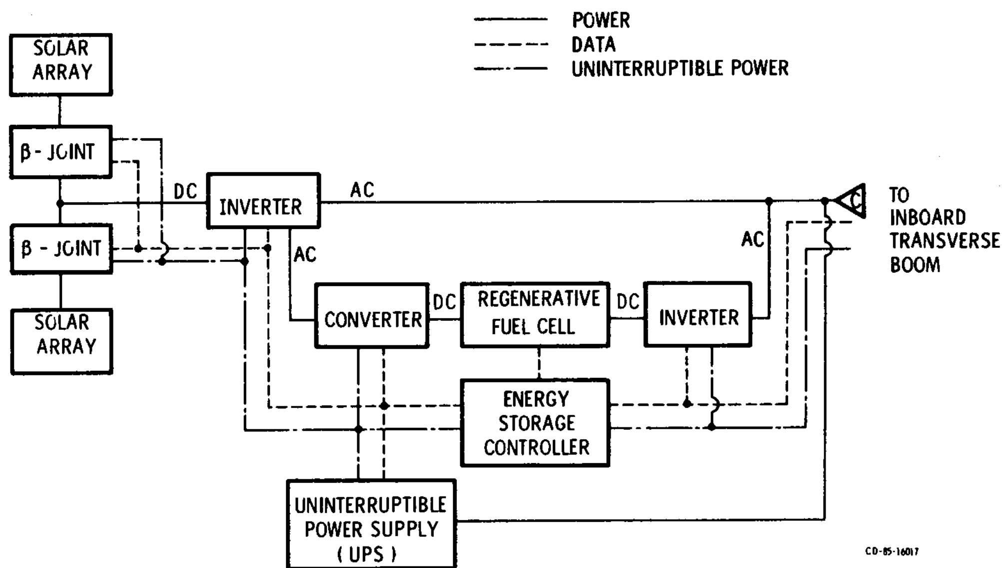

Figure 3.

REFERENCE PHOTOVOLTAIC POWER SYSTEM ARCHITECTURE
INBOARD TRANSVERSE BOOM

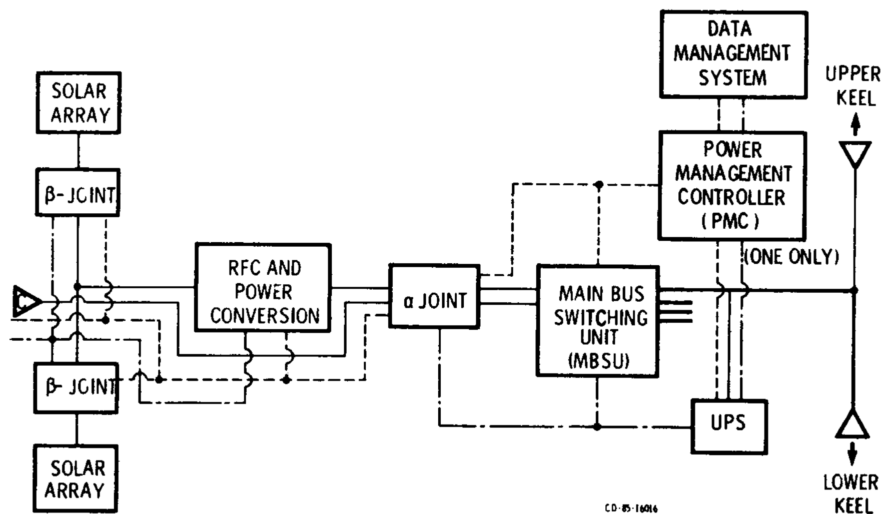

Figure 4.

REFERENCE PHOTOVOLTAIC SYSTEM ARCHITECTURE (LOWER BOOM)

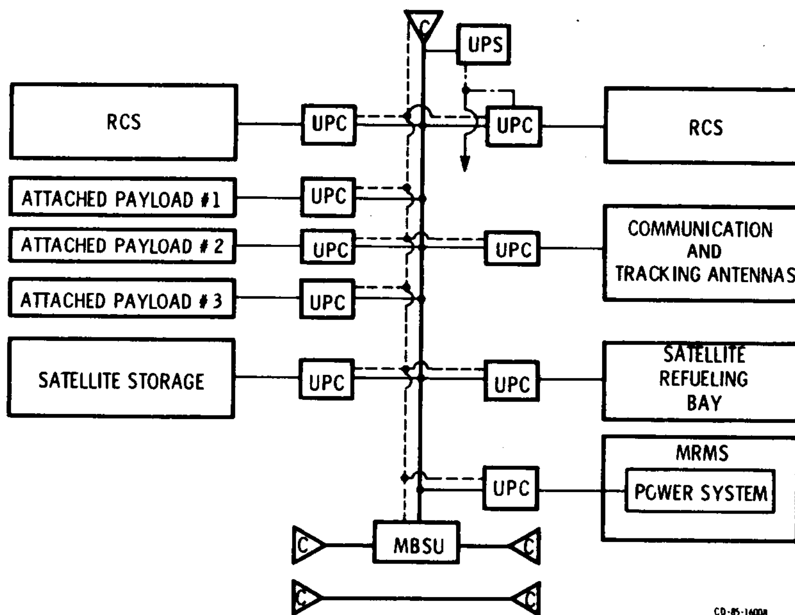

Figure 5.

REFERENCE PHOTOVOLTAIC POWER SYSTEM ARCHITECTURE
(STARBOARD KEEL EXTENSION AND LOWER BOOM)

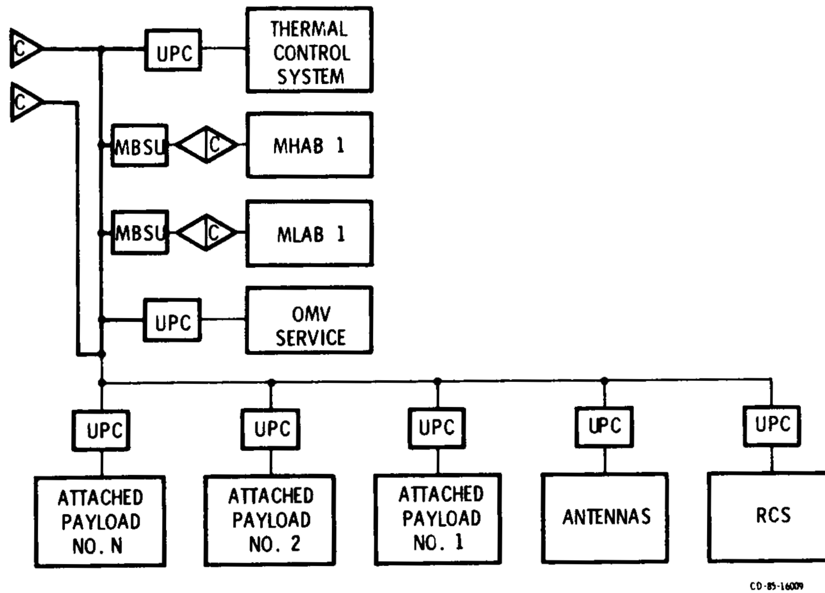

Figure 6.

REFERENCE PHOTOVOLTAIC POWER SYSTEM ARCHITECTURE
(MHAB NO. 1)

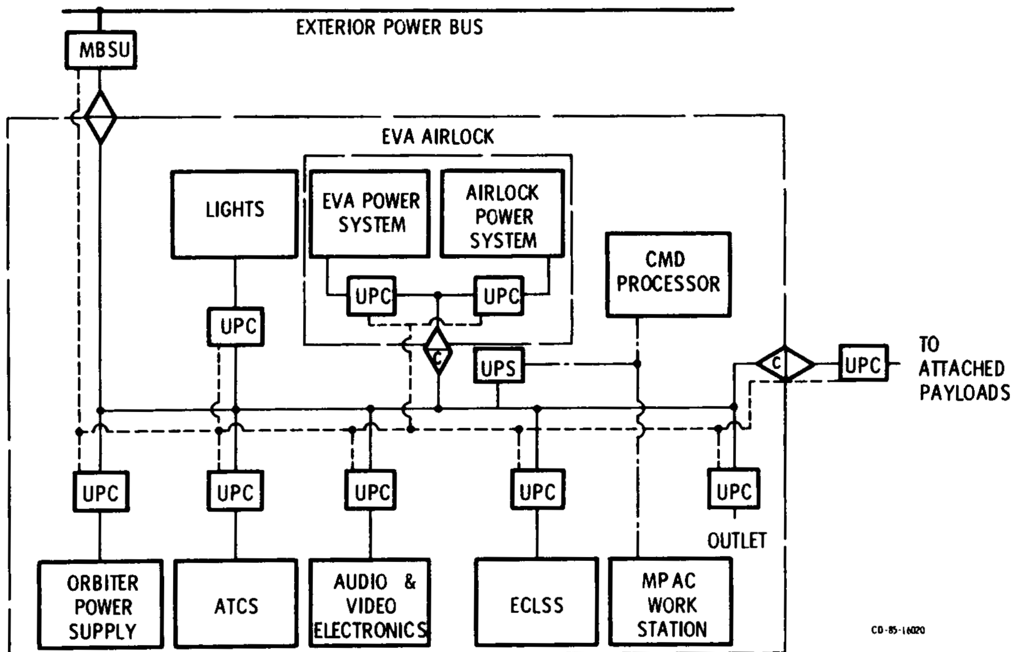

Figure 7.

REFERENCE SOLAR DYNAMIC POWER SYSTEM ARCHITECTURE
(INBOARD TRANSVERSE BOOM)

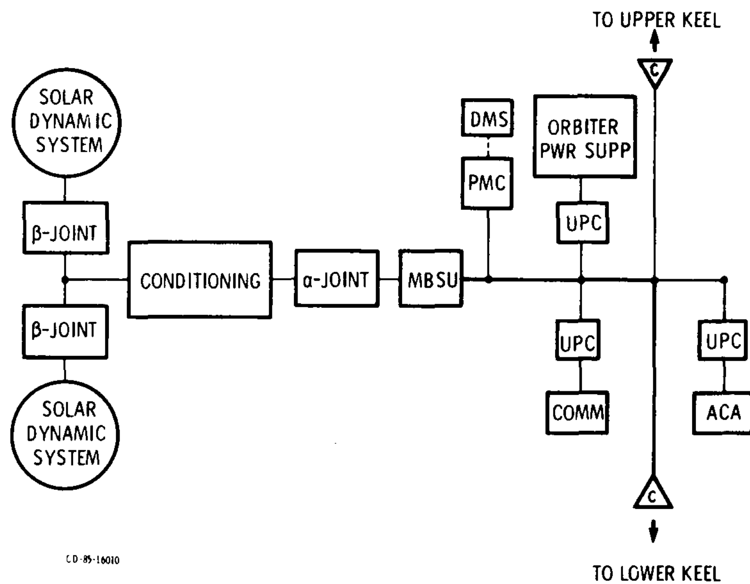

Figure 8.

ADVANCED DEVELOPMENT TASKS

- POWER COMPONENT AND SUBSYSTEM DEVELOPMENT
  - FUNCTIONAL AND LIFE TESTING
  - SYSTEM DEMONSTRATION
- POWER MANAGEMENT INTEGRATED CONTROL NETWORK
  - COMPUTER CONTROL HARDWARE
  - NETWORK CONTROL SCHEME
  - SYSTEM SOFTWARE
- POWER SYSTEM SIMULATION AND CONTROL
  - COMPONENT AND SYSTEM MODELS
  - REAL AND NON - REAL TIME SIMULATION
  - CONTROL ALGORITHMS
  - POWER MANAGEMENT ALGORITHMS
- POWER MANAGEMENT AND DISTRIBUTION SYSTEM DEMONSTRATIONS

CD-85-16013

Figure 9.

ADVANCED DEVELOPMENT

POWER COMPONENTS

- ROLL RINGS
- TRANSMISSION LINE
- AC POWER CONTROLLERS AND BUS ISOLATORS
- SEMI - CONDUCTOR PACKAGING
- DC SWITCHGEAR

POWER SYSTEM HARDWARE

- HIGH FREQUENCY (20KHZ) POWER SYSTEM
- HIGH EFFICIENCY CONVERTERS
- LOW FREQUENCY (400 Hz) POWER SYSTEM

POWER MANAGEMENT AND CONTROL

- NETWORK CONTROL SYSTEM
- SIMULATIONS
- CONTROL ALGORITHMS

CD-85-16012

Figure 10.

ORIGINAL PAGE IS
OF POOR QUALITY

Figure 11.

LEWIS RESEARCH CENTER POWER SYSTEMS TEST FACILITY

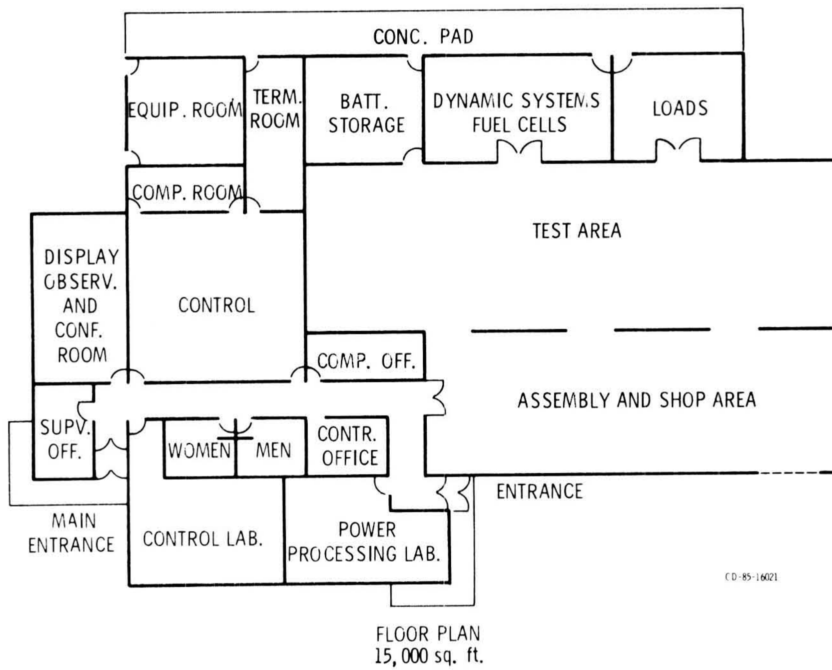

Figure 12.

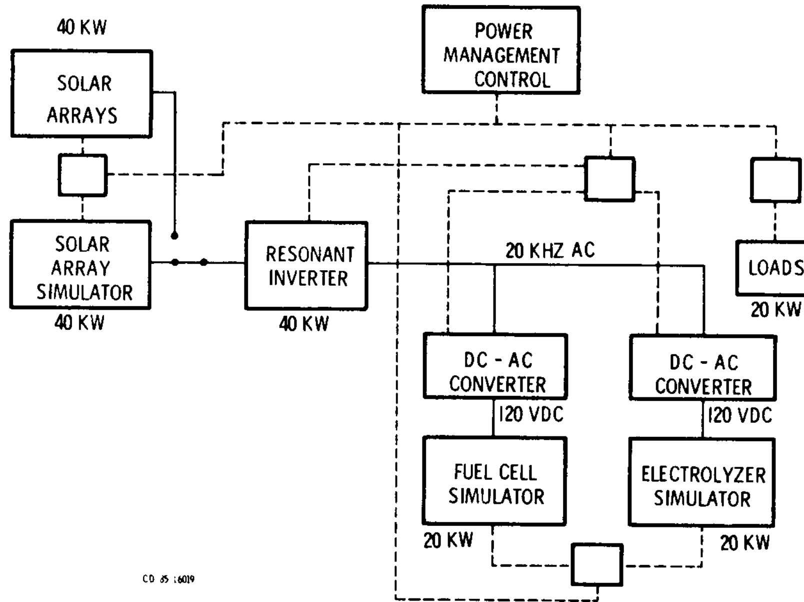

Figure 13.

N86-17870

CELL RESEARCH AND TECHNOLOGY WORKSHOP

James Hutchby
Research Triangle Institute
Research Triangle Park, North Carolina

Four major areas were considered in this workshop. These were (1) the silicon cell, (2) the GaAs cell, (3) the multibandgap cell, and (4) novel ideas. In each area we considered material research issues, cell research issues, and the cell technology that needs development.

THE SILICON CELL: The areas of technical concern that were itemized included base resistivity, cell thickness, back (and front) surface field layers, back (and front) surface passivation, contact area, passivation under contacts, surface texturization vs broad band AR coatings, ion-implanted vs diffused emitters, and radiation hardness (Lithium doping, thin emitters, lead doping).

Among the questions raised concerning the silicon cell were:
1. What can GaAs researchers learn from Si technology?
2. Can the new, high efficiency Si cells be manufactured?
3. What about Pb doping to enhance radiation tolerance?
4. Are top contacts reliable for high voltage (700 mV) cells?

It was generally agreed that:
1. 16 percent AMO silicon cell can be manufactured.
2. 18 percent AMO is still a good goal for the planar junction silicon cell.
3. Surface passivation is a key barrier. Promising approaches to SRV control include the use of GaP isotype heterojunction, a-Si:H, and SIPOS.
4. Texturized surfaces may be good for some applications, but cell heating problems certainly have to be addressed.
5. Both ion implantation and diffusion result in comparable efficiencies.
6. User requirements should be driver in cell development funding.

Recommendations for silicon research:
1. Surface passivation techniques should be developed, especially critical for low resistivity cells. Recommended approaches include GaP isotype heterojunction, a-Si:H, poly Si, thermal SiO_2, PC-CVD, and SIPOS.
2. Techniques for passivation under contacts should be developed.
3. Subsequent to the solution of the SRV control problem, thin cell technology should be developed, both for high efficiency and radiation hardness.

THE GALLIUM ARSENIDE CELL: The areas of concern that were brought up included the N/P vs P/N argument, means of passivating both N-type and P-type surfaces, the use of graded bandgap structures, manufacturability, scaleability, cost vs efficiency, material purity, growth processes - LPE vs OMCVD, and cell thickness.

The questions raised concerning the GaAs cell were:
1. What limits performance of GaAs cell?
2. Is substrate development required (cutting, polishing, cleaning, QC, etc.)?
3. Is OMPVE improvement required?

PRECEDING PAGE BLANK NOT FILMED

4. OMVPE or LPE Layer perfection, thickness control, window composition, safety issues (AsH_3 vs TMAs).
5. What are the radiation induced defects in GaAs?
6. What is the status of defect passivation technology?
7. What causes voltage and current degradation during array fabrication?
8. What are the causes of metallization stability?
9. What role do thermal and mechanical stresses have on cell performance?

Conclusions/recommendations for GaAs research:

1. SRV control key issue here, also. Research needed to determine adequate passivation techniques.
2. Substrate materials also need improvement.
3. Higher utilization of OMVPE materials required.
4. The purity of Ga, Al, and As dopant sources must be improved.
5. LPE vs OMVPE question not answered. OMVPE offers higher throughput and better thickness control.
6. GaAs planar cell efficiency arbitrarily set at 20 percent higher planar silicon cell efficiency, based on past experience.
7. Experimental/theoretical research needed to understand radiation effects on both bulk and junction.
8. N/P vs P/N not clear experimentally.
9. Users need GaAs thickness less than 1/2 that of present silicon cell thickness.

THE MULTIJUNCTION CELL: The following questions/issues were raised:

1. Monolithic vs mechanical stack?
2. 2 vs 4 terminal?
3. What is best top cell material for two layer stack (AlGaAs vs GaAsP)?
4. What is best bottom cell material for two layer stack (Si, Ge, InGaAs, GaAsSb)?
5. What are the prospects for a 25-30 percent AMO cell in the near term, far term?
6. What are the stresses on the multibandgap cell in the space environment?

The following conclusions were generally agreed to:

1. Beginning of life efficiency: 2 junction 25 percent, 3 junction 30 percent.
2. End of life efficiency: 2 junction ??, 3 junction ??.
3. Near term goal should be a mechanical stack.
4. Far term goal should be a monolithic stack.
5. Top cell materials: AlGaAs or GaAsP.
6. Bottom cell materials: monolithic Si or InGaAs, mechanical GaAsSb.

NOVEL CELLS: The following three suggestions were briefly discussed:

1. A GaAs thin cell on a GaP substrate.
2. Compositional superlattices or NiPi cells.
3. InP radiation hard cell.

N86-17871

SPACE ENVIRONMENT WORKSHOP

W.E. Horne, Chairman
Boeing Aerospace Company
Seattle, Washington

The Space Environment Workshop started its deliberations by ranking the various environmental effects according to their perceived importance. Figure 1 is a semi-quantitative summary of the result. Obviously, the relative importance of any particular environmental component listed must be viewed within the context of the anticipated mission environment. Nonetheless, the chart does serve as an indication of what have historically been the major environmental concerns for operating space power systems. The workshop presented its findings in a question and answer format, which is reproduced here with minimal editing.

E-2706-33

RADIATION EFFECTS:

Silicon Technology-

Are high-efficiency, low-resistivity silicon cells suitable for high-radiation orbits?

Conclusion:
They are not suitable in their present state.

Recommendation:
The silicon cells are promising enough to warrant further research.

Areas to investigate:
(1) New base dopants
(2) Base thickness
(3) Dopant (p^+) profiles
(4) Low-resistivity MVJ cell (perhaps)

Is the BOL efficiency of back-illuminated, high-resistivity cells ($\rho \geq 500$ Ω-cm) high enough?

Conclusion:
No, but if the BOL performance can be raised to 14 to 15 percent, then its radiation resistance makes it very competitive.

Recommendation:
Improve fabrication techniques and make cells thinner.

Gallium Arsenide Technology-

What environmental considerations are important in GaAs structures?

Conclusions:
(1) Radiation resistance of n on p versus p on n GaAs cells needs to be explored on cells of both type that are optimized for radiation resistance.

(2) 1-MeV electron data are suitable for evaluating GaAs cells, but more electron energy dependence data are needed in order to define cell limitations.
(3) More work is needed in omnidirectional proton environments (at variable energies).

Area of concern:
As the efficiency of GaAs cells is optimized, will new radiation damage mechanisms dominate their low fluence response?

Multibandgap Cells-
What is the radiation performance of multibandgap cells?

Conclusion:
Since relatively little is known, we urge the community to make available state-of-the-art samples for testing and evaluation.

Other Cell Technologies-

Areas to investigate:

Thin films
- (1) Amorphous silicon cells
- (2) $CuInSe_2$ cells

Geometries
- (1) Superlattice structures
- (2) Ultrathin cells

Other materials
- (1) Lithium counterdoping
- (2) Indium phosphide
- (3) Other high absorption materials

What other methods can improve power system performance in high radiation orbits?

Conclusions:
(1) Annealing is an acceptable approach if temperatures can be kept compatible with array materials.
(2) Concentrators help by shielding cells if optical surfaces are hard.

Recommendation:
NASA should look at ultralightweight radiation resistant concentrators.

UV RADIATION:

What problems does UV pose for power systems?

Conclusions:
(1) UV still presents problems for some coverglass/adhesive systems.
(2) UV may be a problem for coatings that may be required to harden dielectric surfaces against atomic oxygen and charging/arcing phenomena in plasma.

ATOMIC OXYGEN:

Conclusion:
Atomic oxygen is potentially a severe problem for array materials in LEO.

Recommendations:
(1) A basic materials studies approach is needed to understand the nature and extent of the problem.
(2) Develop better ground simulation techniques.

PLASMA EFFECTS:

Conclusion:
Plasma effects (leakage, arcing, EMI) are a serious power system problem.

Area of concern:
Size of test articles being flown may lead to different conclusions than would be the case if large arrays were flown.

Recommendation:
Prepare an experiment to fly a large test sample (>10 m^2) in order to determine scalability of small specimen results.

THERMAL CYCLING:

Area of concern:
What are the effects of mismatched intersections of multiple bandgap cells?

Recommendation:
Photovoltaic community should make state-of-the-art specimens available for evaluation.

ADDITIONAL RECOMMENDATIONS IN AREAS OF UV RADIATION, ATOMIC OXYGEN, PLASMA EFFECTS, AND THERMAL CYCLING:

Recommendations:
Begin development of coatings/materials with following properties:
(1) Good thermal emittance
(2) Resistant to UV
(3) Resistant to atomic oxygen
(4) Conductive

Approach should be more basic than simply a quick fix for existing materials if 20-year lifetime is to be achieved.

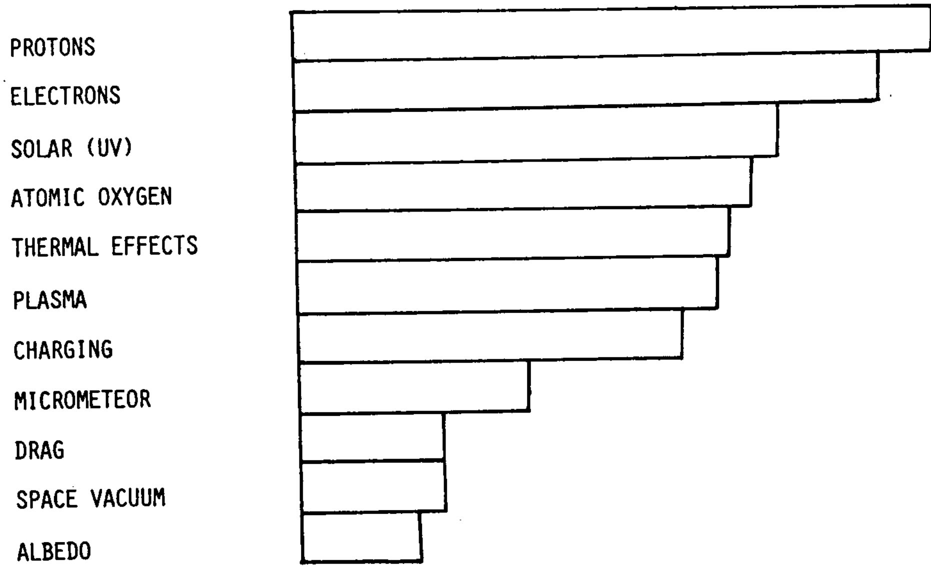

Figure 1. - Environment importance survey.

N86-17872

ARRAY TECHNOLOGY AND APPLICATIONS

Paul Goldsmith
TRW Space and Technology Group
Redondo Beach, California

ROLE OF PV IN ADVANCED MISSIONS

- What limits use of PV
  - Cost, panel efficiency, system efficiency, control problems, weight, environmental factors
- Limits are mission dependent
- What are mission system goals
- What system goals are required to compete with other power systems
- What goals should be used to drive array technology
- Recommend setting goals and timetable for evolving missions
- Determine both enabling and growth objectives
- Concentrators can have an important role

MISSION GOAL ANALYSIS

- Defined as critical need
- Allows analysis of commonality
- Defines multi-mission benefits of PV funding

Example

*Missions	Pwr. kW	W/kg	W/M2	Life years
1	200		300	5-10
2	5-25	50		10
3	10-50	20	200	5
4	5-10	150		5

*1. LEO, high power
2. GEO, medium power, lightweight
3. Intermediate, radiation resistant
4. Interplanetary, ultralightweight

TESTING OF ADVANCED CONCEPTS

- o Flight and ground demonstration critical to getting project support
- o Expensive facilities required for testing concentrator and ultralight flexible arrays
- o What risks related to minimum testing are acceptable to projects
- o Need to coordinate and expedite flight experiments
- o Testing needed to provide feedback to device development

COST CONSIDERATIONS

- o Relationship between array and system cost is not straight line
- o Effect of array on system level costs are mission dependent and include:
  - -- Array development, fabrication and test
  - -- System testing
  - -- Array life
  - -- Related PV system costs
  - -- Costs related to requirements on other spacecraft systems
- o PV community needs to become more aware and active in system level design and planning

VIABILITY OF U.S. ARRAY INDUSTRY

- o Minimum funding of panel technology
- o European structures superior for many near term missions
- o Heavy European government support
- o U.S. companies making serious make/buy decisions for European arrays
- o More U.S. structural programs required for both near and far term missions

1. Report No.	2. Government Accession No.	3. Recipient's Catalog No.
NASA CP-2408		
4. Title and Subtitle SPACE PHOTOVOLTAIC RESEARCH AND TECHNOLOGY - 1985 High Efficiency, Space Environment, and Array Technology		5. Report Date
		6. Performing Organization Code 506-55-42
7. Author(s)		8. Performing Organization Report No. E-2706
		10. Work Unit No.
9. Performing Organization Name and Address National Aeronautics and Space Administration Lewis Research Center Cleveland, Ohio 44135		11. Contract or Grant No.
		13. Type of Report and Period Covered Conference Publication
12. Sponsoring Agency Name and Address National Aeronautics and Space Administration Washington, D.C. 20546		14. Sponsoring Agency Code
15. Supplementary Notes		

16. Abstract

This three-day conference, seventh in a series that began in 1974, was held at the NASA Lewis Research Center on April 30 - May 2, 1985. The conference provided a forum to assess the progress made, the problems remaining, and the strategy for the future of space photovoltaic research. Papers were presented and workshops conducted in a variety of technical areas, including cell research and technology, space environmental effects, and array technology and applications. The reports of the three workshops are also included in this proceedings.

17. Key Words (Suggested by Author(s))	18. Distribution Statement
Space power; Photovoltaic cells; Solar cells; Solar arrays	Unclassified - unlimited STAR Category 44

19. Security Classif. (of this report)	20. Security Classif. (of this page)	21. No. of pages	22. Price*
Unclassified	Unclassified	302	A14

*For sale by the National Technical Information Service, Springfield, Virginia 22161